RESPONSE OF SUBCHONDRAL BONE AND ARTICULAR CARTILAGE TO JOINT SURFACE INCONGRUITY

An equine osteochondral defect model

Megan Elizabeth Thomas

Orcid ID: 0000-0002-6851-875X

Doctor of Philosophy

April 2019

Faculty of Agricultural and Veterinary Sciences

Thesis submitted in total fulfilment of the degree of Doctor of Philosophy in Veterinary Science.

Abstract

Many diseases and injuries of synovial joints result in a focal loss of articular surface congruity. These conditions are known to lead to degenerative changes within the affected joint and subsequent osteoarthritis (OA). Incongruity due to loss of articular cartilage is also a feature of OA itself. However there is little work specifically investigating how the tissues of a synovial joint respond to loss of congruity. The aim of this study was to observe how articular cartilage and subchondral bone (SCB) respond to a focal loss of surface congruity using an equine model. It was hypothesised that the degree of remodelling and bone volume of SCB is dependent on local loading of the overlying joint surface and that intact cartilage would respond to changes in local surface pressure in a way that attempts to restore congruity.

An osteochondral defect was created in one surface of the midcarpal joint of six adult horses. Two weeks post-operatively the animals began an eight-week treadmill training program. Following this, osteochondral samples were collected from the site of the defect and immediately adjacent to it in the radial carpal bone (Cr), and from the unloaded site directly opposing the defect and a loaded site immediately adjacent to this in the third carpal bone (C3). Control samples were collected from equivalent sites in the sham-operated contralateral limb and from un-operated, untrained control animals. Undemineralised samples were imaged with microCT and backscattered scanning electron microscopy (BSEM) and stained with Masson's Goldner trichrome to measure cartilage thickness and osteoid. Decalcified cryosections were stained for TRAP to identify osteoclasts. Cartilage was examined with routine histology and differential interference contrast microscopy.

In SCB immediately below the Cr lesion in treated joints bone volume fraction (BV/TV) was 32% lower and bone formation and erosion were markedly increased, whereas in the deeper bone formation was increased, erosion activity became less prominent and BV/TV did not change. In the unloaded region of C3 opposing the defect in treated joints the hyaline cartilage (HC) was 50% thicker, while SCB displayed a mild increase in remodelling activity with a net decrease in BV/TV of 5.3%.

In the loaded region adjacent to the lesion in Cr HC was 30% thinner in treated joints while there was no change in SCB parameters. At the loaded site of C3 the HC thickness was unchanged while the calcified cartilage in treated joints was 40% thicker than in controls. In the underlying SCB in treated joints there was a mild reduction in remodelling activity and unchanged BV/TV.

In this equine osteochondral defect model the articular cartilage and SCB of adult synovial joints responded in a focal manner to changes in joint surface congruity. Local unloading due to a loss of surface contact resulted in thickened HC and, in the underlying SCB, increased remodelling activity and loss of bone volume. Focally increased loading resulted in thickened calcified cartilage and decreased SCB bone remodelling activity. These focal responses may play a role in normal joint homeostasis and in the pathogenesis of OA.

Declaration

This is to certify that the following thesis:

- comprises only original work completed by myself except where indicated in the preface (page v),
- contains due acknowledgement in the text to all other material used and,
- is fewer than 80,000 words in length.

Signed:

Megan Thomas

April 2019

Preface

The study concept and design for the work described in this thesis are attributable to Professor Chris Whitton, Professor Eleanor Mackie and Dr. Gareth Trope.

Housing and training of the horses and all surgical and gross post mortem procedures were undertaken at the Veterinary Clinical Centre, School of Animal and Veterinary Sciences at Charles Sturt University, Wagga Wagga, NSW, Australia.

The horses in this trial were sourced, cared for and trained by Dr Gareth Trope, BVSc (Hons), DipVCS, CertES (Orth), MVSc, FANZCVS, Dr Thomas O'Brien, BVSc (Hons) and their team. Surgical creation of the osteochondral defect was performed by Dr Gareth Trope. Post mortem examinations and sample collection were performed by Dr Gareth Trope and Professor Chris Whitton, BVSc FANZCVS (Equine Surgery) PhD.

Lameness evaluations from video recordings were performed by Professor. Chris Whitton and Dr Liz Walmsley, BVSc, MACVSc, MRCVS, FANZCVS (Equine Surgery). Radiographic evaluations were performed by Professor Chris Whitton.

Analysis of synovial fluid was performed by staff at the Veterinary Diagnostic Laboratory, School of Animal and Veterinary Sciences, Charles Sturt University. Synovial membrane specimens were prepared for histology by members of the pathology service at the Melbourne Veterinary School, University of Melbourne and assessed by Dr Andrew Stent (BVSc, PhD, MANZCVS).

The remainder of the work described in this thesis was performed by the student at the University of Melbourne, Faculty of Veterinary and Agricultural Sciences with assistance from those people acknowledged in the following section (page vii).

Funding for this work was provided by The University of Melbourne and Charles Sturt University. The student was supported by the Australian Government through the Australian Postgraduate Award.

Acknowledgements

I am extremely grateful for all the support I have received throughout this project, especially for the invaluable input of my supervisors, without whom this project would not have existed.

My sincere thanks go to Professor Chris Whitton, for developing the project initially, guiding it throughout and for allowing me to be a part of it. I would like to thank him for being available whenever I needed help, for his guidance, advice, financial support and for his skill as an editor.

I would also like to thank Professor Eleanor Mackie for her support, guidance and advice, especially in regards to maintaining scientific rigour and bone histology, and for her assistance in editing the thesis.

I am very grateful to Liliana Tatarczuch who was so very generous with her time and was always willing to help. She is a wonderful mentor and taught me everything I know about preparation of histological sections.

Thanks go also to Dr Gareth Trope for all his work with the horses, without which I would not have had any specimens, and for donating his time and support; and to Professor Simon Bailey for his time and diligence in acting as chair of my supervisory committee.

It was a pleasure to work within the Laboratory of Bone and Muscle Biology in the Melbourne Veterinary School and my thanks especially to Dr Charlie Pagel, Dr

Babatunde Ayodele and Dr Reza Sanaei for all their advice and assistance with laboratory techniques as well as their ongoing friendship.

I would like to thank Dr Fatemeh Malekipour, and Dr Kathryn Stock at the Department of Biomedical Engineering in the Melbourne School of Engineering for their generous advice and technical support for everything regarding microCT scanning of bone.

I am also grateful to Dr. Michiko Mirams for kindly taking the time to teach me what I needed to know about backscattered scanning electron microscopy of equine bone and sectioning and staining methacrylate-embedded bone. Thanks also go to Roger Curtin in the Advanced Microscopy Unit at the University of Melbourne Bio21 Institute, for his guidance and technical support while I was using the scanning electron microscope at their facility.

I am very grateful to Associate Professor Ashvin Thambyah, Professor Neil Broom and their team in the Department of Chemical and Materials Engineering at the University of Auckland for welcoming me so warmly into their group, teaching me all I needed to know about differential interference contrast microscopy and generously making their facilities available to me.

My thanks go to Dr Andrew Stent in the Pathology Department at the Melbourne Veterinary School for his work in assessing synovial histology sections and for taking the time to guide me through the process.

I would also like to say thank you to Professor Natalie Sims of the Bone Cell Biology and Disease Unit at the St Vincents Institute for encouraging me and always taking an interest in my work, her enthusiasm is infectious.

Untold thanks and love go to dad who never refused my endless requests for advice and technological support and gave his steadfast moral support unasked. Finally, thanks and love to mum, my family and my friends who, each in their way, all helped me through.

Table of Contents

CHAPTER 1: LITERATURE REVIEW 1

1.1 Introduction 1

1.2. Synovial joint anatomy and histology 2

1.2.1. Overview 2

1.2.2 Articular cartilage 3

1.2.3 Subchondral bone 8

1.2.4 Joint capsule 11

1.2.5 Synovial fluid 13

1.2.6 Periarticular structures 14

1.2.7 The equine carpus 14

1.3 Normal function and homeostasis of synovial joints 16

1.3.1 Function 16

1.3.2 Homeostasis 18

1.4 Pathophysiology of joint disease 39

1.5 The study of joint disease 45

1.5.1 Animal models 45

1.5.2 Clinical and laboratory techniques 50

1.6 Osteochondral defects and joint incongruity 56

1.7 Aims and Hypotheses 64

CHAPTER 2: GENERAL MATERIALS AND METHODS 66

2.1 Live animal procedures 66

2.1.1 Selection of horses for inclusion 66

2.1.2 Surgical procedure 68

2.1.3. Exercise protocol 70

2.1.4. Bone labelling 71

2.1.5. Lameness evaluation 71

2.1.6. Synovial fluid collection 71

2.1.7. Radiographic evaluation 72

2.2 Post mortem procedures 72

2.2.1 Macroscopic examination 72

2.2.2 Synovial membrane collection 72

2.2.3. Osteochondral Sample collection 73

2.2.4 Bone analysis 77

2.2.5 Cartilage Analysis 93

2.3 Statistical Methods 98

CHAPTER 3: CLINICAL FINDINGS, GROSS PATHOLOGY AND SYNOVIAL HISTOPATHOLOGY 100

3.1 Introduction 100

3.2 Materials and Methods 102

3.2.1 Lameness evaluation, flexion tests and carpal circumference and effusion scores.....102

3.2.2 Synovial fluid evaluation 104

3.2.3 Radiographic evaluation 104

3.2.4 Post mortem macroscopic examination 105

3.2.5 Synovial histopathology..... 107

3.3 Results..... 109

3.3.1 Lameness evaluation, flexion test scores, carpal circumference and effusion scores.....109

3.3.2 Synovial fluid evaluation 114

3.3.3 Radiographic evaluation 117

3.3.4 Macroscopic examination 119

3.3.5 Synovial histopathology..... 125

3.4 Discussion 129

3.4.1 Summary of major findings 129

3.4.2 Comparison with current literature..... 129

3.4.3 Interpretation of major findings 135

3.4.4 Conclusion..... 140

CHAPTER 4: BONE PARAMETERS OF THE RADIAL CARPAL BONE..... 142

4.1 Introduction 142

4.2 Materials and Methods..... 143

4.3 Results 149

4.3.1 Region below the defect 156

4.3.2 Region adjacent to the defect 185

4.4 Discussion 200

4.4.1 Summary of major findings 200

4.4.2 Comparison with current literature 200

4.4.3 Interpretation of major findings 203

4.4.6 Conclusion 210

CHAPTER 5: BONE PARAMETERS OF THE THIRD CARPAL BONE 211

5.1 Introduction 211

5.2 Materials and Methods 214

5.3 Results 219

5.3.1 Region opposing the defect 222

5.3.2 Weight bearing region 242

5.4 Discussion 251

5.4.1 Summary of major findings 251

5.4.2 Comparison with current literature 251

5.4.3 Interpretation of major findings 255

5.4.6 Conclusion 260

CHAPTER 6: CARTILAGE PARAMETERS 261

6.1 Introduction 261

6.2 Materials and Methods 263

6.2.1 Cartilage histomorphology - C3 and Cu 263

6.2.2 Differential Interference Contrast microscopy - C3 cartilage 267

6.2.3 Cartilage thickness on Masson's Goldner stained sections 273

6.2.4 Calcified cartilage thickness and tidemark number on BSEM 273

6.2.5 Tidemark fluorescence 276

6.3 Results 276

6.3.1 Radial Carpal bone adjacent to the defect 279

6.3.2 Third Carpal bone opposing the defect 283

6.3.3 Third Carpal bone weight bearing region 293

6.3.4 Ulnar Carpal bone 299

6.4 Discussion 300

6.4.1 Summary of major findings 300

6.4.2 Comparison with current literature 300

6.4.3 Interpretation of major findings 306

6.4.6 Conclusion 311

CHAPTER 7: GENERAL DISCUSSION 312

7.1 Summary 312

7.2 Interpretation 314

7.2.1 Effect of articular surface incongruity on joint homeostasis 314

7.2.2 Role of articular surface incongruity in joint pathology..... 315

7.2.3 The role of inflammation and biochemical changes within the joint 317

7.3 Limitations 319

7.4 Further study..... 323

7.5 Conclusion..... 326

REFERENCES 327

APPENDICES 379

Appendix 1: Key to colours on individual value graphs..... 379

Appendix 2: Position of Cr defect on undecalcified sections 379

Appendix 3: Osteocyte lacunae size, region below the lesion, Cr 380

Appendix 4: Incidental cartilage lesions..... 382

List of Figures and Tables

Figure 1.1 Generalised diagram of a synovial joint showing the major anatomical structures **4**

Figure 1.2 Differential Interference Contrast microscopy image of equine third carpal bone joint surface **4**

Figure 1.3 Diagram of the zones of hyaline cartilage depicting predominant chondrocyte morphology and collagen orientation **6**

Figure 1.4 Organisation of collagen and PGs in articular cartilage ECM. **8**

Figure 1.5 Backscattered scanning electron microscopy images of subchondral bone from equine third carpal bone showing the arrangement of compact and trabecular subchondral bone **9**

Figure 1.6 Examples of osteoclasts (arrows) stained for tartrate resistant acid phosphatase within resorption spaces (A) and osteoblasts (open arrow heads) on an osteoid seam (pink) in a Masson's Goldner trichrome stained section (B). **11**

Figure 1.7 Histological section of synovium from an equine carpus **13**

Figure 1.8 Dorso-palmar (A) and flexed lateral (B) radiographic views of the equine carpus **15**

Figure 1.9 Equine carpal bones, dorsal view **15**

Figure 1.10 Diagram of the remodelling process on a bone surface **33**

Table 2.1 Signalment and limb randomly selected for treatment of trial horses. **67**

Table 2.2 Signalment of horses selected for the un-operated, untrained control group. **67**

Figure 2.1 Arthroscopy image of osteochondral defect **69**

Table 2.3 Treadmill training protocol. **70**

Figure 2.2 Sectioning of the radial carpal bones. **73**

Figure 2.3 Example of a section of the radial carpal bone from horse 1 ..... **74**

Figure 2.4 Sectioning of the third carpal bones. **75**

Figure 2.5 Example of a section of the third carpal bone from horse 1. ..... **75**

Table 2.4 Method of fixation and purpose of each section from C3 and Cr **76**

Figure 2.6 Example of a reconstructed BSEM image of the disto-dorsal quadrant of Cr **81**

Figure 2.7 Example of a reconstructed BSEM image of the proximo-dorsal quadrant of C3 ..... **81**

Figure 2.8 Eroded (open arrow heads) and mineralising (filled arrow heads) perimeters on a high magnification BSEM image of SCB **83**

Figure 2.9 Examples of 8-10 um thick undecalcified sections of C3 prior to deplasticisation and staining. **84**

Figure 2.10 Masson's Goldner stained, undecalcified section of C3 from the control limb of horse 1. ..... **85**

Figure 2.11 Masson's Goldner stained section **86**

Figure 2.12 Example of an unstained, 8-10 um thick section of C3, deplasticised and mounted in gelvatol under a coverslip, used for fluorochrome analysis. **87**

Figure 2.13 Fluorescent microscopy images showing single (A), double (B) and triple (C) oxytetracycline labels **88**

Table 2.5 Components of TRAP stain **91**

Figure 2.14 Examples of osteoclasts (arrow heads) stained pink with pale-staining nuclei (arrows).A: bright field image of a cryosection stained for TRAP, f **92**

Figure 2.15 Example of a decalcified and trimmed osteochondral section prior to embedding for histomorphology **94**

Figure 2.16 Example of an osteochondral specimen embedded in Spurr's resin prior to sectioning for histomorphology. **94**

Figure 2.17 Methylene blue stained semi-thin section **95**

Figure 2.18 Dissecting microscope images of partially decalcified sections of cartilage and SCB cut from C3 of horse 1 ..... **97**

Figure 2.19 Brightfield images of unstained, partially decalcified, 20µm cryosections of the articular surface of C3 ..... **97**

Table 3.1 American Association of Equine Practitioners lameness grading scale . **103**

Table 3.2 Scoring system used for grading of macroscopic joint pathology **106**

Table 3.3 Microscopic Grading System for synovial membrane histology **108**

Table 3.4 Median lameness grades. **110**

Table 3.5 Carpal flexion and carpal effusion scores. **111**

Figure 3.1 Median Carpal Effusion Scores. **112**

Table 3.6 Carpal circumference measurements **113**

Figure 3.2 Mean carpal circumference **114**

Figure 3.3 Mean total protein concentration (TP, g/L) of synovial fluid through the trial. **115**

Table 3.7 Total protein concentration (TP, g/L) and total nucleated cell count (TNCC, x109cells/L) of synovial fluid. **116**

Figure 3.4 Mean total nucleated cell count (TNCC, x109cells/L) of synovial fluid through the trial. **117**

Table 3.8 Radiographic scores. **118**

Table 3.9 Cr osteochondral defect size at post mortem. **119**

Table 3.10 Macroscopic pathology scores. **121**

Figure 3.5 Gross post mortem photographs of treated mid-carpal joints **122**

Figure 3.6 Post mortem photographs of Crs from horse 4 showing peri-articular modelling on the dorsal articular margin **123**

Figure 3.7 Peri-articular modelling score. **123**

Figure 3.8 Gross post mortem images showing cartilage lesions (arrows) in control joints. **124**

Figure 3.9 Combined macroscopic pathology score: cartilage erosion, peri-articular modelling and synovial inflammation scores **124**

Table 3.11 Total synovial pathology scores **125**

Figure 3.10 Synovial pathology scores **126**

Figure 3.11 Synovium from the dorso-medial aspect of the mid-carpal joint. **127**

Figure 3.12 Synovium from the dorso-lateral aspect of the mid-carpal joint. **128**

Table 4.1 Location of dorsal edge of Cr ROIs **144**

Figure 4.1a Left: MicroCT images of Cr (top) and C3 (bottom) from the treated limb of Horse 5. Right: Radial carpal bone ROIs **145**

Figure 4.1b MicroCT image of dorso-distal Cr from the treated limb of Horse 5 showing measurement of the position of the dorsal articular margin. **146**

Table 4.2 Position of base of defect in mm below the osteochondral junction **147**

Figure 4.2 ROIs for osteoclast counts on sections stained for TRAP **148**

Figure 4.3 MicroCT images of Cr bones **150**

Figure 4.4 BSEM images of Cr bones **151**

Figure 4.5 Cryosections stained for TRAP **152**

Figure 4.6 Masson's Goldner stained sections showing varying degrees of fibrocartilaginous tissue (arrows) within defects in treated Cr bones. **153**

Figure 4.7 Masson's Goldner stained sections of the treated Cr from trial horses 4 (A and B) and 5 (C and D), showing islands of chondroid tissue within SCB voids (arrows)..... **154**

Figure 4.8 Calcified cartilage defect (arrowheads) and surrounding resorption spaces (arrows) in the dorsal weight bearing region of Cr from the control limb of Horse 2**.** **155**

Figure 4.9 Examples of mild (B, Horse 3) and more marked (D, Horse 1) peri-articular modelling..... **156**

Table 4.3 Measures of bone volume and bone surface, Cr, region below the defect. **..** **158**

Figure 4.10 BSEM images showing increased porosity in the treated limbs, Cr, region below the defect, 0-3mm deep to the cartilage. **159**

Figure 4.11 Bone volume fraction (Bone Volume/ Total Volume) and bone surface ratio (Bone surface/ Bone Volume [mm-1]), below the lesion on the radial carpal bone **160**

Table 4.4 Trabecular parameters from MicroCT images, Cr, region below the defect. **162**

Figure 4.12 Trabecular parameters from MicroCT images, Cr, region below the defect, 0-3 and 9-12mm deep to the cartilage..... **163**

Table 4.5 Mineralisation parameters from microCT, Cr, region below the lesion**. 165**

Figure 4.13 Tissue mineral density (TMD, mgHA/cm3) and bone material density (BMD, mgHA/cm3) measured on microCT images, Cr, region below the lesion, 0-3mm and 9-12mm deep to the cartilage. **166**

Table 4.6 Erosion and formation parameters from BSEM images, Cr, region deep to the defect **168**

Figure 4.14 Erosion and formation parameters from BSEM images, Cr, region deep to the defect, 0-3mm and 3-6mm deep to the cartilage. **169**

Figure 4.15 BSEM images showing increased mineralising surface (arrowheads) in the treated limbs: Cr, region below the defect, 3-6mm deep to the cartilage. **170**

Figure 4.16 Mineralising perimeter (mm-1) and ratio of erosion to mineralising perimeter, measured on BSEM images, Cr, region below the lesion, 6-9mm and 9-12mm deep to the cartilage. **171**

Figure 4.17 Number of osteoclasts (cells/mm2) on TRAP stained sections, Cr, region below the lesion, 0-3.3mm and 3.3-6.6mm deep to the cartilage. **172**

Table 4.7 Cellular markers of remodelling, Cr, region deep to the defect. **173**

Figure 4.18 Cryosections stained for TRAP showing increased osteoclasts (arrows) in the treated limbs: Cr, region deep to the lesion. **174**

Figure 4.19 Osteoid perimeter as a percentage of bone perimeter and osteoid width (um) Cr, region below the lesion, 0-3mm and 3-6mm deep to the cartilage. **175**

Figure 4.20 Masson's Goldner stained sections showing increased osteoid (stained pink) in treated limbs, Cr, region below the lesion, 0-3mm deep to articular surface. **176**

Figure 4.21 Osteoid perimeter as a percentage of bone perimeter and osteoid width (μm), Cr, region below the lesion, 6-9mm and 9-12mm deep to the cartilage **177**

Figure 4.22 Masson's Goldner stained sections showing increased osteoid (stained pink) in treated limbs, Cr, region below the lesion, 6-9mm deep to articular surface. **178**

Table 4.8 Measures of fluorochrome labels, Cr, region deep to the defect **180**

Figure 4.23 Measures of oxytetracycline labels, Cr, region below the lesion, 0-3mm and 3-6mm deep to the cartilage. **181**

Fig 4.24 Fluorescent light microscopy images of undecalcified, unstained sections showing an increase in labelled perimeter (arrowheads) at 0-3mm deep to the cartilage and an increase in single labelled perimeter in treated limbs at 3-6mm deep to the cartilage: Cr, region deep to the lesion. **182**

Figure 4.25 Measures of oxytetracycline labels, Cr, region below the lesion, 6-9mm and 9-12mm deep to the cartilage. **183**

Fig 4.26 Fluorescent light microscopy images of undecalcified, unstained, sections showing an increase in labelled perimeter (arrowheads) in treated limbs at 6-9 and 9-12mm deep to the cartilage: Cr, region deep to the lesion. **184**

Figure 4.27 Porosity (%) measured on BSEM images, Cr, region adjacent to the lesion, 0-3mm deep to the cartilage. **185**

Table 4.9 Measures of bone volume, bone surface and trabecular **186**

Figure 4.28 BSEM images, Cr, region adjacent to the defect, 0-3mm deep to the cartilage. **187**

Table 4.10 Erosion and formation parameters from BSEM images, Cr, region adjacent to the defect. **189**

Figure 4.29 Erosion and formation parameters measured on BSEM images, Cr, region adjacent to the lesion. **190**

Figure 4.30 BSEM images showing increased mineralizing perimeter (arrowheads) in treated limbs: Cr, region adjacent to the defect, 9-12mm deep to the cartilage. **191**

Table 4.11 Cellular markers of remodelling, Cr, region adjacent to the defect **193**

Figure 4.31 Osteoid parameters from MG stained sections, Cr, region adjacent to the defect, 6-9mm and 9-12mm deep to the cartilage **194**

Figure 4.32 Osteoid perimeter as a percentage of bone perimeter and osteoid width (μm), on MG stained sections, Cr, region adjacent to the defect, 3-6mm deep to the cartilage. **..... 195**

Figure 4.33 Masson's Goldner stained sections in which osteoid is stained pink. There is an increased osteoid width and area in the treated limbs compared to the untrained controls: Cr, region adjacent to the lesion, 6-9mm deep to articular cartilage. **.... 196**

Figure 4.34 Masson's Goldner stained sections in which osteoid is stained pink. Osteoid width is greater in treated limbs compared to the untrained controls: Cr, region adjacent to the lesion, 9-12mm deep to articular cartilage. **..... 197**

Figure 4.35 Single-labelled perimeter as a percentage of bone perimeter (%), Cr, region adjacent to the lesion, 3-6mm deep to the cartilage. **..... 198**

Table 4.12 Measures of fluorochrome labels, Cr, region adjacent to the defect, **..... 199**

Table 5.1 Location of dorsal edge of C3 ROIs in individual horses, mm palmar to the dorsal articular margin in a line parallel to joint surface. **..... 215**

Figure 5.1a Left: MicroCT images of Cr (top) and C3 (bottom) from the treated limb of Horse 5. The white box indicates the enlarged area on the right. Right: C3 ROIs**.** **..... 216**

Figure 5.1b MicroCT image of dorso-proximal C3 from the treated limb of Horse 5 showing measurement of the position of the dorsal articular margin**. 216**

Figure 5.2 Image of a cryosection stained for TRAP, C3, Horse 4, control limb depicting ROIs **..... 218**

Figure 5.3 MicroCT (A) and BSEM (B and C) images showing an area of calcified cartilage and subchondral bone damage (arrows) in the proximal articular surface of C3 from the control limb of Horse 6. **..... 219**

Figure 5.4 MicroCT images of C3 bones. **..... 220**

Figure 5.5 Examples of mild (B, Horse 3) and more marked (D, Horse 4) peri-articular modelling **221**

Table 5.2 Measures of bone volume and bone surface in the region opposing the defect, C3. ..... **223**

Figure 5.6 Bone Volume Fraction (BV/TV) measured on microCT images and porosity (%) measured on BSEM images, C3, region opposing the defect. **224**

Figure 5.7 Measures of bone surface, C3, region opposing the lesion. **225**

Figure 5.8 BSEM images, C3, region opposing the defect, 0-3mm deep to the cartilage **226**

Figure 5.9 Bone surface per bone volume (mm-1) C3, at different depths deep to the cartilage in the region opposing the lesion, measured on microCT images. **227**

Table 5.3 Trabecular parameters and mineral density measurements from MicroCT images, C3, region opposing the lesion. **229**

Figure 5.10 Trabecular parameters and tissue mineral density measured on microCT images, C3, region opposing the lesion, 3-6mm and 9-9mm deep to the cartilage. **230**

Figure 5.11 Active perimeter per bone area (mm-1) measured on BSEM images, C3, region opposing the lesion, 0-1mm deep to the cartilage. **231**

Table 5.4 Erosion and formation parameters from BSEM images, C3, region opposing the lesion. **232**

Figure 5.12 Erosion perimeter and mineralising perimeter per bone area (mm-1) measured on BSEM images, C3, region opposing the lesion, 0-1mm deep to the cartilage. **233**

Figure 5.13 Osteoclast number (cells/mm2) measured on TRAP stained cryosections, C3, region opposing the lesion, 3.3-6.6mm deep to the cartilage. **234**

Table 5.5 Cellular markers of remodelling and measures of fluorochrome labelling, C3, region opposing the defect. **235**

Figure 5.14 TRAP stained sections, C3, region opposing the lesion, 3.3-6.6mm deep to the cartilage..... **236**

Figure 5.15 Masson's Goldner stained sections of C3, region opposing the lesion, 0-3mm deep to cartilage **237**

Figure 5.16 Osteoid width (um) measured on Masson's-Goldner stained sections, C3, region opposing the lesion, 0-3.0mm deep to the cartilage. **238**

Figure 5.17 Measures of fluorochrome labelling, C3, region opposing lesion. **239**

Figure 5.18 Unstained, undecalcified sections, fluorescent light microscopy of C3, region opposing the lesion, 3-6mm deep to the surface. **240**

Figure 5.19 Enlargements from Figure 5.18 showing fluorescent labels (arrowheads) in treated limbs of Horse 1 (A), Horse 2 (B) and Horse 5 (C). C3, region opposing the lesion, 3-6mm deep to surface **241**

Figure 5.20 Pore perimeter (mm-1), measured on BSEM images, C3, weight bearing region, 0-3mm deep to the cartilage..... **242**

Table 5.6 Measures of bone volume and bone surface in the weight bearing region, C3 ..... **243**

Figure 5.21 BSEM images, C3, weight bearing region, 0-3mm deep to the cartilage. **244**

Figure 5.22 Erosion and formation parameters from BSEM images, C3, weight bearing region, 0-3mm deep to the cartilage. **246**

Table 5.7 Erosion and formation parameters from BSEM images and cellular markers of erosion and formation, C3, weight bearing region. **247**

Figure 5.23 Osteoclast number (cells/mm2) measured on TRAP stained cryosections, C3, weight bearing region, 0-3.3mm deep to the cartilage. **248**

Figure 5.24 Osteoid parameters measured on Masson's Goldner stained sections, C3, region adjacent to the defect. **249**

Figure 5.25 Masson's Goldner stained sections, C3, weight bearing region, 0-3mm deep to cartilage **250**

Figure 6.1 Methylene blue stained semi-thin sections showing examples of metachromatic staining..... **264**

Table 6.1 Semi-quantitative scoring system used to assess cartilage pathology on methylene blue stained semi-thin sections (Modified from McIlwraith et al. 2010).. ..... **265**

Figure 6.2 Formula for calculating the combined cartilage pathology score for the entire surface of C3. ..... **266**

Figure 6.3 Measurement of total (A), hyaline (B) and calcified (C) cartilage thickness from DIC images..... **268**

Figure 6.4 Tangential layer thickness measurement on DIC images. **269**

Figure 6.5 Measurement of tangential cell aspect ratio. **270**

Figure 6.6 Estimation of rugosity from DIC images **271**

Figure 6.7 DIC images showing chondrocyte clustering, collagen crimping and collagen fibrillation **272**

Figure 6.8 Areas used for C3 cartilage thickness measurements from Masson's Goldner stained sections. **274**

Figure 6.9 Calcified cartilage (CC) thickness on BSEM images **275**

Figure 6.10 Positions of measurements of number of tidemarks **275**

Figure 6.11 Fibrillation and fissuring (arrow) of hyaline cartilage opposing the dorsal edge of the osteochondral defect. **277**

Figure 6.12 DIC images of the superficial cartilage of C3 in the region opposing the edge of the defect **277**

Figure 6.13 Combined Cartilage pathology score for the entire C3 articular surface **278**

Figure 6.14 Hyaline cartilage thickness (mm), Cr, weight bearing region. From Masson's Goldner stained sections. **279**

Table 6.2 Cartilage thickness and TM number in the weight bearing region of Cr..... ..... **280**

Figure 6.15 Hyaline cartilage (pink or pink and pale green) of the weight bearing region of Cr, dorsal to the defect **281**

Figure 6.16 Mean number of tidemarks, Cr, weight bearing region from BSEM images (original magnification 200x). **282**

Figure 6.17 Hyaline cartilage thickness (mm), C3, region opposing the lesion. From MG stained sections. **283**

Table 6.3 Cartilage thickness (mm) and tidemark observations, C3, region opposing defect. **284**

Figure 6.18 Masson's Goldner stained sections, C3, region opposing the defect, . **285**

Figure 6.19 Cell aspect ratio (width: depth), tangential cell layer thickness (mm) and chondrocyte clustering score, C3, region opposing the defect. **286**

Table 6.4 Hyaline cartilage morphology, C3, region opposing the defect. **287**

Figure 6.20 DIC Images of hyaline cartilage of C3 in the region opposing the lesion **288**

Figure 6.21 Chondrocytes (arrows) in hyaline cartilage of C3 in the region opposing the defect **289**

Figure 6.22 Metachromatic staining score, cartilage pathology score and chondrocyte area (x10-5 mm2/cell), C3, region opposing the defect, from MB stained sections. **290**

Figure 6.23 Mean number of tidemarks, C3, region opposing the lesion. Measured on BSEM images. **291**

Figure 6.24 Proportion of tidemark fluorescence C3, region opposing the lesion. Measured on unstained, undecalcified sections under UV fluorescent light..... **292**

Figure 6.25 Fluorescent microscopy images of C3, region opposing the defect ... **292**

Table 6.5 Cartilage thickness, tidemark number and hyaline cartilage morphology, C3, weight bearing region. **294**

Figure 6.26 Hyaline cartilage thickness (mm), C3, weight bearing region. From Masson's Goldner stained sections. **295**

Figure 6.27 Chondrocyte area (x10-5 mm^2/cell) and cartilage pathology score.... **295**

Figure 6.28 Masson's Goldner stained sections of C3, weight bearing region..... **296**

Figure 6.29 Calcified cartilage thickness, C3, weight bearing region. **297**

Figure 6.30 BSEM images of the weight bearing region of C3 showing thicker CC in the treated limbs..... **298**

Figure 6.31 Total cartilage pathology scores (out of a possible score of 20) for sites within the midcarpal joint of treated limbs..... **299**

Figure 7.1 Schematic representation of the major differences between the treated and control limbs of the trial animals from all chapters..... **313**

Figure A1.1 Key to colours used for trial horses on all individual-value graphs.... **379**

Table A2.1 Location of surgical lesion on..... **379**

Figure A3.1 Examples of larger osteocyte lacunae on BSEM images. **380**

Figure A3.2 Examples of variation in osteocyte lacunae size on BSEM images. .. **381**

Figure A4.1 Naturally occurring lesion (solid arrowhead) in the dorsal CC and SCB of Cr of the control limb of horse 2 associated with abnormal calcified tissue (open arrowhead).. ..... **382**

Figure A4.2 BSEM image showing lesions (arrows) in the proximal CC of C3, in the region opposing the lesion in the treated limb of Horse 6..... **383**

Figure A4.3 Dorso-proximal articular surface of C3 from the treated limb of horse 6. ..... **384**

Figure A4.4 BSEM image showing lesions (arrows) in the proximal CC of C3, in the weight bearing region of the control limb of Horse 6. Proximal to top, dorsal to right of image. **385**

Figure A4.5 Splitting of the CC in the region opposing the lesion of C3 of untrained control horse 2. Methylene blue stained semi-thin section, bright field image. ... **386**

Figure A4.6 Thickened, irregular CC (white arrows) in the dorsal region of Cr from untrained control horse 3. BSEM image. **386**

Chapter 1

LITERATURE REVIEW

1.1 Introduction

The investigation described in this thesis used an equine model of osteochondral defects to study how the tissues of synovial joints respond to incongruity of the articular surface. Incongruity in this context describes a condition where there is focal loss of contact between the two surfaces of a synovial joint. This may occur through loss of articular cartilage or collapse of the underlying subchondral bone and leads to focal changes in loading of the joint surface (1-4).

Diseases and injuries that affect joint congruity are common in man, horses and other domestic species and include conditions such as osteoarthritis (OA), osteochondrosis dissecans (OCD), fatigue fractures, traumatic injuries and, in horses, palmar osteochondral disease (POD). These conditions can all cause pain and loss of function of an affected joint (5-16).

OA, a syndrome of degenerative changes within synovial joints, is a common consequence of conditions that cause joint surface incongruity, while focal areas of articular cartilage erosion and subsequent loss of congruity are a feature of OA itself (7, 16-23). This condition is a significant burden on working and companion animals as well as human health care systems (5, 6, 8, 10-12, 24, 25).

There is a large body of work on joint disease, in particular on cartilage defects and OA. Despite this, the pathogenesis of degenerative changes within synovial joints is not completely understood and there are few effective treatments to prevent or slow the progression of disease (26-28). How joint tissues respond to loss of congruity and the role this plays in the initiation and progression of OA is one area that is less well studied. This review covers what is known about synovial joint anatomy, homeostasis and disease as well as the animal models and laboratory techniques used to study them. Particular attention is paid to work on osteochondral defects, incongruity and the mechanobiology of cartilage and bone.

1.2. Synovial joint anatomy and histology

1.2.1. Overview

A joint is the meeting point of two bones. While there are three types of joints in the mammalian body: fibrous, cartilaginous and synovial, this study is concerned specifically with the synovial joint, the anatomy of which is well described in the literature as is the histology of its component tissues (Figure 1.1) (29, 30).

In synovial joints the opposing ends of bone are each covered by a layer of articular cartilage. The articular cartilage rests on a layer of compact bone which is continuous with underlying trabecular bone. Together, the compact and trabecular bone constitute the subchondral bone (SCB). The boundary between the articular cartilage and the SCB is called the osteochondral junction (29-32).

The space between the two articular surfaces is filled with synovial fluid and bounded by a joint capsule that attaches to the bones at the periphery of the articular surfaces. Peri- and intra-articular ligaments are also part of the joint organ and may be intra-capsular such as collateral ligaments or intra-articular such as the cruciate ligaments of the stifle. Menisci are fibrocartilaginous pads that are present in some joints (notably the stifle) and serve to enhance stability and spread loads more evening across joint surfaces (29-31).

1.2.2 Articular cartilage

Articular cartilage is composed of cells (chondrocytes) located within lacunae surrounded by an extracellular matrix (ECM) which they produce and maintain (Figure 1.2) (30, 33, 34). Within the articular cartilage there is a superficial hyaline layer and a deeper calcified layer. The hyaline cartilage (HC) is delineated from the calcified cartilage (CC) by the 'tidemark' (29-32).

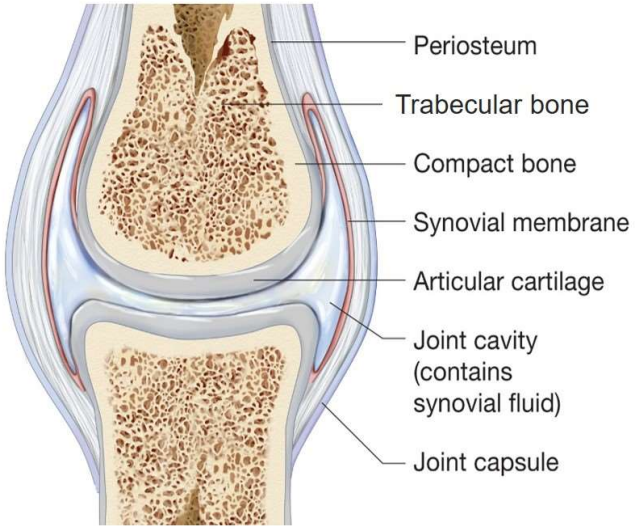

Figure 1.1 *Generalised diagram of a synovial joint showing the major anatomical structures* (http://biology-forums.com/index.php?action=gallery;sa=view;id=8793, 2012).

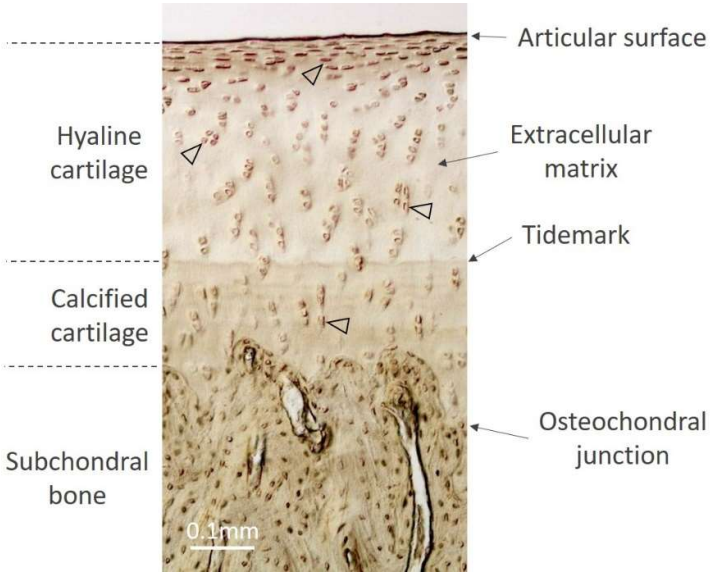

Figure 1.2 *Differential Interference Contrast microscopy image of equine third carpal bone joint surface showing hyaline and calcified cartilage containing chondrocytes (open arrowheads), subchondral bone and the boundaries between these layers of tissue.*

Cartilage ECM is composed of a collagen network containing proteoglycans, hyaluronan and water. Hyaline cartilage is so-named because of its translucent, glass-like appearance which is conferred by the high water content (65-80% of the wet weight in human adults) and the fine structure of the collagen network within the ECM. Collagen comprises 10-20% of the wet weight of cartilage and proteoglycans 10-15%. The remainder is comprised of the chondrocytes and other molecules including hyaluronan, small amounts of minerals and lipids (30, 33, 35-37). The HC is further subdivided into three zones: tangential (or superficial), transitional (middle) and radiate (deep) in order from the articular surface to the CC (Figure 1.3).

The tangential zone has the highest cell density of the three zones and the chondrocytes are relatively small and flat with their long axis parallel to the joint surface. The collagen fibrils are relatively thin (20-30nm) in this zone and are oriented predominantly parallel to the joint surface. Through the middle zone collagen fibrils transition through an oblique orientation to become perpendicular to the joint surface and become thicker, while chondrocyte density decreases and the cells become larger and more rounded. In the radiate zone, the collagen fibrils are entirely oriented perpendicular to the joint surface and are thickest of the three zones (70-120nm). The chondrocytes are lower in density, larger and arranged in vertical columns with their long axes perpendicular to the articular surface (9, 30, 33, 35, 38).

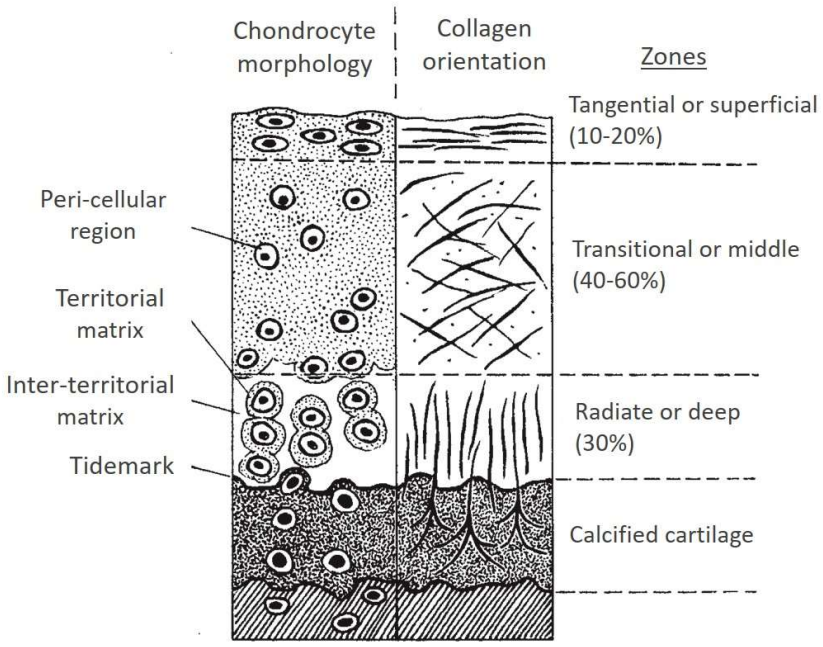

Figure 1.3 *Diagram of the zones of hyaline cartilage depicting predominant chondrocyte morphology and collagen orientation (Adapted from March L. Articular Cartilage in Health and Disease. p.86. In Sambrook P [Ed]: The Musculoskeletal System. Churchill Livingstone, New York, 2001).*

The collagen component of the ECM is predominantly type II collagen with small amounts of types IV, VI, IX, X and V/XI (now considered a single type). Type II collagen forms fibrils and provides most of the structural support of the cartilage (Figure 1.4). Type VI is found around the chondrocytes and is thought to bind the cell surface to the surrounding ECM. Type IX is thought to hold the type II fibrils together to prevent them being separated excessively when the proteoglycans swell with water (33, 35-37).

Proteoglycans are monomers composed of a central protein surrounded by glycosaminoglycan side chains (GAGs). The major proteoglycan of cartilage ECM is aggrecan, which contains the GAGs chondroitin sulphate and keratan sulphate, and which forms aggregates with hyaluronan (Figure 1.4). Hyaluronan is a glycosaminoglycan that, unlike the other GAGs, is not sulphated and does not bind to a core protein; instead, it forms chains with itself and binds to both aggrecan and collagen. The retention of aggrecan within the collagen framework is a result of its ability to bind to hyaluronan (9, 33, 38).

The tidemark is the demarcation between the HC and CC (Figure 1.2). It is a site of ongoing endochondral calcification (31, 39). Collagen fibrils are continuous from the HC into the CC and, like the collagen fibrils in the deep zone of the HC, those of the CC are oriented perpendicular to the joint surface. The collagen in this layer forms a more rigid mesh that is impregnated with hydroxyapatite crystals and contains few proteoglycans. The convoluted and interdigitating osteochondral junction is the boundary between the CC and the underlying SCB (30, 31, 33).

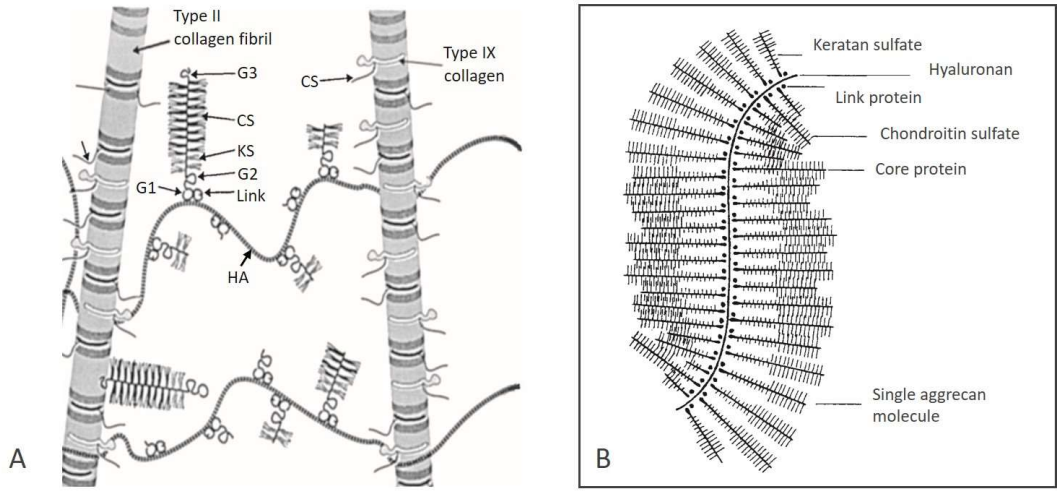

Figure 1.4 *A: Organisation of collagen and PGs in articular cartilage ECM. Single aggrecan molecules consists of a core protein with three globular domains (G1 to G3), to which are attached multiple chondroitin sulfate (CS) and keratin sulfate (KS) sidechains. B: Proteoglycan aggregate: formed by binding of multiple individual aggrecan molecules with hyaluronan (HA), stabilized by a link protein. (Modified from Koopman WJ [ed]: Arthritis and Allied Conditions A Textbook of Rheumatology, Vol 1, 13th Ed. Williams & Wilkins, Baltimore, 1997 (A), and Rosenberg L: Structure of Cartilage Proteoglycan. In Simon WH [Ed]: The Human Joint in Health and Disease. University of Pennsylvania Press, Philadelphia, 1978 (B)).*

1.2.3 Subchondral bone

The subchondral bone that supports the articular cartilage has two contiguous layers: the subchondral bone plate formed by compact bone and the underlying trabecular bone (Figure 1.5). Compact bone is solid with spaces only for cell lacunae, canaliculi, blood vessels and erosion cavities. Trabecular bone is formed by an irregular arrangement of connected sheets and struts of bone (trabeculae) separated by large spaces filled with bone marrow (8, 30, 40, 41).

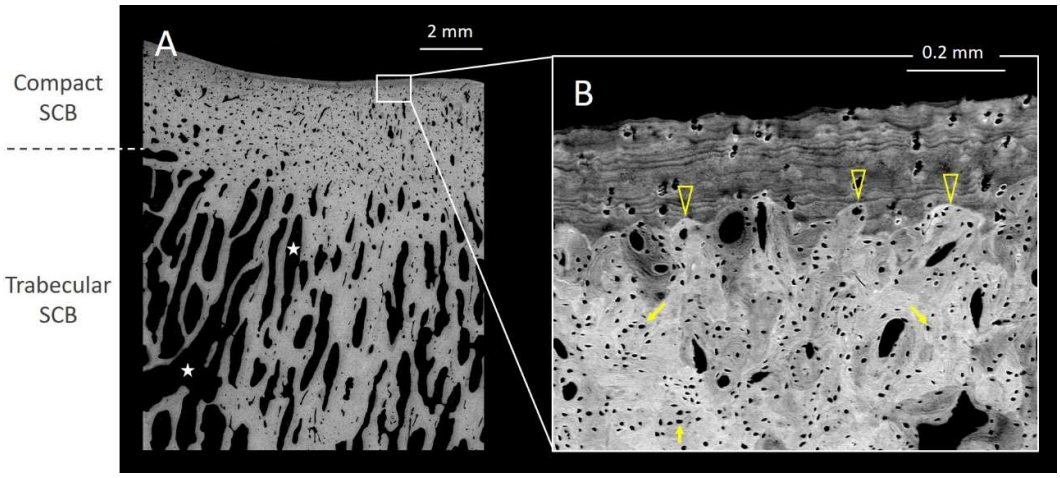

Figure 1.5 *Backscattered scanning electron microscopy images of subchondral bone from equine third carpal bone showing the arrangement of compact and trabecular subchondral bone (A) with marrow spaces (white stars) and an enlargement (B) showing the osteochondral junction (open yellow arrowheads) and osteocyte lacunae (yellow arrows).*

Bone, like cartilage, consists of cells (osteocytes) within lacunae surrounded by ECM that is supported by a network of collagen fibrils. In bone this collagen is predominantly Type I and in mature bone these collagen fibrils are surrounded by and impregnated with the mineral hydroxyapatite ($Ca_{10}(PO_4)_6(OH)_2$). The mineral component of the ECM makes up about 65% of the bone by weight, 25% is water, and the remainder is predominantly collagen with small amounts of proteoglycans, glycoproteins and cells (30, 32, 40, 41).

Osteocytes are connected to each other and to blood vessels within the bone via canaliculi, narrow channels, 0.2-0.3 micrometers in diameter, through which osteocyte cell processes pass. Each osteocyte has approximately 60 cell processes. Osteocytes are responsible for maintenance of the surrounding ECM and have the capacity to both resorb and produce ECM under certain conditions (40-42).

In addition to osteocytes, there are three other types of bone cells. These are found on the surface of the mineralised ECM within pores or trabecular spaces: bone lining cells, osteoblasts and osteoclasts (Figure 1.6). Bone lining cells are mesenchymal cells present in the periosteum lining the outside of the bone and the endosteum lining the marrow cavities and the vascular channels, and are considered to be potential osteoprogenitor cells. Osteoblasts are immature bone cells that are responsible for bone formation. They are capable of replication and are responsible for secretion of collagen, proteoglycans and glycoproteins to make the unmineralised ECM known as osteoid. They probably also have a role in mineralisation of this matrix. As the matrix becomes mineralised some osteoblasts become trapped in lacunae and become osteocytes. Osteoclasts are large, multinucleated cells that are derived from precursors within blood. They are responsible for resorption of bone which is required for the process of bone remodelling (32, 40, 41, 43).

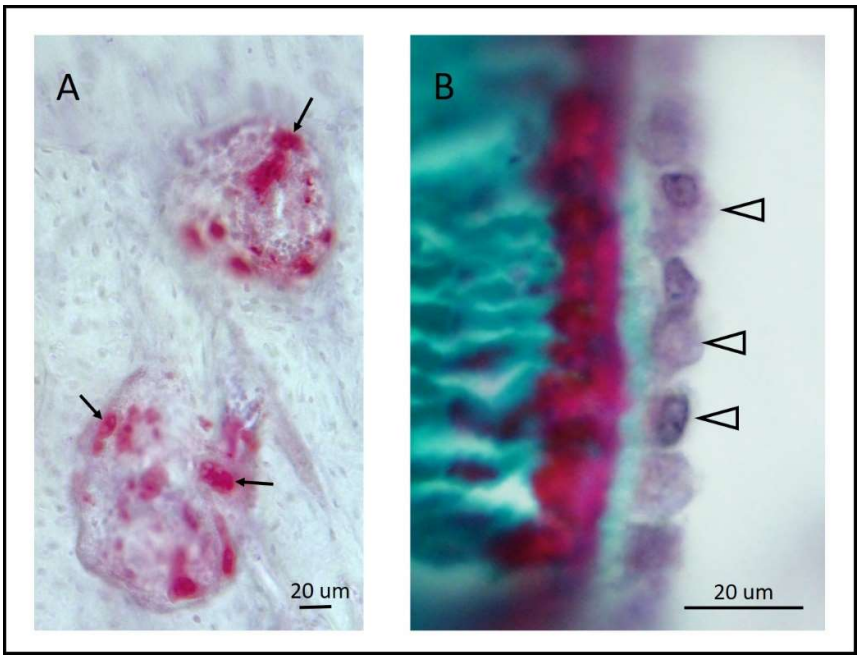

Figure 1.6 *Examples of osteoclasts (arrows) stained for tartrate resistant acid phosphatase within resorption spaces (A) and osteoblasts (open arrow heads) on an osteoid seam (pink) in a Masson's Goldner trichrome stained section (B).*

1.2.4 Joint capsule

The joint capsule is comprised of three layers: the synovium (intima), sub-synovium (sub-intima) and fibrous capsule. It attaches at the margins of the articular surfaces via a fibrocartilaginous insertion (29, 30, 33).

The synovium (intima) is the layer lining the joint space (Figure 1.7). It is an incomplete layer, one to five cells thick. It lacks a basement membrane which, in conjunction with the spaces between cells allows for diffusion of small molecules and electrolytes between the sub-intimal capillaries and the joint fluid. The synovium is comprised of two types of synoviocytes. One third of the synoviocyte population are Type A synoviocytes which

are bone marrow derived mononuclear phagocytes responsible for removing waste products from the synovial fluid and processing antigens. The remainder are Type B synoviocytes which are fibroblasts that secrete hyaluronan and lubricin (a mucinous glycoprotein). Both cell types produce metalloproteinases, cytokines and other mediators (29, 30, 33, 44).

The synovium rests on the sub-synovium or sub-intima which is a layer of connective tissue and fibroblasts that may be fibrous, areolar or adipose in nature. The sub-intima serves to allow movement between the synovium and the fibrous outer layer of the joint capsule and contains nerve endings and blood vessels (9, 29, 30, 33, 44).

The arrangement of synovium and sub-synovium varies with its position within the joint depending on the biomechanical environment. In areas of high stress such as between the joint and a ligament, synoviocytes are present in a flat layer over a fibrous sub-intima. In areas of low stress such as the synovial recesses the synovium is folded into villi providing a large surface area. This, in addition to a greater density of blood vessels in the sub-intima of these areas make them preferential sites for solute and macromolecule exchange and secretion of hyaluronan (29, 30, 33, 44).

The outermost layer of the joint capsule is a fibrous layer of low cellularity composed of bundles of collagen fibres separated by loose connective tissue. The collagen is mostly Type I with smaller amounts of Type III and V. The fibrous joint capsule is vascular and contains proprioceptive and nociceptive nerve endings (7, 30, 33).

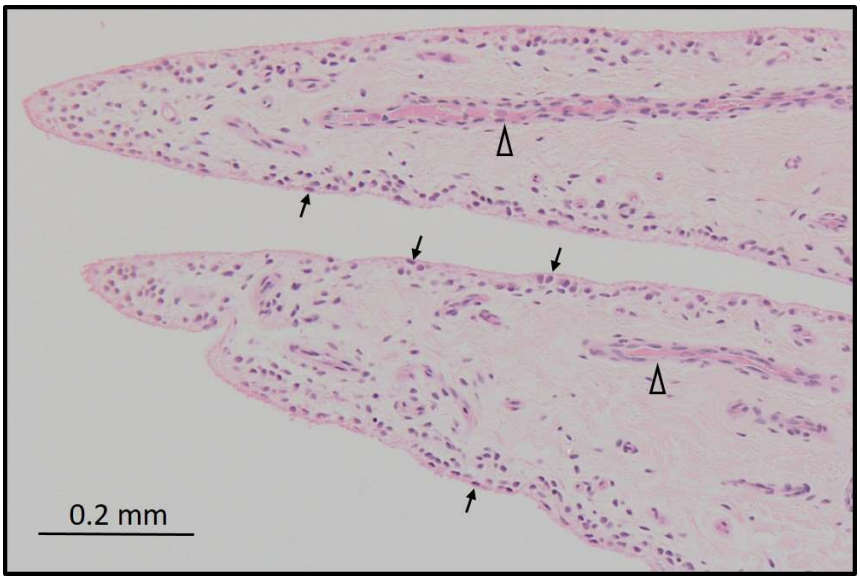

Figure 1.7 *Histological section of synovium from an equine carpus demonstrating synoviocytes of the intima (arrows) and blood vessels within the sub-intima (open arrowheads) in a villous arrangement. Haematoxylin and eosin stained section.*

1.2.5 Synovial fluid

Synovial fluid is a viscous fluid that is an ultrafiltrate of plasma. The synovium selectively prevents large molecules from entering the joint space but allows entry of small molecules and electrolytes. Hyaluronan and lubricin produced by Type B synoviocytes are added to this ultrafiltrate. Normal equine joint fluid contains fewer than 500 nucleated cells per µl, including synoviocytes, monocytes, lymphocytes and polymorphonuclear cells. Synovial fluids plays a role in both lubrication of the joint and transport of nutrients to the articular cartilage (9, 29, 30, 45).

1.2.6 Periarticular structures

Peri-articular ligaments are often incorporated into the fibrous capsule. These, in addition to the muscles spanning the joint serve to provide additional stability and reduce the load that the joint capsule itself experiences, absorb shock and provide proprioception to the joint (8, 9, 30, 33).

1.2.7 The equine carpus

The equine carpus is a useful site for the study of joint disease. The mid-carpal joint is a site of naturally occurring disease and is large enough to allow arthroscopic access for treatment and *in vivo* examination, and for observations to be made in a site-specific manner (46).

The carpus, situated in the distal forelimb, is composed of three individual joints (Figure 1.8). The antebrachiocarpal joint is the most proximal and is the articulation between the distal end of the radius and the proximal row of carpal bones (the radial (Cr), intermediate (Ci), ulnar (Cu) and accessory carpal bones). The mid-carpal joint (MCJ) is the articulation between the proximal and distal rows of carpal bones. The most distal of the three joints is the carpometacarpal joint which is the articulation between the distal row of carpal bones (the first (C1), second (C2), third (C3) and fourth (C4) carpal bones) and the proximal ends of metacarpals II-IV (47). The MCJ is of the most importance to the current study, specifically the articulation between the distal facet of Cr and the proximal (or radial) facet of C3 (Figure 1.8 and 1.9).

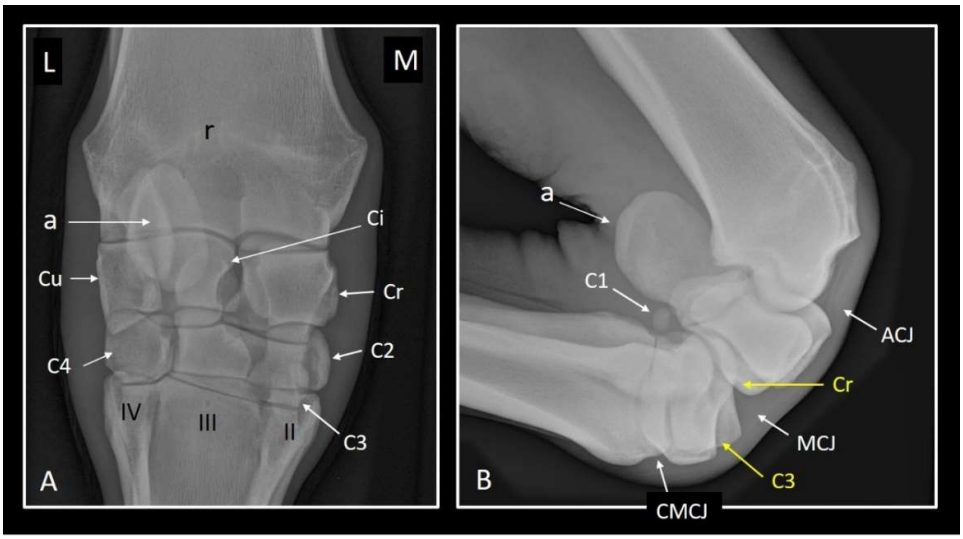

Figure 1.8 *Dorso-palmar (A) and flexed lateral (B) radiographic views of the equine carpus showing the distal end of the radius (r), the accessory (a), the ulnar (Cu), intermediate (Ci), radial (Cr), first, second third and fourth (C1-C4 respectively) carpal bones, as well as the three joints: antebrachiocarpal (ACJ), mid-carpal (MCJ) and carpo-metacarpal (CMCJ). Yellow arrows in B show the distal articular facet of the radial carpal bone (Cr) and the radial facet of the third carpal bone (C3). L=lateral, M=medial. Images courtesy of Dr. Gareth Trope and Tom O'Brien.*

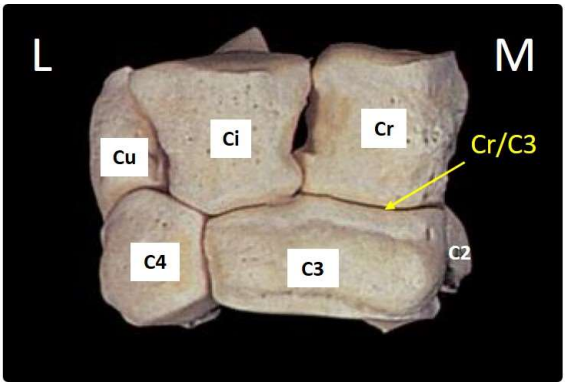

Figure 1.9 *Equine carpal bones, dorsal view**,** with the articulation between the radial carpal bone (Cr) and third carpal bone (C3) indicated (Cr/C3). Cu= ulnar, Ci= intermediate, C4=fourth, C2=second, carpal bones. L=lateral, M=medial, proximal to top, distal to bottom. Modified from: Clayton (ed.), Clinical Anatomy of the Horse, 1st Ed, Elsevier Mosby, Edinburgh, 2005.)*

1.3 Normal function and homeostasis of synovial joints

Although all joint tissues and the synovial fluid play significant roles in the normal functioning and homeostasis of the joint organ, the current investigation is concerned primarily with how the articular cartilage and SCB respond to changes in joint surface congruity so this review will focus on these tissues.

1.3.1 Function

The function of synovial joints is well known, their role being to allow almost frictionless movement between two bones, to transfer loads from one bone to another and to absorb shock (29, 30). Normally functioning synovial joints are required for adequate mobility to allow animals to seek food, water and shelter and to perform normal behaviours while abnormal synovial joints may result in pain (5, 23, 48). Therefore, the ability for synovial joints to function normally is important for the welfare of our companion and working animals and to minimise morbidity in the human population (16, 23, 49, 50).

Movement of the two opposing articular surfaces relative to each other exposes both sides of the joint to friction, shear and tensile forces while weight-bearing results in compressive forces. Joint lubrication is such that, under normal conditions, friction and shear at the articular surface is minimal. This is achieved through weeping lubrication (loading of the joint and deformation of the cartilage results in water being extruded from the cartilage), through the viscosity of the joint fluid as a result of its hyaluronan and lubricin content which enables it to act as a boundary lubricant at the cartilage surface and through fluid pressure between the two articular surfaces (33, 34, 44, 51, 52).

The material properties and morphology of hyaline cartilage create a tissue that is resistant to both tensile and compressive forces. Collagen confers tensile strength while proteoglycans trap water and confer resistance to compression (53). The negatively charged, strongly hydrophilic PGs and GAGs attract several times their weight in water, however the collagen framework limits how much is actually bound leaving the ECM only partially hydrated. It is the resulting swelling pressure that gives cartilage its compressive stiffness (9, 33, 38, 54).

The superficial layer of HC, with collagen fibrils oriented tangential to the joint surface, higher density of collagen and lower PG content is considered to be relatively more resistant to tensile and shear stresses than deeper layers. The deep, radiate layer is relatively more resistant to compression due to the perpendicular alignment of collagen fibrils and a higher proteoglycan content relative to collagen. The middle zone is intermediate in both collagen alignment and density and PG density and is also intermediate in its ability to withstand tensile/compressive forces (30, 31, 33, 55).

Although the material properties of cartilage also confer shock absorbing qualities and it has been shown to absorb more energy per unit volume than SCB, the thin layer of articular cartilage cannot absorb most of the shock associated with impact which is instead transferred to the SCB. This holds true for impact loads as well as more slowly applied loads (56-58).

The CC has been hypothesised to modulate the forces that would otherwise be experienced at the junction between the HC and the SCB by creating a more gradual

stiffness gradient between the two tissues. While the stiffness of HC is significantly lower than that of the SCB, CC stiffness has been shown in several studies to be intermediate between the two (59-62). However studies employing nano-indentation methods have found no difference in stiffness between the CC and SCB of both human and equine joints (63, 64). The studies observing similar stiffness in CC and SCB have measured stiffness of the tissues after dehydration and embedding in methacrylate, compared to the fresh or fresh-frozen specimens utilised in the other studies. This difference in sample preparation and hydration may account for the variation in observed mechanical properties between studies (65). It has been suggested that the interdigitating nature of the OC junction also aids in diffusion of loads at the boundary between the CC and the SCB as well as enhancing attachment of the cartilage to the underlying bone (66).

The compact bone of the SCB plate provides structural support to the articular cartilage, while the trabecular bone transfers loads from the SCB plate to the dense cortex of the diaphysis. The trabecular SCB also plays a major role in shock absorption, being relatively more deformable than compact bone, reducing the peak load experienced by the joint (30-33, 40, 58).

As noted in sections 1.2.4 and 1.2.5 synovial fluid makes an important contribution to joint function through roles in lubrication, provision of nutrients and waste removal (30, 33, 44).

1.3.2 Homeostasis

In order to maintain normal function joints have the ability to adapt to the prevalent conditions they experience (55, 67-74). While nutritional, metabolic and neurological

factors play important roles in joint homeostasis, a discussion of these is outside the scope of this review (44). The following discussion will focus on the role of the biomechanical environment and summarise the major biochemical pathways involved in mediating the response of cartilage and bone to biomechanical stimuli. There is a large amount of published data on the response of cartilage to exercise and loading. However, while it has been long recognised that bone responds to its mechanical environment (75), there are fewer existing studies on the response of SCB to exercise.

1.3.2.a Hyaline cartilage

Proteoglycans and collagen in cartilage ECM are continuously produced and resorbed, although under normal conditions this turnover is slow (30, 76). Homeostatic turnover of ECM by chondrocytes has been shown to be modulated by both biomechanical and biochemical stimuli (35, 76). This ability to modulate ECM metabolism and composition in addition to ongoing calcification at the tidemark and remodelling at the osteochondral junction allows cartilage to adapt to the predominant stresses that it experiences. The degree and distribution of shear, tensile and compressive forces across a joint have been shown to affect development and maintenance of the HC (55, 73, 77-80).

Biochemistry

There are a large number of biochemical factors that regulate and mediate the synthesis and degradation of the ECM macromolecules by chondrocytes and detailed discussion of these is outside the scope of this review. The most important molecules with an anabolic effect on chondrocytes and synthesis of ECM components are growth factors, the best known of which include transforming growth factor beta (TGF-β), the bone morphogenic

proteins (BMPs) and insulin-like growth factor 1 (IGF-1). These are all present in small amounts in normal cartilage and variably stimulate cell division, collagen and PG synthesis and inhibit catabolic activity. TGF-β also appears to have some involvement in normal ECM breakdown. Important catabolic factors include the metalloproteases (MMPs) and serine proteases (especially plasminogen activators) which result in enzymatic cleavage of PGs and collagen. Fibronectin is a component of normal cartilage that once cleaved itself becomes pro-catalytic through the stimulation of MMP-13 and nitrous oxide (NO) production. The pro-inflammatory cytokine interleukin 1 beta (IL-1β) is also present in normal cartilage and results in suppression of PG synthesis. Catabolic activity is further regulated by a series of inhibitors of catabolic pathways such as tissue inhibitor of metalloproteases (TIMPs) and plasminogen activator inhibitor (PAI) (35, 76).

Cellular biology – in vitro work

In vitro studies of both cell cultures and cartilage explants have shown that moderate dynamic (cyclic) compressive loading stimulates increased PG, GAG and collagen type II synthesis by chondrocytes. However, excessive loading, of either high magnitude or long duration, results in cell death and reduced PG synthesis (81-87). Cyclic stretching of immature chondrocytes results in increased proliferation and differentiation (88) and both constant and intermittent shear stress have been shown to stimulate GAG, PG and collagen production as well as increasing expression of TIMP, prostaglandin E2 and IL-6 in normal chondrocytes (89, 90).

In the majority of *in vitro* cartilage loading studies, the control samples are unloaded compared with cartilage *in vivo* which normally experiences some degree of compressive, tensile and shear strains. Madej et al. (2016) specifically investigated the effect of

unloading on cartilage explants after removal from normal joints and documented a loss of GAGs that was reversed upon restoration of cyclic loading (91).

Effect of training

Results of *in vitro* studies of cartilage response to changes in loading are complemented by *in vivo* studies of increased loading, via training or passive loading, and of reduced loading via hind-limb suspension or limb immobilisation. Moderate exercise, and the associated increase in loading of joint surfaces, has been shown to increase cartilage thickness, GAG content and stiffness (79, 92). However, the magnitude of loading has been shown to be important as studies in rabbits, dogs and horses have found that under conditions of strenuous exercise or prolonged repetitive loading HC becomes thinner and less stiff with lower GAG content (93-97). In addition, there is good evidence that response to training is site specific likely due to differences in local loads of the joint surface as discussed below (69, 73, 92, 97, 98).

Effect of site and local loading of the articular surface

While there has been a significant amount of work modelling load distribution in human joints, especially the hip and knee (99-105) , in horses the assumed patterns of load are largely based on observations of where pathology occurs or on cadaveric studies, which do not account for active muscle forces across the joint (106-108). I am not aware of work measuring or modelling loading across the joint surfaces of other species. Therefore, care is needed when interpreting how site-specific loads might affect cartilage homeostasis from animal models.

In human joints under physiological conditions, sites predicted to be experiencing greater surface pressures are found to have thicker HC than sites of lower loading (99, 109-111). However, in the healthy equine mid-carpal joint, HC in the central region of the radial facet of C3, which is thought to experience lower, more continuous loading, is thicker than at dorsal sites of the radial facet of C3 which is thought to be exposed to higher magnitude intermittent loading (69, 106, 112).

Joint surface sites thought to experience higher compressive loads show the greatest increase of GAGs in beagles subjected to moderate exercise (92) but are also the sites of greatest loss of PGs or GAGs, loss of stiffness and decrease in HC thickness in situations of more intense exercise in both dogs and horses (93, 97, 98). Conversely, sites that are likely to experience relatively lower compressive loads within a joint respond to strenuous training with an increase in cartilage thickness (69, 73, 97, 106). For example, the cartilage of the central radial facet of C3 in the equine mid-carpal joint displays an increase in HC thickness upon training while dorsal sites of the radial facet of C3 show no change in thickness, a decrease in GAG content and a decrease in stiffness upon intense training (69, 97, 106).

Palmer et al. (1995) found that PG content and stiffness were greater in the central region when compared to the dorsal region of the radial facet of C3 in horses, although they found no effect of training (98, 113). However, cultured chondrocytes from both sites in exercised horses had a higher rate of PG synthesis than non-exercised horses (98). The above findings are consistent with those of Brama et al. (1999 and 2000) who found, in the metacarpophalangeal joint of a general population of horses with un-specified training history, higher GAG and lower collagen concentrations in central sites (114, 115) where

there is likely more constant, low magnitude loading compared with dorsal sites which likely experience intermittent high magnitude loading (107).

Although not a focus of this review, it is recognised that immature cartilage may not respond in the same way as that of adults. While a study by van Weeren et al. (2008) comparing foals trained from an early age to those raised with no training reports differences in GAG and collagen content between the two groups and between different sites on the joint surface (116), a similar study by Kawcak et al. (2010) found no differences either between sites on the articular surface or between the trained and untrained groups (117). There is no apparent reason for the difference between these two studies. Although different articular surfaces were used in each study, the pattern of collagen and GAG distribution has been found to be similar on both of these surfaces in adult horses (115).

Effect of depth below the articular surface

The response to exercise also varies with depth below the surface. Murray et al. (2001) found, in addition to an overall increase in GAG content in the cartilage of C3 of exercised horses, there was lower PG content (determined by toluidine blue staining intensity), in the superficial compared to deep layers of cartilage both at the more highly loaded sites of untrained horses and at all sites in trained animals (74). This suggests that the increase in GAG content was occurring preferentially in the deeper cartilage in the trained animals. These findings are consistent with canine studies in which there is an increase in GAG content in the deep cartilage in moderately trained dogs and a loss of GAGs from the superficial layer in strenuously exercised animals (92, 118).

Effect of loading on proteoglycan type and aggregation

Proteoglycan synthesis may also change qualitatively with exercise. Moderate training in horses resulted in greater amounts of large aggregating PGs (such as aggrecan) in cartilage from all sites across the proximal surface of C3 compared with that from animals housed in stalls (98) and strenuous training was associated with lower aggrecan synthesis and greater decorin (a smaller PG) synthesis at sites of high magnitude loading on proximal C3 compared to the same sites in moderately exercised horses (80). This apparent increase in production of large aggregating proteoglycans by equine chondrocytes when experiencing moderate loading compared with either minimal or high magnitude loading is consistent with the findings of Palmoski et al. (1980) who noted reduced aggregation of proteins in cartilage of unloaded canine limbs when compared with the moderately overloaded contralateral limbs (119).

Effect of unloading

Lower than normal loading results in thinner HC with reduced PG content in the stifle joints of mice and rats that have undergone tail suspension (120, 121). Reduced GAG content has also been consistently demonstrated in the HC of canine stifles that have been unloaded due to casting or paw amputation (79, 119, 122). Like the rodent studies, Palmoski et al. (1979 and 1980) reported decreased HC thickness in the cast or paw-amputated limbs of dogs however this was when compared with the overloaded contralateral limb which is known to have increased HC thickness and GAG concentration (79, 119, 122). In a study where HC in the stifle of cast limbs was compared to that of control dogs (ambulatory on both limbs) there was no difference in HC thickness (79).

In regions of lower magnitude loading in equine joints the rate of production of matrix proteins by chondrocytes has been reported to be greater, despite the net PG content being lower, suggesting a greater rate of turn-over favouring catabolism, compared with regions of higher loading (123, 124). This is similar to findings in immobilised and unloaded rabbit stifles in which increased PG metabolism with no net change in GAG content has also been found (125). Contrary to this Palmoski et al. (1979, 1980) reported lower PG synthesis in both unloaded but mobile and immobilised limbs (119, 122). Once again this was relative to the contralateral limb in which there was likely to be greater PG synthesis due to a moderate increase in loading (79). Kiviranta et al. (1987) did not comment on the rate of synthesis in cast limbs compared to normally ambulating controls (79).

Population studies

The observation from scientific trials that moderate but not high magnitude loading results in thicker HC is reflected in the general equine and human populations. Hyaline cartilage thickness was found to be greater in the tarsi of horses used for general riding or elite competition (show jumping, dressage or eventing) when compared to horses resting at pasture (72). However there was no significant difference in HC thickness in the metacarpophalangeal joint between Thoroughbred race horses that were training at the time of euthanasia due to a musculoskeletal injury compared with horses with no recent history of racing or training that had been euthanised for un-related reasons (126).

Increased loading due to increased bodyweight is associated with greater cartilage thickness in young, normal weight people, but the relationship is lost in older and overweight individuals (127). Similarly, HC is thickest in regions of greatest loading

during walking in the human knee and hip (99, 110). In addition, Koo et al. (2007) found that the ratio of cartilage thickness in the medial and lateral compartments varies with gait such that if there is greater transfer of load to the lateral compartment of the knee when walking the ratio of lateral to medial cartilage thickness was greater (99).

Mechanisms of response to biomechanical stimuli

Increased PG content may be one mechanism that mediates the increase in HC thickness with moderate loading as the two are often observed together (79, 92). Other possible mechanisms include reduced calcification at the TM or greater collagen volume (128, 129). There are several proposed mechanisms for thinning of the articular cartilage in response to either excessive loading or unloading. Physical erosion of the articular surface is one possibility however in the studies of training and unloading there is often no sign of disruption to the cartilage (80, 95, 118, 121, 130).

Chondrocyte death has been suggested to play a role in mediating a decrease in cartilage thickness and Basso and Heershe (2006) noted apoptosis of chondrocytes in cartilage from the stifle of hind limb unloaded rats (120). However other studies report a normal number and distribution of chondrocytes in unloaded but mobile limbs (119, 121). Increased DNA content suggesting a greater number of cells has been observed at sites of high magnitude loading in the equine fetlock implying that loss of cells is not responsible for thinner HC in this region (115). There may be a difference between unloading alone and unloading in combination with immobilisation as lower chondrocyte densities have been observed in cartilage from joints that have been both unloaded and immobilised in mice and dogs (121, 122). Increased ECM breakdown is also a possible mechanism as in addition to reductions in GAG concentrations, increases in biochemical

factors involved in ECM catabolism including NO and ADAMTs have been measured in unloaded cartilage (120, 121). Calcification at the TM and advancement of the CC has also been hypothesised to be a mechanism for thinning of the HC (96, 121, 131).

The way in which chondrocytes transform mechanical stress into biochemical signals is not fully understood but several mediators have been suggested including activation of membrane-associated calcium channels, G-protein receptors, phospholipase C, altered TGF-β expression, changes in NO production or changes in ECM pH (83, 90, 91, 120, 132, 133).

1.3.2.b Calcified cartilage

Calcified cartilage also responds to both training and unloading, and varies in thickness with site across the joint surface in a manner that is likely to be related to local loading (59, 73, 110).

Effect of training

Trials in dogs and horses have found the calcified cartilage layer to become thicker in response to strenuous exercise (59, 73). In agreement with these trials, CC thickness was shown to be greater in horses used for either general riding or trained at an elite level when compared with horses that were kept at pasture (72).

However several studies have found no effect of training or repetitive loading on CC thickness (68, 69, 96, 126). It is of note that those studies which found no difference were

either in young animals (68, 69) or in which the trained group were under excessive loading (96, 126) and the magnitude of loading may affect how CC responds as discussed below.

Effect of unloading

Unloading is also thought to affect CC thickness although reports of how it does so are not consistent. In the unloaded but mobile hind limbs of tail-suspended rats O'Connor (1997) observed an increase in CC thickness (131). Immobilisation combined with unloading has been found to result in thinner CC in the cast limbs of dogs (79) but no change in CC thickness in mice and rats (121, 131). The rodent studies were of shorter duration than the canine trial which may account for the variation in observations, as may species differences or age of the animals (131).

Effect of site and local loading of the articular surface

Variation in CC thickness depending on site across the joint surface was observed in early studies of human cadavers however there is some disagreement between these reports. Lane and Bullough (1980) found that CC was thicker in regions of lower loading in human femoral and humeral heads (134)whereas Mullergerbl et al. (1987) reported that CC was thicker in regions of greater habitual loading in femoral heads (110). The latter paper used more advanced methods of thickness measurement and is also more consistent with studies of horses that find CC is thicker at sites of greater compressive loading (59, 68, 126).

The response of CC to training also varies with site. The observed increased CC thickness of canine stifles in dogs that were running 40km daily occurred only in the peripheral, less loaded, regions (73). Conversely CC thickening is greatest at sites of greater peak loads in the equine carpus and tarsus in trained horses (59, 72). This apparent difference may reflect the change in loading with a change in gait rather than the absolute load at each site. In the carpus of cantering or galloping horses the greatest loads are experienced by sites that are relatively unloaded in standing or walking animals (106). While I am not aware that loading of the canine stifle during exercise has been measured, it is possible that the peripheral regions where the greatest increase in CC thickness was seen is relatively unloaded during less strenuous exercise but becomes loaded during running activity. Other factors such as the relative shear or tensile strains or the age of the animals may also play a role as the dogs in Oettermeier et al. (1992) were growing animals (68, 131, 135).

Mechanisms of response to biomechanical stimuli

The mechanisms that mediate CC response to changes in loading have been investigated to some degree although they are not fully understood. In general, CC thickness is understood to be a function of the relative rates of mineralisation of HC at the TM and ossification at the OC junction (135). These processes are most active during development however there is evidence that they continue slowly throughout life under normal conditions. Lane and Bullough (1980) found that CC in humans becomes thinner with age while the number of tidemarks increased and suggested that calcification of HC at the TM and resorption of the CC at the OC junction were ongoing in adults (134). Animal trials have confirmed that the rate of calcification at the TM slows as growing animals approach maturity but does not stop (135). Oegema (1997) demonstrated advancement of

the TM at a rate of approximately 1 μm per week in the patellae of seven month old rabbits compared with rates of up to 8 μm per week in those at four months of age (135).

Finite element models of developing synovial joints created by Carter and Beaupre et al. (2000 and 2003) have predicted that intermittent hydrostatic pressure inhibits and that tensile strain stimulates advancement of the TM and endochondral ossification (128, 136). These FE models are largely corroborated by animal trials. The rate of advancement of the TM and endochondral ossification were both found to be greater in regions of lower surface pressure compared with regions of higher surface pressure in growing horses (68). In this study, the rate of SCB advancement through remodelling at the osteochondral junction was relatively greater than mineral apposition at the TM resulting in thinner CC at sites of lower surface pressures and thicker CC at sites of higher surface pressures, consistent with other studies in man and horses (59, 68, 110, 137). Unloading of mobile joints resulted in a doubling of the mineral apposition rate (MAR) at the TM in young rats (131) however, unlike Doube et al. (2007) (68) no change in resorption at the OC junction was noted and unloaded joints had ultimately thicker CC.

It has been speculated that immobilisation in combination with unloading, likely to cause a reduction in both compressive and tensile/shear strains, results in an increase in ossification at the OC junction with no increase in the rate of advancement of the TM, ultimately resulting in thinning of the CC (79, 131), consistent with the part of the hypotheses proposed by Beaupre et al. (2004) that compression inhibits ossification at the OC junction and potentially also supporting the idea that tensile strains are required to stimulate mineralisation of HC at the TM (67).

King et al. (2005) proposed an apparently contradictory hypothesis to those above, suggesting that intermittent compressive strains stimulate rather than inhibit calcification at the TM (96). This was based on loading of joints under anaesthesia prompting the authors to acknowledge that there may have also been increased shear strains at the joint surface due to loss of constraint by the periarticular muscles (96).

Biochemical regulation

Although there is much information on the cellular and biochemical regulation of endochondral ossification in growth cartilage there is limited work on this process in articular cartilage. However, due to their expression of type X collagen, a protein associated with hypertrophy and mineralisation in growth cartilage, it has been suggested that chondrocytes just above the TM retain some characteristics of growth plate chondrocytes and may be involved in the regulation of mineralisation at the TM in adult cartilage (138, 139). In support of this theory, chondrocytes from the deep zone, but not the middle or superficial zones, of adult bovine cartilage can be stimulated to undergo hypertrophy and increase expression of alkaline phosphatase (ALP) *in vitro* (140). ALP, along with osteopontin (OPN), is synthesised by chondrocytes in the deep zone of articular cartilage during growth and has an important role in matrix mineralisation (141, 142). Increased chondrocyte expression of OPN is observed under conditions of repetitive loading and hypothesised to be one mechanism to increase the rate of calcification at the TM (96).

Administration of exogenous parathyroid hormone [1-34] (PTH [1-34]) resulted in an increase in CC thickness in rabbits and parathyroid hormone related protein (PTHrP) was found to suppress the expression of ALP by adult articular cartilage chondrocytes

undergoing hypertrophy *in vitro* suggesting a potential role for these molecules in regulation of CC thickness (140, 143).

It has been suggested that an increase in the ratio of receptor activator of nuclear factor kappa-B ligand (RANKL) to osteoprotegrin (OPG) in CC might play a role in stimulating osteoclastic resorption at the OC junction (121, 144). In support of this, an increase in RANKL:OPG in chondrocytes associated with increased osteoclast numbers at the OC junction was observed in the knee joint of unloaded and immobilised mouse hind limbs (121). In addition, Bouaziz et al. (2015) observed an increase in the expression of sclerostin by CC chondrocytes in murine stifles within 4-6 weeks following meniscectomy and suggested that this may be part of the early response to changes in mechanical loading (145).

1.3.2.c Subchondral bone

Remodelling and modelling

Subchondral bone, like all bone, is continually undergoing remodelling (Figure 1.10) which is essential to maintain healthy bone and minimise damage accumulation. Remodelling involves resorption of bone by osteoclasts followed by deposition of osteoid by osteoblasts at the previous site of resorption. Modelling in the form of resorption without subsequent formation or *de novo* bone formation (formation without prior resorption) also occurs allowing bone morphology to alter in response to external stimuli. The net amount of bone present at any site is a result of the balance between the rates of resorption and formation (40, 146, 147).

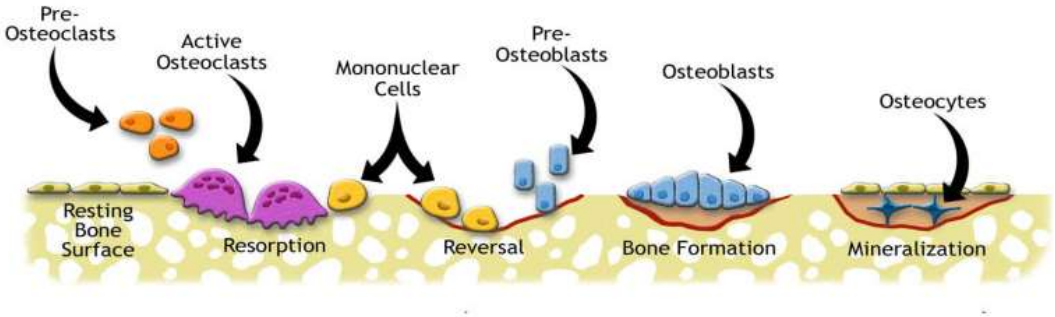

Figure 1.10 *Diagram of the remodelling process on a bone surface***,** *showing the progression from resorption of old/damaged bone by osteoclasts, their transformation back to mononuclear cells to the recruitment of osteoblasts followed by osteoid deposition and subsequent mineralisation of new bone. From: http://www.orthopaedicsone.com/ (2016).*

Effect of changes in loading

Bone resorption and formation are regulated by multiple factors including the prevalent strain that the bone is experiencing (40, 146-155). Increased loading within physiological limits, due to training, immobilisation of the contralateral limb or passive loading, results in an increase in bone volume fraction (BV/TV) and, in trabecular bone, thicker trabeculae. This is achieved through increased new bone formation and reduced osteoclastic resorption (69, 70, 73, 151, 156-160). Conversely, decreased loading due to unweighting of a limb results in a loss of bone volume and fewer, thinner trabeculae via an increase in osteoclastic resorption and a decrease in bone formation (121, 152, 161-163). These alterations in bone volume and structure increase stiffness returning strains towards normal limits (164).

There is good evidence that SCB responds to biomechanical stimuli in the same way as metaphyseal or diaphyseal bone. Subchondral bone of canine stifles was found to have increased trabecular bone volume after strenuous training (73). Higher BV/TV through increased bone formation has also been observed in equine SCB as a consequence of repetitive loading due to training experiments (69, 70, 74, 156). This is reflected in studies of horses in the general population where those that are used for either pleasure riding or elite competition have greater BV/TV in SCB than those at pasture (72). Conversely, unloading of mice hind limbs resulted in reduced BV/TV and increased tartrate-resistant acid phosphatase (TRAP) staining in femoral and tibial SCB (121).

It has been suggested that loading during training of horses causes buckling of the subchondral bone and microdamage with subsequent remodelling, resulting in increased BV/TV in SCB of trained animals (8). However it has been demonstrated that training causes increased thickness of the SCB trabeculae via direct apposition of bone indicating that microdamage is not required (73, 156).

More recent work has also shown that repetitive loading inhibits remodelling within equine subchondral bone and that cessation of training results in a marked increase in remodelling activity and loss of bone volume (165-167). Mathematical modelling suggests that SCB reaches homeostasis again at a lower BV/TV by 4-10 weeks after training stops, and that SCB with higher initial BV/TV takes longer to reach homeostasis than that with lower initial BV/TV (168).

Effect of site and local loading of the articular surface

Bone volume fraction varies depending on site across a joint surface in both horses and man, and SCB regions that are known to be under greater loading have greater bone volume fraction than those sites that experience lower peak forces (8, 69, 74, 101, 157, 169, 170). It is also recognised that the response to training in equine SCB is site dependent with a greater increase in BV/TV found at sites known to experience the greatest increase in loading. For example, the greatest increase in BV/TV in the SCB of C3 in trained horses is seen in the dorsal region of the radial facet which experiences the greatest peak loads at a canter or gallop (69, 74, 106). The inhibition of remodelling observed in the SCB of trained animals is also most marked in regions of greater loading (165).

The proposition that the variation by site of BV/TV and remodelling activity in SCB is a result of local variation in loading is supported by more recent work that has demonstrated a link between local strains and resorption/formation activity (171-173). *In vivo* microcomputed tomography (microCT) has been used to visualise regions of bone formation and resorption over time in repetitively loaded mice vertebrae. When 3D maps of bone formation and resorption activity were compared with FE models of local strain energy density within the loaded vertebrae, it was found that formation was most likely to occur at sites of high strain energy density and resorption most likely at sites of low strain energy density (171, 172).

Biochemistry and mechanisms of response to mechanical stimuli

Although the way in which biomechanical signals are translated into changes in formation and resorption activity is not completely understood, it is generally accepted that osteocytes and their lacunocanalicular network play an important role in this process. It is believed that osteocytes sense fluid flow within the lacunocanalicular network as a result of bone loading (174-179). FE modelling supports this hypothesis (180, 181) and *in vitro* work has demonstrated that osteocytes respond to strain and fluid flow (176, 178, 182, 183).

Osteocytes respond to strains with altered expression of a number of proteins (184-186). It is thought that the most important of these are RANKL, OPG, sclerostin and dickkopf-related protein 1 (DKK-1) (187-189). Osteopontin (OPN) may also play a role in mediating the increase in osteoclastic resorption and reduction in osteoblastic bone formation caused by unloading as these are not observed upon unloading in OPN-null mice (190).

RANKL is required for the fusion, differentiation and maturation of osteoclasts and acts via a receptor on osteoclast precursors and mature osteoclasts. OPG is a soluble factor that inhibits RANKL activity by preventing it from binding to its receptor, RANK. It has been demonstrated that in unloaded limbs there is an increase in RANKL and a decrease in OPG expression by osteocytes and that without osteocyte-secreted RANKL the bone loss as a result of unloading does not occur (121, 187, 191, 192).

Sclerostin and DKK1 are also produced by osteocytes, although hypertrophic chondrocytes also express sclerostin. They both act as inhibitors of bone formation via

inhibition of Wnt (wingless-type mouse mammary tumour virus integration site) signalling pathways, the activation of which is required for the differentiation and survival of osteoblasts (193-195). Osteocyte expression of both these factors is reduced by loading (185), while hind limb unloading has been shown to increase expression of genes coding for sclerostin and DKK1 in mice (186, 189, 196). In addition, it has been shown that the loading-induced reduction in sclerostin is greatest at sites of greatest strain and that a decrease in sclerostin is associated with an increase in bone formation (189).

Osteocyte apoptosis is also hypothesised to be associated with bone loss as a result of unloading while repetitive loading within physiological limits results in lower osteocyte apoptosis (197). Osteocyte apoptosis observed in unloaded bone occurs prior to an increase in resorption activity (187, 198, 199). Tatsumi et al. 2007 showed osteocyte death resulted in increased RANKL expression and increased osteoclast numbers, decreased sclerostin expression and increased osteoid surface but a reduced mineral apposition rate. Forty days after osteocyte ablation there was a net loss of bone volume fraction (196). In addition they demonstrated that killing of osteocytes prior to unloading prevented the increase in RANKL and sclerostin expression and decrease in bone volume that occurred in control animals (196).

1.3.2.d Development and maintenance of congruity

Congruity of articular surfaces is considered to be important for maintenance of healthy joints and normal joint function (14, 17, 18, 21, 46, 200-206). It has been postulated that there is a mechanism by which developing joints grow towards congruity and that this mechanism is likely to be sensitive to joint surface pressures (67, 77, 78, 128).

Observations from human and animal studies also suggest that adult joints become more congruous throughout life; that is, there is a degree of physiological incongruity within joints that becomes less with advancing age (77, 78, 169, 207, 208).

Goodfellow and Mitsou (1977) found that if joints of growing rabbits were unloaded through disarticulation or muscle transection they developed greater congruity than normal developing joints (78). This was demonstrated by increased contact between opposing surfaces upon re-loading, detected through a dye-exclusion technique. They concluded that this was evidence that pressure from contact with the opposing surface inhibits continued growth. However these authors recognised that the increased surface contact could be due to increased compliance of the tissues rather than a change in resting shape (78).

In their study of growing horses Doube et al. (2007) noted that the faster rate of advancement of the tidemark and higher rate of endochondral ossification at the osteochondral junction resulted in subchondral bone that was advancing more quickly toward the articular surface at sites of lower surface pressure compared to those under greater loading (68). They hypothesised that this lead to a tendency of the developing tissues to increase joint congruity and even-out joint surface pressures (68).

The findings from the above studies are consistent with FE models developed by Carter and Beaupre et al. (2000 and 2003) which predict that, during growth, intermittent hydrostatic pressure inhibits the process of cartilage thickening and endochondral ossification (128, 136). In addition, they predict that tensile strain stimulates cartilage growth and endochondral ossification. These models suggest that the ultimate thickness

of the articular cartilage is a consequence of the balance between these two forces and that in normal joints there will be thicker cartilage in areas of increased compressive load and thinner cartilage in areas of either lower compressive load or increased tensile strains (67, 128, 136). Finite element analysis models also predict that SCB density adapts to the shape and dominant loading pattern of joints and that incongruity plays important role in determining SCB density (169).

There is some evidence that articular cartilage and subchondral bone respond to incongruities and the resultant changes in joint surface pressures in ways that tend towards restoration of joint congruity and the literature regarding this is discussed in detail in section 1.6 (209-212). However, this process and whether it plays a role in the pathogenesis of joint diseases is not well understood.

1.4 Pathophysiology of joint disease

A variety of pathological processes occur in synovial joints. Inflammatory conditions such as infectious or auto-immune arthropathies are outside the scope of this review as are neoplastic and metabolic diseases. Non-inflammatory conditions that are associated with incongruity of the joint surface arise predominantly from congenital, developmental, traumatic or degenerative disease. Incongruity may occur through a focal loss of cartilage due to trauma, OCD, or OA; through malalignment due to intra-articular fracture or congenital deformities; or through collapse of SCB underlying an intact joint surface as observed in bone cysts or POD lesions in horses (10, 13, 204, 205, 213-217).

OCD and subchondral bone cysts are developmental lesions of young animals and man that cause clinical signs of joint swelling, pain and lameness. OCD is an important disease of horses with a reported prevalence of 6-10% in young Thoroughbreds and up to 25-30% in Warmbloods (218, 219). It was found to comprise 3.4% of canine orthopaedic cases presented to general practice in UK in 1996 (10). The pathogenesis remains unclear however it is thought to be a result of defective endochondral ossification leading to retention of cartilage within SCB, subsequent fissuring of this tissue and, in some cases, detachment of an osteochondral fragment. Genetic predisposition, trauma and vascular abnormalities have been postulated to play a role in development of these lesions (14, 21, 220, 221). Clinical signs include pain and joint effusion (14). Subchondral bone cysts are most commonly located in the femoral condyle of horses, their pathogenesis is not understood but may be related to OCD lesions or to altered mechanical forces due to flattening of the femoral condyle (213, 215).

Traumatic injuries may arise from an acute insult as a result of a single large force and can involve cartilage tears, osteochondral fragmentation or damage to the ligaments, synovial capsule or menisci (16, 222). Trauma may also present in the form of fatigue injuries which result from chronic repetitive forces and are common in both equine and human athletes (16, 222). Repetitive loading may cause material fatigue and an accumulation of microdamage at a rate greater than that which can be repaired. This microdamage, seen in both CC and SCB, may coalesce and lead to fracture or collapse of the joint surface. Alternatively, SCB responses such as inhibition of remodelling and increased bone formation in response to repetitive loading can result in changes to the material properties of the bone or cartilage and contribute to subsequent injury (15, 154, 156, 165, 222-225).

Fatigue fractures (also known as stress fractures) are reported to comprise 10-20% of athletic injuries in the human population and to have a 4-30% incidence rate amongst military personnel (15, 223). Whitton et al. (2018), in a study of racing Thoroughbreds in Victoria, found some degree of microdamage present in the SCB of the distal metacarpus in all animals while gross POD lesions, thought to be a result of fatigue damage to the CC and SCB, were observed in 18 of 46 horses (226). The incidence of microfractures in equine SCB is positively correlated with age and the number of race starts (13, 126, 226).

The response of bone to fatigue injuries has been the subject of some study. In a rat ulna model of cortical fatigue fractures there is an early upregulation of pro-inflammatory cytokines COX-2 and IL-6 as well as osteocyte apoptosis at the site of fracture. Osteoprotegrin expression is increased within hours as is that of vascular endothelial growth factor (VEGF). This is followed by an increase in RANKL and OPN expression and a subsequent increase in osteoclastic activity at the fracture site (227-229). The authors of the above studies concluded that osteocyte apoptosis is an important aspect of microfracture pathophysiology, however in a study of SCB in athletic horses microfractures were not associated with osteocyte apoptosis (230). Hopper et al. (2018) also found an increase in sclerostin expression at the site of fractures which is in contrast to other studies that have found either a decrease in sclerostin (227) or no change (229) at the site of fatigue fracture. It should be noted that Hopper et al. (2018) were studying SCB from animals that had suffered a catastrophic fracture rather than bone that had been loaded just to the point of fatigue so the magnitude and duration of the loading and fatigue damage may affect osteocyte responses (230).

Increased remodelling is observed at sites of fatigue injury in equine SCB (231). This remodelling is seen even if there is continued repetitive loading, a condition which would usually inhibit osteoclastic activity and remodelling activity (165, 167, 232). Resorption at sites of microfractures causing a focal loss of bone is hypothesised to be involved in the focal collapse of an intact joint surface observed in association with focal SCB injuries (166).

There is evidence that those conditions associated with incongruity of the joint surface are associated with an increased risk of OA development. Untreated OCD lesions in man are associated with early onset OA (14, 21, 200) and a history of intra-articular fractures increases the risk of a joint developing OA (201). In support of these associations in humans, experimental osteochondral defects, chip fractures and mal-aligned articular fractures are used to study degenerative pathology in animal models (17, 46, 202, 203). It is thought that degeneration of the joint tissues secondary to incongruity is related to alterations in the magnitude and distribution of loads across the joint surface as discussed in detail in section 1.6 (211, 233).

Interestingly, some studies of human patients have shown only a mild medium-term clinical impact of traumatic cartilage defects. In subjective analysis of patients treated surgically for anterior cruciate ligament (ACL) rupture, at a mean of eight years post-operatively, there was only a minor difference between outcomes of patients that had concurrent cartilage defects and those that did not (234). Messner and Maletius (1996) also found, at a mean time of 14 years after arthroscopic diagnosis of cartilage defects, excellent to good function in 22 of 29 cases despite a high incidence of radiographic joint space narrowing (22). In addition, some degree of incongruity due to poor alignment of

intra-articular fracture causes no overt OA (235) and any sort of joint injury, regardless of whether it results in surface incongruity, is associated with an increased risk of OA (201). Therefore it is likely that the degree of incongruity affects subsequent degeneration and there are other factors aside from incongruity that result in degeneration secondary to traumatic injury.

Osteoarthritis is the term used to describe the progressive degeneration and, ultimately, organ failure of synovial joints (5, 222, 236, 237). It is the most common form of arthritis in man, estimated to affect 10-15% of the Australian population (5, 6, 48, 237-239). OA is also considered a common and economically important disease in both racing and pleasure horses (13, 24, 25). In a 1996 survey in the United Kingdom it was found to comprise 19% of canine orthopaedic cases presented to first opinion practices (10) and more recently it has become recognised as a common disease of cats (11, 12, 240).

OA has many predisposing, initiating and perpetuating factors, in addition to joint incongruity, one or more of which may be involved in any affected joint. Any abnormality, present due to injury or disease, in any of the joint tissues may result in osteoarthritis; as may any abnormality in either the magnitude or distribution of loading (7, 33, 57, 241). Whatever the initiating factor, it is followed by common, interacting biochemical, cellular and biomechanical processes that perpetuate the disease (7, 33, 60, 241, 242). OA is considered by some authors to be an acceleration of the normal aging process of synovial joints (67).

The pathological changes observed in HC in degenerative disease include an initial increase in matrix synthesis with altered PG structure and decreased aggregation,

cartilage swelling and increased water content followed by fibrillation and fissuring and eventual erosion and complete loss of cartilage in end-stage disease. Chondrocyte clustering or cell death is observed histologically (19, 33, 57, 241, 243). In the CC of OA joints there is advancement and duplication of the TM, vascular invasion of CC from underlying SCB and in advanced cases complete loss of CC and ossification of the HC (8, 244, 245). The SCB of joints with OA exhibits sclerosis with or without focal lysis. There is also development of osteophytes and enthesiophytes (periarticular modelling) and inflammation and thickening of the synovium. However, while inflammation is present in OA it is thought to play a secondary role rather than to be a part of the primary pathogenesis (33). When clinical, OA results in pain and loss of function of the affected joint (19, 33, 57, 237, 241, 242, 246).

In OA the biochemical mechanisms responsible for normal cartilage ECM turnover are dysregulated and become responsible for a net destruction of the matrix. A detailed discussion of the biochemical pathways involved is outside the scope of this review however the most important enzymes involved in cartilage breakdown in OA are the metalloproteinases (MMPs). Of these the collagenases (MMP-1, MMP-8 and MMP-13) are responsible for collagen degradation while the stromelysins (MMP-3, MMP-10, and MMP-11) and aggrecanase (ADAMTS-5) cause enzymatic PG proteolysis. Other enzymes play secondary roles, mostly as activators of the MMPs. Pro-inflammatory cytokines released by the synovial membrane, importantly IL-1β and TNF-α (and IL-6 in horses), have been shown to play an important role in triggering release of MMPs as well as suppression of matrix synthesis by chondrocytes. In a self-perpetuating cycle, cartilage breakdown products are thought to trigger synovial inflammation, neutrophil chemotaxis

and release of IL-1, TNF-α as well as leukotrienes, NO, prostaglandin E2 and bradykinins (35, 241, 242, 247).

It is of note that all the forms of pathology discussed above are focal in nature and localised regions of cartilage pathology are often associated with pathology of the underlying subchondral bone and sometimes with pathology of the opposing surface (166, 202, 248-253). Even in advanced OA there is regional variation in the changes across a joint surface (101, 243, 251). It has been suggested that these focal variations may be related to local loading of the joint surface (101, 249, 251).

1.5 The study of joint disease

There are many methods available to investigate synovial joint biology, mechanobiology and pathophysiology, including *in silico* modelling, *in vitro* studies of cellular and molecular activity, studies of *ex vivo* specimens as well as *in vivo* animal trials. This section will focus on the existing literature surrounding animal trials, as it is of most relevance to the current investigation, in addition to reviewing the clinical and laboratory techniques available to study the synovial joint tissues.

1.5.1 Animal models

Existing literature contains many studies of naturally occurring joint disease in both man (101, 251, 254, 255) and, to a lesser extent, companion animals including horses (144, 166, 252, 256-258). These are limited, however, by the progressive, generalised degeneration which obscures early events in the pathophysiology of these conditions

(259-261). Studies utilising joint tissues from food producing animals such as cattle (262, 263), from which a large number of samples of varying severity and chronicity are easily obtained, are one solution to this issue. However these opportunistic samples do not facilitate investigation of the initiation of the disease process or allow interventions, and provide no control over nutritional, environmental or exercise factors.

Animal models enable the study of early and more specific changes in joint pathology (259-261). Large animal models in general, and those using horses in particular, are promoted as good models for human disease as well as for joint disease in horses themselves (46, 260, 264, 265). Equine joints are the closest in size and in cartilage thickness to those of man, and horses are athletic and their exercise can be well controlled. Some equine joints are amenable to arthroscopy for *in vivo* examination and they provide ample tissues for specimen collection. Recently, an equine model of OA has been developed in which the animals need not be euthanased at the conclusion of the trial (265).

The equine carpal chip fracture model involves fracturing a fragment of bone from the disto-dorsal radial carpal bone via arthroscopy. This fragment (otherwise called a chip) of bone is left *in situ* while the animals undergo a standard post-operative training regimen (266-272). This model has been used extensively and induces changes consistent with naturally occurring equine OA such as mild lameness, increased response to carpal flexion, joint effusion, synovial inflammation, osteophytes, cartilage fibrillation, chondrocytes cloning and chondrocyte death. It has also been used to test various systemic and intra-articular medical treatments for equine OA (266-272). A chip fracture model of OA utilising the fetlock joint of horses has also been developed (265).

Of the small animal models of joint disease the most common involve creation of instability, often within the stifle joint. Instability of the stifle can be created through transection of cruciate or collateral ligaments or partial or total meniscectomy. Most studies use surgical transection of the anterior cruciate ligament which has been performed in mice, rats, rabbits, cats and dogs (273-284). Meniscectomy has also been used in a number of species including rabbits, mice, guinea pigs and sheep (285-288). Although not common, creation of instability in the equine fetlock, via transection of the lateral collateral ligament and lateral collateral sesamoidean ligament, has also been shown to cause clinical and radiographic signs of OA as well as increased PG synthesis in the HC (289). It is thought that a change in the distribution of surface contact pressures and reduction in loading as well as changes in muscle forces, range of motion and kinematics are the mechanisms by which instability results in joint pathology (290-292). It has been demonstrated that the greater the instability the greater the degree of pathologic change (282, 283, 285).

Both single impact and repetitive impulse loading of joints have been found to induce HC, CC and SCB changes. These models, in rabbits, dogs, goats and horses, have been used to study OA, intra-articular fractures and equine POD (293-302). Changes in the CC and SCB such as microfracture and increased formation activity and bone volume tend to occur early following repetitive impact loading, followed by cartilage fibrillation and later still, changes in PG content and synthesis (293-295). Single impact in rabbits also results in CC microfractures, SCB sclerosis and HC surface lesions (301). Single impact in dogs results in CC microfracture at relatively low loads while at higher loads overt SCB fracture occurs (296). Single impacts at loads that resulted in CC microfracture initially

were also associated with SCB sclerosis, loss of PG and fibrillation of HC at later time-points (298).

Single impact injuries in equine models have resulted in mild focal cartilage changes such as a reduction in GAGs and histological degenerative changes but no evidence of POD lesions, leading the authors to conclude that while single impacts may play a role in equine OA, repetitive loading is required for development of POD (297, 300).

Immobilisation through casting or pinning of limbs induces degenerative changes such as reduced GAG content, increased GAG turnover, reduced collagen density, thinning of HC, chondrocyte hyperplasia and fibrillation and fissuring progressing to loss of cartilage in rat, rabbit and dog models (125, 129, 303, 304). These models are of particular relevance to human joint disease in patients that are bedridden or paralysed (305, 306).

Surgical creation of cartilage grooves has been used to create OA in dog, sheep and horse models (292, 307-310). Mastbergen et al. (2006) and Intema et al. (2008) both created grooves on the femoral condyles of canine stifle unilaterally and bilaterally respectively (307, 308). Cartilage changes consistent with OA were seen by 10 weeks although not at three weeks suggesting that these changes were a result of degeneration rather than a direct result of the surgical intervention. Mastbergen et al. (2008) used a similar model in the ovine fetlock that resulted in both cartilage and SCB changes consistent with OA, including periarticular modelling (309). However this model was technically difficult as the HC in this joint is thin and difficult to access. They recommended that this could be done better in a horse fetlock model, which Maninchedda et al. (2015) subsequently

developed. This equine groove model resulted in mild OA with little inflammation, consistent with naturally occurring OA in horses (310).

Chemically induced OA models have also been used in various species including guinea pigs, rats, rabbits, dogs and horses. Chemical preparations include sodium monoiodoacetate (MIA), papain, Freund's adjuvant, filipin and autologous cartilage particles (260, 261, 311-316). These models all result in microscopic and macroscopic changes consistent with cartilage degeneration as well as clinical signs consistent with pain and loss of function (311-314, 316). However, they may not be as applicable to the study of OA as surgically induced models due to the rapid cell death and cartilage loss which is unlike slowly progressive naturally occurring disease (260, 311).

The Hartley guinea pig strain develops spontaneous OA and has been used to study this disease. In addition, genetic modification of mice has been widely used to study the role individual genes and their protein products play in joint disease (26). These models are useful for identification of potential therapeutic targets, however the development of disease or treatments tested on these models may not relate well to naturally occurring disease which is likely to be multi-factorial and occurring on different genetic backgrounds (26, 260, 261).

Of the above models those involving joint instability and the creation of cartilage grooves both result in incongruity of the joint surface, however this incongruity is relatively generalised and difficult to define. In addition, all the above models will ultimately involve incongruity due to cartilage loss as a result of degeneration, however this occurs once there is significant cartilage pathology which makes distinguishing the effects of

incongruity from the effects of degenerative changes challenging. Animal models that involve well-defined, localised incongruity as part of the primary condition, and hence the opportunity to study its effects, include osteochondral defects and step defects and are discussed in detail in section 1.6.

1.5.2 Clinical and laboratory techniques

In addition to clinical examination and lameness evaluation the clinical techniques that may be used to evaluate synovial joints *in vivo* include radiography, ultrasonography, scintigraphy, computed tomography (CT) and magnetic resonance (MR) imaging to image the bony and soft tissue structures of the joint; arthrocentesis for collection and analysis of synovial fluid; and arthroscopy to visualise the joint surfaces and collect cartilage and synovial biopsies; and assessment of biomarkers in body fluids.

Lameness evaluation is commonly used to assess pain and loss of function due to musculoskeletal disease, including that involving synovial joints. Evaluation of equine lameness by clinicians is subjective but can standardized to some degree and made semi-quantitative by using grading scales such as that provided by the American Association of Equine Practitioners (AAEP) (317). More objective and quantitative assessments of lameness can be provided by force-plate or pressure-plate analysis, optical motion capture or inertial measurement units (318), however a detailed discussion of these techniques is beyond the scope of this review.

Radiography is a cheap and easily accessible way to image the bony and, to a lesser extent, soft tissue structures of synovial joints. It can be used to visualize SCB sclerosis, lysis,

periarticular modelling, bony fragments within the joint space and fractures or defects of the SCB. However it is an insensitive imaging modality that will detect only relatively large changes within the tissues of the joint (319-321). It lacks the ability to effectively image articular cartilage aside from the joint space narrowing observed with end stage disease and significant cartilage loss. While it is able to detect joint effusions and soft tissue swelling surrounding joints, these are non-specific markers of joint disease (310, 320). Computed tomography provides similar information to radiography but has the advantages of creating 3D images which reduces issues associated with imposition of structures and has greater sensitivity than radiography (321, 322). However CT is not useful for imaging articular cartilage without the use of contrast agents (322).

Ultrasonography and MR imaging can be used to visualize menisci, ligaments, periarticular structures as well as the joint space. Ultrasonography is cheap and readily available but provides little information about bony structures apart from surface contour (323). Magnetic resonance imaging can be used to image cartilage (324) but has been considered inferior to CT for imaging of bony structures of the joint (320, 321, 324). Recently however, it has been demonstrated to be effective for the imaging of chondral and osteochondral defects (324). Both CT and MR imaging are relatively expensive and time-consuming modalities that may require general anaesthesia (321). Unlike the above imaging modalities that provide only morphological information about bony structures, scintigraphy is able to give an *in vivo* estimation of local osteoblastic activity in bone however it generates only a poor resolution 2D image (321).

Arthroscopy provides a means to visualize the joint surface and assess for macroscopic evidence of joint disease without the need for euthanasia and equine joints are good

candidates for arthroscopy due to their large size (46, 265). Arthroscopy has also been used for collection of synovium and osteochondral samples in a non-terminal study of joint disease of the equine fetlock (265). However the size and number of the samples collected in this manner are limited. Arthroscopy also requires the animals to be under general anaesthetic, unless it is being performed on fetlocks of the forelimbs, and results in some trauma to the synovium (265).

Synovial fluid is easily collected and evaluated *in vivo* in equine models of joint disease (46, 265, 325). This can provide information on the degree of inflammation and assess for the presence of infection. Synovial fluid can also be analysed for biomarkers of cartilage and bone metabolism. While these biomarkers require more validation for use in a clinical setting they can be useful for research purposes (325, 326). Serum and urine may also be used to measure biomarkers of cartilage and bone metabolism (327-330).

Various imaging and histopathological techniques can be used to study tissues of the synovial joint once harvested either via biopsy or at post mortem. Post mortem collection enables investigation of specimens of a greater number and size. The methods for most of these techniques are widely used and well described in the literature.

The Osteoarthritis Research Society International (OARSI) histopathology initiative recommends equine synovial samples be fixed in 10% neutral buffered formalin (NBF), embedded in paraffin blocks from which 5µm sections are cut and stained with haematoxylin and eosin (H and E). This processing is used widely throughout the literature (265, 266, 271, 272, 331).

Osteochondral specimens collected from joint surfaces can be studied with or without prior decalcification. Undecalcified samples are required if the mineral component of the bone and CC ECM is important for imaging or the measurement of interest. Decalcification improves embedding and sectioning of the specimen if the mineral component is not necessary (332). Existing literature reports a number of techniques to image the mineralised structures of SCB specimens. Earlier studies were limited to microradiography which provides only two dimensional (2D), qualitative information at relatively low resolutions. More recently dual x-ray absorptiometry (DXA) and peripheral quantitative computed tomography (pQCT) have become available to provide quantitative measurements of bone density in 2D or 3D respectively, however both of these are limited somewhat by relatively low resolution and the inability to provide good quality images of trabecular structure (69, 333, 334).

Micro-computed tomography (microCT) creates 3D images of the mineralised structures of SCB at relatively high resolution. Equine SCB has been imaged at voxel sizes down to 4μm (335). Easily accessible software is available to provide quantitative evaluation of both cortical and trabecular parameters from these 3D images. Specimens up to 10cm in diameter may be imaged however the maximum resolution decreases for larger samples (336). MicroCT by synchrotron beam is considered the gold standard for image quality (255, 337) however this modality is not readily available.

Backscattered scanning electron microscopy (BSEM) provides high resolution images in which variation in bone mineral content can be visualised and quantified at less than $1\mu m^3$ volume resolution. This variation in tissue composition is best imaged on polymethylmethacrylate (PMMA) embedded bone (338, 339), a process that has been

used successfully with equine SCB (156, 165, 231). BSEM images can be used to identify bone surfaces that are mineralising, those that are resorbing or resorbed and those that are quiescent (165, 231, 339).

While BSEM imaging provides information about the activity on bone surfaces at a given time-point, intra-vital fluorescent dyes can be used to evaluate formation activity at various points during a trial as well as the rate of bone formation. These dyes bind to calcium as it is incorporated into bone if they are present in the extracellular fluid at the time of mineralisation, and appear as a fluorescent line in the bone when illuminated with ultraviolet light microscopy. As they are bound to the mineral component of the bone ECM these must be viewed on undecalcified sections (332). A range of fluorescent dyes (fluorochromes) have been used in equine trials: calcein blue, xylenol orange, calcein, oxytetracycline and alizarin complexone (157), however the most common in the literature are oxytetracycline and calcein (68, 156, 244, 266, 297, 340, 341). Calcein has a brighter fluorescence and shorter half-life so tends to give brighter and more distinct labels compared with tetracyclines (332) however is significantly more expensive than tetracyclines when used in large animals. Oxytetracycline is registered for intravenous use, which gives labels of better definition than other routes of administration, in horses in Australia and is an inexpensive choice of fluorochome.

In addition to the mineralised components of bone ECM, the amount and distribution of unmineralised osteoid is an important part of investigations into bone modelling and remodelling activity (342). Osteoid is not apparent on microCT or BSEM which image the mineralised tissue. Masson's Goldner trichrome (MG) and von Kossa stains can be used to distinguish osteoid from mineralised bone, however the haematoxylin component

in MG gives better nuclear staining and hence better cellular detail than von Kossa (332, 342). Masson's Goldner staining has also been used to measure cartilage thickness in addition to bone parameters (287) and has been used in existing literature to study equine SCB (165, 340).

Identification of osteoclasts in SCB is of interest because of their important role in bone remodelling. This has been done in existing literature by histochemical staining for either TRAP or cathepsin-K, both of which are enzymes produced in high concentrations by osteoclasts (343, 344). Staining for TRAP is a sensitive method for identification of osteoclasts, although other cells may also express this enzyme (332, 345). It has been used extensively for identification of osteoclasts in laboratory animals and humans (121, 250, 346-348). In equine studies, it has been used as a marker for osteoclastic cells in culture and cytology (349-351) and to identify odontoclastic cells in histological sections in a study by Staszyk et al. (2008) (352). Its use in equine SCB is less common. Bertuglia et al. (2015) used cathepsin-K as a marker for osteoclasts in their study of equine SCB (144).

Cartilage histology can be performed on sections stained with a number of different agents. The OARSI histopathology initiative recommends staining of osteochondral sections with Safranin-O, which binds to the anionic PGs and can be used to estimate PG content of cartilage, in addition to H and E (331, 332). Toluidine blue or a combination of Safranin-O/fast green are other common stains used for cartilage histology (332). In situations where it is desirable to perform both light microscopy and transmission electron microscopy (TEM) on the same specimen staining techniques must be altered as the resin embedding medium needed for TEM affects routine stains (353, 354). The use of

methylene blue alone or in combination with other stains on resin-embedded sections has been described in the literature and is a simple method providing good staining of cartilage and chondrocytes where quantification of PG is not required (220, 353-356). It has been used successfully in previous investigations of equine cartilage (220, 355, 356).

High resolution images of cartilage microstructure including collagen fibre aggregates, chondrocytes and their peri-cellular matrix can be obtained through differential interference contrast (DIC) microscopy (262, 357). This method allows visualisation of the cartilage ECM in a hydrated state, closer to its condition *in vivo*, avoiding the dehydration required for many embedding and staining techniques and has been used previously to image equine osteochondral sections (258).

1.6 Osteochondral defects and joint incongruity

Surgically induced chondral (cartilage only) or osteochondral (OC, cartilage and SCB) defects are one way in which incongruity of a joint surface can be created experimentally and there is good evidence that these defects cause altered strains in the surrounding and opposing cartilage and SCB (1-4, 233, 358, 359).

Increased peak surface pressure surrounding OC defects as well as loss of surface pressure over and opposing defects has been demonstrated by direct measurement in cadaver experiments in rabbits, dogs, horses and man (3, 18, 106, 233, 360). The magnitude of the increase in peak pressure on the surface surrounding the defects has varied slightly between investigations with increases of 10-30% reported in animal studies of defects 2-

7mm in diameter (18, 360) while studies of defects 10-20mm in diameter on human femoral condyles measured increases of 50-90% (3, 233). Unlike other studies, Nelson et al. (1988) found no change in peak contact stresses or total contact area of the joint surface at 11 months after creation of a 6mm diameter osteochondral defect on the femoral condyle of dogs (361).

It appears that there may be a critical size above which contact stresses are increased as Guettler et al. (2004) found that defects in human femoral condyles only resulted in a significant increase in rim stress if they were equal to or greater than 10mm in diameter (233). However animal studies have found an increase in peak surface pressures surrounding defects as small as 2mm in diameter (18, 360). This difference may be due to the different shapes of the femoral condyles in humans and animals or because the relative size of the defect to total articular surface area is important (233).

Guettler et al. (2004) (233) and Brown et al. (1991) (360) agree that, if there is an increase in the peak surface pressure, its magnitude does not change with the size of the defect. These two studies also agree that as the size of the defect increases, the distance between the rim of the defect and the peak pressure point decreases. Brown (1991) observed peak pressures approximately 0.4mm outside the rim of 2mm defects and 0.15mm for 6mm defects (360) while Guettler (2004) reported peak pressures approximately 4.2mm outside 10mm defects and 1.5mm outside 20mm defects (233).

Ex-vivo studies have also allowed gross visualisation of cartilage deformation around osteochondral defects. Braman et al. (2005), using a rabbit model of 2.5mm diameter defects in femoral condyles, and Gratz et al. (2008), using 4mm diameter cartilage defects

in human femoral condyle explants, both observed a greater degree of flattening of cartilage surrounding the defect upon loading compared to cartilage in intact joints and hypothesised that this could be due to either an increased load on this cartilage or because it was less resistant to compression, or both (2, 4). Both also observed that cartilage opposing these defects bulged into the defect when the joint was loaded, suggesting that it, too, is experiencing abnormal strain (2, 4). Increased strain has also been measured in bovine cartilage explants in a narrow (1mm) region between two parallel indenters, the effect of which upon loading is similar to two sides of a defect (362).

Greater detail regarding strains experienced by cartilage and SCB in the vicinity of chondral and osteochondral defects is provided by FE models. Models of HC predict increased compressive and tensile strains adjacent to defects and in the in-contact cartilage on the opposing joint surface, increased shear stress in cartilage at and opposing the rim of the defect and increased collagen fibre strain in cartilage opposing the defect (4, 358, 359). Similarly, FE models of SCB predict increased stresses and strains adjacent to osteochondral defects and SCB cysts (1, 215, 363).

A reduction in stress and strain at the base of chondral and osteochondral defects is also predicted by FE models (1, 364). Duda et al. (2005) in a model of osteochondral defects on the femoral condyle of pigs estimated a reduction in strain at the base of an osteochondral defect to approximately 27% that of an intact joint surface (1). An FE model used by Fisher et al. (2015), in addition to predicting lower than normal stress at the base of chondral defects, further predicted that compressive stress would increase gradually with increasing distance below the defect but remain lower than normal in bone up to 5mm deep to the osteochondral junction (364).

Using a simplistic two-dimensional FE model of human hip joints Durr et al. (2004) predicted that an osteochondral defect on the femoral head would result in an approximately four-fold increase in von Mises stress (a sum of stresses regardless of direction, indicating shear behaviour) in the directly opposing acetabular SCB (363). This effect was not apparent in the femoral head SCB when a defect was modelled on the acetabulum, so the shape of the articular surface is likely to affect predictions using this model and it may not be applicable to other joints. In addition, this report does not provide details of the mechanical properties they have attributed to the tissues which makes interpretation of their findings more difficult.

While there are many histological and biochemical studies of chondral and OC defects, most of these using large animal models have focussed on defect healing rather than the effect of the lesion on the surrounding tissues or the joint as a whole (1, 20, 202, 311, 365-370).

Several studies have, however, observed changes surrounding or opposing the OC defects. Reported abnormalities in cartilage surrounding equine osteochondral defects include subjective thinning of the HC, increased water content, decreased proteoglycan content and chondrocyte cloning and cell death (20, 253, 311, 340, 366). Progressive thinning, fibrillation, cleft formation and chondrocyte cloning in the articular cartilage surrounding such defects have also been demonstrated in a goat model (365).

SCB deep to OC defects in horses has also been investigated, finding in most cases reduced bone volume fraction (340, 370-373). Unlike others, Hanie et al. (1992) reported

sclerosis below osteochondral defects in the third carpal bone of horses and it is not clear why observations in this study differed from others (202).

In SCB adjacent to OC defects in the femoral condyles of horses and ponies increased bone volume has been reported (340, 370). Kold et al. (1986) also investigated remodelling activity surrounding OC lesions in an equine model, finding that it was increased at the periphery of the defects as suggested by increased osteoclastic resorption, increased uptake of fluorescent markers and increased amounts of woven bone (340).

Models of OC defects in sheep, goats and pigs also describe loss of bone volume, including the formation of cavitatory lesions, at the base of osteochondral defects and an increase in bone volume in the adjacent SCB (1, 365, 368, 374).

Observations of SCB below cartilage-only defects are less consistent. Reduced bone volume (375, 376) or cyst formation (377, 378) has been reported when cartilage defects have been treated with autologous cell transplantation, SCB microfracture or SCB drilling, however this has not been observed in other studies of lesions treated similarly (364, 370, 379-382). Conversely, some equine studies of chondral defects have reported sclerosis of underlying SCB (202, 373). Time since creation of a chondral defect may affect findings as Hurtig et al. (1988) reported bony lysis below chondral defects on the radial facet of equine C3s up to 4 months after defect creation but normal to increased density at 5 and 9 months (373). Depth and diameter of the lesion may also be important. Fisher et al. (364) observed a loss of bone volume below untreated, full-thickness, but not partial-thickness, cartilage lesions in a mini-pig model, and Salonius et al. (371) observed

a subjective loss of bone volume below untreated, full-thickness cartilage defects of 8mm in diameter, but not smaller defects, on equine C3s.

Step defects are an alternative method of creating joint incongruity and have been used in sheep, pig and rabbit models (203, 209, 211). Trumble et al. (2001) used an osteotomy to create a 1mm step in the surface of the medial tibial plateau in sheep and showed that the higher edge of the defect was under greater contact pressure than the lower edge (209). The hyaline cartilage on the lower side was thickened compared to normal with increased matrix material, increased cellularity and hypertrophy of the chondrocytes. Conversely, cartilage on the higher edge was significantly thinner with compression and bending of collagen fibrils (209). Llinas et al. (1993) reported similar cartilage changes in a study of rabbit stifles in which step defects had been created on the medial femoral condyle (211). Both Trumble et al. (2001) (209) and Llinas et al. (1993) (211) noted that the cartilage changes resulted in an improvement in joint congruency and partially restored normal contact pressures. Llinas et al. (211) reported advancement of the tidemark on both high and low sides of the step which would be consistent with FE models of Beaupre and Carter (2000, 2003) (128, 136) as the lower side is likely to be under reduced hydrostatic pressure and the higher experiencing greater tensile strains.

While Trumble et al. (2001) observed no change in the SCB (209), Llinas et al. (1993) documented thickening of trabeculae and SCB plate under the high side of the step off and hypothesised that this could be an adaptive change to the increased pressure experienced by this part of the joint surface which was found to be as much as three times normal (211).

In agreement with the above animal models of incongruity Bani Hassan (2013), in a study of naturally occurring palmar/plantar osteochondral disease in racing horses, found that articular cartilage as a whole and calcified cartilage in particular were thicker in areas overlying collapsed subchondral bone than where they were covering intact SCB (212). He hypothesised that this was a result of unloading of this cartilage after the SCB collapse and that it may be an attempt by these tissues to restore joint congruity (212).

All the studies discussed above have investigated changes in the cartilage and bone immediately surrounding OC or step defects which is likely to be influenced by inflammatory cytokines and other biochemical changes as a result of tissue damage at the time of defect creation (383-387). There is much less work studying the joint surface opposing OC defects and that which has been done has been concerned with the initiation of OA rather than studying the specific local effects of the presence of the defect.

Grossly raised areas of cartilage ("kissing lesions") have been frequently observed on joint surfaces immediately opposing osteochondral defects in equine mid-carpal joints and are noted to be subjectively more marked in exercised horses compared to those rested after creation of the defect (123, 202, 253, 311, 388). While I am not aware of histological studies of kissing lesions, biochemical studies have been performed. Fibronectin, a glycoprotein that is present in small amounts in normal cartilage and markedly greater amounts in OA cartilage, was found in elevated concentrations and the GAG content was found to be decreased in cartilage opposing full thickness defects (123, 253).

There is little information on the changes in SCB opposing OC defects and I am not aware that subchondral bone opposing step defects has been studied. Hanie et al. (1992) observed bony lysis radiographically in the SCB of Crs opposing an induced C3 articular surface defect (202). Durr et al. (2004) hypothesised that increased strain in SCB opposing defects as predicted by their FE model could result in focal lysis due to remodelling of fatigue damage, however, as discussed above, their model of the human hip joint may not be applicable to other joints (363). Alternatively, it is possible that a focal decrease in loading would directly result in increased remodelling and loss of bone volume (121, 152, 161-163).

Studies of OC and step defects in all species have consistently found evidence of degeneration such as chondrocyte cloning, chondrocyte necrosis, PG depletion, fibrillation, cleft formation and thinning of cartilage opposing the defects (17, 18, 202, 366). Unlike the majority of osteochondral defect studies, Salonius et al. (2018) reported no degenerative changes opposing osteochondral lesions 2-8mm in diameter in the equine mid-carpal joint (371). Size of the defect may influence the development of degenerative lesions on the opposing surface as Convery et al. (1972) found degeneration opposing defects of diameter 9mm or greater but not 3mm on the femoral condyle of ponies (366). However, Schinhan et al. (2012) (17) documented that both 7mm and 14mm diameter defects in the medial femoral condyle of sheep induced osteoarthritic changes in cartilage surrounding and opposing the defects and Vaseenon et al. (2011) (18) found degenerative changes opposite 2mm diameter defects on rabbit femoral condyles and hypothesised that these degenerative changes may have occurred due to altered loading of this cartilage.

Most osteochondral defect studies in large animal models report no macroscopic changes in cartilage distant to the defect (17, 18, 202, 366). Todhunter et al. (1993) reported linear striations in all mid-carpal joint surfaces in joints with a Cr osteochondral lesion, however these defects were larger than those of other studies, involving approximately 1/3 of the articular surface of distal Cr (253). In rabbit models, joints with 2mm osteochondral defects on the medial femoral condyle were observed to have degenerative changes in the lateral compartment of the stifle and the presence of peri-articular modelling was reported at 20 weeks after creation of a 5mm step defect on the medial femoral condyle suggesting that focal regions of incongruity can result in global joint pathology at least in small animal models (18, 389).

1.7 Aims and Hypotheses

In order to better understand the homeostasis of synovial joints and the pathogenesis of conditions affecting them, the aim of this investigation was to determine how articular cartilage and subchondral bone in adult animals respond to a focal loss of congruity and the subsequent changes in loading.

It was expected that a model utilising an osteochondral defect within the equine carpus would allow analysis of focal regions of joint surface experiencing either increased or decreased loading depending on their position relative to the defect.

It was hypothesised firstly that the degree of remodelling and bone volume of SCB in adult animals is dependent on the local loading of the overlying joint surface and that this

would change rapidly due to a focal change in loading; and secondly that the intact cartilage of adult animals could respond to a change in local surface pressure in a way that attempts to restore congruity.

Chapter 2

GENERAL MATERIALS AND METHODS

2.1 Live animal procedures

Selection of horses (with the exception of the un-operated control animals), surgical procedures, training, clinical assessments, clinical pathology, radiography and bone labelling were all performed by Dr Gareth Trope and his team at the School of Animal and Veterinary Sciences at Charles Sturt University, Wagga Wagga, NSW, Australia. All animal procedures were performed with Animal Care and Ethics Committee approval from Charles Sturt University (CSU ACEC 14/021).

2.1.1 Selection of horses for inclusion

Six horses were selected for inclusion in the trial. Each was a 3-4 year-old Standardbred (Table 2.1). Prior to inclusion no abnormalities were observed on physical examination and the animals displayed no lameness at a straight trot, no response to carpal flexion, minimal carpal effusion and no abnormalities on radiographic examination of the carpus.

Horse number	Sex	Age	Treated limb
1	Female	4	Left
2	Female	4	Right
3	Female	3	Left
4	Gelding	4	Left
5	Gelding	4	Right
6	Female	4	Left

Table 2.1 *Signalment and limb randomly selected for treatment of trial horses**.** All animals were 3-4 years of age and of Standardbred breed.*

Six *ex vivo* joints were also collected to be included in an un-operated and untrained control group. These joints were sourced from Standardbred horses that had been euthanased for unknown reasons. One forelimb from each horse was chosen randomly by coin toss for sample collection. Joints were excluded if there were any gross abnormalities of the midcarpal joint. Signalment and the selected limb of these control horses are shown in Table 2.2.

Horse number	Sex	Age (years)	Selected limb
UC1	Female	5	Right
UC2	Gelding	5	Left
UC3	Female	4	Left
UC4	Female	4	Right
UC5	Gelding	5	Left
UC6	Female	3	Right

Table 2.2 *Signalment of horses selected for the un-operated, untrained control group. All were of Standardbred breed.*

2.1.2 *Surgical procedure*

One mid-carpal joint of each trial horse was randomly selected by coin toss (Table 2.1) for treatment. Each contralateral mid–carpal joint was assigned as a control to be sham-operated.

Thirty minutes prior to anaesthesia horses were sedated with acepromazine[1] at 0.03 mg/kg intravenously (IV), given tetanus toxoid[2] intramuscularly (IM), procaine penicillin[3] at a dose of 22 mg/kg IM, gentamycin[4] 6.6 mg/kg IV and phenylbutazone[5] at a dose of 4.4 mg/kg IV. Anaesthesia was induced with 1.1 mg/kg xylazine[6] IV followed by 2.2 mg/kg ketamine[7] and 0.05 mg/kg diazepam[8] IV. Following anaesthetic induction the horses were intubated and maintained with isoflurane[9] in 100% oxygen. Animals were monitored for the duration of anaesthesia with pulse oximetry, direct arterial blood pressure, capnography, end-tidal gas monitoring and blood gas analysis.

Once under anaesthesia each treated joint was clipped and aseptically prepared then approached arthroscopically to facilitate creation of a defect in the cartilage and subchondral bone of the distal surface of the radial carpal bone (Cr). The arthroscopic portal was situated dorsolateral and instrument portal dorsomedial.

[1] (A.C.P. 10, Ceva Animal Health, Glenorie, NSW, Australia)
[2](Equivac® T, Zoetis Australia, Rhodes, NSW, Australia)
[3] (Ilium Propercillin, Troy Laboratories (Australia), Glendenning, NSW, Australia)
[4] (Ilium Gentam 100, Troy Laboratories, Glendenning, NSW, Australia)
[5] (Ilium Nabudone P, Troy Laboratories, Glendenning, NSW, Australia)
[6] (Ilium Xylazil 100, Troy Laboratories, Glendenning, NSW, Australia)
[7](Ilium Ketamil injection, Troy Laboratories (Australia), Glendenning, NSW, Australia)
[8] (Ilium Pamlin injection, Troy Laboratories (Australia), Glendenning, NSW, Australia)
[9] (Aerrane, Baxter, Toongabbie, NSW, Australia)

The osteochondral defect (Figure 2.1) was created via curettage of the articular cartilage followed by debridement of the underlying SCB with a motorised burr. The defect measured approximately 10 mm dorsal to palmar, 15-20 mm medial to lateral and extended through the full depth of the articular cartilage and between 0.5 and 1.3mm deep into the SCB. The dorsal edge of the defect was located approximately 0.5 cm palmar to the dorsal rim of the radial carpal bone. Following creation of the defect the joint was lavaged copiously with sterile saline to remove all cartilage and bone debris and the arthroscopy and instrument portals closed routinely.

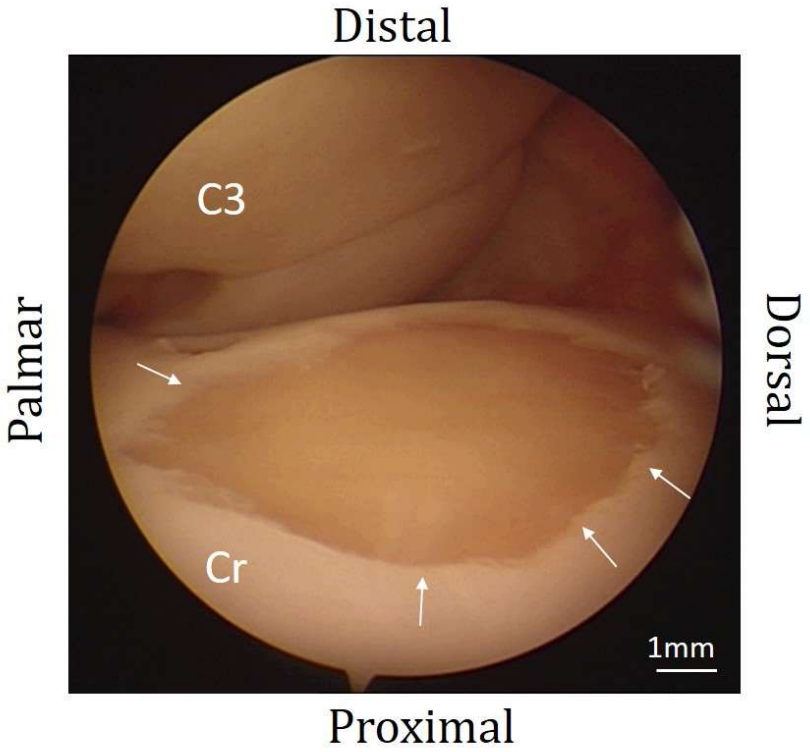

Figure 2.1 *Arthroscopy image of osteochondral defect (arrows) in Cr of horse 2. Opposing C3 can be seen distally. View dorsolateral to palmaromedial. Image: Dr Gareth Trope.*

The sham operated joints were similarly clipped, aseptically prepared and approached arthroscopically with equivalent portals. They were lavaged with sterile saline and the arthroscopic and instrument portals closed routinely.

Both limbs were bandaged for two weeks post-operatively with the bandages changed every two-three days. Each horse received phenylbutazone[10] orally for 10 days post-operatively. The Procaine penicillin dose was repeated twice at 12 and 24 hours after the pre-operative dose and the gentamycin dose was repeated once 24 hours after the pre-operative dose. Skin sutures were removed 10 days after surgery.

2.1.3. Exercise protocol

Each horse was exercised on a high speed treadmill five days per week from day 15 until the end of the study (Table 2.3). They were housed individually in stalls at all other times.

Gait	Speed	Duration
Walk	8km/hr	4 minutes
Trot	16km/hr	2 minutes
Canter	32km/hr	2 minutes
Trot	16km/hr	2 minutes
Walk	8km/hr	4 minutes

Table 2.3 *Treadmill training protocol. Each trial animal completed the above regimen five days per week with the exception of Horse 6 which underwent a modified training program due to illness.*

[10] (Bute Paste, Ranvet Pty Ltd, East Botany, NSW, Australia)

2.1.4. *Bone labelling*

All horses received oxytetracycline[11] (10 mg/kg intravenously) on days 0, 30, 60 and 67 of the trial. The last two doses were administered only seven days apart as it was expected the bone formation rate would be greatest at this time. This was also an attempt to make it easier to differentiate these doses from the earlier ones, 30 days apart. The final dose was given three days prior to euthanasia to allow adequate time for the fluorochrome to be assimilated into mineralising tissues and covered by enough additional bone so that the label would not be lost into the fixative. This interval between the final fluorochrome dose and sacrifice has been previously published (70, 209).

2.1.5. *Lameness evaluation*

Horses were assessed daily for evidence of lameness at the walk and trot in a straight line on flat ground and on the treadmill. Videos of the animals at a straight trot on flat ground and on the treadmill were also recorded weekly for grading of lameness by independent examiners as described in Chapter 3.

2.1.6. *Synovial fluid collection*

Synovial fluid was collected weekly as described in Chapter 3.

[11] (Engemycin 100, Coopers Animal Health, Bendigo East, Victoria, Australia)

2.1.7. Radiographic evaluation

Radiographic evaluation of the carpus was performed prior to inclusion of horses in the study, on day 14, and at the end of the study on day 70. Five views were taken of each carpus: lateromedial, flexed lateromedial, dorso-palmar, dorsolateral-palmaromedial oblique and dorsoproximal-dorsodistal skyline of the third carpal bone (General Electric Proteus x-ray room (150kVp, 1000mA), Radincon x-ray room (100kVp, 300mA) and AGFA CR-30 processor, Agfa, Greenville, SC, USA).

2.2 Post mortem procedures

Horses were euthanased on day 70 via administration of intravenous sodium pentobarbitone[12] following sedation with 1.1 mg/kg xylazine IV.

2.2.1 Macroscopic examination

The middle carpal joint was opened and examined grossly as described in Chapter 3. All findings were documented photographically and in writing.

2.2.2 Synovial membrane collection

Sections of synovium, approximately 3-5mm square, were collected by sharp dissection from both the dorsolateral and dorsomedial aspects of each mid-carpal joint. The synovium from the dorsolateral aspect was adjacent to the lesion on the radial carpal bone

[12] (Lethabarb, Virbac Animal Health, Milperra, NSW, Australia)

in treated joints. These specimens were fixed in 10% neutral buffered formalin (NBF) then processed and assessed histologically as described in Chapter 3.

2.2.3. Osteochondral Sample collection

Following macroscopic examination, osteochondral sections from the radial, third and ulnar carpal bones were harvested from each carpus.

2.2.3.a Radial Carpal Bones

To allow multiple analytical procedures to be performed all Crs were sectioned using a band saw into five sections in an oblique dorso-palmar plane (Figure 2.2 and 2.3). The method of fixation and storage, and purpose of each section is summarised in Table 2.4.

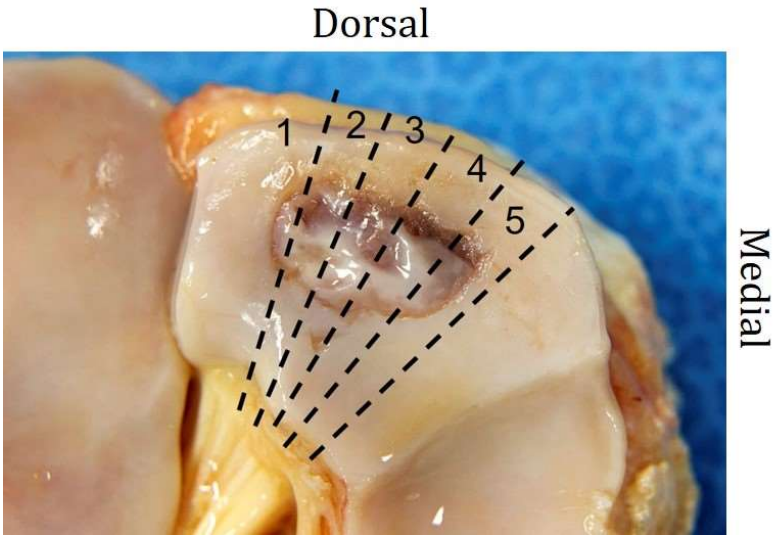

Figure 2.2 *Sectioning of the radial carpal bones. View of distal articular surface of Cr. Dotted lines indicate the oblique dorso-palmar cuts which created sections of bone (Figure 2.3), each including some part of the surgical defect as well as adjacent cartilage and bone, numbered here 1-5 from axial to medial.*

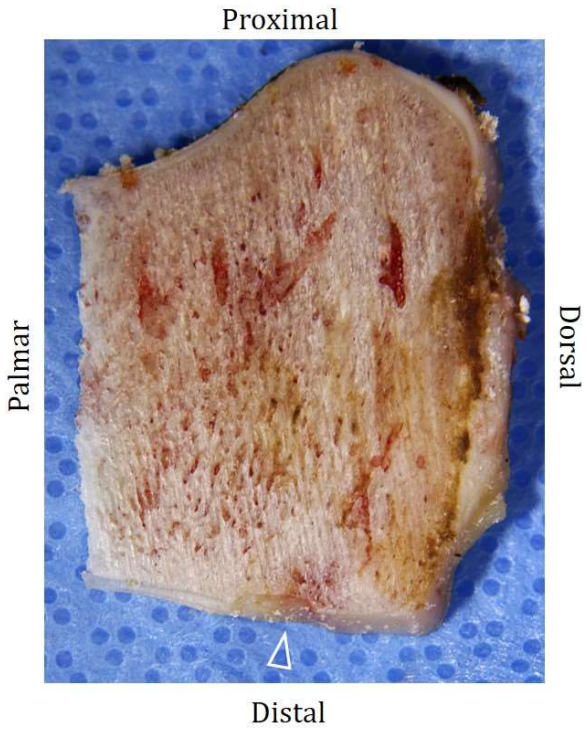

Figure 2.3 *Example of a section of the radial carpal bone from horse 1. Arrowhead indicates the lesion. Proximal to top of image, dorsal to right of image.*

2.2.3.b Third Carpal Bones

The C3s were also cut with a band saw into five sections in an oblique dorso-palmar plane (Figures 2.4 and 2.5). The method of fixation and storage, and purpose of each section is summarised in Table 2.4.

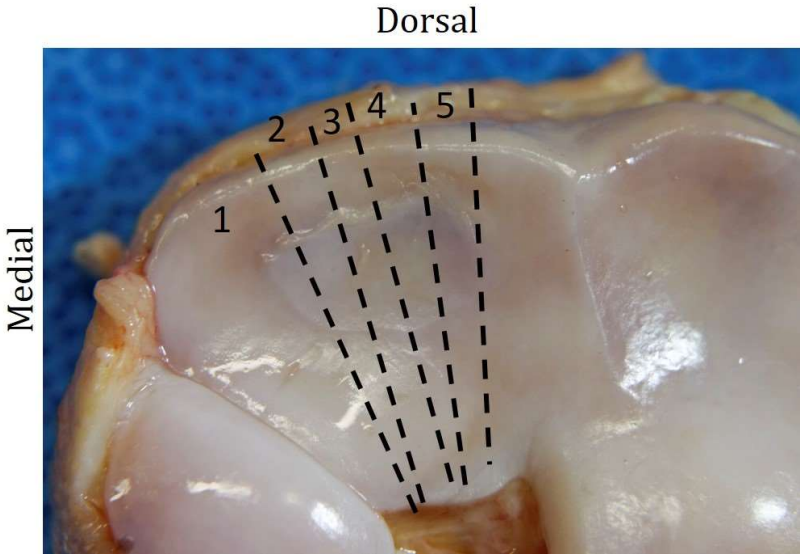

Figure 2.4 *Sectioning of the third carpal bones. View of proximal articular surface of C3. Dotted lines indicate the oblique dorsopalmar cuts which created sections of bone, each including some part of the surgical defect as well as adjacent cartilage and bone (Figure 2.5). Numbered here 1-5 from medial to axial.*

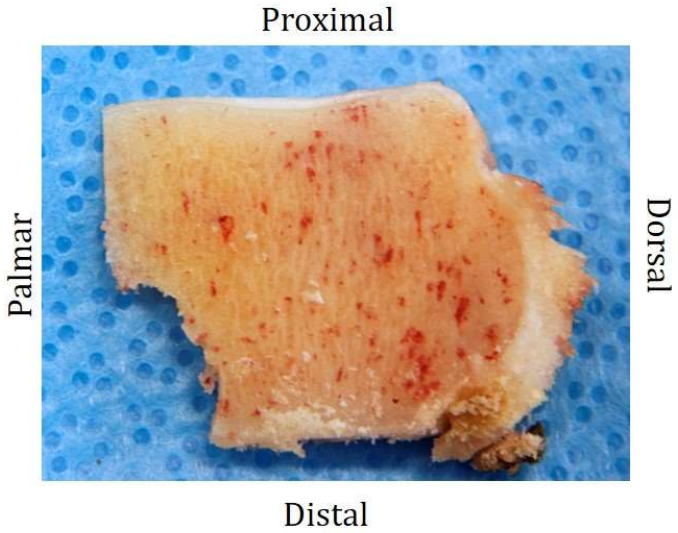

Figure 2.5 *Example of a section of the third carpal bone from horse 1. Proximal to top of image, dorsal to right of image.*

Section number	Radial carpal bone	Third carpal bone
1	Snap frozen in liquid nitrogen and stored at -80ºC for future matrix metabolism and RNA extraction studies	Snap frozen in liquid nitrogen and stored at -80ºC for future matrix metabolism and RNA extraction studies
2	Fixed and stored in 70% ethanol, protected from light, for studies on undecalcified bone: microCT, BSEM, Masson's Goldner staining and fluorochrome analysis (Section 2.2.4.a-d)	Fixed in a modified Karnovsky's solution prior to decalcification for histomorphology (Section 2.2.5.c)
3	Fixed in 10% NBF for histology in a companion study.	Fixed and stored in 70% ethanol, protected from light, for studies on undecalcified bone: microCT, BSEM, Masson's Goldner staining and fluorochrome analysis (Section 2.2.4.a-d)
4	Fixed in a modified Karnovsky's solution prior to decalcification for histomorphology (Section 2.2.5.c)	Fixed in 4% paraformaldehyde prior to decalcification, cryosectioning. and staining for TRAP to identify osteoclasts (Section 2.2.4.e)
5	Fixed in 4% paraformaldehyde prior to decalcification, cryosectioning. and staining for TRAP to identify osteoclasts (Section 2.2.4.e)	Snap frozen in liquid nitrogen and stored at -80ºC prior to decalcification, cryosectioning and imaging with DIC microscopy (Section 2.2.5.b)

Table 2.4 *Method of fixation and purpose of each section from C3 and Cr (numbered as in Figures 2.2 and 2.4).*

2.2.3.c Ulnar Carpal Bones

Two sections approximately 3-5mm thick were cut in a dorso-palmar plane from each ulnar carpal bone with a band saw. One was fixed in modified Karnovsky's solution prior to decalcification and processing for histomorphology (Section 2.2.5.a) and the other was fixed in 10% neutral buffered formalin for use in a companion study.

2.2.4 Bone analysis

2.2.4.a MicroCT analysis

Undecalcified osteochondral blocks, preserved in 70% ethanol, from each radial carpal (Cr) and third carpal (C3) bone were imaged with microCT (µCT50, Scanco Medical, Bassersdorf, Switzerland) at a voxel size of 24.2µm, voltage of 70kV, current of 200µA with a frame averaging of three and using a 0.5mm aluminium filter. Samples were secured within the specimen containers with polystyrene foam to prevent motion and covered with 70% ethanol to prevent drying. Mineral density calibration was performed internally within the device software.

Regions of interest (ROIs) were defined as described in chapters 4 and 5 and were analysed using in-built evaluation software for bone volume fraction (BV/TV, %), bone surface ratio (BS/BV, mm^{-1}), bone material density (BMD, $mgHA/mm^3$), tissue mineral density (TMD, $mgHA/mm^3$) and trabecular number (Tb.N, mm^{-1}), thickness (Tb.Th, mm) and separation (Tb.Sp, mm). Gaussian support of one and Gaussian filter of 0.8 were used based on the manufacturer's recommendations. For all evaluations a lower threshold of

250 was used, meaning that all voxels with a gray value above 250 were considered bone while those with a gray value below this were considered non-bone. This value was chosen by averaging the lower thresholds for all samples that gave the best approximation of bone and non-bone when the binary (segmented) images were compared visually to grayscale images (390).

2.2.4.b Backscattered Scanning Electron Microscopy

Methacrylate embedding of undecalcified specimens

Following microCT analysis the undecalcified osteochondral specimens were embedded in PMMA to enable further analysis.

Samples were first dehydrated in increasing concentrations of ethanol. Having been fixed in 70% ethanol they were transferred to 90% and then 100% ethanol, remaining in each concentration for at least 48 hours. They were then transferred to 100% dehydrated ethanol. This solution was changed twice with at least 48 hours between each change.

An infiltrating solution of 4:1 butyl- : methyl-methacrylate (Sigma Aldrich, Missouri, USA) was prepared and dehydrated by filtration through calcium chloride (CaCl). Samples were placed in glass containers and covered with methacrylate infiltrating solution in dehydrated ethanol at room temperature. They were initially placed in 70% methacrylate in dehydrated ethanol for 48 hours followed by 95% methacrylate for 48 hours then 100% methacrylate for 4 days. The final infiltration step consisted of 10 days in a fresh solution of 100% methacrylate.

Following infiltration the samples were transferred to a methacrylate embedding solution prepared in the same way as the infiltrating solution with the addition of 1.5% w/v benzoyl peroxide. These jars were then covered and kept at 4ºC for 7 days.

The samples were finally transferred to glass jars that contained a layer of polymerised methacrylate at the bottom and then covered with fresh embedding solution. These were kept under vacuum for at least three days then allowed to polymerise at 37ºC for two-five days. Polymerisation was completed at 60ºC overnight. Embedded samples were then removed from the glass jars and stored wrapped in foil.

Backscattered Scanning Electron Microscopy

The methacrylate-embedded undecalcified specimens were first used for analysis by BSEM. Methacrylate blocks were cut with a diamond saw (IsoMet Low Speed Precision Cutter, Buehler, Illinois, USA) to expose the surface of the bone sample. This surface was then sanded and polished (Metkon Forcipol IV Grinder Polisher, Kemet International Ltd, Kent, UK). Coarse sanding with 80 grit silicon carbide paper (Met Discs, Kemet International Ltd, Kent, UK) was performed to completely expose the entire surface of the area of interest if this had not been achieved with the diamond saw. Fine sanding with 1200 grit silicon carbide paper was performed to remove all grooves left by the course sanding. Surfaces were then polished with 6 μm diamond paste (Kemet diamond compound, Kemet International Ltd, Kent, UK) for 10 minutes followed by either 20 minutes with 1 μm diamond paste or 10 minutes with 3 μm diamond paste and 10 minutes with 1μm diamond paste. Once the bone surface was polished to a high shine, the methacrylate blocks were dried at room temperature for at least 48 hours then stored under

vacuum. Samples were carbon-coated in a vapouriser (Emitech K950X, Quorum Technologies, Laughton, UK) prior to BSEM imaging.

BSEM images were obtained using a variable pressure and environmental scanning electron microscope (Quanta 200F, FEI Company) under a vacuum of 0.5mbar, a high voltage of 20kV, a spot size of four and a dwell time of 10 microseconds. Images were taken at a focal working distance (FWD) of 35mm for low magnification images or 10mm for high magnification images.

Initially 120x magnification images of the entire distal dorsal quadrant of each Cr specimen (Figure 2.5) and of the proximal dorsal quadrant of each C3 (Figure 2.6) were obtained. Higher magnification images at 200x magnification were then obtained of specific ROIs as described in Chapters 4 and 5. Images were stitched using photo imaging software (Adobe Photoshop Elements 11, Adobe Systems Incorporated, 2001-2012).

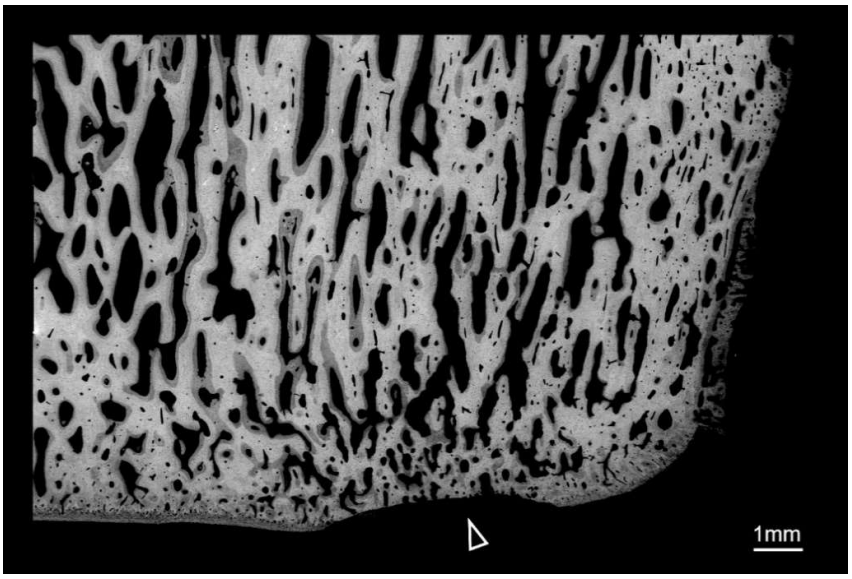

Figure 2.6 *Example of a reconstructed BSEM image of the disto-dorsal quadrant of Cr. Arrowhead indicates osteochondral defect. Dorsal to right of image, proximal to top of image.*

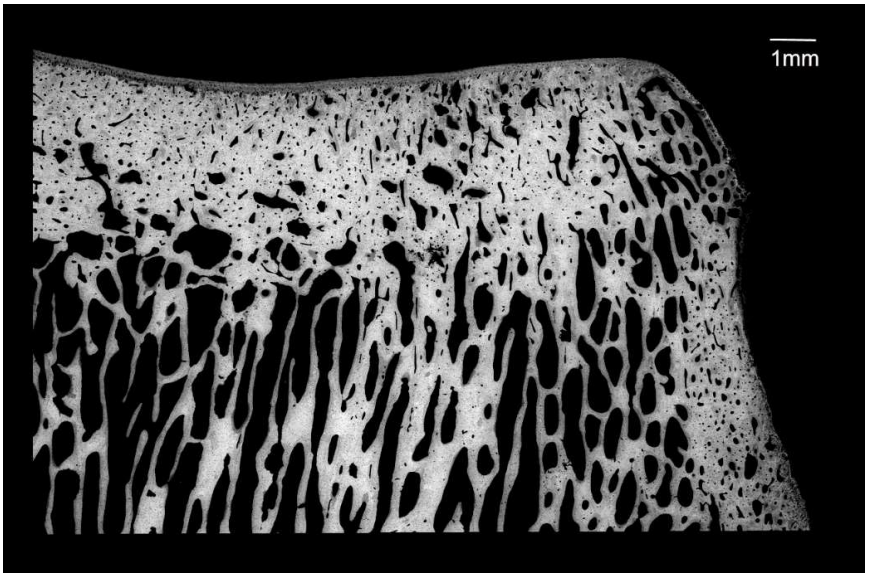

Figure 2.7 *Example of a reconstructed BSEM image of the proximo-dorsal quadrant of C3. Dorsal to right of image, proximal to top of image.*

Freely available image analysis software (ImageJ 1.50i, National Institutes of Health, USA(391)) was used to measure the following parameters from the 200x magnification images of each ROI: bone area fraction (B.Ar/T.Ar [%] = [bone area/ total area]100), porosity (%, [pore area/total area]100), pore perimeter (P.Pm [mm^{-1}] = [pore perimeter/ bone area]), eroded perimeter (E.Pm [mm^{-1}] = [eroded perimeter/ bone area]), mineralising perimeter (Md.Pm [mm^{-1}] = [mineralising perimeter/ bone area]). Active perimeter was calculated by adding eroded and mineralising perimeters (Act.Pm [mm^{-1}] = E.Pm + Md.Pm). Erosion, mineralisation and active perimeters were also calculated as a percentage of pore perimeter. The ratio of erosion: mineralising perimeter was also calculated (E.Pm/Md.Pm).

B.Ar/T.Ar, porosity and P.Pm were automatically measured from a thresholded image. Eroded and mineralising perimeters were measured manually (Figure 2.7). Eroded perimeter was defined as scalloped bone surface that crossed bone layers and had no low BSEM density bone parallel to surface. Low BSEM density bone that had a scalloped surface with a sharp edge was included in eroded surface. Mineralising perimeter was defined as low BSEM density bone parallel to the surface. All bone that had a lower density than surrounding bone was deemed mineralising unless it appeared to be an eroding perimeter (i.e. scalloped, sharp edge).

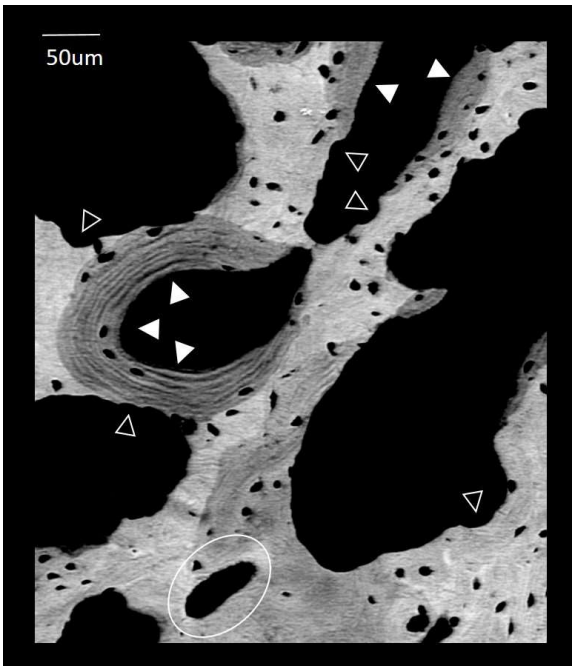

Figure 2.8 *Eroded (open arrow heads) and mineralising (filled arrow heads) perimeters on a high magnification BSEM image of SCB. Eroded perimeter defined as scalloped bone surface that crosses bone layers and has no low BSEM density bone parallel to surface. Mineralising perimeter was defined as low BSEM density bone parallel to the surface. Circle indicates an area of quiescent bone perimeter.*

2.2.4.c Masson's Goldner staining

Masson's Goldner (MG) staining was performed on 8-10 µm sections of undemineralised bone (Figure 2.8). These sections were cut from the PMA embedded specimens previously used for the BSEM analysis using a sledge microtome (Polycut E, Leica microsystems) then mounted on gelatin-coated slides and flattened using 30% ethyleneglycolmonobutylether (Sigma Aldrich, St Louis, Missouri, USA) in ethanol.

These were then covered with plastic sheets also coated in the ethylene-glycolmonobutylether solution, clamped flat and air dried at 37ºC for 24 hours.

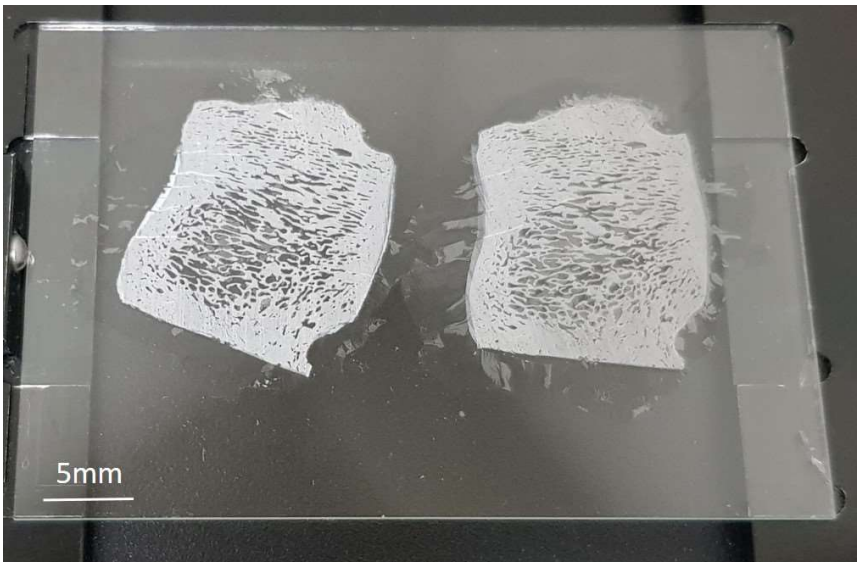

Figure 2.9 *Examples of 8-10 um thick undecalcified sections of C3 prior to deplasticisation and staining.*

Sections were deplasticised in 2-methoxyethyl acetate (MEA, Sigma Aldrich Pty Ltd, Castle Hill, NSW, Australia) then stained with a modified MG staining protocol using a commercial stain kit (Australian Biostain Pty Ltd, Traralgon, Vic, Australia). After staining sections were dehydrated in increasing concentrations of ethanol, cleared with xylene and mounted in a non-aqueous mounting medium (DPX new, Merck, Darmstadt, Germany) under a coverslip (Figure 2.9).

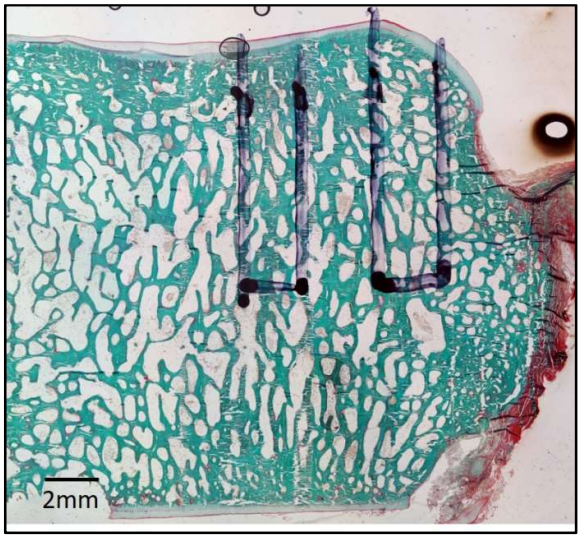

Figure 2.10 *Masson's Goldner stained, undecalcified section of C3 from the control limb of horse 1. Regions of interest were measured under a dissecting microscope then drawn with ink over the coverslip. Light microscopy, reconstructed image. Dorsal to right of image, proximal to top.*

Digital images of the MG stained sections, collected through a light microscope (Olympus BX53F, Olympus, Tokyo, Japan) and camera (Olympus DP73), were viewed on a touch sensitive screen (Wacom Cintiq 27QHD, Wacom Co. Ltd., Kazo, Saitama, Japan). A bone histomorphometry system (OsteoMeasure^{TM}, Version 3.3.0.2, OsteoMetrics, Georgia, USA) was used to measure osteoid parameters in each ROI (defined in Chapters 4 and 5) from the MG stained sections (Figure 2.10).

Osteoid parameters measured directly were: osteoid perimeter (O.Pm) expressed as a percentage of bone perimeter ([O.Pm/ B.Pm] x 100 [%]) and osteoid area (O.Ar) expressed as a percentage of bone area ([O.Ar/ B.Ar] x 100 [%]). Osteoid width was

calculated by the software (O.Wi, um). Osteoid was defined as pink-stained tissue parallel to a bone surface. Osteoid perimeter was defined as the boundary between the osteoid and the void. Solid osteoid (where no void, and hence no osteoid perimeter, could be seen) was not included. Any pink-stained tissue parallel to a bone surface that was narrower than the two lines used to trace it on the image was also excluded. This tissue is likely to be mostly unmineralised connective tissue under bone lining cells (Parfitt 1987) and accurate measurement of the width of any osteoid this thin would not be practical.

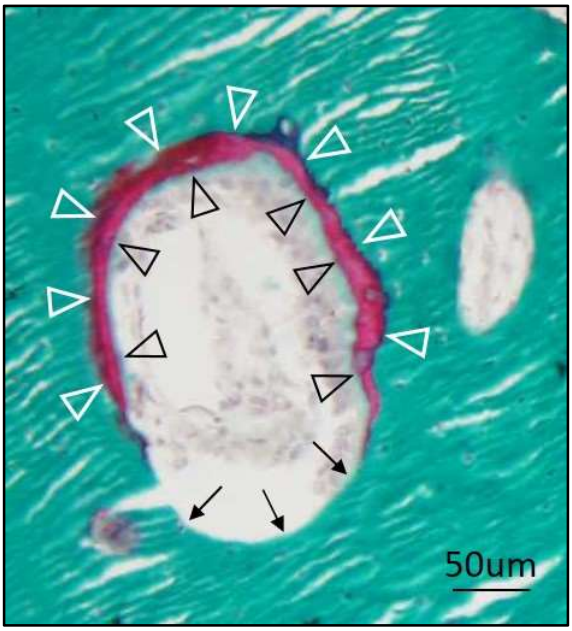

Figure 2.11 *Masson's Goldner stained section showing a void (unstained) within mineralised bone (green), partly lined with osteoid (pink). Osteoid perimeter indicated by black arrowheads, non-osteoid bone perimeter indicated by black arrows, osteoid-bone boundary indicated by white arrowheads. Bone perimeter is the sum of the osteoid and non-osteoid perimeters. Osteoid area is the area bounded by the osteoid perimeter and the osteoid-bone boundary. Osteoid width is the average distance between the osteoid perimeter and the osteoid-bone boundary. Light microscopy.*

2.2.4.d Fluorochrome analysis

Undemineralised sections (8-10µm thick) cut from the PMA embedded blocks were used to evaluate the fluorochrome labels. These sections were cut, mounted and deplasticised as described for the MG staining. They were then rehydrated in decreasing concentrations of ethanol and finally rinsed in distilled water. They were left unstained and mounted in gelvatol under a coverslip (Figure 2.11). They were protected from light at all times during storage.

Figure 2.12 *Example of an unstained, 8-10 um thick section of C3, deplasticised and mounted in gelvatol under a coverslip, used for fluorochrome analysis. Dorsal to right of image, proximal to top.*

ROIs were defined as described in Chapter 4 and 5, measured under a dissecting microscope and drawn over the coverslips with a marker. Light from a fluorescence illuminator (Xcite series 120Q, Excelitas technologies corp., Fremont, California, USA) passed through an ultra-violet filter was used to visualise the labels through a microscope (Olympus BX53F) mounted with a camera (Olympus DP73). Digital images were viewed on a touch sensitive screen (Wacom Cintiq 27QHD). The OsteoMeasure^{TM} system was used to measure fluorescent labels in each ROI. Single (sL.Pm), double (dL.Pm), triple (tL.Pm) labelled perimeter were measured and expressed as a percentage of bone perimeter (Figure 2.12). The leading edge (furthest from the bone perimeter) of each label was used for all measurements. There were no instances where all four labels could be seen on the same bone perimeter.

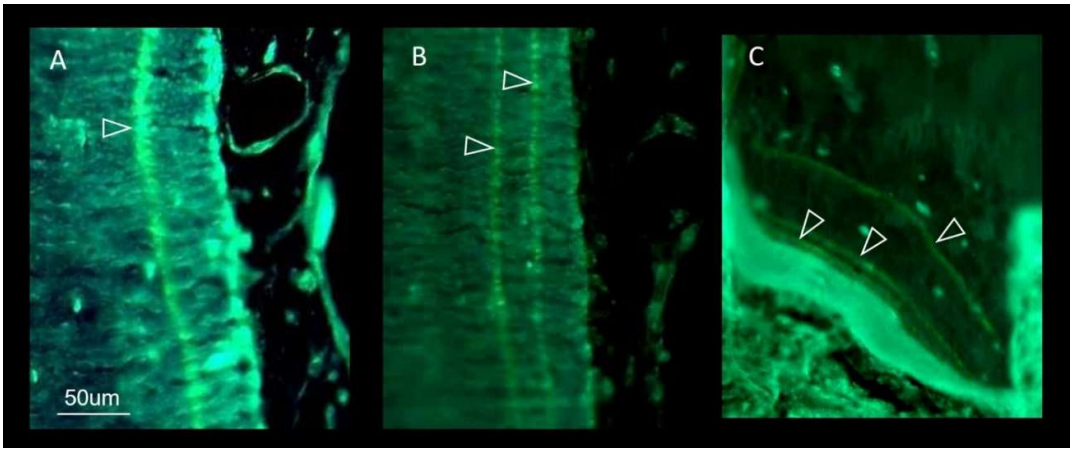

Figure 2.13 *Fluorescent microscopy images showing single (A), double (B) and triple (C) oxytetracycline labels (arrow heads).*

Total labelled perimeter (L.Pm) was calculated by the software using the formula:

$$L.Pm\ (mm) = dL.Pm + sL.Pm/2$$

This was chosen as it is a commonly used calculation when labels of the same vital dye are used (345). Labelled perimeter was also expressed as a percentage of bone perimeter (L.Pm/B.Pm [%]).

Mineral apposition rate (MAR) and bone formation rate (BFR) were calculated by the software using the following formulae:

$$MAR\ (um/d) = (Int.L.Wi/WF)/Int.L.T$$

$$BFR\ (\%/d) = MAR \times L.Pm$$

Where Int.L.Wi = Interlabel width, WF=width correction factor and Int.L.T= interlabel time.

MAR and BFR were calculated only from the double label measurements as there were too few triple labels to be meaningful. As it was not possible to identify individual labels, interlabel time was set at 30 days (the time between the first and second and second and third labels). BFR was expressed as a percentage of bone area ([BFR/B.Ar]100, %/d) (392).

2.2.4.e Staining of cryosections for TRAP

Following fixation in 4% paraformaldehyde at 4ºC for 3-12 hours, osteochondral sections were decalcified in 0.33M EDTA solution, pH 7.4, changed two to three times weekly. The EDTA solution was tested weekly for sedimentation when 0.5ml of the EDTA solution in which each sample had been bathed was mixed with 1.0ml citrate-phosphate buffer and 2.5ml saturated ammonium oxalate solution. If sedimentation occurred this was interpreted as an indication that there was calcium in the solution and that the bone was still calcified. Once there was no sedimentation using the above test, decalcification was continued until a scalpel or needle was able to easily penetrate the tissue in an area distant to the region of interest. Once decalcified, specimens were infiltrated with 25% sucrose for 2-12 hours then embedded in Optimum Cutting Temperature (OCT) compound (Tissue-Tek® O.C.T. Compound, Sakura Finetek, Tokyo, Japan), frozen in liquid nitrogen and stored at -80 degrees C.

Frozen specimens were then cut into sections approximately 10 µm thick using a cryostat (Leica CM 1900, Leica Biosystems, Nussloch, Germany) at a temperature of -15 to -18ºC, and placed on 3-aminopropyltriethoxysilane (AES, Sigma Aldrich) coated slides. These sections were sealed in nylon autoclave film (Smiths Medical, Minneapolis, Minnesota, USA) and stored at -80ºC until further processing.

Three slides from each specimen were stained for the presence of TRAP with the exception of the C3 from the control limb of Horse 1 for which there were only two good quality slides available. Sections were thawed to room temperature, post-fixed in 4% paraformaldehyde then immersed in TRAP stain (Table 2.5, final pH 5.0) for 30 minutes at room temperature following which the sections were counterstained with Crazzi's

haematoxylin. Stained sections were mounted under a coverslip in Gelvatol containing a fluorescent marker for nucleic acid (4',6'-diamidino-2-phenylindole; DAPI; 1 μg/ml; Sigma Aldrich). Remaining sections were reserved for possible future immunohistochemical studies.

Amount	Ingredient
10mg	Naphthol AS-MX phosphate
0.3mg	Fast Red Violet LB
10ml	0.3M Sodium Tartrate
100μl	Triton X-100
50ml	0.1M Acetate buffer
39.9ml	Distilled water

Table 2.5 *Components of TRAP stain (per 100ml). All components from Sigma Aldrich.*

Sections stained for TRAP were used to determine osteoclast numbers in each ROI defined in Chapters 4 and 5. Osteoclast numbers were expressed as a function of tissue area (Osteoclast.N, cells/mm^2). The mean of the counts from the three sections from each specimen was calculated and used as the final observation.

Osteoclasts were defined as TRAP-positive, multinucleate cells that were attached to a bone surface or had obviously been detached from one during processing (Figure 2.14).

In some samples there was considerable disruption of soft tissue within bone spaces resulting in dislodgment of cells, including osteoclasts, from the bone surfaces. Counting was performed using the 20x objective of a light microscope (Olympus BX60F5, Olympus Optical Co. Ltd., Tokyo, Japan). Representative images were captured with a digital camera (Olympus DP73, Olympus Optical Co. Ltd., Tokyo, Japan) and commercial image capture software (Olympus cellSense Entry 1.16, Olympus Optical Co. Ltd., Tokyo, Japan). Ultraviolet fluorescence was used to identify nuclei stained with DAPI if there was doubt regarding their presence in a TRAP-positive cell (Figure 2.14).

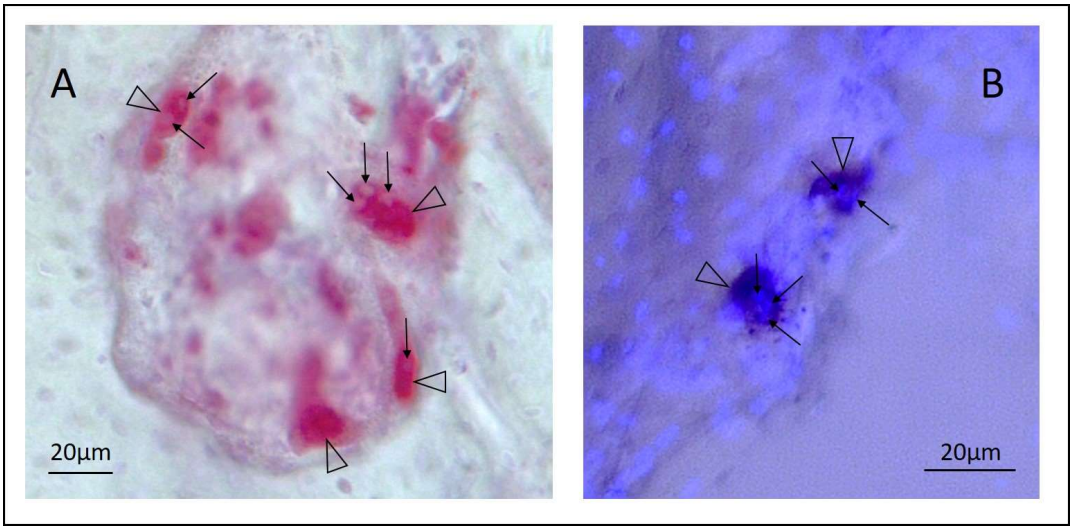

Figure 2.14 *Examples of osteoclasts (arrow heads) stained pink with pale-staining nuclei (arrows).A: bright field image of a cryosection stained for TRAP, focussing through the depth of the sample was often required to visualise multiple nuclei. B: composite image of bright field and UV fluorescence microscopy showing fluorescent, DAPI-stained nuclei.*

2.2.5 Cartilage Analysis

2.2.5.a Calcified cartilage thickness and tidemarks on BSEM images

Specimens were prepared and images obtained as described in *2.2.4.b*. Calcified cartilage thickness (CC.Th, µm) and the average number of tidemarks (Tm.N) were calculated in each defined ROI as described in Chapter 6.

2.2.5.b Cartilage thickness on Masson's-Goldner-stained sections

Specimens were prepared and viewed as described in *2.2.4.c*. Hyaline cartilage thickness (HC.Th, µm) and calcified cartilage thickness (CC.Th, µm) were measured in each defined ROI as described in Chapter 6.

2.2.5.c Histomorphology

Following fixation in a modified Karnovsky's solution (4 grams of paraformaldehyde in 100ml 0.1M sodium cacodylate buffer at pH 7.4, mixed with 25ml of 25% glutaraldehyde) sections were decalcified in 0.33M EDTA as described in *2.2.4.e*.

Once decalcified ROIs were dissected with a scalpel to include the region below or opposing the lesion in Cr and C3 bones respectively and the adjacent, dorsal, weight bearing region in both Cr and C3 as well as from Cu samples as described in Chapter 6 (Figure 2.15).

The dissected sections were rinsed thoroughly and underwent secondary fixation with osmium tetroxide (2% osmium tetroxide in water). They were then dehydrated in increasing concentrations of acetone and embedded in Spurr's resin (Figure 2.16).

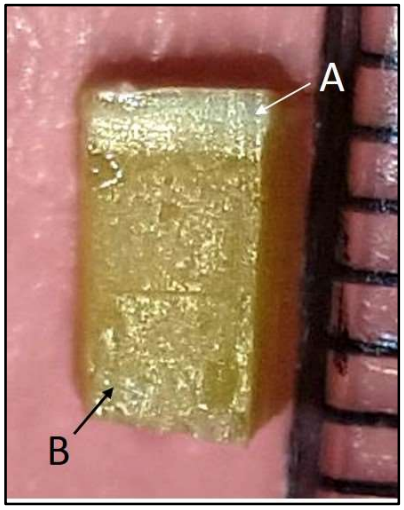

Figure 2.15 *Example of a decalcified and trimmed osteochondral section prior to embedding for histomorphology, showing cartilage (A) and SCB (B). Graduations on scale = 1mm.*

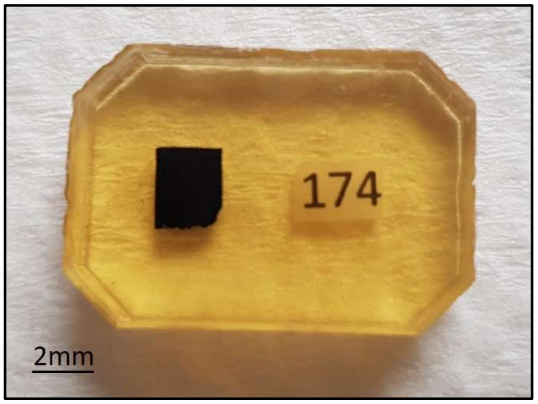

Figure 2.16 *Example of an osteochondral specimen embedded in Spurr's resin prior to sectioning for histomorphology.*

Semi-thin sections (1.0 µm thick) were cut using an ultra-microtome (Reichert, Austria) from the embedded osteochondral samples, stained with new methylene blue and mounted in a non-aqueous mounting medium (DPX new, Merck) under a coverslip (Figure 2.17). They were examined with a light microscope (Olympus 53F) fitted with a digital camera (Olympus DP73). Cartilage pathology was graded using a standardised system, and hyaline cartilage thickness (HC.Th, mm), calcified cartilage thickness (CC.Th, µm), chondrocyte size (μm^2) and chondrocyte density (cells/mm^2) were measured using the OsteoMeasure™ software as described in Chapter 6.

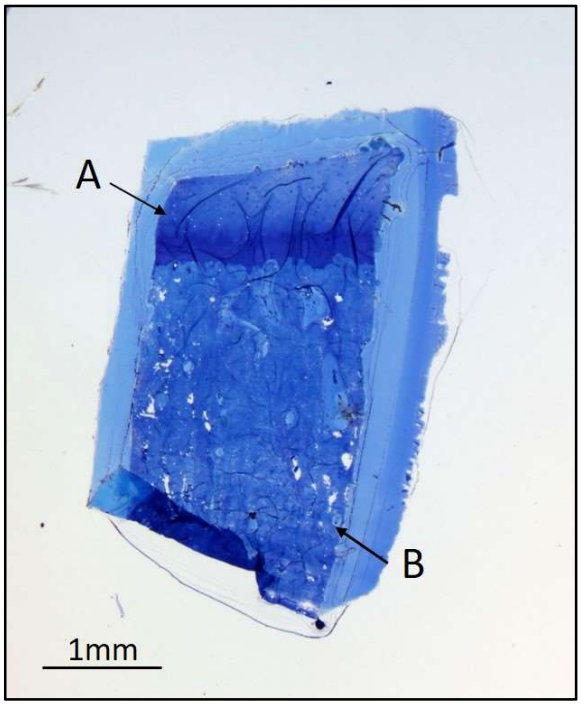

Figure 2.17 *Methylene blue stained semi-thin section showing cartilage (A) and SCB (B). Light microscopy.*

2.2.5.d Differential Interference Contrast imaging

Differential Interference Contrast (DIC) imaging was performed on sections of C3 from the trial horses. The specimen from Horse 3 was excluded from this study as there was no evidence of the thickened area of cartilage in the region opposing the lesion that was visible on gross examination (Figure 2.18), suggesting the sample was taken from adjacent to the lesion rather than directly opposing it.

Osteochondral sections designated for DIC imaging were collected from C3 as described in *2.3.3*. They were removed from storage at -80ºC and fixed in 10% NBF. The cartilage and most superficial 3-5mm of SCB were cut from the dorsal edge to several mm palmar to the area opposing the lesion with a hack saw (Figure 2.18) and partially decalicified in 10% formic acid for 6-7 days. Sections were mounted on a cryotome with OCT (Tissue-Tek® O.C.T. Compound, Sakura Finetek) and frozen with liquid nitrogen. Twenty µm thick sections were cut and wet-mounted on glass slides under coverslips for imaging.

Bright field images at 6x magnification were first captured of the entire section through a Nikon AZ100 stereomicroscope with a Nikon Digital Sight DS-Fi2 camera. These images were stitched using a commercially available photo editing program (Adobe Photoshop Elements 11, Adobe Systems Incorporated, 2001-2012) to create a single image of the entire section (Figure 2.19).

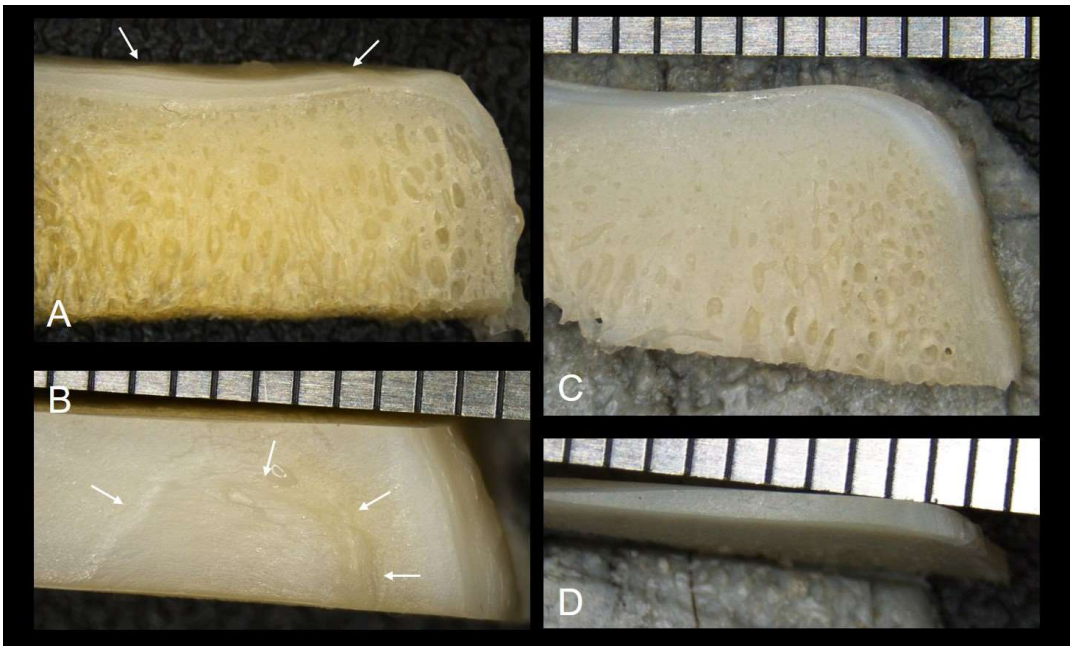

Figure 2.18 *Dissecting microscope images of partially decalcified sections of cartilage and SCB cut from C3 of horse* 1 *(A and B) where a raised area of cartilage can be seen (white arrows) and horse 3 where no raised area is apparent (C and D). A and C medio-lateral view. B and D proximo-distal view of the proximal articular surface. These specimens were sectioned for DIC imaging. 1mm increments on scale.*

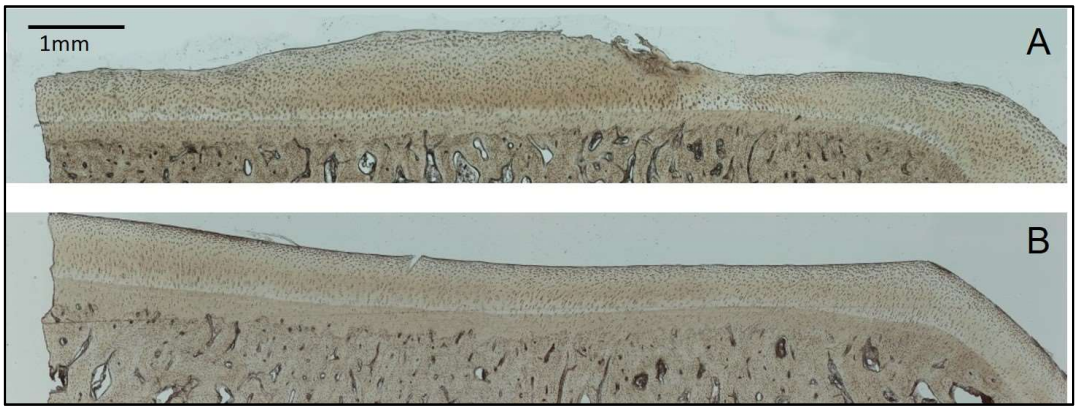

Figure 2.19 *Brightfield images of unstained, partially decalcified, 20µm sections of cartilage and superficial SCB from treated (A) and control (B) C3 from horse 5. Proximal to top, dorsal to right of images. Light microscopy.*

DIC images were taken using the 10x and 20x objectives through a Nikon Eclipse 80i microscope fitted with Nikon D-DP polariser and Nikon DIC lenses. Images were captured with a Nikon Digital Sight DS-Fi1 camera. Images were taken of the hyaline cartilage and of the calcified cartilage and subchondral compact bone at two ROIs as defined in Chapter 6.

At each ROI the following observations and measurements were made as described in Chapter 6: hyaline cartilage thickness (HC.Th, mm), thickness of the tangential zone of the hyaline cartilage (Tang.Th, μm), aspect ratio of chondrocytes in the tangential layer, degree of fibrillation and crimping of the hyaline cartilage, calcified cartilage thickness (CC.Th, μm), degree of rugosity (irregularity) of the cement line, and presence and morphology of bone spicules extending from SCB into the CC layer.

2.3 Statistical Methods

Unless otherwise specified, results from treated and control limbs of trial horses were compared statistically using a paired t-test if there was a reasonable assumption of normal distribution of the differences between pairs based on a Ryan-Joiner test of normality. Data from the untrained control horses were compared with those values from both the control and treated limbs of the trial horses using an independent t-test if there was a reasonable assumption of normal distribution for each group based on a Ryan-Joiner test of normality.

Where an assumption of normality of the differences between paired data was not valid a one-sample Wilcoxon test was used to test the hypothesis that the median difference was equal to 0. Where an assumption of normality of either of two independent groups was not valid a Mann-Whitney U test was used to compare the two groups.

Minitab (Minitab 17.2.1, Minitab Inc., USA, licensed to the University of Melbourne) was used for all statistical analyses.

Chapter 3

CLINICAL FINDINGS, GROSS PATHOLOGY AND SYNOVIAL HISTOPATHOLOGY

3.1 Introduction

Naturally occurring and experimental models of joint disease are characterised by clinical signs such as synovial effusion, soft tissue swelling, response to flexion of an affected joint and lameness on an affected limb. Radiological and synovial fluid abnormalities may also be present and equine models allow monitoring of these *in vivo* (9, 265, 268, 272, 310, 323).

Pain associated with surgical intervention or training of animals with orthopaedic injuries can negatively impact the welfare of animals used in experimental trials. In horses lameness is used as an indicator of pain within an affected limb while response to carpal flexion can be used to assess pain within the carpal joint (268, 300, 317, 323, 393). The American Association of Equine Practitioners (AAEP) grading scale provides a semi-quantitative, standardised measure of the degree of lameness and is commonly used in studies of equine joint disease (265, 268, 317, 323).

In the presence of synovial inflammation multiple inflammatory cytokines are released into the synovial fluid (241, 394, 395). These cytokines are known to affect chondrocyte behaviour, cartilage matrix metabolism and bone remodelling activity (35, 385, 394, 396-398). In order to understand what role inflammation may be playing in any observed cartilage changes in a joint disease model it is important to assess the degree of inflammation within the joints. Synovial histopathology can be used as a direct measure of synovial inflammation at the conclusion of a trial (331). A number of indirect measures can be used clinically to assess the degree of inflammation in joints including carpal effusion and synovial fluid total protein concentration (TP) and total nucleated cell counts (TNCC) (268, 323, 325). In addition, carpal circumference can be used to assess oedema and swelling of soft tissues surrounding the joint (399).

Bony changes within joints, such as osteochondral defects themselves or changes associated with the development of OA can be monitored *in vivo* via radiography (320, 323). However, radiography has been shown to have poor sensitivity and specificity for diagnosis of joint conditions in horses (319). Its use in this trial allowed assessment of whether it is possible to observe radiographically changes that are later documented on macroscopic assessment, higher resolution imaging or histopathology.

Post-mortem macroscopic evaluation is used in studies of both osteochondral defects and osteoarthritis to assess overall gross pathology of joint surfaces and to guide higher resolution imaging and histological evaluation (202, 253, 311, 331).

The aims of this chapter were to monitor the welfare of the trial animals and the clinical and clinical pathology changes associated with creation of the defect, to assess the degree of inflammation in the joints throughout the trial and to evaluate macroscopic appearance of the joints at post mortem. It was hypothesised that this model would result in minimal pain and inflammation with mild degenerative changes in the mid-carpal joint being apparent radiographically and on macroscopic examination.

3.2 Materials and Methods

Selection of the horses, arthroscopic creation of the defect and training were performed by Dr. Gareth Trope and his team as described in Chapter 2.

3.2.1 Lameness evaluation, flexion tests and carpal circumference and effusion scores

Trial horses were assessed weekly for evidence of lameness at the walk and trot in a straight line and on the treadmill by the team conducting training. Videos of the trial horses at a straight trot on flat ground and on the treadmill were also recorded weekly. These were assessed twice each by two independent examiners blinded to animal identification and treated limb (Prof. Chris Whitton BVSc FANZCVS *(Equine Surgery)* PhD and Dr Liz Walmsley, *BVSc, MACVSc, MRCVS, FANZCVS (Equine Surgery))*. Lameness was graded on a scale of 0-5 (Table 3.1) (317). The median lameness grade at each time point and the overall median lameness grade in treated and control limbs was compared using a Wilcoxon signed rank test. Inter- and intra-observer variation was also assessed using a Wilcoxon signed rank test.

Carpal circumference (cm) was measured with a tape measure at the level of the middle carpal joint prior to surgery then weekly from day 14. Measurements from treated and control limbs were compared at each time point and values at each time point were compared with baseline for each group.

Grade	Description
0	No lameness
1	Lameness difficult to observe and not consistently apparent regardless of circumstance
2	Lameness difficult to observe at a walk or trotting in a straight line but is consistently apparent under certain circumstances
3	Lameness consistently observable at a trot under all circumstances
4	Obvious lameness with marked head nodding, hitching or shortened stride
5	Minimal weight bearing

Table 3.1 *American Association of Equine Practitioners lameness grading scale used to grade lameness on both treadmill and trot-up videos (From Definition and Classification of Lameness in Guide for Veterinary Service and Judging of Equestrian Events, American Association of Equine Practitioners, 1991).*

Carpal effusion was monitored in both treated and control limbs and scored using a scale of 0-3 with 0 = nil, 1= mild effusion, 2 = moderate effusion and 3 = marked effusion. A pain response to carpal flexion was assessed in both treated and control limbs and scored using a scale of 0-3 with 0 = no response, 1 = mild response, 2 = moderate response and 3 = marked response. A Wilcoxon signed rank test was used to compare median carpal effusion and flexion response scores between treated and control limbs at each time point as well as to compare scores at each time point with baseline within each group.

3.2.2 Synovial fluid evaluation

Synovial fluid was collected from treated and control limbs of the trial horses on day 0, day 14 and then weekly until the end of the study. It was collected by arthrocentesis via a dorsal approach, preserved in EDTA and submitted to a clinical pathology laboratory (Veterinary Diagnostic Laboratory, The School of Animal and Veterinary Sciences, Charles Sturt University) for measurement of total protein (TP, g/L) and cytological analysis including total nucleated cell counts (TNCC, $x10^9$ cells/L) counts. TP and TNCC values were compared between treated and control limbs at each time point and values at each time point were compared with baseline for each group with a paired t-test.

3.2.3 Radiographic evaluation

Images, collected as described in section 2.1.7, were assessed by a registered specialist equine surgeon (Prof. Chris Whitton BVSc FANZCVS PhD) for evidence of joint effusion, subchondral osteolysis and sclerosis, narrowing of the joint space, periarticular

modelling (osteophytes) and periarticular enthesiophyte formation. Radiographic changes were graded on a scale of 0-3 with zero being normal, one mild, two moderate and three severe on each of the five views. Scores from treated limbs at day 70 were compared with their respective scores at day -7 as well as scores from the contralateral control limbs at day 70 using a Wilcoxon signed rank test on the paired differences.

3.2.4 Post mortem macroscopic examination

Post mortem the middle carpal joint was opened dorsally and examined grossly and photographs obtained as described in Chapter 2. A semi-quantitative scoring system based on that described by McIlwraith et al. (2010), modified and expanded for the current project, was used to assess the macroscopic photographic images (Table 3.2) (331). Blinding was not attempted as the defects were obvious within treated joints. The individual scores for cartilage erosion, peri-articular modelling and synovial inflammation as well as the combined score for all three parameters were compared between treated and control joints using a Wilcoxon signed rank test on the paired differences.

Parameter	Grade	Description
Cartilage Erosion (Cr and C3)	0	No erosion
	1	Focal, superficial erosion
	2	Focal partial and/or full thickness erosion
	3	Diffuse partial and full thickness erosion
	4	Extensive full thickness erosion to level of SCB
Modelling (Cr and C3)	0	No modelling
	1	Mild modelling
	2	Moderate modelling – new bone up to 1mm thickness
	3	Marked modelling – new bone greater than 1mm thickness
Synovial inflammation	0	No inflammation
	1	Mild inflammation focal/ confined to the region adjacent to the defect
	2	Moderate inflammation focal/ confined to the region adjacent to the defect
	3	Mild-moderate inflammation extending distant to the lesion
	4	Marked inflammation extending distant to the lesion
Lesion healing (Cr)	0	No lesion
	1	75-100% filled
	2	50-75% filled
	3	25-50% filled
	4	0-25% filled
Cartilage changes opposing lesion (C3)	0	Normal cartilage
	1	Mildly raised cartilage across <50% of the area opposing lesion
	2	Mildly-moderately raised cartilage over >50% of the area opposing the lesion
	3	Markedly raised cartilage over <50% of the area opposing the lesion
	4	Markedly raised cartilage over >50% of the area opposing the lesion

Table 3.2 *Scoring system used for grading of macroscopic joint pathology modified from McIwraith (2010) (331).*

3.2.5 Synovial histopathology

Sections of synovium were collected and fixed as described in Chapter 2. Specimens were embedded in paraffin then sections (5µm) were cut, mounted on glass slides and stained with haematoxylin and eosin (331).

Stained sections were examined by a veterinary pathologist (Andrew Stent BVSc, PhD, MANZCVS) who was blinded to site and treatment group and graded according to the microscopic grading system for synovial histopathology recommended by the OARSI histopathology initiative (Table 3.3) (331). This grading system was designed for use with the osteochondral chip fracture model of OA (331). It was chosen for use as the equine osteochondral chip fracture model is the current model that most closely resembles the current study, and to aid comparison of this study with existing literature. Due to mis-labelling of four specimens not all could be accurately paired so an independent t-test was used to compare all groups. All possible combinations of sample identification of the unknown samples were tested.

Parameter	Grade	Description
Cellular Infiltration (CI)	0	No mononuclear cells in the section
	1	Occasional small areas of mononuclear cells in the section
	2	Mild presence of mononuclear cells in 25% of the section
	3	Moderate presence of mononuclear cells in 25-50% of the section
	4	Marked presence of mononuclear cells in >50% of the section
Vascularity (V)	0	Normal
	1	Slight increase in vessels in focal locations throughout the section
	2	Mild increase in number and dilation of vessels in focal locations throughout the section
	3	Moderate increase in number and dilation of vessels in up to 50% of the section
	4	Marked increase in number and dilation of vessels in >50% of the section
Intimal Hyperplasia (IH)	0	None
	1	Villi with 2-4 rows of intimal cells in the section
	2	Villi with 4-5 rows of intimal cells over 25-50% of the section
	3	Villi with 4-5 rows of intimal cells over 50% of the section
	4	Villi with 5 or greater rows of cells over 50% of the section
Subintimal Oedema (SO)	0	No oedema
	1	Slight oedema detected within section
	2	Mild oedema within 25% of the section
	3	Moderate oedema within 25-50% of the section
	4	Marked oedema in >50% of the section
Subintimal Fibrosis (SF)	0	Normal
	1	Slight increase in fibrosis within the section
	2	Mild increase in fibrosis in 25% of the section
	3	Moderate increase in fibrosis in 25-50% of the section
	4	Marked increase in fibrosis in >50% of the section

Table 3.3 *Microscopic Grading System for synovial membrane histology* (331).

3.3 Results

3.3.1 Lameness evaluation, flexion test scores, carpal circumference and effusion scores

When all time points were considered together, the median lameness scores were significantly greater in treated compared with control limbs (estimated difference 0.5, P=0.004, Table 3.4). There was a persistent, grade 1-2 lameness in the treated limb of horse 1. Horse 2 had a grade 1 lameness in the control limb prior to surgery and at day 35 and a grade 1 lameness in the treated limb at day 70 while horse 3 demonstrated a persistent grade 1-2 lameness in the control limb both prior to surgery and throughout the trial. There was a persistent, grade 1-2 lameness in the treated limb of all other trial animals. Horse 4 was found to have pain in the foot of the treated limb at days 35-49 while Horse 6 was found to have pain in the foot in the treated limb at days 49-63.

There was no intra-observer variation in the lameness scores however an inter-observer variation was present in the scores for horse 5 (estimated difference 0.5, P=0.02). At no point was lameness considered severe enough to preclude any animal from continuing the trial on welfare grounds.

Time	Horse					
(days post-op)	1	2	3	4	5	6
0	1	-1	-2	1	-1	1
14	2	0	-1	2.5	1	1
21	2	0	-1	1	0.5	1
28	2	0	-1	2	0.5	1
35	0.5	-1	-2	2	0.5	1
42	2	0	-1	1	0.5	1.5
49	2	0	-1	2	0.5	1
56	2	0	-2	1	0.5	2
63	3	0	-2	1	1	1
70	2	1	-2	1	1	1
Overall grade	2	0	-1.25	1	0.5	1

Table 3.4 *Median lameness grades. Medians of all values from both observations from both observers for both trot-up track and treadmill videos. Data from all time points post-operatively as well as a cumulative median. Positive numbers represent lameness in the treated limb, negative numbers represent lameness in the control limb.*

Response to carpal flexion in treated limbs was significantly greater than baseline and the control limbs at days 28, 35 and 49, while in control limbs it was never significantly elevated above baseline (Table 3.5). The carpal effusion score in treated limbs was significantly greater than baseline at all time points post-surgery and greater than in the control limbs at day 21 and day 70, while in control limbs it was only significantly elevated above baseline at the earliest time points (days 14 and 21, Table 3.5, Figure 3.1).

Time (Days post-op)	Carpal Flexion Score (0-3)					Carpal Effusion Score (0-3)				
	Median (Maximum, Minimum)		P-value			Median (Maximum, Minimum)		P-value		
	Treated	Control	Treated v Control	Treated v Day 0	Control v Day 0	Treated	Control	Treated v Control	Treated v Day 0	Control v Day 0
0	0.0 (0.0, 0.0)	0.0 (0.0, 0.0)	NA	NA	NA	0.0 (0.0, 0.0)	0.0 (0.0, 0.0)	NA	NA	NA
14	1.0 (0.0, 1.0)	0.0 (0.0, 0.0)	0.1	0.1	NA	1.5 (1.0, 3.0)	1.0 (1.0, 2.0)	0.18	**0.04**	**0.04**
21	1.0 (0.0, 2.0)	0.0 (0.0, 0.0)	0.1	0.1	NA	2.0 (2.0, 2.0)	1.0 (1.0, 1.0)	**0.04**	**0.04**	**0.04**
28	1.0 (1.0, 3.0)	0.0 (0.0, 0.0)	**0.04**	**0.04**	NA	1.5 (1.0, 2.0)	1.0 (0.0, 2.0)	0.18	**0.04**	0.37
35	1.0 (1.0, 2.0)	0.0 (0.0, 1.0)	**0.04**	**0.04**	1.0	1.5 (1.0, 2.0)	0.0 (0.0, 2.0)	0.06	**0.04**	0.1
42	1.0 (0.0, 3.0)	0.0 (0.0, 1.0)	0.18	0.1	1.0	1.5 (1.0, 2.0)	1.0 (1.0, 1.0)	0.06	**0.04**	0.1
49	1.0 (1.0, 2.0)	0.0 (0.0, 1.0)	**0.04**	**0.04**	1.0	1.0 (1.0, 2.0)	1.0 (0.0, 1.0)	0.18	**0.04**	0.1
56	1.0 (0.0, 3.0)	0.0 (0.0, 0.0)	0.1	0.1	NA	1.0 (1.0, 2.0)	0.0 (0.0, 1.0)	0.06	**0.04**	1.0
63	1.0, (0.0, 2.0)	0.0 (0.0, 1.0)	0.1	0.06	0.37	1.0 (1.0, 2.0)	1.0 (0.0, 1.0)	0.1	**0.04**	0.1
70	0.0 (0.0, 2.0)	0.0 (0.0, 1.0)	0.12	0.06	1.0	1.0 (2.0, 3.0)	0.0 (0.0, 1.0)	**0.04**	**0.04**	0.37

Table 3.5 *Carpal flexion and carpal effusion scores. Numbers in bold indicate P<0.05 on a Wilcoxon Signed Rank test on paired differences.*

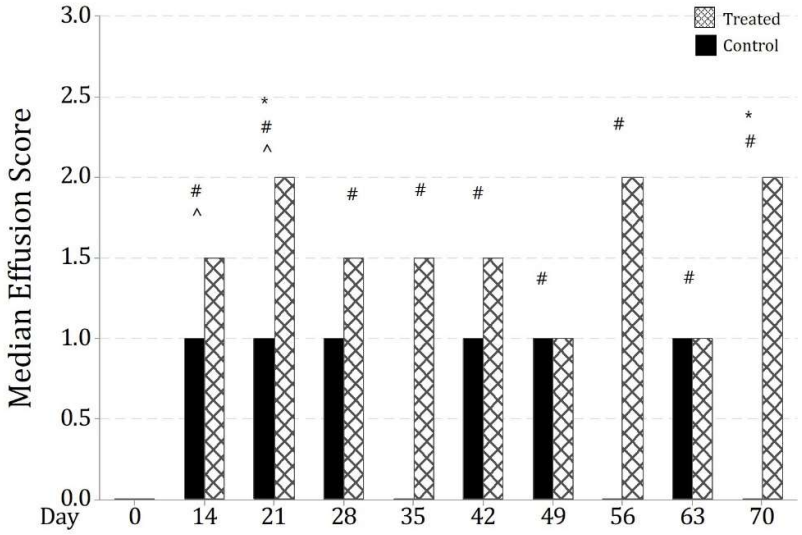

Figure 3.1 *Median Carpal Effusion Scores.* ******* *= significant difference between treated and control limbs at that time point, # = score in treated limbs significantly greater than baseline, ^ = score in control limbs significantly greater than baseline. Significance at a level of P<0.05 on a Wilcoxon signed rank test on the paired differences.*

There was a small but significant increase in carpal circumference in treated limbs at all time points after surgery relative to baseline. Carpal circumference of the control limbs was also greater than baseline at all time points however this difference was not always significant at a level of P<0.05. The carpal circumference of treated limbs was slightly greater than control limbs at most time points but this difference was only significant at days 21 and 70 post surgery, coinciding with significant differences in carpal effusion scores (Figure 3.2, Table 3.6).

Time (Days post-op)	Carpal circumference (cm)				
	Mean (Median), Range		P-value		
	Treated	Control	Treated v Control	Treated v Day 0	Control v Day 0
0	29.1 (28.5), 5.00	29.0 (29.0), 5.00	0.79	NA	NA
14	29.9 (30.0), 4.50	30.1 (30.0), 4.80	0.35	**0.04**	**0.001**
21	30.3 (30.0), 4.00	29.7 (29.3), 5.00	**0.01**	**0.007**	**0.01**
28	30.2(30.0), 5.00	29.4 (29.3), 3.00	0.09	**0.04**	0.40
35	30.5(30.0), 5.00	29.7 (29.0), 4.50	0.08	**0.02**	0.12
42	30.4 (30.5), 5.00	30.3 (29.8), 5.00	0.83	**0.04**	**0.003**
49	30.1 (29.5), 5.00	29.4 (29.0), 3.50	0.10	**0.02**	0.14
56	31.2 (30.8), 4.50	30.3 (30.5), 6.50	0.12	**0.001**	**0.05**
63	31.0(30.8), 5.00	30.3 (30.3), 5.00	0.09	**0.01**	**0.01**
70	31.4(30.8), 6.00	30.3 (29.5), 6.00	**0.001**	**0.01**	**0.02**

Table 3.6 *Carpal circumference (cm). Numbers in bold indicate P<0.05 on a paired t-test.*

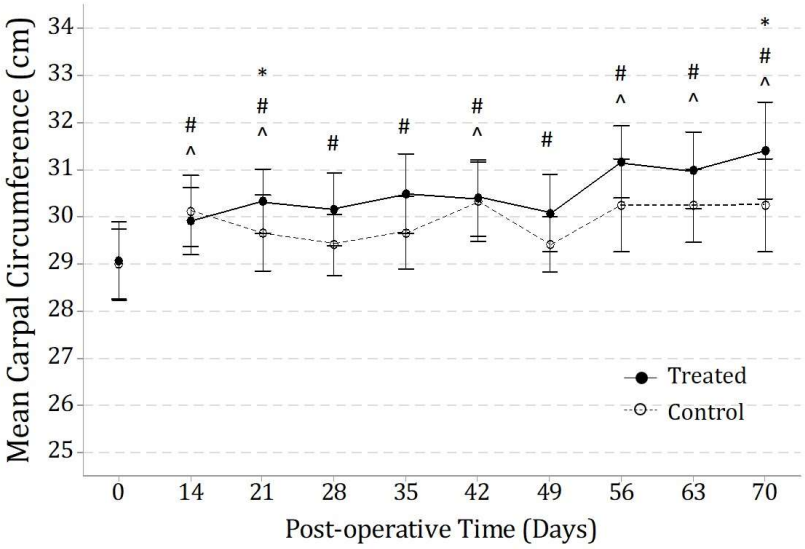

Figure 3.2 *Mean carpal circumference (cm). * = significant difference between treated and control limbs at that time point, # = score in treated limbs significantly greater than baseline, ^ = score in control limbs significantly greater than baseline. Significance at a level of P<0.05 on a paired t-test. Interval bars = 1 standard deviation.*

3.3.2 Synovial fluid evaluation

There was no difference in TP or TNCC of the synovial fluid between treated and control limbs prior to surgery. TP was consistently greater in the treated limbs than in the control limbs at all other time points with the difference being significant at 14, 21, 28 and 49 days following creation of the lesion. TP of the treated limbs was also consistently greater than baseline throughout the trial with the difference being significant at 28 and 49 days following creation of the lesion. At day 35 the synovial fluid TP of the control limbs was also significantly greater than baseline (Table 3.7, Figure 3.3).

There was no significant difference in TNCC between treated and control groups at any time point although at day 21 the TNCC in treated limbs was greater than in the control limbs at a level that approached significance (mean difference = 0.147 $x10^9$ cells/L, P=0.052). At various time points the TNCC of both treated and control limbs was significantly elevated above baseline although this was inconsistent and there was marked variation both within groups and between time points (Table 3.7, Figure 3.4).

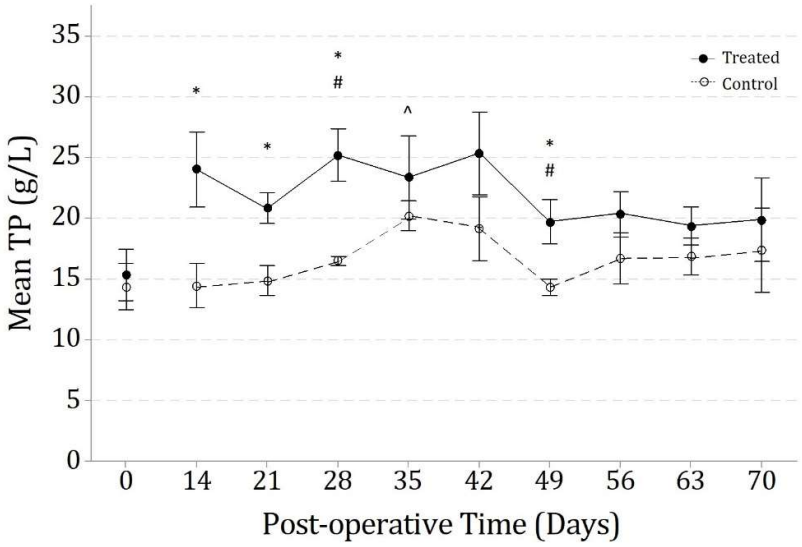

Figure 3.3 *Mean total protein concentration (TP, g/L) of synovial fluid through the trial.* ******* *= significant difference between treated and control limbs at that time point, # = value in treated limbs significantly greater than baseline, ^ = value in control limbs significantly greater than baseline, at a level of P<0.05 on a paired t-test. Interval bars = 1 standard deviation.*

Time (Days post-op)	Total Protein (g/L)					TNCC (x10^9 cells/L)				
	Mean (Median), Range		P-value			Mean (Median), Range		P-value		
	Treated	Control	Treated v Control	Treated v Day 0	Control v Day 0	Treated	Control	Treated v Control	Treated v Day 0	Control v Day 0
0	15.3, (16.0) 12.0	14.3, (14.0) 10.0	0.36	NA	NA	0.067, (0.080) 0.090	0.052, (0.045) 0.100	0.49	NA	NA
14	24.0, (25.0) 16.0	14.4, (14.0) 8.00	**0.008**	0.08	0.67	0.333, (0.250) 0.600	0.283, (0.150) 0.900	0.80	**0.04**	0.15
21	20.8, (20.0) 8.00	14.8, (15.5) 8.00	**0.004**	0.07	0.85	0.280, (0.300) 0.200	0.133, (0.100) 0.300	0.052	**0.01**	0.07
28	25.2, (23.5) 12.0	16.5, (16.0) 2.00	**0.009**	**0.01**	0.26	1.07, (0.350) 4.10	0.117, (0.100) 0.100	0.20	0.18	**0.009**
35	23.3, (22.5) 22.0	20.2, (19.0) 6.00	0.21	0.07	**0.03**	0.633, (0.250) 1.40	0.733, (0.500) 1.60	0.72	0.11	0.07
42	25.3, (25.5) 20.0	19.1, (21.5) 14.0	0.14	0.053	0.28	0.800, (0.250) 3.40	0.333, (0.300) 0.300	0.40	0.24	**0.006**
49	19.7, (20.0) 10.0	14.3, (14.0) 4.00	**0.02**	**0.04**	1.0	0.283, (0.300) 0.400	0.417, (0.300) 1.10	0.53	**0.02**	0.08
56	20.3, (20.0) 12.0	16.7, (16.0) 10.0	0.14	0.06	0.32	0.183, (0.150) 0.200	0.091, (0.100) 0.200	0.10	0.06	0.33
63	19.3, (18.5) 8.00	16.8, (16.0) 10.0	0.07	0.08	0.27	0.973, (0.100) 3.26	0.300, (0.250) 0.400	0.26	0.18	**0.02**
70	19.8, (17.5) 22.0	17.3, (15.0) 22.0	0.12	0.12	0.34	0.617, (0.150) 2.90	0.208, (0.150) 0.455	0.38	0.31	0.12

Table 3.7 *Total protein concentration (TP, g/L) and total nucleated cell count (TNCC, x109cells/L) of synovial fluid. P-values in bold < 0.05.*

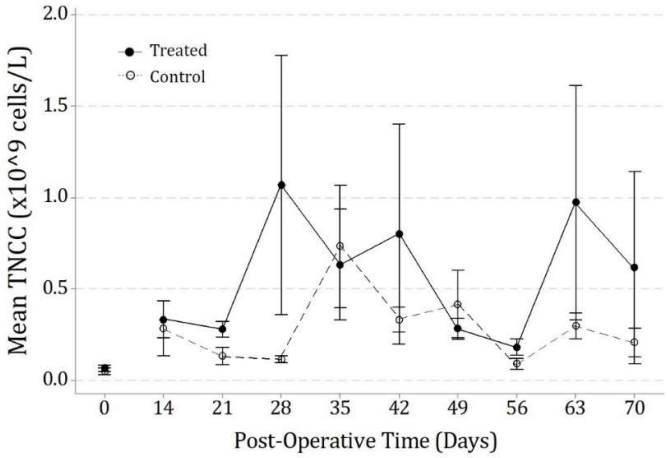

Figure 3.4 *Mean total nucleated cell count (TNCC, x109cells/L) of synovial fluid through the trial. There was no significant difference between treated and control limbs at any time point although the difference at 21 days approached significance (P=0.052). Interval bars = 1 standard deviation.*

3.3.3 Radiographic evaluation

There was radiographic evidence of mild to moderate peri-articular modelling and focal areas of subchondral lysis in both treated and control limbs at all time points. While there appeared to be a tendency towards increased peri-articular modelling in the treated limbs at day 70, there were no significant differences between limbs or time points for any radiographic parameter (Table 3.8).

A region of lysis and/or a defect in the articular surface was apparent in Cr of the treated limb in horse 1 at days 14 and 70 that had not been present prior to surgery. Horses 4, 5 and 6 had radiographic evidence of lysis in the distal Cr of treated limbs prior to surgery

that was also present at days 14 or 70. In the proximal C3 in treated limbs of horses 5 and 6 there was also evidence of lysis present at day 0 and day 14.

Peri-articular modelling became apparent at the dorsal Cr and/or C3 of the treated limb of horse 2 at days 14 and 70 and in both limbs of horse 3 on day 70. Both limbs of horses 4, 5 and 6 and the control limb of horse 1 had evidence of peri-articular modelling throughout the trial.

Soft tissue swelling was the only parameter observed exclusively in treated limbs post-surgery, in horse 1 at days 14 and 70 and in horse 2 at day 14.

Radiographic parameter (Range of possible scores)	Median (Minimum, Maximum)				P value	
	Day -7		Day 70		Treated day 70 v day -7	Day 70 treated v control
	Treated	Control	Treated	Control		
Periarticular modelling (0-15)	1 (0, 2)	1 (0, 2)	2 (0, 4)	1.5 (0, 2)	0.10	0.60
Subchondral lysis (0-15)	0.5 (0, 3)	1 (0, 2)	0 (0, 3)	0.5 (0, 3)	0.89	0.59
Subchondral sclerosis (0-15)	0 (0, 0)	0 (0, 1)	0 (0, 0)	0 (0, 1)	NA	1.0
Enthesiophytes (0-15)	0 (0, 0)	0 (0, 0)	0 (0, 0)	0 (0, 0)	NA	NA
Joint effusion (0-15)	0 (0, 0)	0 (0, 0)	0 (0, 1)	0 (0, 0)	1.0	1.0
Joint space narrowing (0-15)	0 (0, 0)	0 (0, 0)	0 (0, 0)	0 (0, 0)	NA	NA
Total score (0-60)	1.5 (0, 3)	2 (0, 4)	2 (1, 6)	2 (1, 4)	0.20	0.79

Table 3.8 *Radiographic scores. Score for each parameter is the total from all 5 radiographic views. The total score is the sum of all individual parameter scores. P values from a Wilcoxon signed rank test on the paired differences.*

3.3.4 *Macroscopic examination*

The osteochondral defects on the distal facet of Cr were apparent in all treated joints at post mortem. They were filled to varying degrees with irregular, opaque, pale tissue that did not quite extend to the margins of the defect (Table 3.9).

Horse	Approximate defect size (mm)
1	17 x 8
2	15 x 10
3	12 x 10
4	20 x 5
5	15 x 5
6	14 x 6

Table 3.9 *Cr osteochondral defect size at post mortem.*

In all trial horses on the radial facet of C3 immediately opposite the Cr defect there was a region of cartilage that was paler, irregular and raised compared to the surrounding cartilage. This region was equivalent in size and shape to the opposing Cr defect. The raised and irregular cartilage was most prominent at the edges of this region in horses 1-3 but involved the entire region in horses 4-6 (Figure 3.5).

There was mild to moderate peri-articular modelling in all treated joints. The peri-articular modelling score was significantly greater in the treated limbs than in the controls (Table 3.10, Figures 3.6 and 3.7).

Cartilage immediately dorsal to both the defect on Cr and the raised area of cartilage on C3 was subjectively thinner than the surrounding cartilage in horses 1-3 and on C3 of horse 4. In Cr of horse 5 there were several linear erosions approximately 1-3mm long both dorsal and palmar to the defect. In both Cr and C3 of horse 6 there were several 1 x 2mm partial thickness cartilage lesions in the area dorsal to the lesion (Figure 3.5). Cartilage of the articular surfaces distant to the defect appeared grossly normal.

In Cr of the control limb of horse 1 there was an area of full thickness erosion approximately 5 x 2mm at the dorsal articular margin. In the control limb of horse 2 there were partial thickness erosions approximately 1mm in diameter in the dorsal cartilage of both Cr (3) and C3 (2) while in Cr and C3 from the control limb of horse 6 there were multiple partial thickness erosions each less than 1mm in diameter in the dorsal cartilage (Figure 3.8).

The combined macroscopic pathology score was greater in treated than control limbs although this difference was not quite significant (median difference=1.5, P=0.06, Figure 3.9, Table 3.10). Untrained controls were only included in the study if there were no macroscopic abnormalities so by definition have a score of 0 and therefore were not included in this discussion.

Macroscopic pathology parameter	Median (Minimum, Maximum)		P-value Treated v Control
	Treated	Control	
Cartilage erosion (0-4)	1 (1, 2)	1.5 (0, 2)	1.0
Peri-articular modelling (0-3)	1.5 (1, 3)	0 (0, 0)	**0.04**
Synovial inflammation (0-4)	0 (0, 3)	0.5 (0, 2)	1.0
Combined score (0-11)	3.5 (3, 6)	2 (1, 3)	0.06
Lesion healing (0-4)	1 (1, 4)	NA	NA
Cartilage opposing lesion (0-4)	2.5 (1, 4)	NA	NA

Table 3.10 *Macroscopic pathology scores. Based on the system described in table 3.2. Combined score is the total of cartilage erosion, peri-articular modelling and synovial inflammation scores, out of a maximum possible total of 11. P-values from a Wilcoxon signed rank test on the paired differences.*

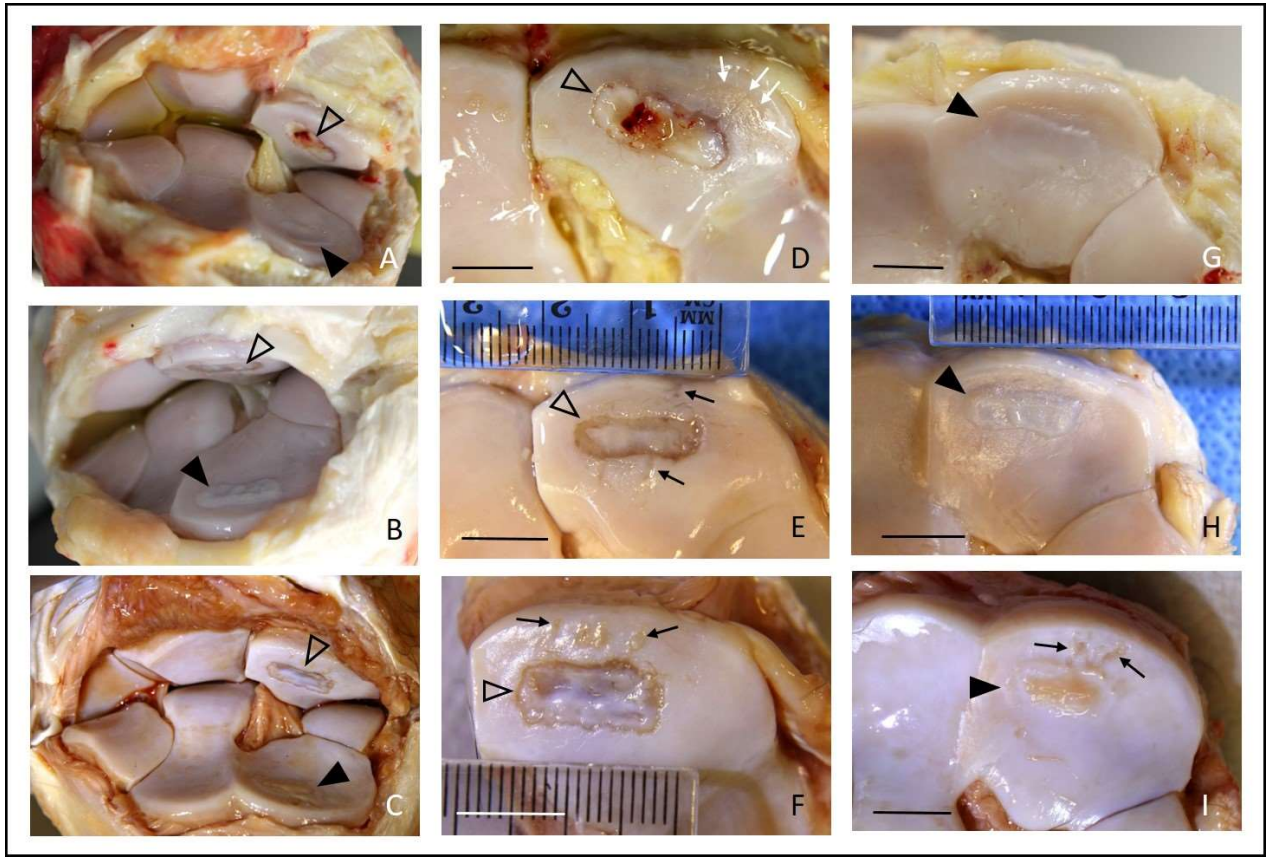

Figure 3.5 *Gross post mortem photographs of treated mid-carpal joints (A, B, C), dissected treated Crs (D, E, F) and dissected treated C3s (G, H, I) from Horse 1, 5 and 6 respectively. Open arrow heads indicate the surgical defect, closed arrowheads show the cartilage opposing the defect, black arrows indicate partial thickness erosions and white arrows indicate an area of apparent cartilage thinning. Scale bars = 10mm.*

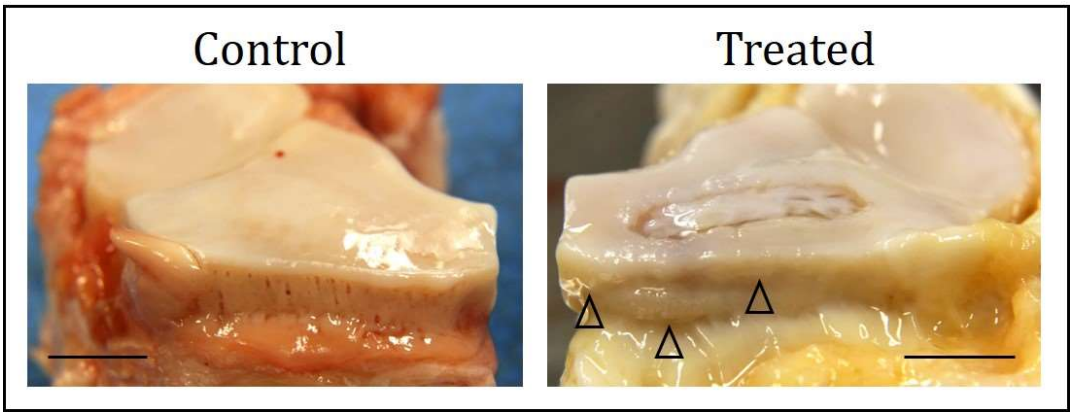

Figure 3.6 *Post mortem photographs of Crs from horse 4 showing peri-articular modelling on the dorsal articular margin in the treated limb (open arrowheads). Scale bar = 10mm.*

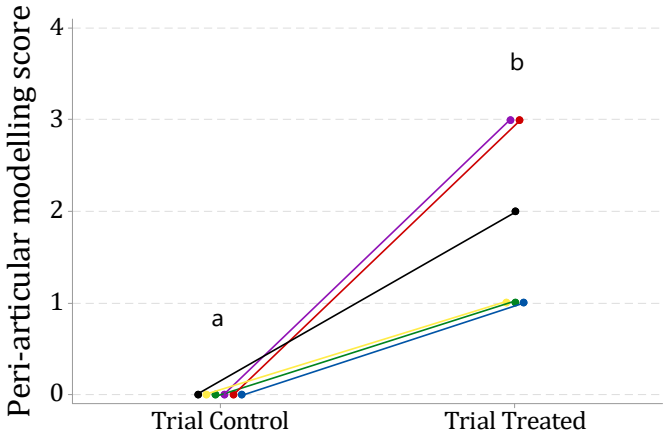

Figure 3.7 *Peri-articular modelling score. From the macroscopic pathology scoring system described in table 3.2. Different letters denote significantly different groups at a level of P<0.05 on a Wilcoxon signed rank test on the paired differences. Different colours indicate individual horses and are consistent throughout thesis (see Appendix 1 for key).*

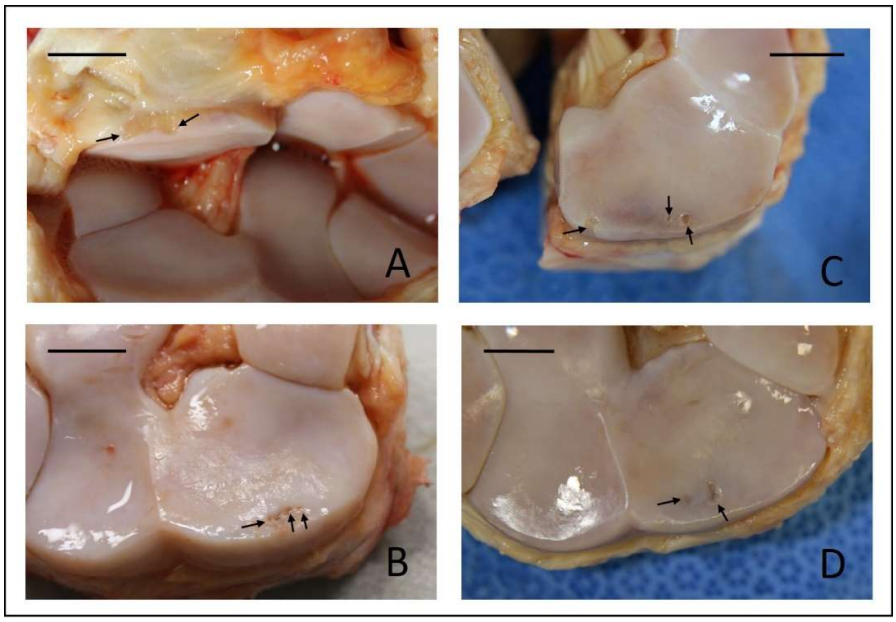

Figure 3.8 *Gross post mortem images showing cartilage lesions (arrows) in control joints. A = Horse 1 control joint with lesions on the dorsal articular margin of Cr, B = Horse 6 control C3, C and D = Horse 2 control Cr and C3 respectively. Scale bars = 10mm.*

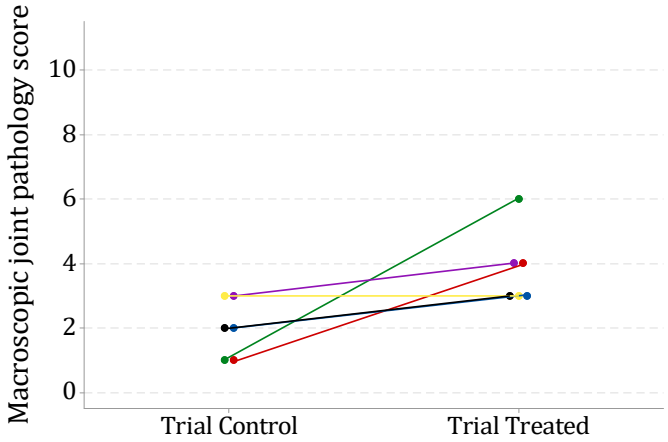

Figure 3.9 *Combined macroscopic pathology score: cartilage erosion, peri-articular modelling and synovial inflammation scores, maximum possible total of 11. P=0.06 on a Wilcoxon signed rank test on the paired differences*

3.3.5 Synovial histopathology

The synovial pathology score was slightly greater in both the treated and control limbs of the trial animals compared with the untrained control group in synovium from the dorso-medial aspect of the joint (mean difference=2.83, P=0.05 and mean difference = 2.17, P=0.04 respectively, Figures 3.10-3.12, Table 3.11). There were no differences between groups when individual parameters were considered separately or when synovium from the dorso-lateral aspect of the joint was considered. There was also no difference between scores from the medial and lateral sites within any group (Table 3.11). There was no difference in the statistical analysis between any possible identifications of the mis-labelled samples.

		Mean (Median), Range			P-value		
		Trial treated	Trial control	Untrained control	Trial treated v Trial control	Trial treated v Untrained control	Trial control v Untrained control
Dorso-medial synovium		4.7 (4.0), 7.0	4.0 (4.0), 4.0	1.8 (2.0), 4.0	0.59	**0.05**	**0.04**
Dorso-lateral synovium		3.2 (2.0), 10.0	3.7 (4.0), 5.0	3.0 (3.0), 4.0	0.77	0.92	0.53
P-value	Dorso-medial v Dorso-lateral	0.43	0.75	0.23			

Table 3.11 *Total synovial pathology scores, out of a possible total of 20. From paraffin embedded, haematoxylin and eosin stained sections. P-values from an independent t-test. Bold numbers P<0.05.*

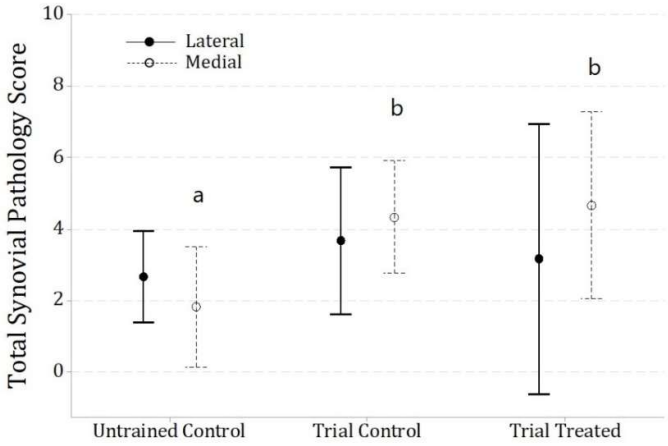

Figure 3.10 *Synovial pathology scores, maximum possible score of 20. Different letters indicate groups significantly different at the dorso-medial site at a level of P<0.05 on an independent t-test. No significant difference between groups at the dorso-lateral site.*

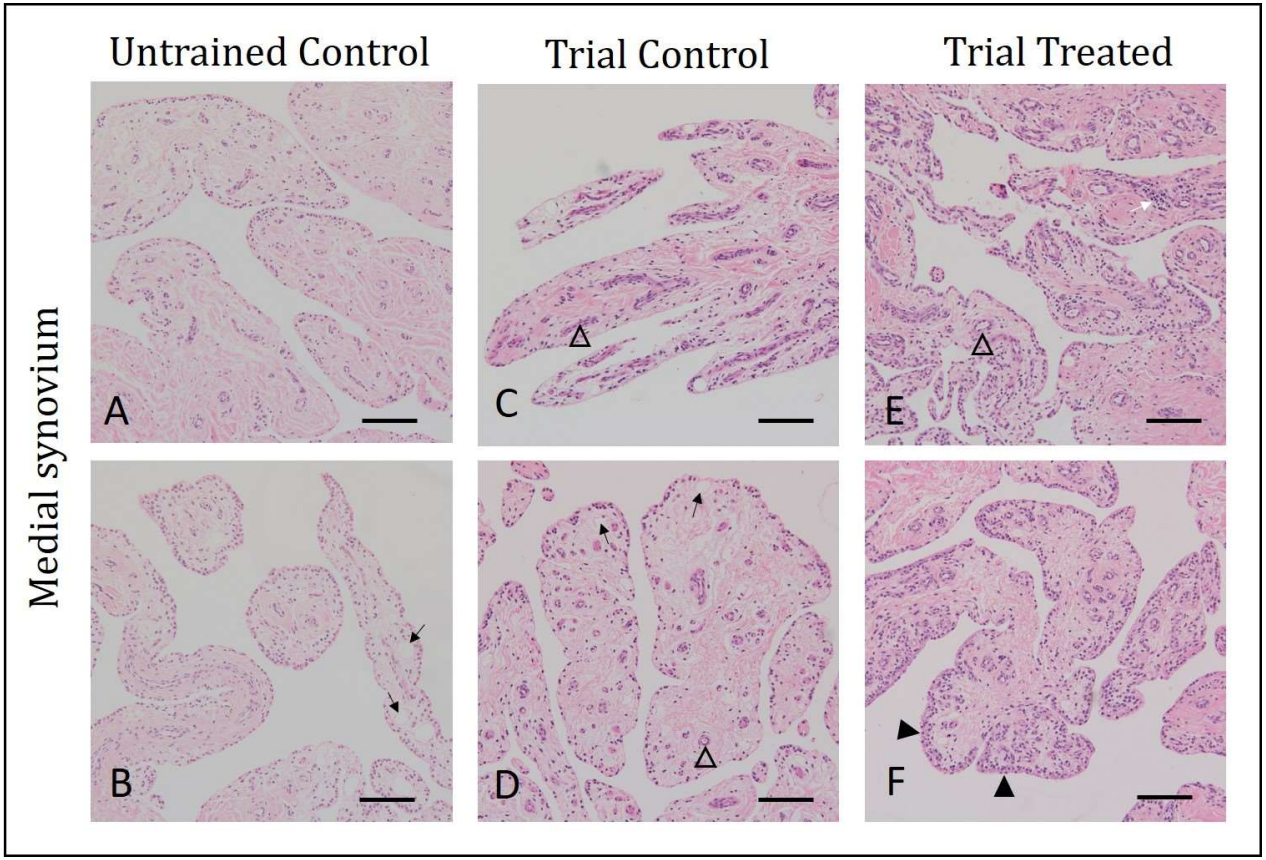

Figure 3.11 *Synovium from the dorso-medial aspect of the mid-carpal joint. Showing examples of vasculature (open arrowheads), intimal hyperplasia (closed arrowheads), subintimal oedema (black arrows) and cellular infiltration (white arrow). Synovium from both control (C and D) and treated limbs (E and F) of the trial animals had a total synovial pathology score greater than that of the untrained control group (A and B). Haematoxylin and eosin stained. Scale bar = 0.2mm.*

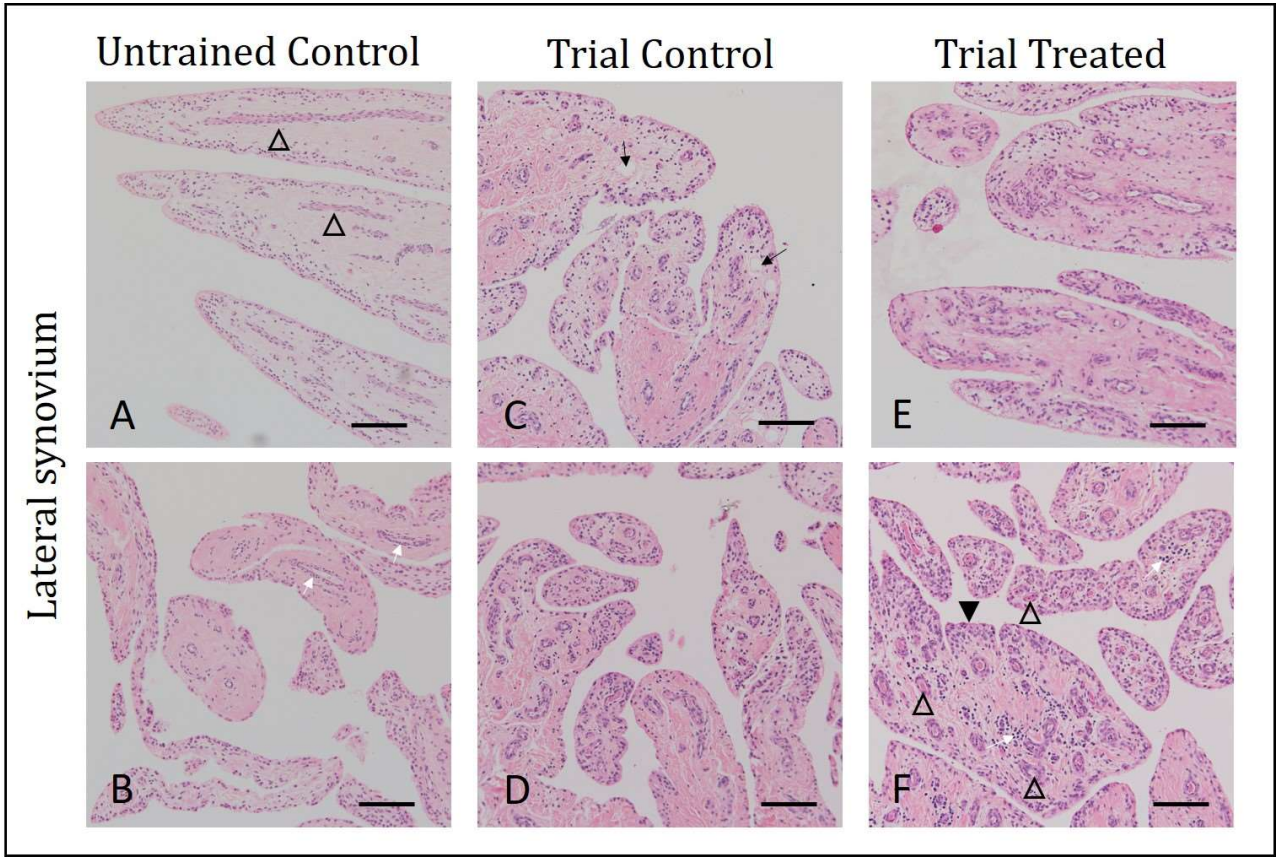

Figure 3.12 *Synovium from the dorso-lateral aspect of the mid-carpal joint. Showing examples of vasculature (open arrowheads), intimal hyperplasia (closed arrowheads), subintimal oedema (black arrows) and cellular infiltration (white arrow). There was no difference in total synovial pathology scores between groups at this site. A and B = untrained control horse 1 and 3 respectively, C and D = control limbs of horse 1 and 3 respectively, E and F = treated limbs of horse 1 and 3 respectively. Haematoxylin and eosin stained. Scale bar = 0.2mm.*

3.4 Discussion

3.4.1 Summary of major findings

After the surgical procedures, horses experienced a subtle to mild lameness together with a mild carpal effusion and mild increase in carpal circumference throughout the trial in treated limbs and to a lesser degree in control limbs. Total protein content of the synovial fluid in treated limbs was greater than baseline and greater than in the control limbs while synovial fluid TNCC was variably and mildly elevated above baseline in both treated and control limbs throughout the trial. Macroscopic examination of the joints at the conclusion of the trial revealed that defects were incompletely filled with opaque, white tissue, and that there was an area of pale, raised irregular cartilage on the surface of C3 opposing the defect. There was gross evidence of peri-articular modelling and subjective thinning of the cartilage and/or cartilage erosions adjacent to the defects in treated joints while the control joints of horses 1, 2 and 6 also contained partial- to full- thickness focal cartilage erosions. Synovium from the dorso-medial aspect of the mid-carpal joint displayed histological evidence of mild synovitis in both treated and control limbs of the trial animals at the end of the trial.

3.4.2 Comparison with current literature

Most previous studies of osteochondral defects in horses have not recorded lameness scores but have observed mild to marked lameness or mild asymmetry on force-plate analysis (253, 366, 371, 388). In a study of chondral defects in both carpal and stifle joints Frisbie et al. (1999) note a mean lameness score of 0.5 using the same grading system as

the current study (370). These are all subjectively consistent with the lameness observed in the current study. In contrast, Hanie et al. (1992) observed no lameness in a study of equine carpal chondral and osteochondral defects however these defects were created bilaterally which may have made recognition of lameness more difficult (202). Also unlike the current study Salonius et al. (2018) found that lameness had resolved by 3-4 weeks after creation of carpal osteochondral defects in horses, however these animals exercised only at walking pace which may have affected the degree of lameness (371).

Lameness scores in the current study, with an overall mean of 1.1, were slightly less than those in carpal chip fracture models which report mean scores of 1.2-2.25 (266-268, 270, 272, 400) and an equine groove model which reported grade 2-3 lameness at 2 weeks (310). Boyce et al. (2013) in a metacarpophalangeal fragment model did not specify lameness scores but measured a decrease in forelimb symmetry with kinetic gait analysis suggesting lameness (265).

The increase in response to flexion is also consistent with other equine models of joint disease as is the increase in carpal circumference (265, 268, 272, 310, 311, 399, 400). Direct comparisons of circumference is difficult as the other studies do not specify breed of the horses however Trotter et al. (1989) reported a mean increase in carpal circumference of 2.8cm in joints with chondral lesions and 2.5cm in joints with MIA-induced synovitis which are similar to the overall mean increase of 2.3cm in treated joints in the current study (311). Like the current study, Boyce et al. (2013) also reported an increase in circumference of sham operated, control limbs in treadmill trained animals (265).

Carpal effusion scores in treated joints in the current study were similar to those reported in carpal chip fracture models (mean scores 1.3-2.0 out of 4 (272) and mean scores 2.4-2.5 out of 4 (267, 268)) and in a fetlock chip fracture model (mean scores 1.5-2 out of 3 (265)). That this was elevated in the treated joints relative to both baseline and to control joints is also consistent with other studies (265, 267, 327). Response to flexion and carpal effusion scores in the current study remained elevated above baseline to a similar degree for the duration of the study which was similar to some chip fracture models (327) but unlike another in which both reduced from day 14 to the end of the study at day 70 (272). The reason for this difference between similar studies is unclear.

Synovial fluid TP and TNCC are not commonly reported in equine osteochondral defect studies. Hanie (1992) reported TP of 26g/L in synovial fluid from mid-carpal joints with osteochondral defects and <25g/L in joints with cartilage only defects. TNCC in the same study was low regardless of the type of lesion in the joint (0.1-1.5 x 10^6 cells/L) (202). Studies using the equine carpal chip fracture model of OA that report averages for the entire time of the trials find that TP in control joints is between 19.7 and 20.8 g/L, while TP in OA joints is between 23.7 - 27.0 g/L, similar to the observations in the current study (268-270). Others using the carpal chip fracture model have found no difference between operated and sham limbs but report that TP was greater than 20 g/L throughout the trial in both limbs (401). Similar to the current study, Frisbie et al. (2008) found TP to be increased above baseline in both treated and control limbs from the time of surgery to create a carpal chip fracture until day 35 as well as significantly greater in treated than in control limbs and that control limb values returned to baseline earlier than treated limbs (327). Like the current study, other models, including impact, carpal chip fracture or cartilage groove models, find that synovial fluid TP is highest in the period immediately

post operatively and returns toward baseline over the course of the trial (272, 300, 310). Some studies report this to occur over a similar time frame (56-70 days) to the current study (272, 310). In contrast, Bolam et al. (2006) found that synovial TP was less than 20g/L by 28 days after surgery, however their model used a single impact which may have caused less trauma than creation of an osteochondral defect or chip fracture(300).

TNCC in studies of physical joint injury (chip fracture or impact) is uniformly low. All report TNCCs below the level considered normal (<2.0 x 10^9 cells/L) (268, 270, 297, 300, 401). Some report no difference between sham and treated joints (297, 300, 401). Others report TNCC to be significantly higher in treated compared with sham joints, however the actual values in these studies were very low (0.0017 – 0.0044 x 10^6 cells/L) so the practical significance of this difference is unclear (268, 270).

Synovial fluid parameters in all the above studies, including the current one, are consistent with those in clinical cases of non-septic joint diseases in which TP and TNCC are usually normal to mildly elevated depending on the degree of active inflammation at the time of sampling (325).

In their study of equine osteochondral defects Trotter et al. (1989) found evidence of mild synovitis which is consistent with the current study (311). Variable and mild increases in all synovial histopathology parameters have been reported in joints with induced chip fractures (265, 267-270, 272, 400). There have been significantly greater scores in joints with chip fractures compared to sham operated in some of these studies (267, 269, 400) but not in others (265, 268). Frisbie et al. (2009) reported mean total synovial pathology scores of 5.17 (treated) and 3.25 (sham) which are similar to the mean total scores in the

trial animals in the current study (3.2 – 4.7) (270). The synovial histopathology findings in the current study are consistent with studies that have found no difference between treated and sham operated limbs. There is no clear difference between studies in which a difference between limbs was noted and those in which it was not.

Unlike the current study, in which the Cr defect was only apparent radiographically in one horse, induced osteochondral defects were observed more consistently on radiographs in a previous study (340). Hanie et al. (1992) also observed radiolucency in the SCB opposing defects which was not observed in the current study(202). Osteophytes and enthesiophytes have also been observed in joints with induced osteochondral defects (202, 311) and are consistently apparent radiographically in chip fracture and groove models of equine OA (265, 268, 272, 310, 400). SCB lysis and sclerosis are more variably evident in equine OA models, however joints with lesions have consistently greater radiographic scores than sham operated joints (265, 268, 272, 310, 400). The osteochondral defects in the current study were more superficial (<1.5mm into the SCB) than those in Kold et al. (340) (5-15mm into the SCB) and greater radiographic change has been noted in deeper defects when compared with more superficial (202, 340) while some studies of cartilage only defects have shown no or only mild radiographic changes (271, 311). Hence, the shallow nature of the lesion in the current study may account for the inconsistent changes observed radiographically. The differences in radiographic changes between the current study and equine models of OA are likely to be a result of the different techniques used to create disease. In addition, there appeared to be a greater degree of radiographic changes both prior to the trial and in control limbs in the current study which may also play a role in the lack of significant difference either between limbs or over time.

The incomplete filling of the defects with opaque whitish tissue observed at post mortem in the current study is consistent with findings from other studies of osteochondral defects in horses and other species (202, 253, 311, 365, 371, 388, 402). The raised, paler region opposing the defects is also a consistent finding in studies of equine osteochondral defects in the carpus (202, 253, 311, 388). Gradual flattening of surrounding cartilage and macroscopic degenerative changes surrounding defects is reported in models in various species (17, 18, 365, 402). Macroscopic evidence of periarticular modelling is also variably reported in equine models (253, 366), as is thickening or inflammation of the synovium (202, 366).

Most osteochondral defect studies report no macroscopic changes to cartilage distant to the defect. However, Todhunter et al. (1993) reported linear striations in all mid-carpal joint surfaces in joints with a Cr osteochondral lesion however the induced defects were larger than those of other studies, involving approximately one third of the articular surface of distal Cr (253). Salonius (2018) reported no macroscopic degenerative changes in surrounding cartilage of joints in which 4 or 8mm diameter defects had been created (371). These animals were exercised only at a walking pace after creation of the defects which may account for the relative lack of changes in the cartilage surrounding the defects. The overall macroscopic pathology observed in the current study is similar to or milder than that reported in other models of equine joint disease (266-270, 272).

3.4.3 Interpretation of major findings

3.4.3.a Lameness

Mild lameness is defined as a score of less than 1.5 on AAEP guidelines (317) however, in the carpal chip-fracture model of equine OA lameness scores of 2/5 have been considered mild (266-268) so the scores observed in the current study are consistent with mild lameness.

The lameness is likely to be related mostly to pain associated with the surgical defect and/or secondary inflammation within the mid-carpal joint given the positive pain response to carpal flexion in treated limbs. However, pain in the feet of the treated limbs in horses 4 and 6 may have contributed to their observed lameness score. Lameness was apparent in the control limb of horses 2 and 3, and while the source of the lameness was not obvious in horse 3, in horse 2 it may have been related to the cartilage lesions observed on Cr and C3 from the control limb or due to pain in another region of the limb.

3.4.3.b Radiographic findings

Radiography was an insensitive method of observing the defects in this model which may be due to the superficial nature of the lesions. However the general insensitivity of radiographs for detecting SCB changes (319, 403-405) or superimposition of bony structures over the defects (319, 393, 403) may also have made identification of lesions more difficult. These factors may also have complicated radiographic assessment of SCB lysis and sclerosis as may the fact that these parameters were apparent in both treated and control limbs and both prior to surgery and variably during the study.

Soft tissue swelling, when evident, was only present in treated limbs post-surgery making it the most specific radiographic marker for joints with osteochondral defects in this study, however it was only observed in 2 of the animals so was not sensitive and, in general, it is a non-specific marker of joint pathology (323).

The increase in periarticular modelling in treated joints was reflected somewhat in the radiographic findings. Lack of radiographic evidence of osteophytes at 14 days post-surgery is expected as previous studies in mice have shown predominantly cartilaginous proliferation with little ossification at this time point (406). The amount of new bone formation associated with this modelling was also relatively small which is likely to have made it more difficult to identify radiographically than on post mortem examination at day 70.

3.4.3.c Markers of inflammation

The observed increases in indirect and direct markers of inflammation in both treated and control limbs in this study may be a consequence of arthroscopy, treadmill exercise and/or repeated arthrocentesis, in addition to the presence of the osteochondral defect in treated limbs (265, 267, 327, 407-412).

Clinical and synovial fluid markers of inflammation may be elevated by arthrocentesis alone so repeated collection of synovial fluid may have contributed to the observed increases. However this effect has been shown to be transient, resolving within 4-7 days in previous studies of repeated arthrocentesis, suggesting that weekly arthrocentesis is unlikely to be playing a significant role in the current study (327, 407-412).

The clinical relevance of changes in carpal circumference is not well established however it has been used to assess soft tissue swelling surrounding the joint (399). Synovial hypertrophy or thickening has been noted at gross post mortem in previous equine osteochondral defect studies (253, 366) and may have contributed to the increase in carpal circumference as may the presence of joint effusion in treated limbs in the current study.

Joint effusion may be a result of acute bleeding, increased synovial fluid production or inflammatory cell infiltration into the synovial fluid (265), and although it has been noted to be a non-specific and insensitive indicator of synovial disease in horses (323) is generally considered to be a reflection of synovitis (327). Mean TNCC, although being inconsistently elevated above baseline in both treated and control joints, remained at or below the level considered normal (<1 x 10^9 cells/L), suggesting that this difference is unlikely to be of clinical significance. There was also only inconsistent blood staining in the arthrocentesis samples, suggesting that the carpal effusion was likely to be a result of increased synovial fluid production. While the degree of effusion in control limbs was less than in treated joints its presence suggests that arthroscopy alone followed by treadmill exercise resulted in some synovial effusion (327). This effusion may be related to synovitis however increased synovial blood flow due to exercise may also be playing a role (413). It is likely that the presence of the lesion in treated limbs combined with the effects of arthroscopy and training to cause the greater effusion in treated limbs when compared with controls.

It is suggested that effusion may change the loading experienced by joint surfaces due to increased pressure within the joint space and changes in the motion of the joint due to increased stiffness, both of which may have affected the treated joints in the current study

(414), however I am not aware of any work directly investigating how synovial effusion affects joint congruity and stability in horses. In addition, the degree of effusion in the current study was moderate and the increase in carpal circumference less than 7% greater than baseline, so while the increase in pressure within the joint was not measured, it is likely to be low relative to the large loads experienced normally by joints in galloping horses (108). Therefore, while possible, it would seem unlikely that the joint effusion had a marked effect on loading of the joint surface.

The elevation in TP in treated joints may be associated with trauma due to creation of the defect or inflammation (325). While mean TP of the treated joints returned to the upper end of what is considered the normal range (<20g/L) by day 49, it remained greater than baseline to a degree that approached significance, which may indicate slight ongoing inflammation.

Synovitis may be a consequence or a cause of increased concentrations of pro-inflammatory cytokines in synovial fluid. Therefore, pro-inflammatory cytokines released due to bone damage during creation of the defect might have been expected to cause synovitis and/or the mild synovitis observed on histology may have caused increased synovial fluid pro-inflammatory cytokines (385, 394, 415). Regardless of their source, pro-inflammatory cytokines within synovial fluid may affect chondrocyte behaviour and matrix metabolism (394, 416, 417). However, there was no difference in synovial histopathology scores between the treated and sham operated limbs of the trial animals suggesting that the presence of the defect did not play a significant role in the observed mild synovitis and that any cartilage differences between the two limbs are unlikely to be a result of inflammatory mediators.

3.4.3.d Peri-articular modelling

Peri-articular modelling is thought to result from either instability of the joint or alterations in the local biochemical milieu (418). A slight increase in joint laxity was observed in rabbit stifles with induced osteochondral defects (18) so while I am not aware that instability has been studied in equine osteochondral defects this may be contributing to peri-articular modelling in the current study.

TGF-β, BMP-2, VEGF and IGF-1 have been associated with the development of osteophytes (280, 406, 418, 419). Unlike other studies, Hsia et al. (2018) found no association between TGF-β and osteophytes in ACL-transected murine stifles, however gene expression was performed on whole joints in this study which may have limited the ability to detect local changes at the site of osteophytes (406). TGF-β, IGF-1, BMP-2 and VEGF have all been shown to be elevated at sites of fracture so may have been increased in the current model due to bone damage at the time of defect creation and therefore played a role in development of peri-articular modelling (229, 406, 420).

3.4.3.e Macroscopic defect healing and cartilage pathology

The subjective thinning and lesions in cartilage immediately adjacent to the osteochondral defects is likely to be due to increased surface pressure and strains within the cartilage and may reflect either physical deformation of the cartilage or degeneration (1-4, 106, 209).

Macroscopic changes in cartilage opposing osteochondral defects are well recognised but not well understood (202, 253, 311, 388). Cartilage opposing defects has been shown to

experience lower surface pressures and to bulge into the opposing defect on loading which may be involved in the observed changes (2, 4, 358). See chapter 6 for a more detailed discussion of cartilage changes.

Observations from macroscopic examination suggest that the effects of focal osteochondral defects on cartilage are localised in this model. It is possible that the length of the trial was insufficient to observe changes at the more distant sites as Todhunter et al. (1993) saw changes distant to Cr defects at 17 weeks(253). However joint-wide cartilage pathology was seen by 8 weeks in a rabbit stifle model of OC defects (18) and other studies of equine OC defects have observed no changes distant to the defects at 6 months (202, 366) suggesting that if these changes are going to occur, they do so within the time-frame of the current study.

Healing of the defects is discussed in detail in Chapter 4. The presence of unhealed defects on Cr and the macroscopic cartilage changes immediately opposing these on C3 allowed easy identification of sites for collection of osteochondral specimens for more detailed examination (see Chapters 2 and 4-6).

3.4.4 Conclusion

Creation of an osteochondral defect in the mid-carpal joint resulted in mild pain and lameness that was considered acceptable in regard to animal welfare.

Inflammation within the joint was minimal and unlikely to significantly affect other findings. However, there was evidence of pathology and lameness in control limbs that should be taken into consideration in the interpretation of other findings in this study.

The induced osteochondral defect resulted in mild, focal changes in the adjacent cartilage and marked cartilage changes on the articular surface immediately opposite. It was obvious macroscopically at 10 weeks and was able to be used to guide specimen collection.

Radiography was found to have limited ability to detect the induced osteochondral defects or secondary changes that were later identified on post-mortem macroscopic examination, higher resolution imaging or histology.

Chapter 4

BONE PARAMETERS OF THE RADIAL CARPAL BONE

4.1 Introduction

The primary aim of creating an osteochondral defect in the radial carpal bone in this study was to produce a loss of congruity within the middle carpal joint and focal changes in the loading of the articular surface of the opposing C3. However, as induced osteochondral defects have been shown to change the loading on the surrounding SCB (1-3), and tissue damage and inflammation have been associated with changes in both erosion and formation activity in bone surrounding sites of injury (383, 385), it provided the opportunity to investigate the combined effects of changes in loading and tissue damage on SCB. Therefore the purpose of this chapter was to examine the SCB of Cr at varying depths below the osteochondral defect and from varying depths below an intact articular surface in a region adjacent to the defect. This would allow comparison with changes observed in the opposing C3 SCB, where the subchondral bone response is likely to be a result of changes in loading without concurrent tissue damage.

It was hypothesised that in this model there would be an increase in resorption and loss of bone volume in SCB deep to the osteochondral defect. It was further hypothesised that an increase in bone formation activity and increase in bone volume would be observed in SCB underlying an intact joint surface adjacent to the defect.

4.2 Materials and Methods

Undecalcified specimens of Cr were collected and processed as described in Chapter 2 for imaging with microCT and BSEM, MG staining and for analysis of fluorochrome labels. Cryosections of decalcified samples were prepared and stained for TRAP as described in Chapter 2 for identification of osteoclasts.

Two series of ROIs were chosen for evaluation in the Cr microCT and BSEM images, Masson's Goldner stained sections and for analysis of fluorochrome labels (Figure 4.1a). One series was positioned in the region deep to the surgical defect and the second in the adjacent, dorsal region, deep to an intact articular surface. The distance from the dorsal articular margin to the defect, along a line parallel to the articular surface, and the length of the defect were measured on images of the treated Cr for each horse (Appendix 2) and these measurements used to define the position of ROIs for that animal (Table 4.). The position of each series of ROIs was chosen so that they were as close as possible to the centre of each region for each animal. The mean of these positions was used for specimens from the untrained control animals.

The dorsal articular margin was defined as the point on the dorsal edge of the bone where the articular cartilage ended. On microCT images this was not obvious as the HC is not visible with this modality and the CC was often indistinct from the SCB. On microCT images of treated limbs the point immediately proximal to the peri-articular modelling was defined as the articular margin. The distance between this point and a line drawn along the distal surface of the CC was measured and this distance used to define the articular margin on images of Cr from control limbs where the articular margin was not otherwise obvious (Figure 4.1b).

Horse	Position of dorsal edge of ROIs (mm palmar to dorsal articular margin)	
	Weight bearing	**Deep to Lesion**
1	1.0	6.0
2	0.4	5.5
3	2.0	7.0
4	0.5	4.0
5	1.0	4.0
6	2.0	6.0
Untrained Control	1.2	5.5

Table 4.1 *Location of dorsal edge of Cr ROIs in individual horses for analyses on undecalcified sections, mm palmar to the dorsal articular margin in a line parallel to joint surface.*

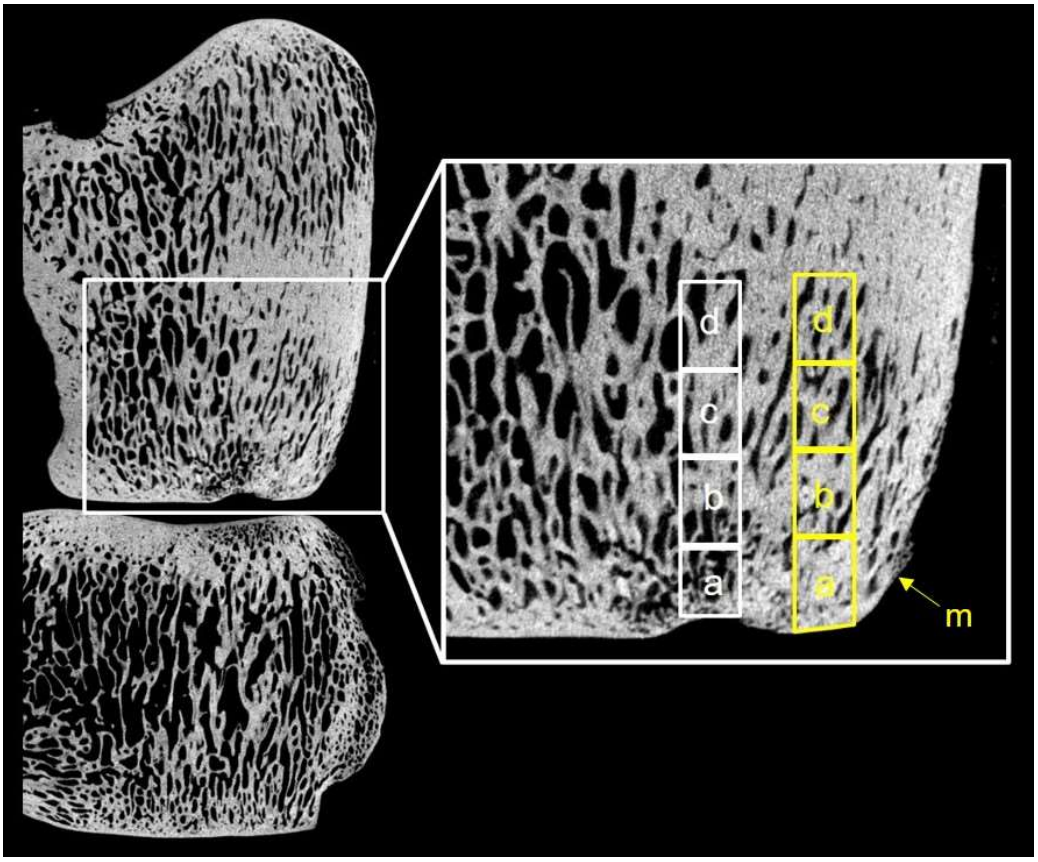

Figure 4.1a *Left: MicroCT images of Cr (top) and C3 (bottom) from the treated limb of Horse 5. Right: Radial carpal bone ROIs*: *yellow = weight bearing region, white = region deep to the lesion, a = 0-3mm, b = 3-6mm, c = 6-9mm, d= 9-12mm deep to articular surface. m = dorsal articular margin. Dorsal to right of image, palmar to left of image. Not to scale.*

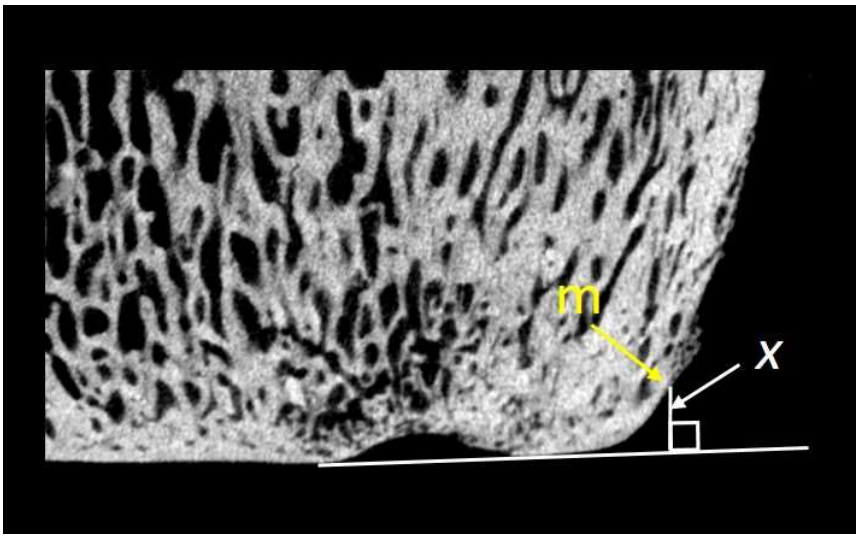

Figure 4.1b *MicroCT image of dorso-distal Cr from the treated limb of Horse 5 showing measurement of the position of the dorsal articular margin.* x *= distance between the dorsal articular margin (m) and a line parallel to the surface of the calcified cartilage.* x *was measured from images of treated limbs and used to define the dorsal articular margin in the contralateral control limbs.*

Each series consisted of four contiguous ROIs arranged in a column. Each ROI was 2mm wide in the dorso-palmar direction and 3mm long in the proximal-distal direction with the exception of the most superficial ROI immediately below the defect.

In treated Cr bones the ROI at 0-3mm below the cartilage in the region deep to the defect was positioned such that its superficial edge was level with the deep border of the defect. The depth of the defect was measured and this depth below the articular margin of the calcified tissue was defined as the superficial boundary for the 0-3mm ROI in control Cr sections and images for each individual horse. In specimens from the untrained control animals the position of the superficial boundary of the 0-3mm ROI was defined as the mean of the depth of the lesions from the trial horses (Table 4.2). This ROI extended to a

position 3mm below the cartilage or where it would have been had it not been removed. This was estimated in treated bones by drawing a line between the osteochondral junctions at either edge of the defect. This ROI had a smaller area than all other ROIs.

The remaining three ROIs in each region were located 3-6, 6-9 and 9-12mm deep to the articular cartilage respectively.

For microCT 3D analysis each ROI was 2.4mm deep with the exception of those in Horse 5 control and treated limbs and untrained control horse 4 where the thickness of the specimen limited the thickness of the ROIs to 1.7mm, 2.2mm and 1.9mm respectively.

Horse	Position of base of defect (mm deep to osteochondral junction)		
	MicroCT (mean)	BSEM	MG stained/ fluorochrome
1	1.2	1.2	1.4
2	0.7	0.7	0.9
3	0.3	0.3	0.6
4	0.8	0.8	0.7
5	0.6	0.5	0.7
6	0.9	0.6	1.0
Untrained Control	0.75	0.7	0.9

Table 4.2 *Position of base of defect in mm below the osteochondral junction. The value for microCT images is the mean of the positions on the first and last slices used for evaluations. The values for the untrained controls are the mean of the positions in the trial animals in each analysis.*

Two series of ROIs were also defined for osteoclast counts on cryosections stained for TRAP: one in the region deep to the defect and one in the dorsal region below the intact joint surface. Not all cryosections used for TRAP staining included the deeper bone so only two ROIs were defined in each series (Figure 4.2). The same positions were used for specimens from all horses. Each was an area 2.2 x 3.3mm. The two ROIs in the dorsal weight bearing series were positioned 0.55-2.75mm from the dorsal edge of the bone on a line parallel to the articular surface, while the two ROIs in the series deep to the surgical defect were positioned 5.5 to 7.7mm from the dorsal edge of the bone in a line parallel to the articular surface. The superficial ROI in each series included bone 0-3.3mm below the cartilage and the deeper ROI included bone 3.3-6.6mm below.

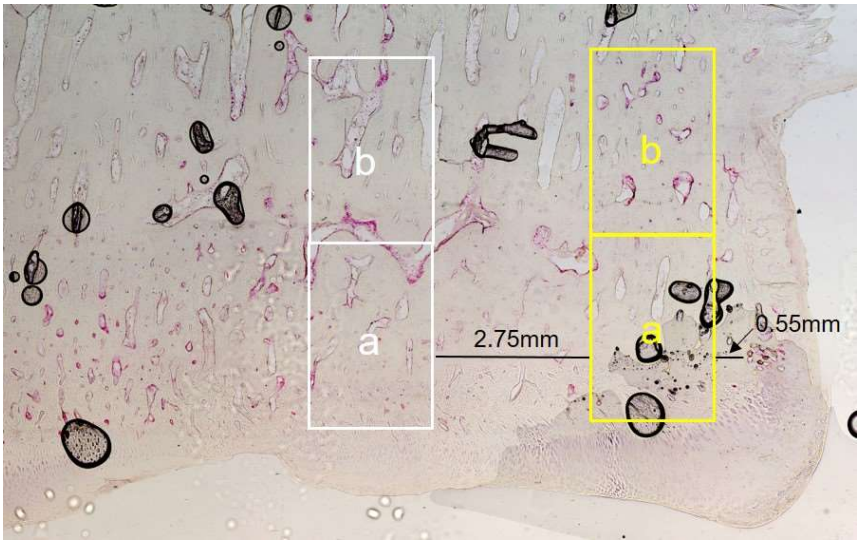

Figure 4.2 *ROIs for osteoclast counts on sections stained for TRAP. Yellow boxes = weight bearing region, white boxes = region deep to the lesion; a = 0-3.3mm, b = 3.3-6.6mm deep to cartilage. Dorsal to right of image. Not to scale.*

Osteoclasts were counted through the microscope eyepiece at a magnification of 200x, rather than from digital images, to allow visualisation of the full depth of the sections and, where needed, to confirm the presence of multiple nuclei within TRAP positive cells. Each field of view had a diameter of 1.1mm and each ROI was defined as an area of 2x3 fields. The position of each series of ROIs was defined such that the ROIs were wholly within the dorsal weight bearing region or in the region deep to the lesion for all animals.

Measurements were made in each ROI described above for each technique as specified in Chapter 2. All observations were analysed with the statistical methods described in Chapter 2.

4.3 Results

The surgical defect was apparent in images and sections from all Cr specimens from the treated limbs with the exception of the sample prepared for staining with TRAP from horse 1 (Figures 4.3-4.7). The sections stained for TRAP were taken from the medial end of the defect and it appears that this section from horse 1 was just adjacent to rather than directly through the defect. While the sections to be stained for TRAP from the treated limbs of all other horses contained some portion of the defect, it appeared more shallow and narrow than in sections collected for other analyses (Figure 4.5).

There was minimal evidence of either osteoid or mineralised tissue filling the defect and minimal evidence of fluorescent labels at the defect boundary. Varying degrees of fibrocartilaginous tissue was apparent within the defects on Masson's Goldner stained

sections (Fig 4.6). There were also islands of chondroid tissue within SCB voids immediately deep to the defect in 4 of the 6 treated Crs (Figure 4.7).

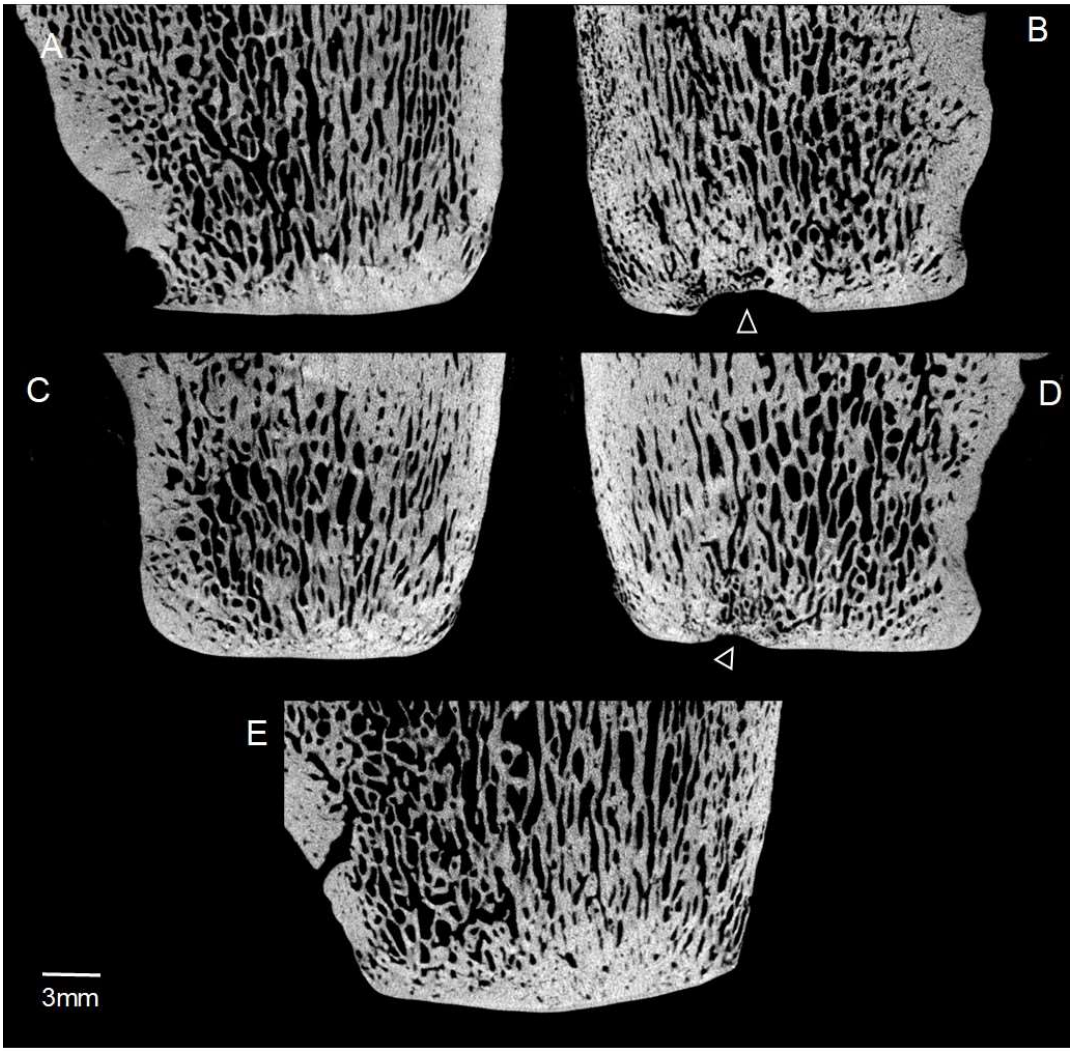

Figure 4.3 *MicroCT images of Cr bones, voxel size 24.2µm. A and B: control and treated limbs of Horse 1 respectively. C and D: control and treated limbs of Horse 5 respectively, E: Untrained control horse 2. Arrow heads indicate surgical defects in treated bones. Dorsal edge of bone towards centre of image, palmar edge outwards for images of trial horses, dorsal to the right for untrained control horse.*

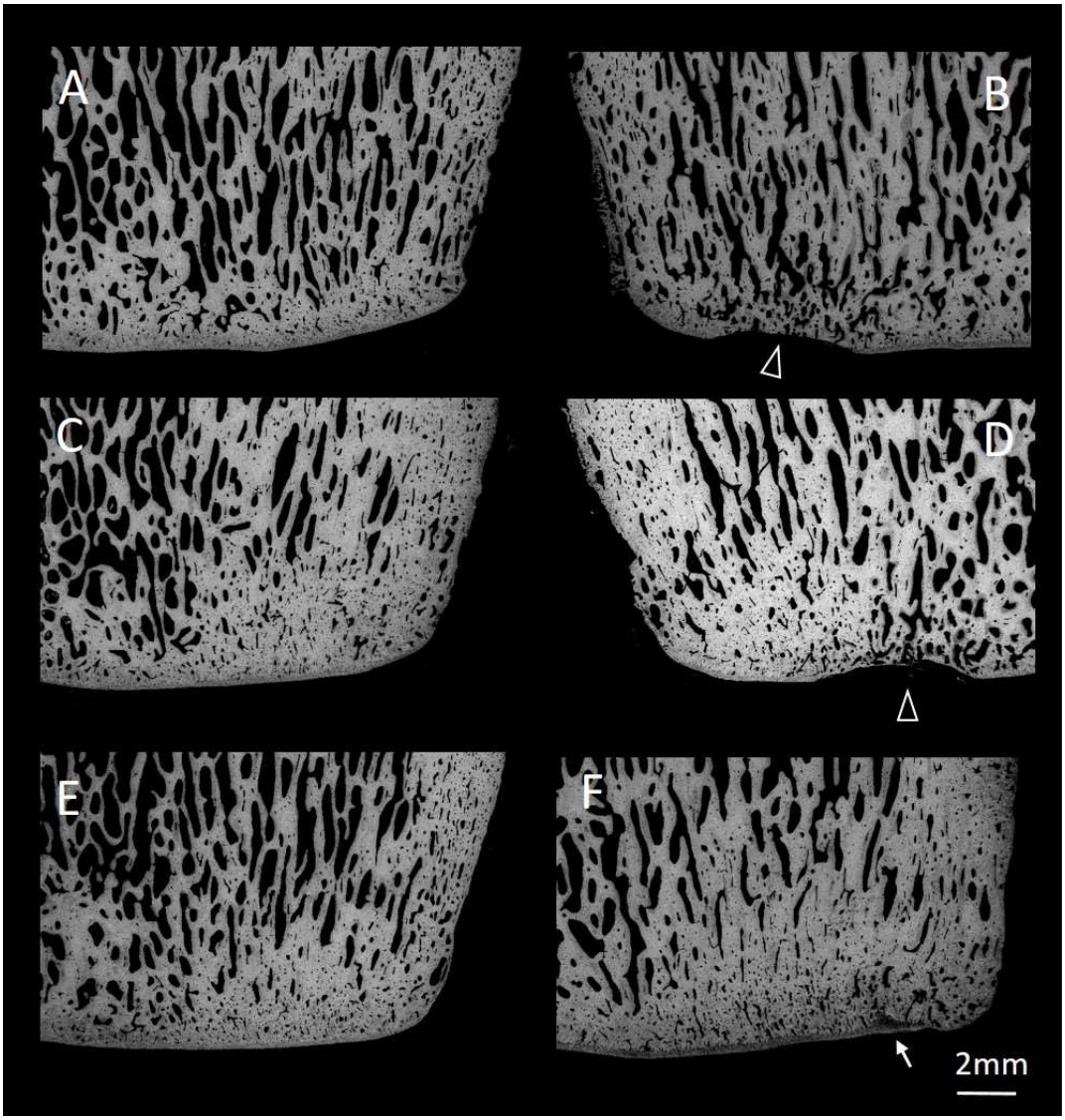

Figure 4.4 *BSEM images of Cr bones. A and B: control and treated limbs of Horse 4 respectively. C and D: control and treated limbs of Horse 6 respectively, E and F: untrained control horses 1 and 3 respectively. Arrow heads indicate surgical defects in treated bones. Arrow indicates abnormality in CC of untrained control horse 3. Dorsal edge of bone towards centre in images from trial animals. Dorsal edge to right for untrained control images.*

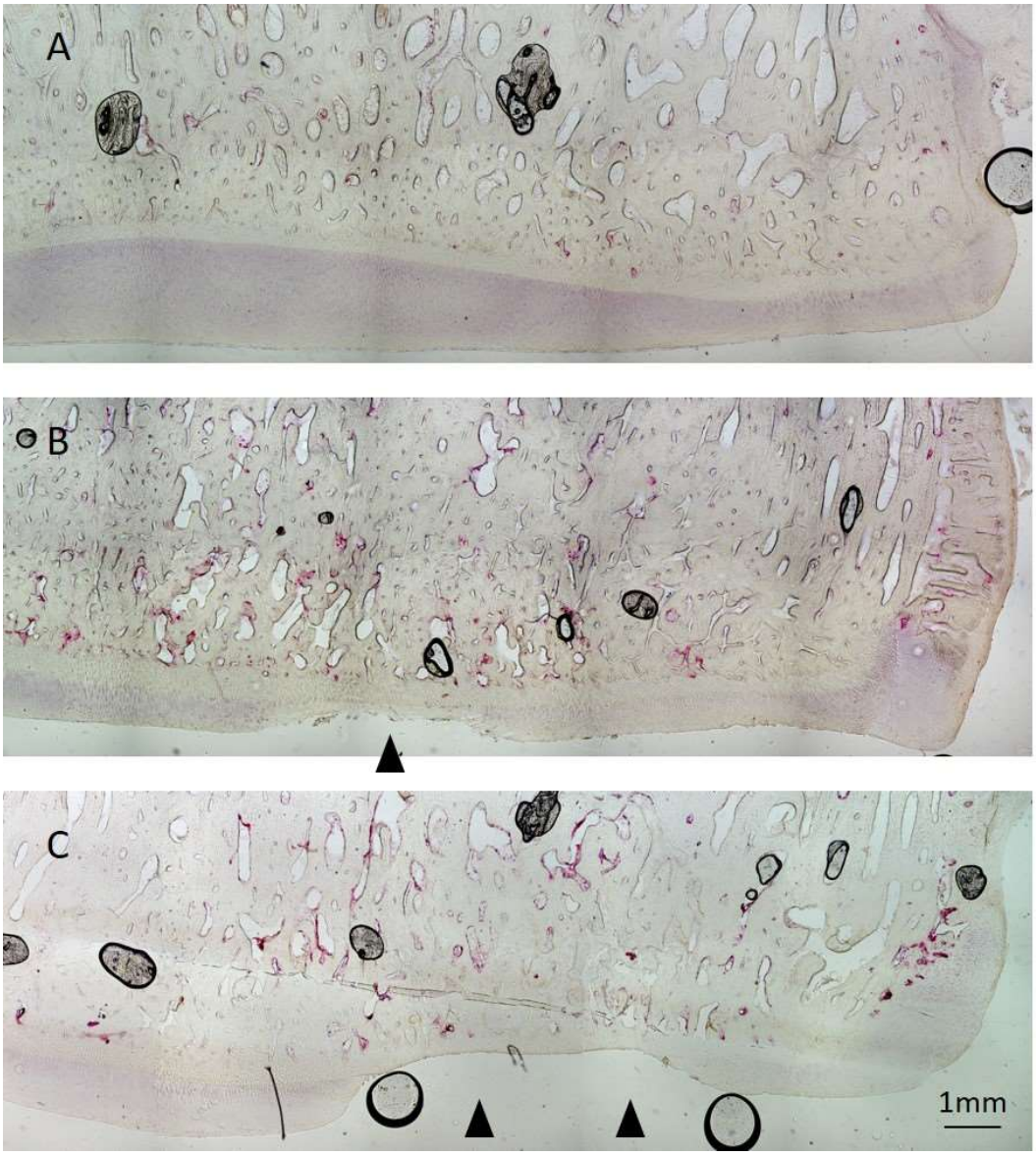

Figure 4.5 *Cryosections stained for TRAP showing varying lengths and depths of surgical defect (arrowheads) in treated Cr bones. There was no evidence of the defect on Cr from the treated limb of horse 1 (A), Cr from the treated limb of horse 2 contained a small, shallow defect (B) while Cr from the treated limb of Horse 5 contained the full depth and length of the defect (C). Reconstructed light microscopy images. Dorsal to right of image.*

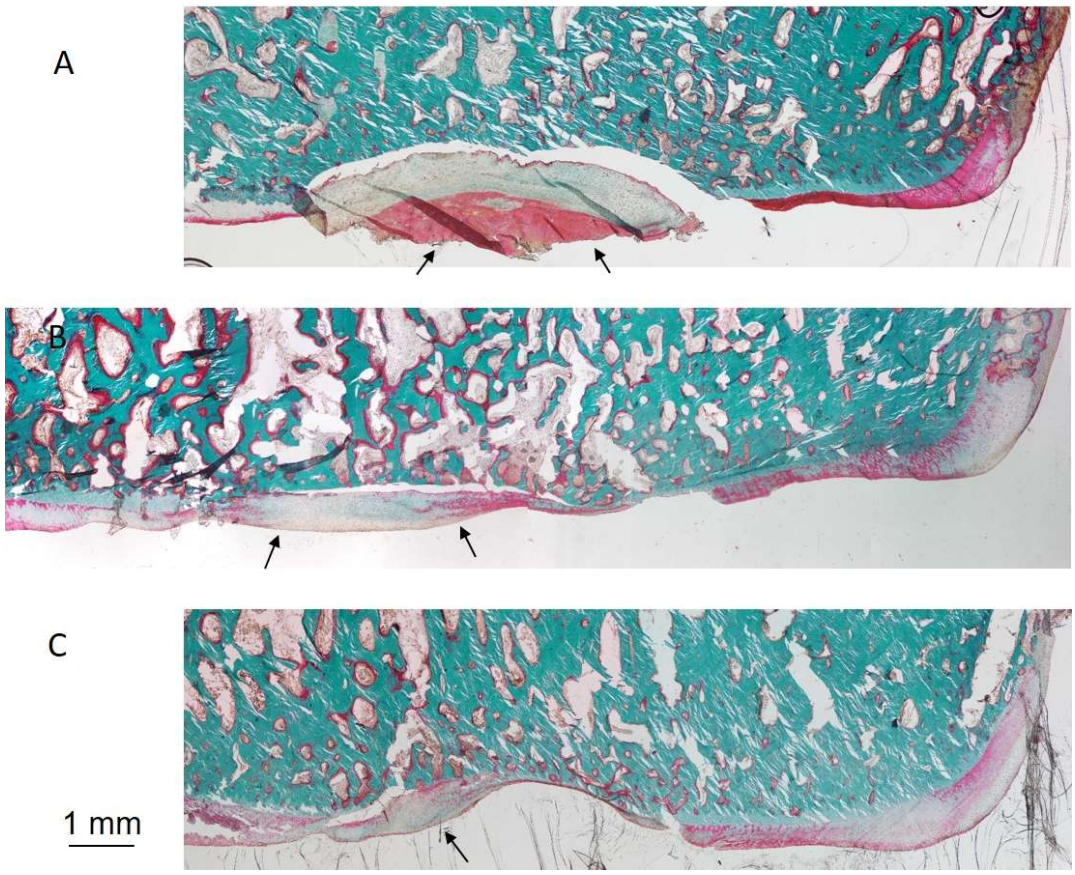

Figure 4.6 *Masson's Goldner stained sections showing varying degrees of fibrocartilaginous tissue (arrows) within defects in treated Cr bones. A = Horse 1, B=Horse 2, C=Horse 6. Reconstructed light microscopy images. Dorsal to right of image.*

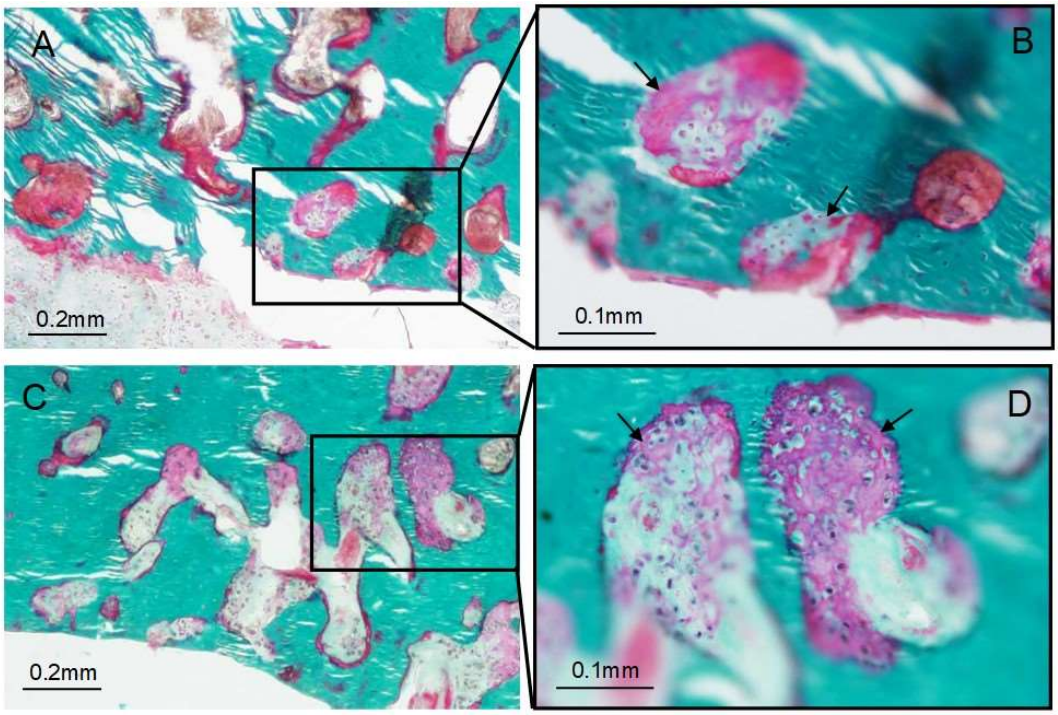

Figure 4.7 *Masson's Goldner stained sections of the treated Cr from trial horses 4 (A and B) and 5 (C and D), showing islands of chondroid tissue within SCB voids (arrows). Light microscopy.*

The SCB of Cr from the control limbs of the trial horses appeared intact with no evidence of pathology in all except one horse. In Cr from the control limb of Horse 2 a superficial discontinuity in the CC and extending into the superficial SCB was apparent on both microCT and BSEM at 2.5mm palmar to the dorsal edge of the bone (Figure 4.8). Resorption spaces were evident in the SCB surrounding this defect.

The SCB of Cr from the untrained controls appeared intact with no evidence of pathology in all except one animal. In the Cr from untrained control horse 3 there was an abnormality of the CC that appeared to extend into the SCB approximately 2mm from the dorsal articular margin (Figure 4.4).

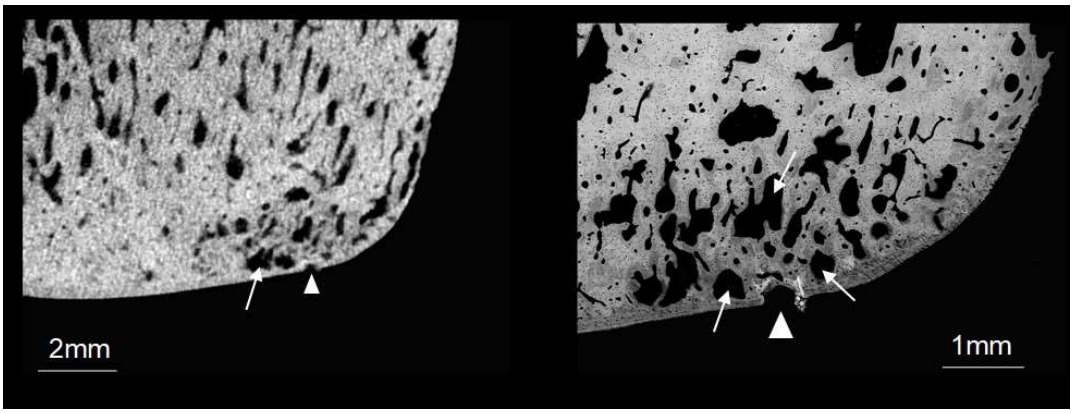

Figure 4.8 *Calcified cartilage defect (arrowheads) and surrounding resorption spaces (arrows) in the dorsal weight bearing region of Cr from the control limb of Horse 2. MicroCT (left) and BSEM (right) images.*

There was evidence of varying degrees of peri-articular modelling on the dorsal aspect of Cr from all treated joints in both microCT and BSEM images (Fig 4.9).

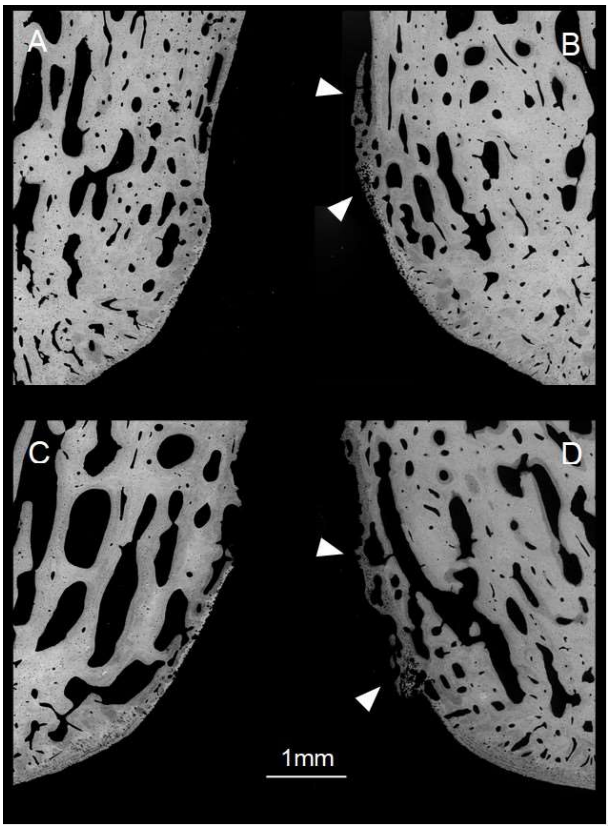

Figure 4.9 *Examples of mild (B, Horse 3) and more marked (D, Horse 1) peri-articular modelling (arrowheads) at the dorsal articular margin of Cr from the treated limbs that is not present on the control limbs of the same horses (A and C respectively). BSEM images.*

4.3.1 Region below the defect

In the region immediately below the defect there was a marked loss of bone volume in the treated limbs when compared to both their contralateral control limbs and the untrained controls (Table 4.2). This was only evident in the region 0-3mm deep to the level of the cartilage where microCT BV/TV was decreased and BSEM porosity increased in the treated limbs when compared with both the contralateral controls and the untrained controls (Figures 4.10 and 4.11).

At 3-6mm and 6-9mm deep to the level of the cartilage there was no significant difference in bone volume between the treated and control limbs of the trial horses. However, at 3-6mm deep to the level of the cartilage the treated limbs had a lower BV/TV and greater porosity than the untrained controls (Table 4.2).

At 9-12mm below the cartilage the BV/TV of the treated and the control limbs of the trial animals were both higher than that of the untrained controls however the difference between the control limbs of the trial animals and the untrained control group did not quite reach significance (P=0.053, Fig 4.11).

The reduced bone volume at 0-3mm deep to the cartilage was associated with a marked increase in bone surface in this region (Table 4.3). Bone surface area on microCT in the treated limbs was higher than either the contralateral or untrained controls (Figure 4.11). In the deeper regions there was no difference in bone surface between the treated and control limbs of the trial animals.

At 3-6mm deep to the level of the cartilage, the microCT bone surface of the treated limbs was higher than that of the untrained controls while at 9-12mm deep the microCT bone surface of the treated limbs was lower than that of the untrained controls (Table 4.3, Figure 4.11)

Depth below cartilage	Parameter	Mean (Median), Range			P-value		
		Trial treated	Trial Control	Untrained control	Trial treated v Trial control	Trial treated v Untrained control	Untrained control v Trial control
0-3mm	BV/TV (%)	62.3 (59.8), 36.1	91.0 (90.7), 9.2	92.7 (95.2), 18.9	**0.005**	**0.002**	0.63
	BS/BV (mm^{-1})	10.2 (10.5), 9.07	3.60 (3.68), 1.73	3.32 (2.75), 3.58	**0.007**	**0.003**	0.68
	Porosity (%)	36.1 (34.4), 31.0	17.1 (16.6), 10.0	13.6 (12.8), 9.21	**0.01**	**0.005**	0.11
	Pore perim. (mm^{-1})	9.36 (8.83), 5.08	6.33 (6.21), 2.02	6.85 (6.39), 3.03	**0.007**	**0.02**	0.39
3-6mm	BV/TV (%)	65.0 (64.9), 11.3	71.3 (68.2), 24.9	76.0 (77.5), 25.4	0.15	**0.05**	0.42
	BS/BV (mm^{-1})	8.28 (8.61), 2.65	6.66 (6.92), 4.49	5.82 (5.56), 4.70	0.09	**0.02**	0.41
	Porosity (%)	34.8 (37.1), 15.3	29.3 (31.5), 28.7	24.4 (21.9), 15.2	0.32	**0.02**	0.34
	Pore perim. (mm^{-1})	6.46 (5.94), 5.81	5.23 (5.18), 1.23	5.05 (4.89), 2.20	0.21	0.16	0.65
6-9mm	BV/TV (%)	63.0 (62.8), 12.4	59.5 (57.5), 24.6	57.7 (58.7), 15.9	0.29	0.13	0.70
	BS/BV (mm^{-1})	7.75 (7.93), 2.69	8.20 (8.58), 4.18	7.93 (7.61), 2.79	0.46	0.77	0.72
	Porosity (%)	38.5 (35.4), 45.3	36.7 (37.0), 39.6	33.9 (33.3), 31.2	0.48	0.69	0.70
	Pore perim. (mm^{-1})	4.02 (3.80), 1.88	4.2 (4.33), 2.03	4.67 (4.37), 2.72	0.27	**0.05**	**0.03**
9-12mm	BV/TV (%)	66.6 (68.0), 16.8	60.8 (56.8), 30.2	48.3 (50.0), 18.8	0.15	**0.001**	0.053
	BS/BV (mm^{-1})	6.87 (6.53), 2.50	7.89 (8.53), 5.17	9.13 (8.67), 4.32	0.20	**0.02**	0.25
	Porosity (%)	28.1(29.3), 17.7	35.4 (31.8), 27.7	42.2 (40.4), 22.9	0.09	**0.02**	0.28
	Pore perim. (mm^{-1})	5.71 (5.16), 3.05	4.95 (4.93), 1.96	4.48(4.15), 1.58	0.30	0.06	0.26

Table 4.3 *Measures of bone volume and bone surface, Cr, region below the defect. BV/TV = Bone volume/ Total volume (%), BS/BV = Bone surface/ Bone volume (mm^{-1}) from microCT images, Porosity = pore area/bone area (%) and pore perim.= pore perimeter/ bone area (mm^{-1}) from BSEM images.*

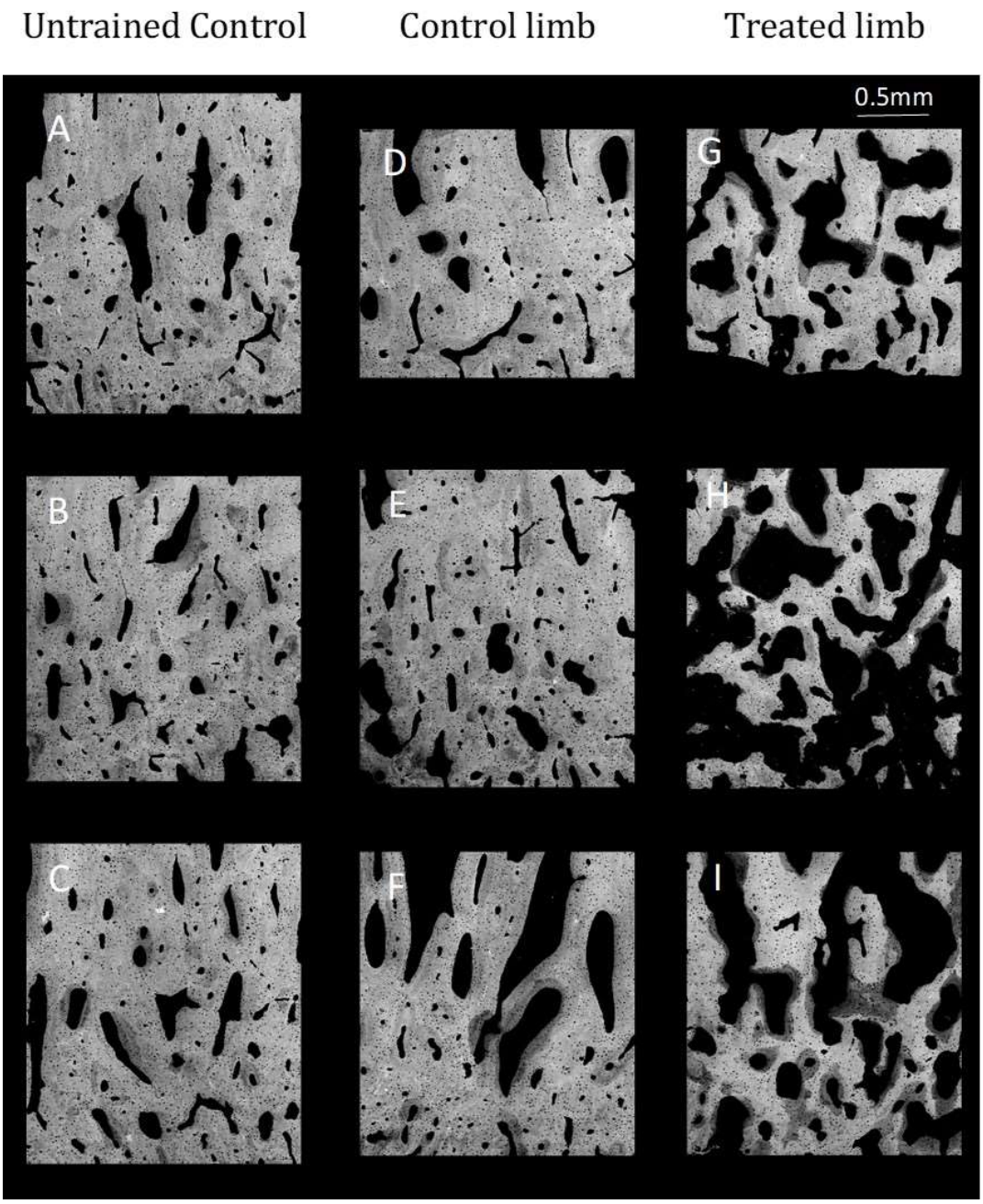

Figure 4.10 *BSEM images showing increased porosity in the treated limbs, Cr, region below the defect, 0-3mm deep to the cartilage. A= untrained control horse 1, B= untrained control horse 2, C= untrained control horse 4, D and G = Horse 1 control and treated respectively, E and H= Horse 2 control and treated respectively, F and I = Horse 4 control and treated respectively.*

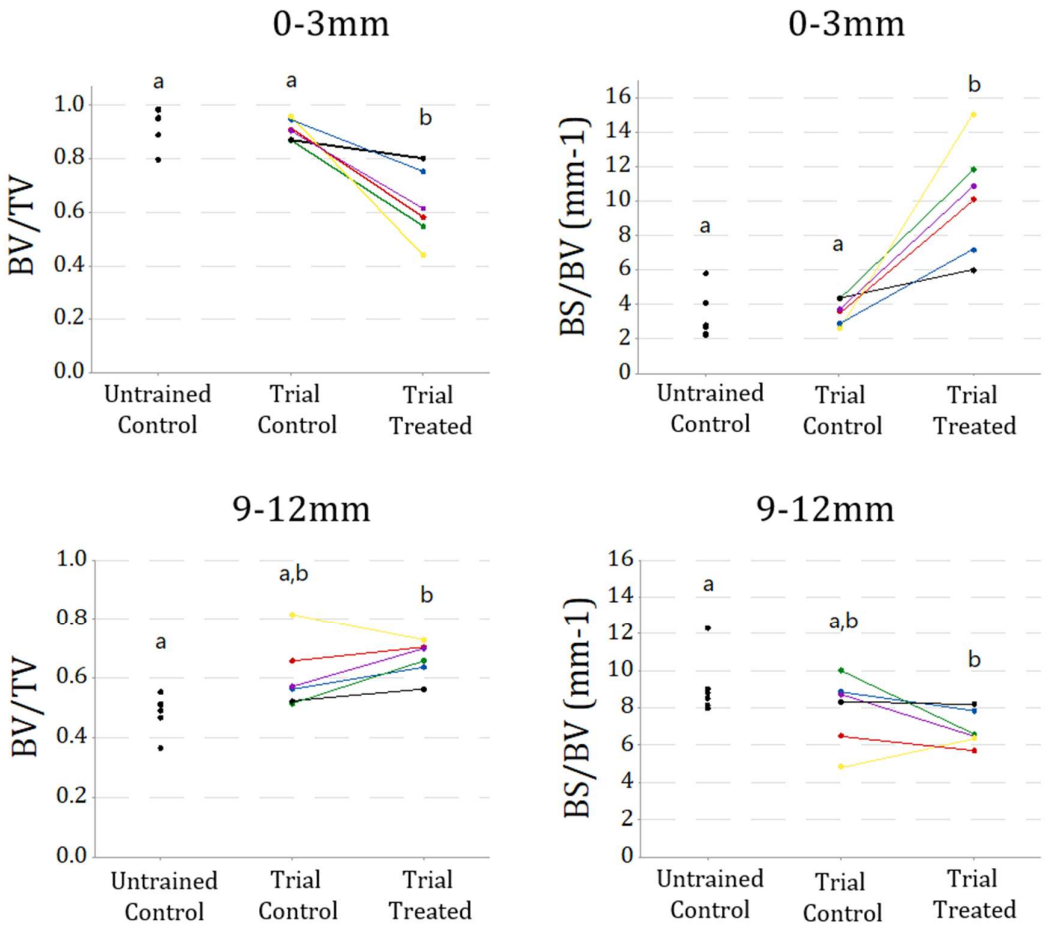

Figure 4.11 *Bone volume fraction (Bone Volume/ Total Volume) and bone surface ratio (Bone surface/ Bone Volume [mm-1]), below the lesion on the radial carpal bone, 0-3mm and 9-12mm deep to the cartilage. Different letters denote statistically different groups at a level of $P<0.05$.*

With the loss of bone volume and increase in bone surface in treated limbs in the region 0-3mm deep to the cartilage the bone structure became more trabecular in nature. In the treated limbs of the trial animals the trabecular number and separation were increased and the trabecular thickness decreased compared to both their contralateral controls and the untrained control group (Table 4.4, Figure 4.12).

In all deeper ROIs (3-6, 6-9 and 9-12mm deep to the cartilage) the trabecular number of both the treated and control limbs of the trial horses was greater than that of the untrained controls (Table 4.4).

In keeping with the increase in bone volume and decrease in bone surface, the trabecular thickness was greater and the trabecular separation less in treated limbs compared to the untrained controls at 9-12mm deep to the level of the cartilage (Table 4.4, Figure 4.12).

Depth below cartilage	Parameter	Mean (Median), Range			P-value		
		Trial treated	Trial Control	Untrained control	Trial treated v Trial control	Trial treated v Untrained control	Trial control v Untrained control
0-3mm	Tb.N (mm^{-1})	3.90 (3.98), 0.590	3.27 (3.17), 0.919	3.13 (3.09), 0.722	**0.006**	**0.001**	0.49
	Tb.Th (mm)	0.219 (0.208), 0.137	0.442 (0.423), 0.215	0.511 (0.557), 0.353	**0.002**	**0.002**	0.31
	Tb.Sp (mm)	0.195 (0.196), 0.074	0.151 (0.147), 0.072	0.130 (0.130), 0.117	**0.03**	**0.01**	0.34
3-6mm	Tb.N (mm^{-1})	3.30 (3.13), 0.766	3.18 (3.18), 0.569	2.93 (2.89), 0.302	0.34	**0.04**	**0.03**
	Tb.Th (mm)	0.239 (0.235), 0.058	0.284 (0.272), 0.157	0.333 (0.330), 0.193	0.13	**0.04**	0.26
	Tb.Sp (mm)	0.222 (0.223), 0.085	0.232 (0.244), 0.079	0.222 (0.205), 0.064	0.42	0.99	0.61
6-9mm	Tb.N (mm^{-1})	3.03 (2.91), 0.639	3.02 (2.99), 0.989	2.53 (2.54), 0.295	0.99	**0.004**	**0.01**
	Tb.Th (mm)	0.253 (0.249), 0.088	0.238 (0.225), 0.090	0.257 (0.264), 0.070	0.45	0.79	0.30
	Tb.Sp (mm)	0.257(0.269), 0.069	0.294 (0.308), 0.122	0.326 (0.338), 0.067	0.06	**0.003**	0.19
9-12mm	Tb.N (mm^{-1})	3.03 (2.96), 0.972	2.95 (2.99), 1.37	2.37 (2.33), 0.259	0.40	**0.008**	**0.03**
	Tb.Th (mm)	0.269 (0.267), 0.075	0.248 (0.234), 0.135	0.228 (0.232), 0.079	0.32	**0.03**	0.44
	Tb.Sp (mm)	0.264 (0.260), 0.124	0.305 (0.307), 0.228	0.395 (0.390), 0.089	0.07	**0.001**	**0.04**

Table 4.4 *Trabecular parameters from MicroCT images, Cr, region below the defect. Tb.N = trabecular number (mm^{-1}), Tb.Th = trabecular thickness (mm), Tb.Sp = trabecular separation (mm).*

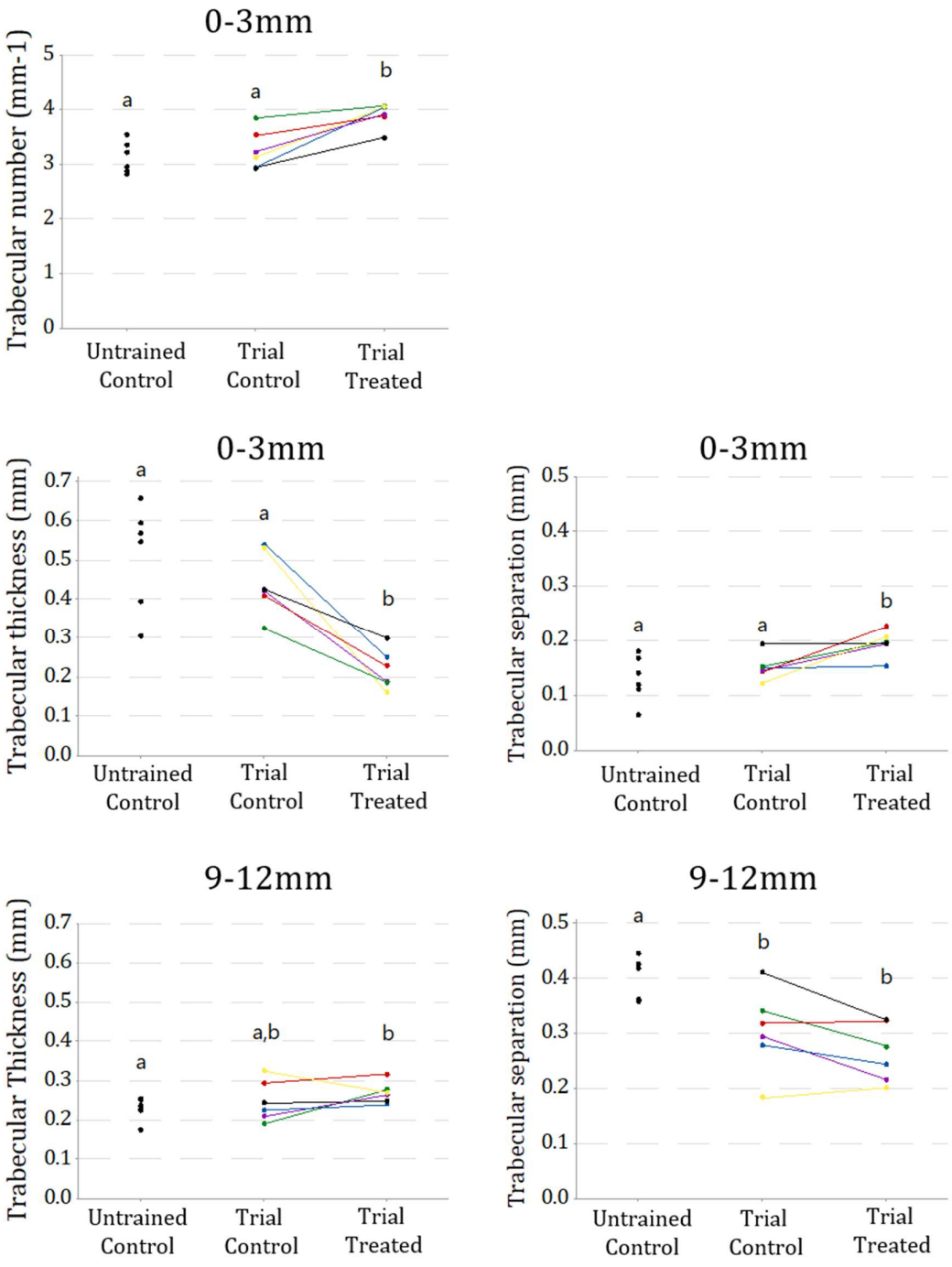

Figure 4.12 *Trabecular parameters from MicroCT images, Cr, region below the defect, 0-3 and 9-12mm deep to the cartilage. Different letters denote statistically different groups at a level of $P<0.05$.*

There was a marked decrease in tissue mineral density (TMD) at a depth of 0-3mm deep to the cartilage in treated limbs when compared with both the contralateral and untrained controls (Table 4.5). This appeared to be a function of both the decrease in BV/TV and a decrease in bone material density (BMD) (Figure 4.13).

At 9-12mm deep to the cartilage the TMD was greater in both treated and control limbs of the trial animals compared to the untrained controls (Figure 4.13). This appeared to be a result of the greater bone volume in these groups as there was no significant increase in BMD (Table 4.5).

Depth below cartilage	Parameter	Mean (Median), Range			P-value		
		Trial treated	Trial Control	Untrained control	Trial treated v Trial control	Trial treated v Untrained control	Untrained control v Trial control
0-3mm	BMD (mgHA/cm^3)	743 (736), 80.0	781 (783), 63.1	779 (783), 68.1	**0.006**	**0.05**	0.91
	TMD (mgHA/cm^3)	593 (573), 169	738 (734), 88.2	744 (748), 115	**0.003**	**0.001**	0.80
3-6mm	BMD (mgHA/cm^3)	725 (726), 62.8	729 (725), 64.8	743 (738), 53.1	0.60	0.20	0.29
	TMD (mgHA/cm^3)	590 (595), 72.1	613 (598), 138	642 (652), 135	0.26	0.07	0.36
6-9mm	BMD (mgHA/cm^3)	710 (707), 44.7	701 (693), 62.1	710 (705), 46.3	0.14	0.97	0.51
	TMD (mgHA/cm^3)	567 (564), 75.6	542 (529), 138	535 (530), 91.1	0.15	0.10	0.78
9-12mm	BMD (mgHA/cm^3)	706 (702), 54.3	699 (689), 69.1	692 (688), 68.0	0.25	0.36	0.67
	TMD (mgHA/cm^3)	576 (573), 80.0	544 (524), 162	477 (481), 98.8	0.12	**0.001**	**0.05**

Table 4.5 *Mineralisation parameters from microCT, Cr, region below the lesion**.** BMD = bone material density (mg hydroxyapatite/cm^3), TMD = tissue mineral density (mg hydroxyapatite/cm^3).*

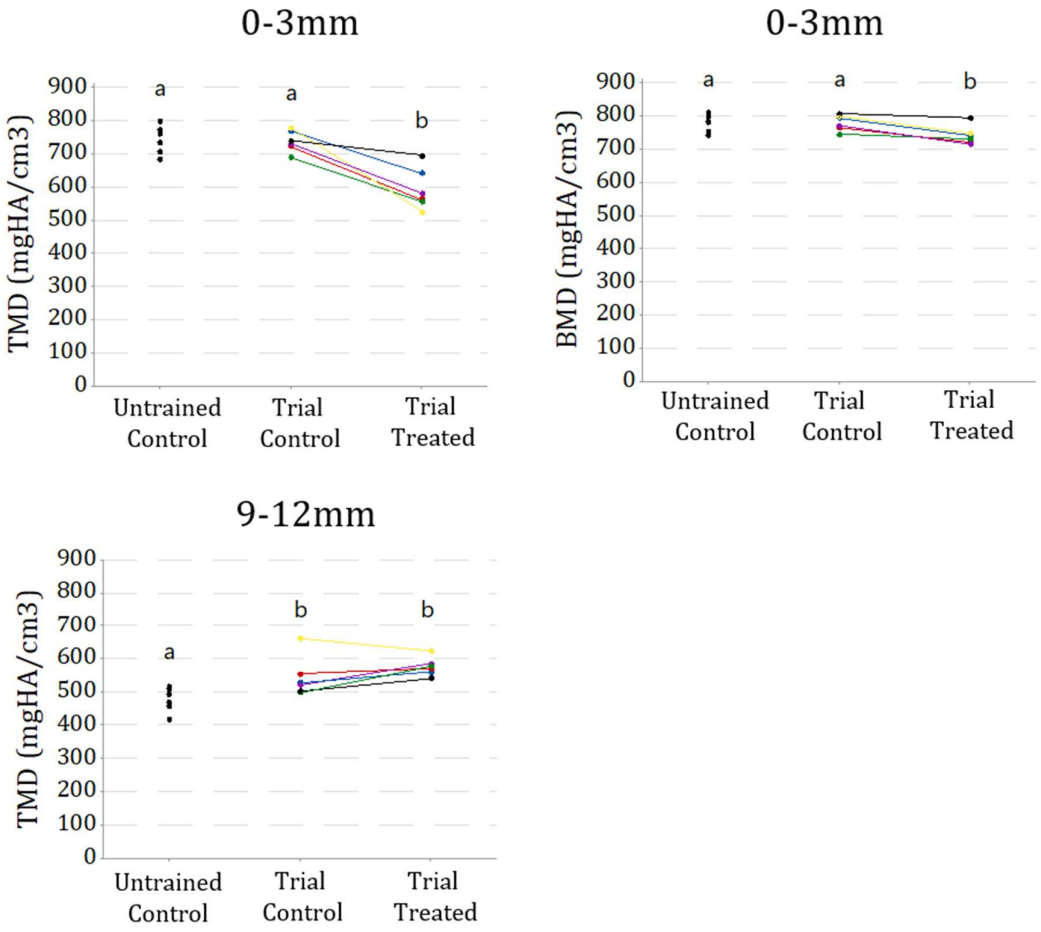

Figure 4.13 *Tissue mineral density (TMD, mgHA/cm3) and bone material density (BMD, mgHA/cm3) measured on microCT images, Cr, region below the lesion, 0-3mm and 9-12mm deep to the cartilage. Different letters denote statistically different groups at a level of $P<0.05$.*

The changes in bone volume and structure were associated with evidence of marked, ongoing remodelling on BSEM images at 0-3mm below the cartilage: in the treated limbs there was a 2.8-fold and 2.1-fold increase in total active perimeter when compared with the contralateral and the untrained controls respectively which was due to a marked increase in both erosion and mineralising perimeter (Figures 4.14, Table 4.6).

In the deeper regions 3-6, 6-9 and 9-12mm deep to the cartilage there was an increase in mineralising perimeter without a concurrent increase in erosion perimeter (Table 4.6, Figures 4.14 -4.16).

At 3-6mm below the cartilage, there was no significant overall change in erosion perimeter, although it was increased to varying degrees in 5 out of the 6 horses (Figure 4.14).

There was no significant change in the ratio of erosion to mineralising perimeter at any depth, however at 6-9mm deep to the cartilage E.Pm:Min.Pm was lower in treated limbs than in their contralateral controls in 5 out of the 6 trial animals (P=0.09, Figure 4.16, Table 4.6).

Depth below cartilage	Parameter	Mean (Median), Range			P-value		
		Trial treated	Trial Control	Untrained control	Trial treated v Trial control	Trial treated v Untrained control	Untrained control v Trial control
0-3mm	Er.Pm (mm^{-1})	2.49 (2.08), 3.22	0.801 (0.835), 1.35	0.991(0.886), 1.77	**0.03**	**0.03**	0.61
	Min.Pm (mm^{-1})	3.40 (3.53), 2.06	0.726 (0.745), 0.810	0.928 (1.01), 1.41	**0.001**	**0.001**	0.42
	Act.Pm (mm^{-1})	5.88 (5.92), 2.77	1.53, (1.53), 1.87	1.92 (1.94), 2.66	**<0.001**	**<0.001**	0.40
	Er:Min ratio	0.838(0.631), 1.68	1.16(1.14), 1.65	2.13 (0.760), 9.26	0.44	0.43	0.56
3-6mm	Er.Pm (mm^{-1})	0.961 (0.890), 0.834	0.588 (0.567), 0.568	0.566 (0.311), 1.37	0.134	0.16	0.93
	Min.Pm (mm^{-1})	2.61 (2.50), 1.45	0.734 (0.808), 0.519	0.933 (0.658), 1.82	**<0.001**	**0.001**	0.54
	Act.Pm (mm^{-1})	3.57 (3.59), 1.65	1.32 (1.29), 0.369	1.50 (1.42), 2.32	**<0.001**	**0.001**	0.65
	Er:Min ratio	0.386 (0.323), 0.424	0.963 (0.664), 1.95	1.11 (0.438), 2.86	0.16	0.22	0.81
6-9mm	Er.Pm (mm^{-1})	0.608 (0.517), 1.25	0.534 (0.478), 0.752	0.298 (0.218), 0.716	0.77	0.19	0.19
	Min.Pm (mm^{-1})	2.52 (2.59), 0.734	0.722 (0.737), 0.814	1.20 (0.884), 1.86	**<0.001**	**0.02**	0.25
	Act.Pm (mm^{-1})	3.12 (3.07), 1.71	1.26 (1.20), 0.987	1.50 (1.34), 1.68	**<0.001**	**0.003**	0.49
	Er:Min ratio	0.237 (0.212), 0.456	0.908 (0.814), 1.83	0.507 (0.282), 1.82	0.09	0.39	0.34
9-12mm	Er.Pm (mm^{-1})	0.791(0.616), 1.86	0.584 (0.446),1.18	0.517(0.531), 0.872	0.63	0.41	0.77
	Min.Pm (mm^{-1})	1.89 (1.69),1.66	0.811(0.842), 0.823	1.55 (1.57), 1.62	**0.008**	0.39	0.05
	Act.Pm (mm^{-1})	2.68 (2.42), 1.97	1.40 (1.27), 1.87	2.07(2.29), 2.11	**0.02**	0.20	0.13
	Er:Min ratio	0.479(0.440), 1.03	0.833(0.531), 2.05	0.367(0.278), 0.739	0.42	0.58	0.21

Table 4.6 *Erosion and formation parameters from BSEM images, Cr, region deep to the defect. Er.Pm = Erosion perimeter/ Bone area (mm^{-1}), Min. Pm = Mineralising perimeter/ Bone area (mm^{-1}), Act.Pm = Active perimeter/ Bone area (mm^{-1}), Er:Min ratio = Erosion perimeter/ Mineralising perimeter.*

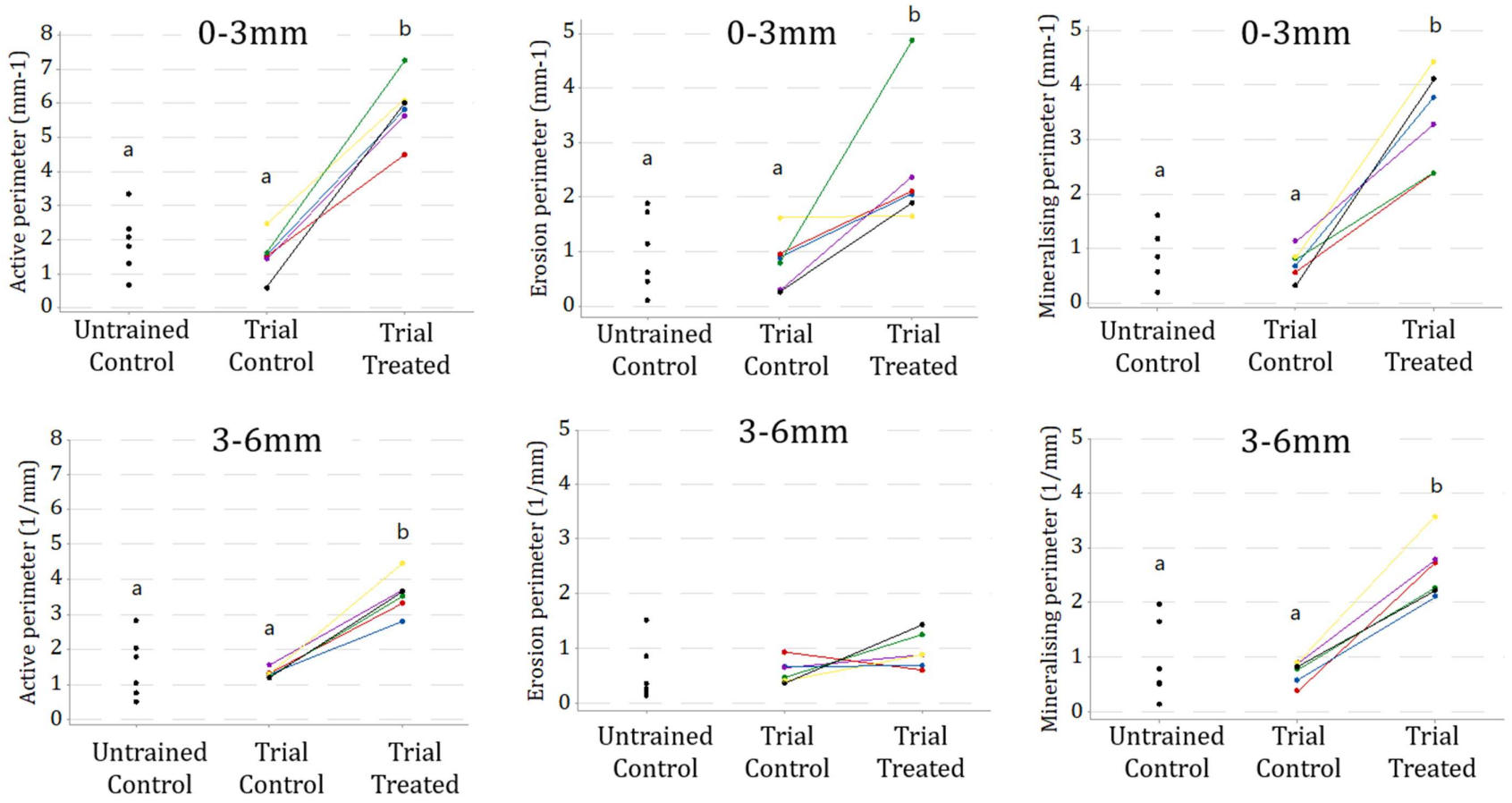

Figure 4.14 *Erosion and formation parameters from BSEM images, Cr, region deep to the defect, 0-3mm and 3-6mm deep to the cartilage. Different letters denote statistically different groups at a level of P<0.05.*

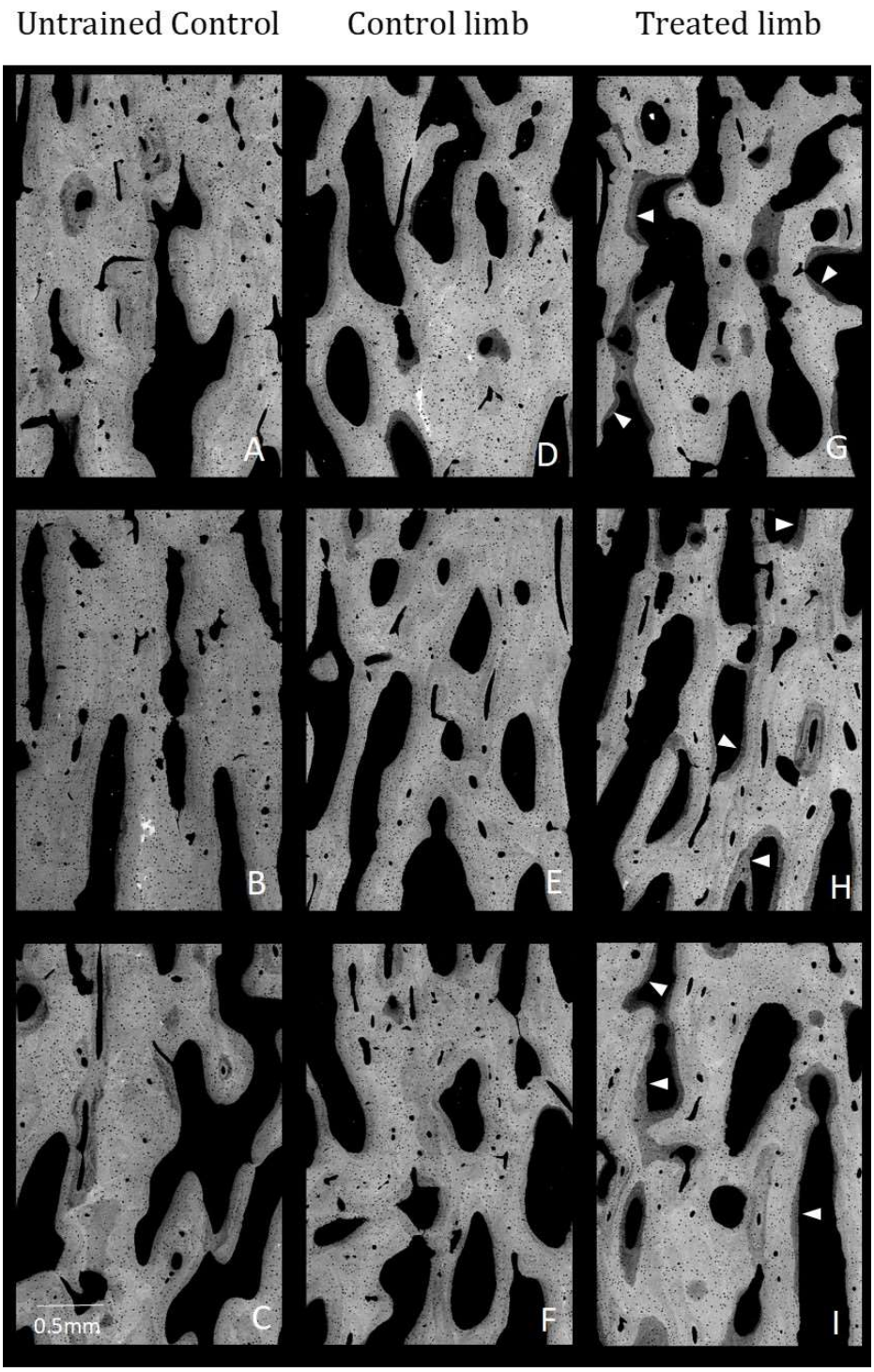

Figure 4.15 *BSEM images showing increased mineralising surface (arrowheads) in the treated limbs: Cr, region below the defect, 3-6mm deep to the cartilage. A= untrained control horse 3, B= untrained control horse 5, C= untrained control horse 6, D and G = Horse 3 control and treated respectively, E and H= Horse 5 control and treated respectively, F and I = Horse 6 control and treated respectively.*

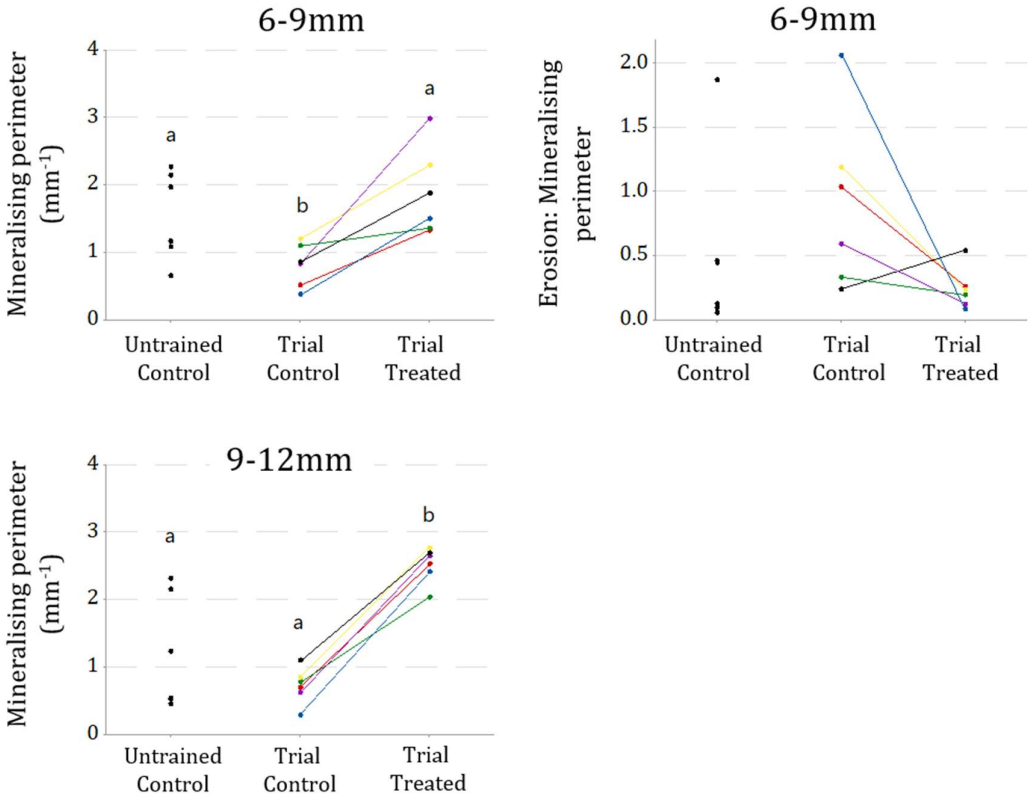

Figure 4.16 *Mineralising perimeter (mm-1) and ratio of erosion to mineralising perimeter, measured on BSEM images, Cr, region below the lesion, 6-9mm and 9-12mm deep to the cartilage. Different letters denote statistically different groups at a level of P<0.05.*

Consistent with the increase in erosion perimeter on BSEM images at 0-3mm deep to the lesion there was also an increase in the number of osteoclasts at 0-3.3mm deep to the lesion when the treated limbs were compared to their contralateral controls (Figures 4.17 and 4.18, Table 4.7). An increase in osteoclast numbers was apparent also at 3.3-6.6mm deep to the cartilage although less marked than in the more superficial region (Figures 4.17 and 4.18, Table 4.7). The specimen of Cr from the treated limb of horse 3 did not include all the deeper region so this was excluded from osteoclast counts at 3.3-6.6mm deep to the cartilage.

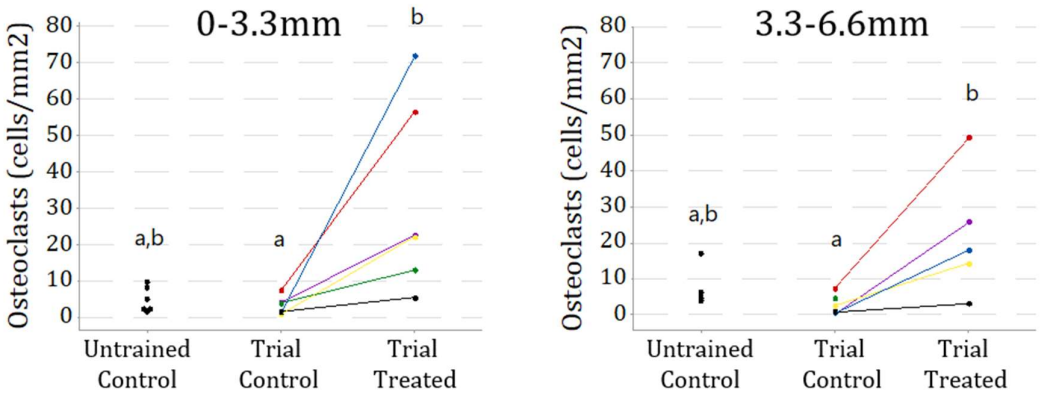

Figure 4.17 *Number of osteoclasts (cells/mm2) on TRAP stained sections, Cr, region below the lesion, 0-3.3mm and 3.3-6.6mm deep to the cartilage. Different letters denote statistically different groups at a level of P<0.05.*

Depth below cartilage (For O'clast N)	Parameter	Mean (Median), Range			P-value		
		Trial treated	Trial Control	Untrained control	Trial treated v Trial control	Trial treated v Untrained control	Untrained control v Trial control
0-3mm (0-3.3)	Osteoclast N (cells/mm^2)	31.9 (22.3), 66.5	3.35 (2.88), 6.67	4.97 (3.79), 8.08	**0.04**	**0.06**	0.37
	O.Pm/B.Pm (%)	51.2 (49.7), 28.0	20.2 (17.9), 16.6	20.0 (20.79), 16.1	**0.001**	**<0.001**	0.96
	O.Wi (um)	9.52 (9.82), 5.13	7.61 (6.77), 8.00	4.43 (4.57), 2.53	0.37	**0.001**	**0.05**
	O.Ar/B.Ar (%)	5.43 (4.14), 8.88	0.938 (0.950), 1.05	0.590 (0.538), 0.498	**0.04**	**0.005**	0.08
3-6mm (3.3-6.6)	Osteoclast N (cells/mm^2)	22.1 (18.0), 46.2	2.81 (1.770), 6.67	6.92 (5.10), 13.2	**0.04**	0.13	0.12
	O.Pm/B.Pm (%)	47.1 (52.9), 40.5	13.2 (13.2), 15.4	5.55 (4.77), 7.38	**0.002**	**0.001**	**0.03**
	O.Wi (um)	10.6 (10.3), 7.69	8.04 (8.35), 8.45	3.29 (3.23), 0.462	0.21	**0.002**	**0.02**
	O.Ar/B.Ar (%)	3.89 (3.48), 6.23	0.842 (0.72), 1.61	0.126 (0.116), 0.205	**0.03**	**0.01**	**0.04**
6-9mm	O.Pm/B.Pm (%)	41.3 (46.0), 50.5	14.2 (10.8), 19.0	9.04 (8.47), 16.0	**0.009**	**0.02**	0.23
	O.Wi (um)	9.56 (9.96), 9.10	8.36 (8.17), 10.4	4.57 (3.67), 6.10	0.55	**0.02**	0.06
	O.Ar/B.Ar (%)	2.67 (2.87), 4.39	1.08 (1.09), 1.87	0.319 (0.212), 0.822	**0.02**	**0.02**	0.09
9-12mm	O.Pm/B.Pm (%)	36.8 (33.0), 50.6	14.3 (12.9), 19.3	9.34 (7.87), 24.6	**0.03**	**0.02**	0.32
	O.Wi (um)	7.60 (6.61), 10.1	9.07 (7.66), 10.1	3.41 (3.30), 2.94	0.33	**0.05**	**0.03**
	O.Ar/B.Ar (%)	2.03 (1.51), 3.86	1.05 (0.799), 2.13	0.330 (0.223), 1.08	0.09	0.07	0.10

Table 4.7 *Cellular markers of remodelling, Cr, region deep to the defect. Osteoclast numbers (cells/mm^2) from cryosections stained for TRAP, O.Wi = osteoid width (um) and O.Pm = Osteoid perimeter/Bone perimeter (%), O.Ar/B.Ar = Osteoid area/ Bone area (%) from Masson's Goldner stained sections.*

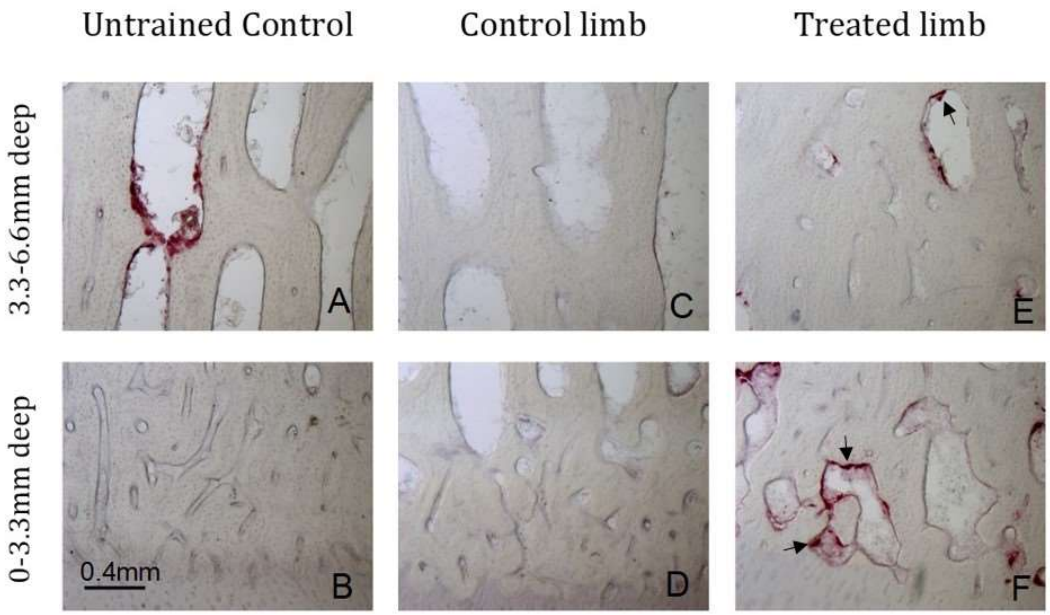

Figure 4.18 *Cryosections stained for TRAP showing increased osteoclasts (arrows) in the treated limbs: Cr, region deep to the lesion. Untrained control horse 4, 0-3.3mm and 3.3-6.6mm deep to the cartilage (B and A respectively); Horse 2 control limb 0-3.3mm and 3.3-6.6mm deep to the cartilage (D and C respectively) and treated limb 0-3.3mm and 3.3-6.6mm deep to the cartilage (F and E respectively) Light microscopy.*

The increase in formation activity deep to the lesion indicated by the increase in mineralising perimeter on BSEM images was further supported by a marked increase in the amount of osteoid (Table 4.7, Figures 4.19-4.22). There was a markedly greater osteoid area as a result of an increased osteoid perimeter in treated limbs when compared to both the contralateral controls and the untrained controls at 0-3, 3-6 and 6-9mm below the cartilage (Figures 4.19-4.22, Table 4.7). At 9-12mm deep to the cartilage there was a greater osteoid perimeter in treated limbs than in either the contralateral controls or the untrained control group (Figure 4.21), however this had not translated to a significant increase in osteoid area at this depth (Table 4.7).

There was no difference between the two limbs of the trial animals when osteoid width was considered, however osteoid width was greater in both limbs of the trial animals when compared with the untrained controls in all ROIs deep to the defect (Figures 4.19-4.22, Table 4.7).

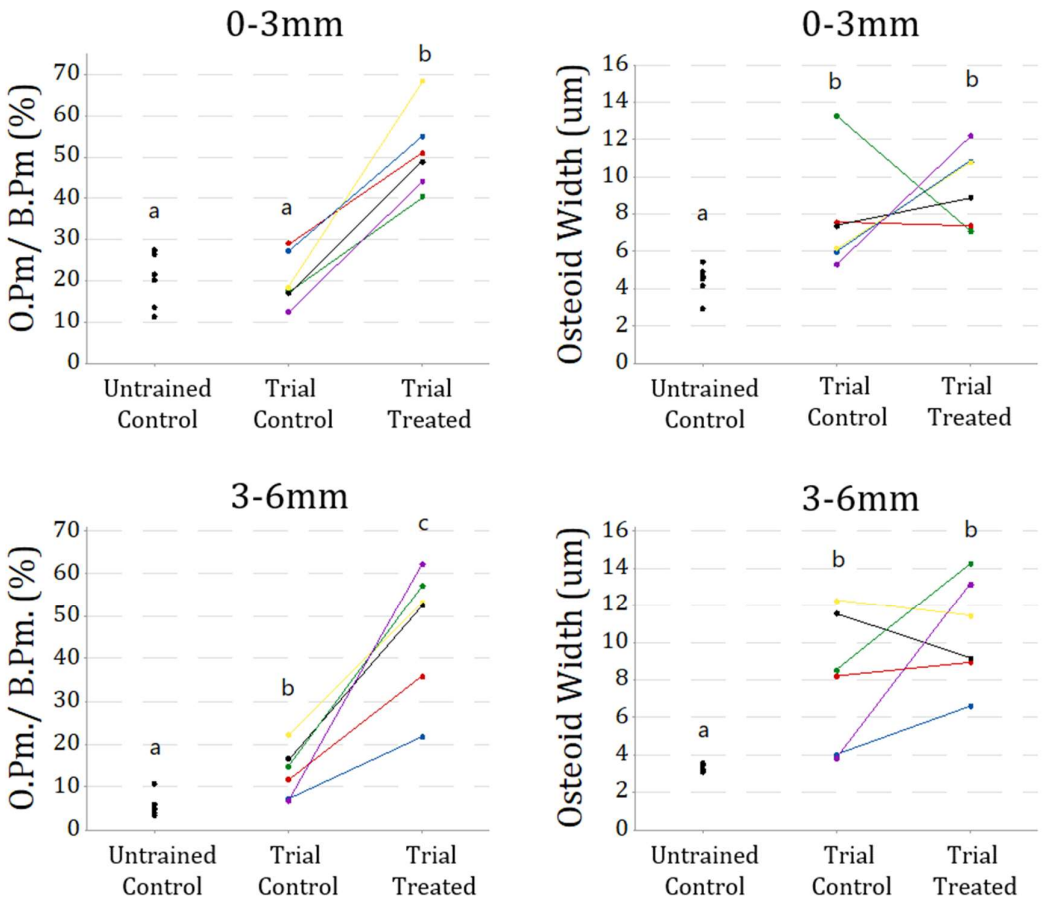

Figure 4.19 *Osteoid perimeter as a percentage of bone perimeter and osteoid width (um) Cr, region below the lesion, 0-3mm and 3-6mm deep to the cartilage. Different letters denote statistically different groups at a level of P<0.05.*

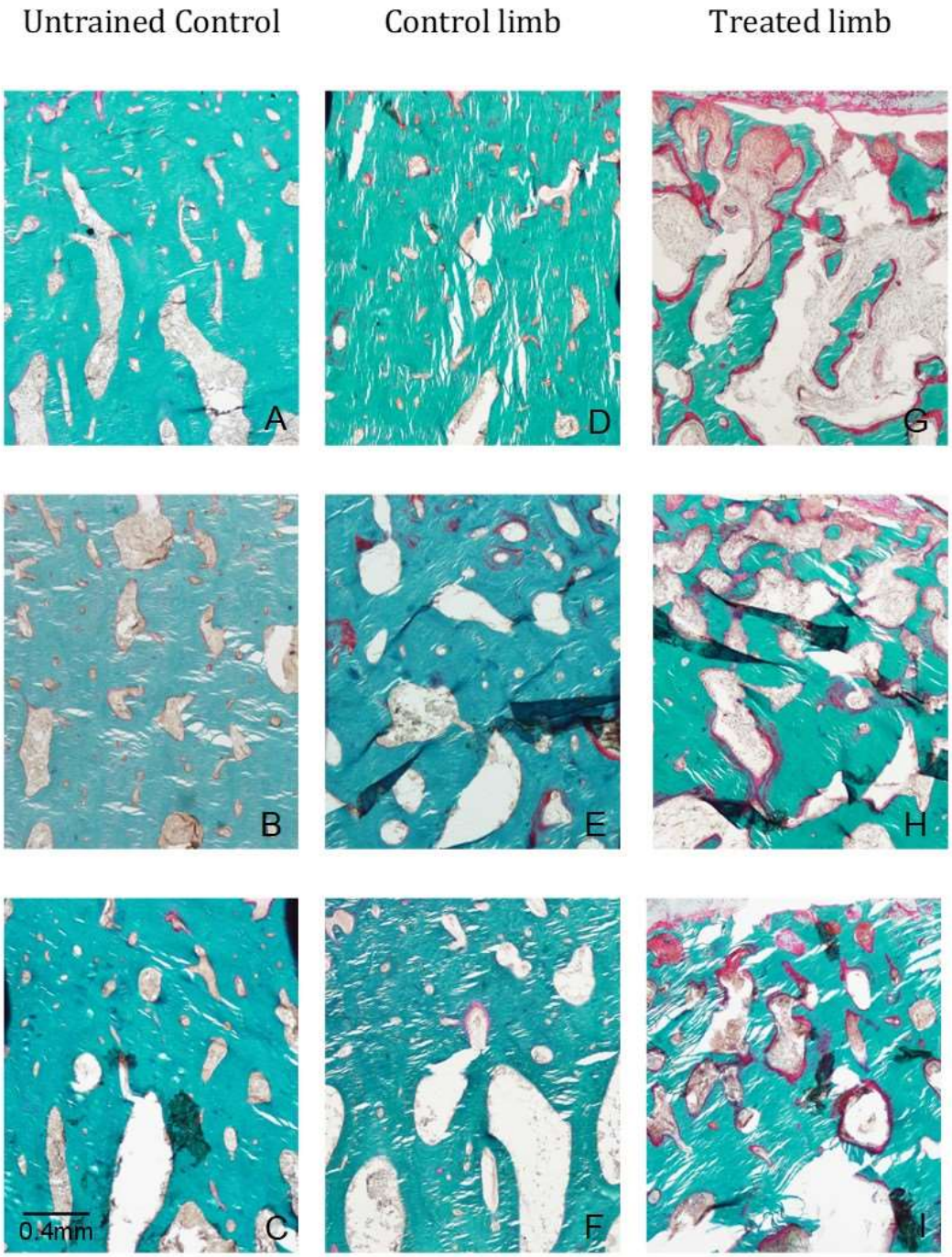

Figure 4.20 *Masson's Goldner stained sections showing increased osteoid (stained pink) in treated limbs, Cr, region below the lesion, 0-3mm deep to articular surface. Untrained control horse 1 (A), untrained control Horse 2 (B), untrained control Horse 4 (C), Horse 2 control (D) and treated (G) limbs, Horse 3 control (E) and treated (H) limbs and Horse 4 control (F) and treated (I) limbs. Light microscopy.*

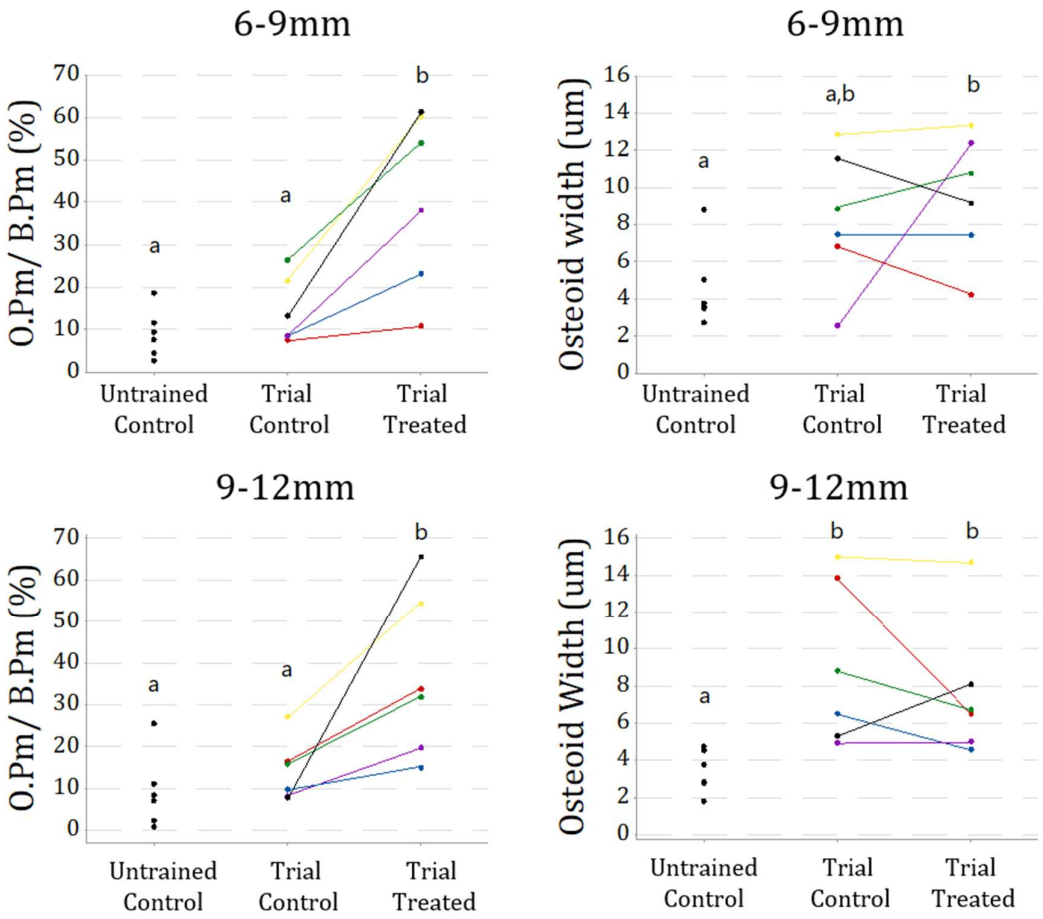

Figure 4.21 *Osteoid perimeter as a percentage of bone perimeter and osteoid width (µm), Cr, region below the lesion, 6-9mm and 9-12mm deep to the cartilage. Different letters denote statistically different groups at a level of P<0.05.*

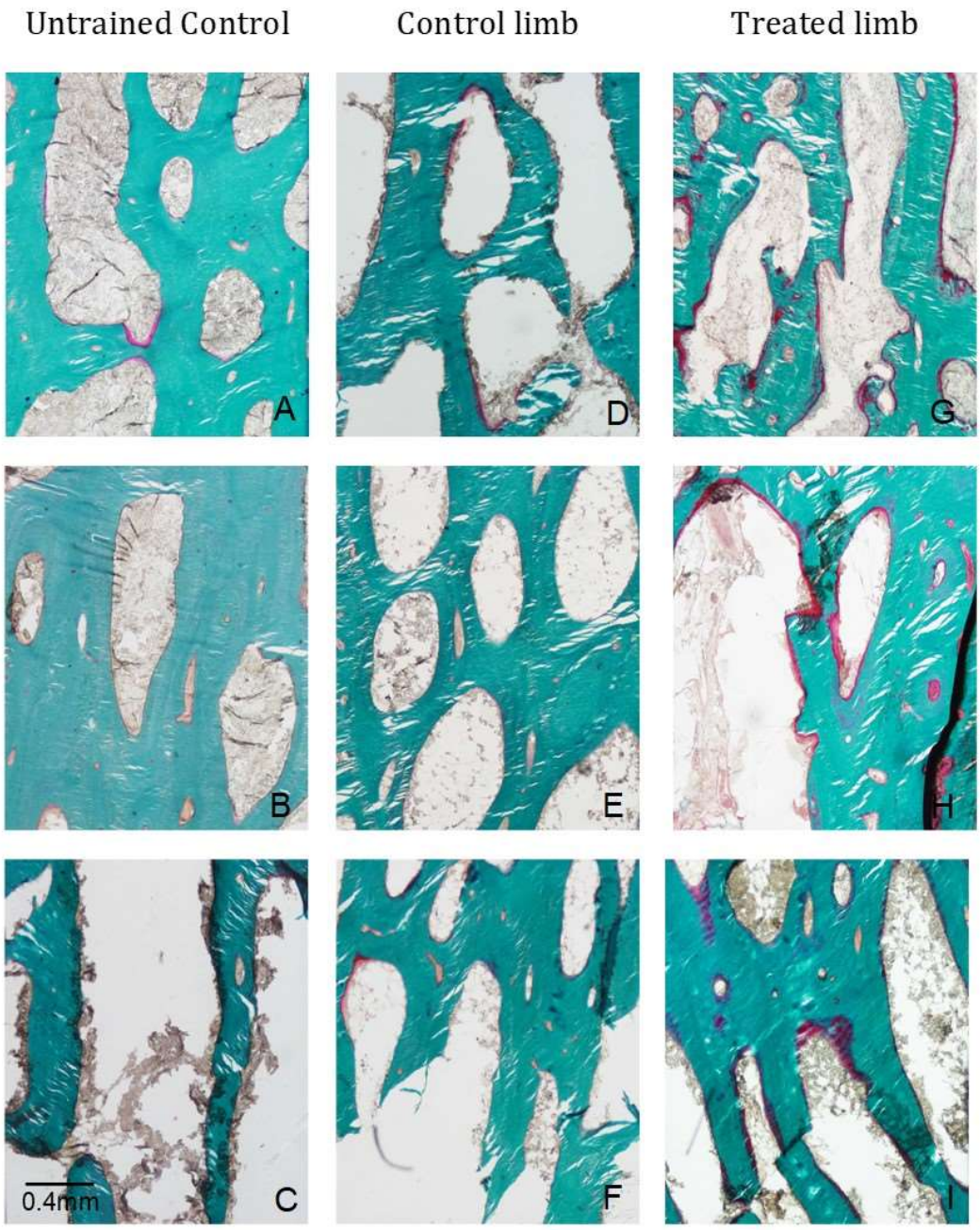

Figure 4.22 *Masson's Goldner stained sections showing increased osteoid (stained pink) in treated limbs, Cr, region below the lesion, 6-9mm deep to articular surface. untrained control Horse 1 (A), untrained control Horse 2 (B), untrained control Horse 4 (C), Horse 1 control (D) and treated (G) limbs, Horse 4 control (E) and treated (H) limbs and Horse 6 control (F) and treated (I) limbs. Light microscopy.*

An increase in oxytetracycline labelled perimeter gave further evidence for increased mineralisation in the region below the lesion in treated limbs (Figures 4.23-4.26). The degree of change varied with depth below the cartilage with bone at 0-3mm deep to the level of the cartilage having a more moderate increase in labelled perimeter than the 3 deeper ROIs (Figures 4.23-4.26, Table 4.8).

The increase in labelled perimeter was predominantly a result of an increase in single labelled perimeter. Double labels were observed commonly although there was no significant difference in double-labelled perimeter between the two groups at any depth below the cartilage (Figures 4.23 and 4.25, Table 4.8). While there were triple labels observed in some specimens they were too few to draw meaningful conclusions. There was no instance where all four labels were present at any one site.

The 0-3mm region was the only region in which there was a measurable increase in BFR in treated limbs (Figure 4.23, Table 4.8). There was no measurable difference in MAR between the two groups in any ROI (data not shown).

Depth below cartilage	Parameter	Mean (Median), Range		P-value
		Trial treated	Trial Control	Trial treated v Trial control
0-3mm	L.Pm/B.Pm (%)	14.8 (13.0), 16.6	8.72 (10.2), 14.1	**0.03**
	sL.Pm/B.Pm (%)	21.2 (18.6), 23.2	11.0 (12.3), 17.6	0.06
	dL.Pm/B.Pm (%)	4.19 (4.06), 8.73	3.22 (2.46), 8.45	0.31
	BFR/B.Ar (%/d)	0.094 (0.081), 0.131	0.054 (0.052), 0.089	**0.03**
3-6mm	L.Pm/B.Pm (%)	19.9 (11.0), 47.9	3.89 (2.36), 11.4	0.06
	sL.Pm/B.Pm (%)	24.2 (17.8), 41.9	5.32 (4.20), 10.9	**0.05**
	dL.Pm/B.Pm (%)	7.75 (4.65), 30.6	1.23 (0.250), 6.36	0.21
	BFR/B.Ar (%/d)	0.113 (0.068), 0.200	0.038 (0.011), 0.093	0.81
6-9mm	L.Pm/B.Pm (%)	24.7 (20.5), 35.8	5.08 (2.21), 17.4	**0.03**
	sL.Pm/B.Pm (%)	34.8 (23.2), 61.9	7.74 (4.41), 21.4	0.07
	dL.Pm/B.Pm (%)	7.33 (7.09), 15.1	1.21 (0.00), 7.00	0.08
	BFR/B.Ar (%/d)	0.146 (0.135), 0.213	0.041 (0.041), 0.070	0.13
9-12mm	L.Pm/B.Pm (%)	19.0 (20.1), 43.1	4.04 (2.25), 8.91	**0.04**
	sL.Pm/B.Pm (%)	27.9 (25.3), 61.1	6.63 (4.30), 16.8	**0.05**
	dL.Pm/B.Pm (%)	5.11 (2.61), 12.9	0.724 (0.659), 1.51	0.12
	BFR/B.Ar (%/d)	0.172 (0.134), 0.203	0.037 (0.027), 0.070	0.20

Table 4.8 *Measures of fluorochrome labels, Cr, region deep to the defect, from undecalcified, unstained sections. L.Pm/B.Pm = labelled perimeter/ bone perimeter (%), sL.Pm/B.Pm = single labelled perimeter/ bone perimeter (%), dL.Pm/B.Pm = double labelled perimeter/ bone perimeter (%) and BFR/B.Ar = bone formation rate/bone area (%/day).*

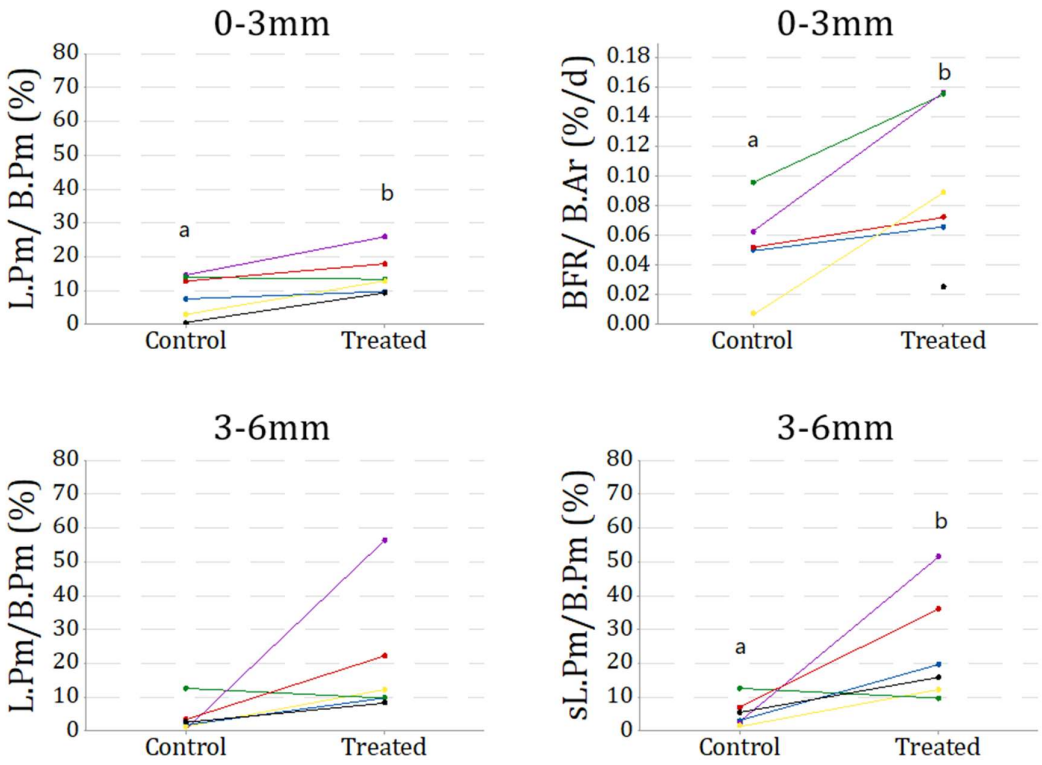

Figure 4.23 *Measures of oxytetracycline labels, Cr, region below the lesion, 0-3mm and 3-6mm deep to the cartilage. L.Pm/B.Pm = Labelled perimeter as a percentage of bone perimeter (%), BFR/B.Ar = Bone formation rate as a function of bone area (%/d), sL.Pm/B.Pm = single-labelled perimeter as a percentage of bone perimeter (%). The control limb from Horse 1 had no double labels so BFR could not be calculated for this specimen. Different letters denote statistically different groups at a level of P<0.05.*

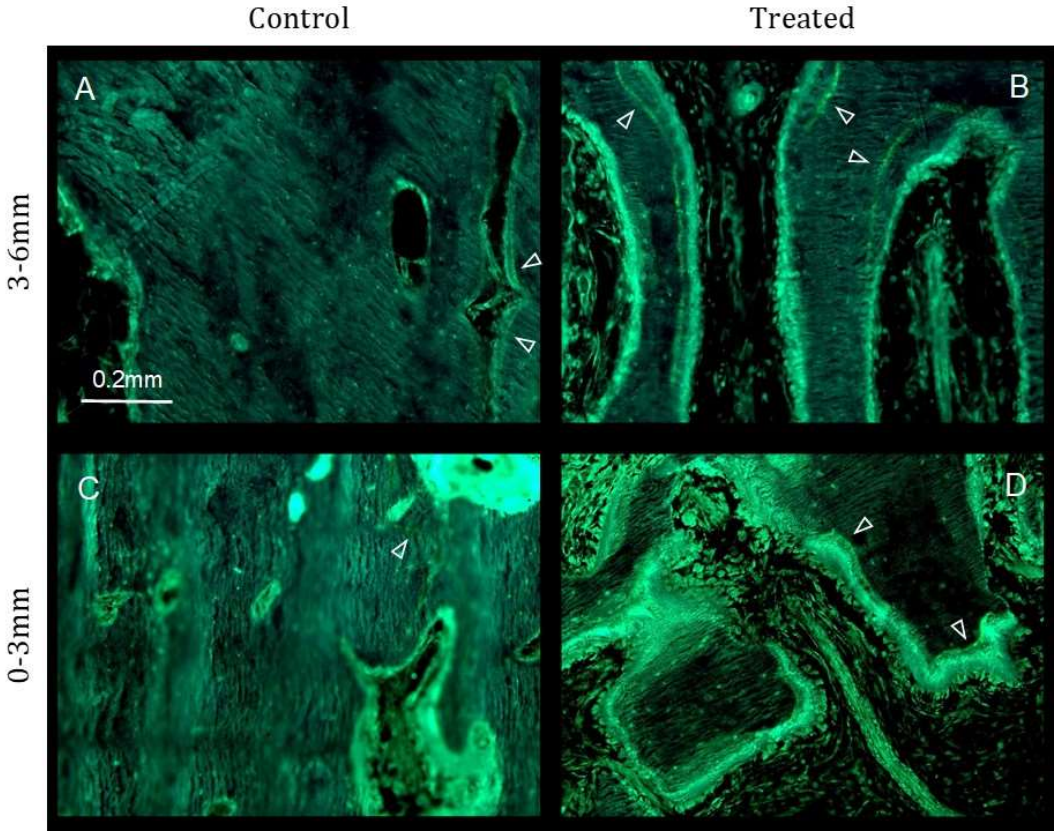

Fig 4.24 *Fluorescent light microscopy images of undecalcified, unstained sections showing an increase in labelled perimeter (arrowheads) at 0-3mm deep to the cartilage and an increase in single labelled perimeter in treated limbs at 3-6mm deep to the cartilage: Cr, region deep to the lesion. Control and treated limbs respectively of Horse 2, 0-3mm deep to articular cartilage (C and D), and Horse 5, 3-6mm deep to articular cartilage (A and B).*

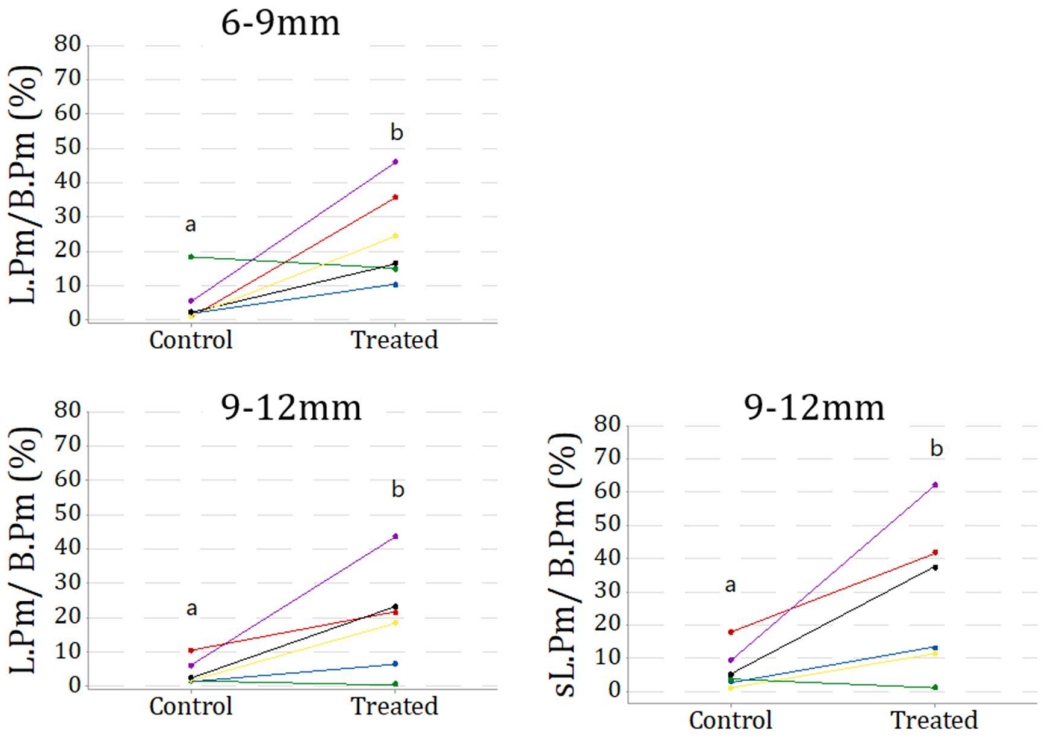

Figure 4.25 *Measures of oxytetracycline labels, Cr, region below the lesion, 6-9mm and 9-12mm deep to the cartilage. L.Pm/B.Pm = Labelled perimeter as a percentage of bone perimeter (%), sL.Pm/B.Pm = single-labelled perimeter as a percentage of bone perimeter (%). Different letters denote statistically different groups at a level of P<0.05.*

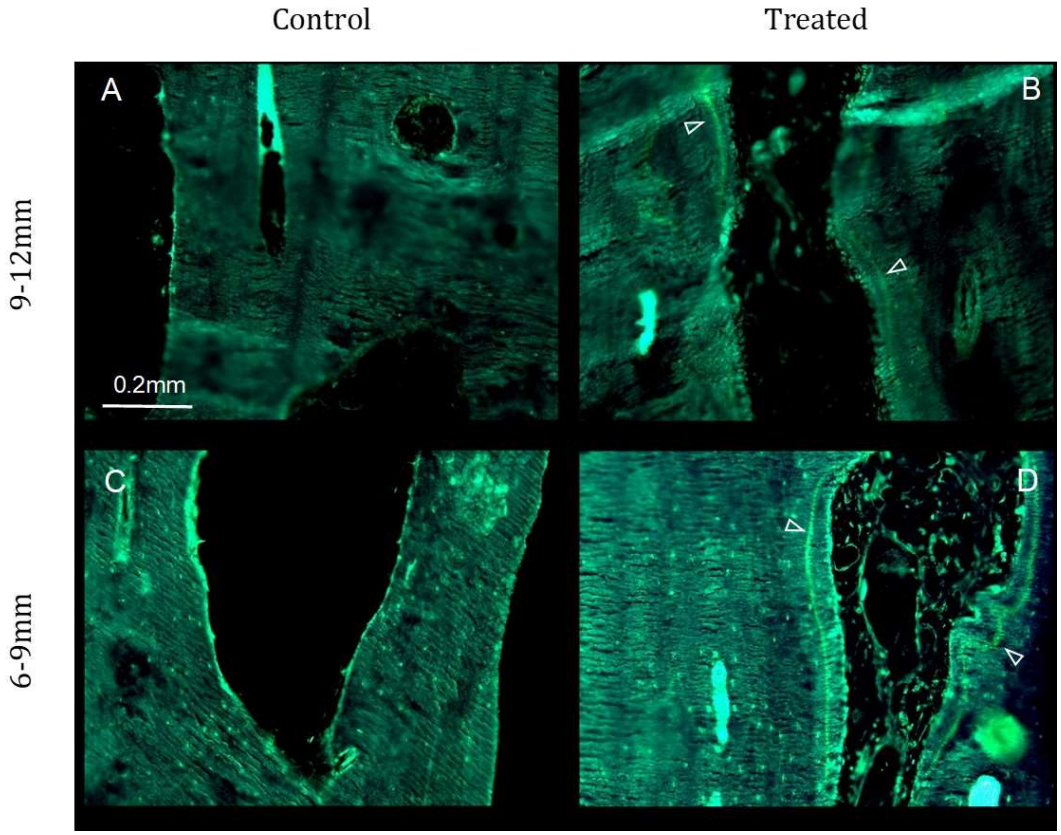

Fig 4.26 *Fluorescent light microscopy images of undecalcified, unstained, sections showing an increase in labelled perimeter (arrowheads) in treated limbs at 6-9 and 9-12mm deep to the cartilage: Cr, region deep to the lesion. Control and treated limbs respectively of Horse 5, 6-9mm deep to articular cartilage (C and D); and Horse 1, 9-12mm deep to articular cartilage (A and B).*

4.3.2 Region adjacent to the defect

In the region adjacent to the surgical defect in Cr, in SCB from below an intact joint surface, there had been no significant change in either bone volume or bone surface over the 10 weeks of the trial (Table 4.9). However, the porosity on BSEM images at 0-3mm deep to the cartilage was lower in treated limbs than in the contralateral controls in all but one of the trial horses and the difference between these two groups approached significance (P=0.07, Figure 4.27 and 4.28).

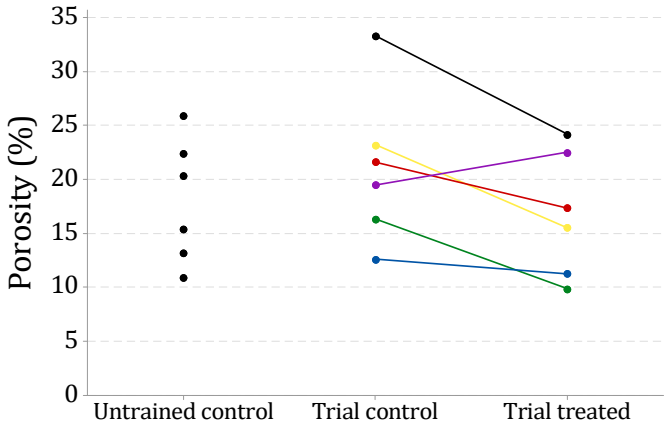

Figure 4.27 *Porosity (%) measured on BSEM images, Cr, region adjacent to the lesion, 0-3mm deep to the cartilage.*

Depth below cartilage	Parameter	Mean (Median), Range			P-value		
		Trial treated	Trial Control	Untrained control	Trial treated v Trial control	Trial treated v Untrained control	Untrained control v Trial control
0-3mm	BV/TV (%)	89.7 (92.0), 20.7	91.0 (90.2), 116	90.2 (89.1), 13.7	0.61	0.88	0.80
	BS/BV (mm^{-1})	4.04, (3.64), 4.87	3.50 (3.84), 1.96	3.81 (4.16), 3.01	0.42	0.81	0.60
	Porosity (%)	16.7 (16.4), 14.3	21.1 (20.5), 20.8	18.0 (17.9), 15.0	0.07	0.72	0.43
	Pore perim. (mm^{-1})	6.92 (6.90), 1.68	6.82 (6.78), 2.79	7.18 (6.85), 3.95	0.87	0.69	0.62
	Tb.Sp (mm)	0.129 (0.126), 0.053	0.158 (0.160), 0.087	0.139 (0.139), 0.071	**0.01**	0.55	0.29
3-6mm	BV/TV (%)	76.2 (74.7), 16.2	75.9 (73.2), 28.7	76.2 (78.6), 18.4	0.92	0.99	0.95
	BS/BV (mm^{-1})	5.87 (6.00), 2.14	5.88 (6.14), 4.49	6.03 (5.78), 3.40	0.99	0.81	0.87
	Porosity (%)	25.6(25.5), 11.7	28.3 (28.0), 26.6	24.9 (26.1), 9.79	0.55	0.81	0.44
	Pore perim. (mm^{-1})	5.65 (5.26), 2.55	5.38 (5.32), 2.11	5.19 (5.13), 1.05	0.66	0.34	0.61
	Tb.Sp (mm)	0.207 (0.215), 0.112	0.217 (0.217), 0.096	0.205 (0.195), 0.047	0.55	0.92	0.49
6-9mm	BV/TV (%)	71.3(68.7),35.7	67.4 (63.9),37.1	69.8 (71.3),23.6	0.43	0.83	0.73
	BS/BV (mm^{-1})	6.87 (7.05), 6.38	7.60 (8.12), 6.82	7.19 (6.84), 5.21	0.37	0.80	0.75
	Porosity (%)	28.9 (27.9), 19.0	28.6 (32.4), 26.3	29.5 (28.7), 11.7	0.94	0.88	0.84
	Pore perim. (mm^{-1})	5.33 (5.26), 2.13	5.47 (5.74), 1.21	5.47 (5.50), 0.772	0.80	0.73	0.99
	Tb.Sp (mm)	0.215 (0.232), 0.149	0.233 (0.234), 0.168	0.224 (0.216), 0.076	0.46	0.71	0.75
9-12mm	BV/TV (%)	74.4 (80.4), 41.3	69.3 (64.2), 39.9	66.9 (67.7), 36.5	0.27	0.43	0.79
	BS/BV (mm^{-1})	6.30 (5.13), 6.98	6.82 (6.94), 7.62	7.72 (7.56), 6.83	0.43	0.42	0.60
	Porosity (%)	25.9 (23.7), 34.4	25.1 (25.8), 23.0	28.1 (29.1), 23.5	0.83	0.74	0.60
	Pore perim. (mm^{-1})	5.66 (5.66), 1.47	5.39 (5.60), 2.01	5.85 (5.62), 1.22	0.58	0.54	0.26
	Tb.Sp (mm)	0.203 (0.195), 0.193	0.244 (0.252), 0.225	0.234 (0.230), 0.154	0.86	0.41	0.80

Table 4.9 *Measures of bone volume, bone surface and trabecular separation in the region adjacent to the defect in Cr. BV/TV = Bone volume/ Total volume (%), BS/BV = Bone surface/ Bone volume (mm^{-1}) and Tb.Sp = trabecular separation (mm) measured from microCT images. Porosity = pore area/bone area (%) and pore perim. = pore perimeter/ bone area (mm^{-1}) measured from BSEM images.*

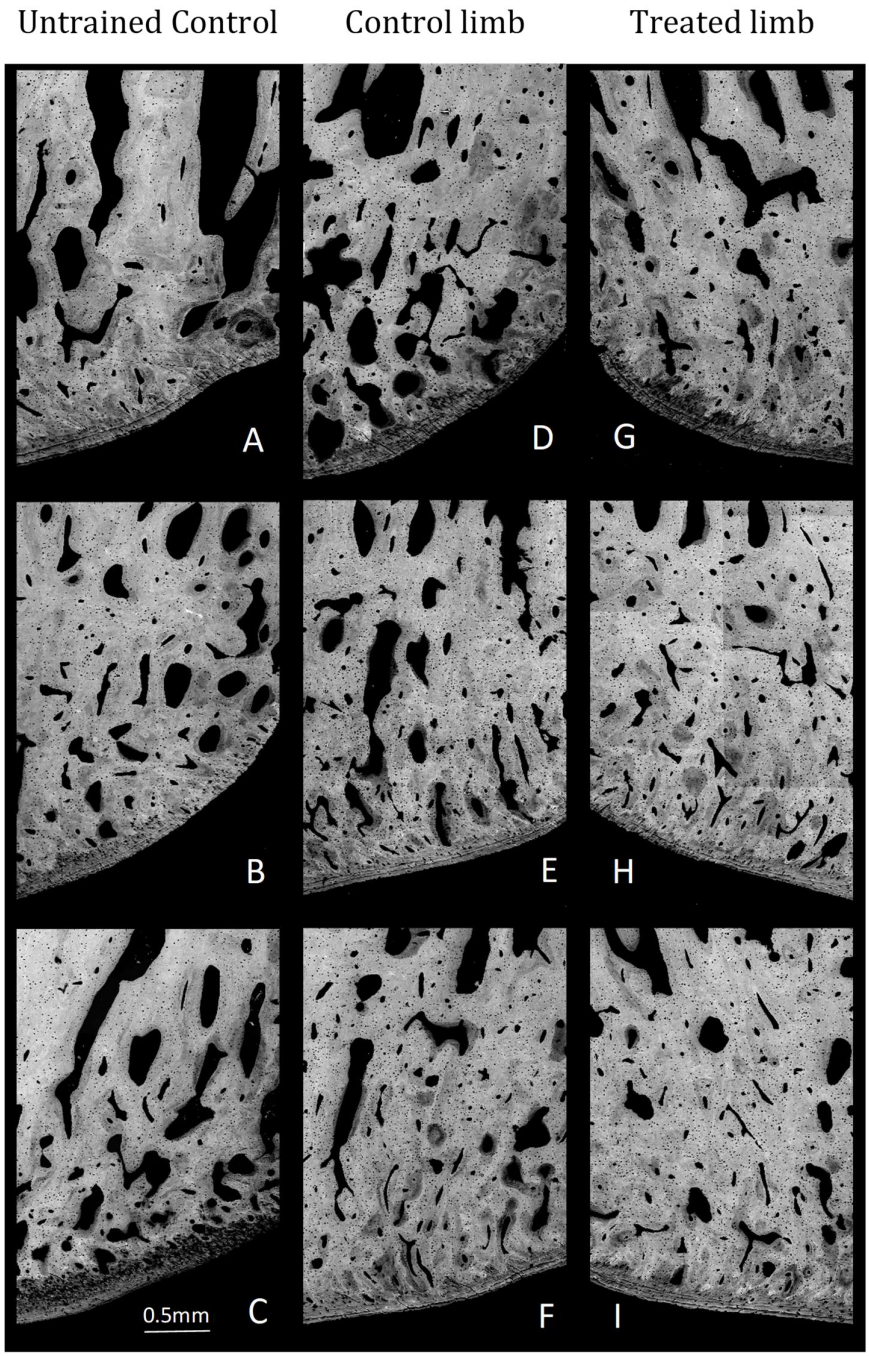

Figure 4.28 *BSEM images, Cr, region adjacent to the defect, 0-3mm deep to the cartilage, in which there is an insignificant (P=0.07) decrease in porosity in treated limbs. A= untrained control horse 2, B= untrained control horse 4, C= untrained control horse 6, D and G = Horse 2 control and treated respectively, E and H= Horse 3 control and treated respectively, F and I = Horse 6 control and treated respectively.*

Although it had not been reflected in any change in bone volume, there was some evidence of a tendency towards formation rather than resorption on BSEM images in the region adjacent to the defect (Figures 4.29 and 4.30, Table 4.10). This was suggested by a decrease in the ratio of erosion to mineralising perimeter in treated limbs when compared to the contralateral controls at 3-6mm deep to the cartilage and an increase in mineralising perimeter in treated limbs when compared to their contralateral controls at 9-12mm deep to the cartilage (Figures 4.29 and 4.30).

There was no increase in active perimeter in treated limbs at any depth below the cartilage when they were compared to their contralateral controls. However, at 3-6mm and 6-9mm deep to the cartilage the active perimeter in treated limbs was higher than in the untrained controls (Figure 4.29).

Depth below cartilage	Parameter	Mean (Median), Range			P-value		
		Trial treated	Trial Control	Untrained control	Trial treated v Trial control	Trial treated v Untrained control	Untrained control v Trial control
0-3mm	Er.Pm (mm^{-1})	1.09(0.872), 1.36	0.929(0.928),1.36	0.690(0.598), 0.899	0.71	0.18	0.37
	Min.Pm (mm^{-1})	1.66 (1.90), 2.06	1.47 (1.51), 1.84	1.62 (1.67), 2.05	0.70	0.93	0.71
	Act.Pm (mm^{-1})	2.75 (2.99), 3.12	2.40 (2.65), 2.46	2.31 (2.13), 1.75	0.65	0.43	0.85
	Er:Min ratio	0.839 (0.903) 1.15	0.706(0.600),0.892	0.720 0.399), 2.52	0.65	0.80	0.98
3-6mm	Er.Pm (mm^{-1})	1.08 (0.832), 1.80	0.842(0.977),0.970	0.617 (0.661),0.825	0.36	0.17	0.33
	Min.Pm (mm^{-1})	1.72 (1.50), 2.75	0.729 (0.532), 1.27	0.874 (0.821), 1.38	0.11	0.12	0.64
	Act.Pm (mm^{-1})	2.80 (2.67), 2.90	1.57 (1.64), 1.96	1.49 (1.43), 1.54	0.12	**0.02**	0.84
	Er:Min ratio	0.929 (0.454),2.08	1.53 (0.959), 2.91	1.42 (0.874), 4.79	**0.01**	0.58	0.91
6-9mm	Er.Pm (mm^{-1})	0.864(0.811), 1.30	0.887 (0.697), 1.88	0.496(0.467), 0.850	0.93	0.17	0.25
	Min.Pm (mm^{-1})	1.85 (1.69), 2.85	0.893 (1.00), 1.17	1.13 (1.03), 1.10	0.09	0.20	0.38
	Act.Pm (mm^{-1})	2.71 (2.58), 2.13	1.78 (1.72), 1.64	1.63 (1.71), 1.68	0.10	**0.03**	0.69
	Er:Min ratio	0.798(0.551), 1.96	1.94 (0.710), 7.99	0.435(0.461), 0.805	0.38	0.32	0.29
9-12mm	Er.Pm (mm^{-1})	0.839 (0.823),1.25	0.780 (0.361), 2.31	0.643 (0.494), 1.35	0.88	0.47	0.75
	Min.Pm (mm^{-1})	1.83 (1.51), 2.95	0.666(0.723),0.631	1.14 (1.14), 1.52	**0.04**	0.22	0.11
	Act.Pm (mm^{-1})	2.67 (2.59), 2.43	1.45 (1.20), 1.80	1.79 (1.73), 1.78	0.09	0.09	0.43
	Er:Min ratio	0.650(0.653), 1.15	2.31 (0.430), 10.5	0.740 (0.542), 1.42	0.36	0.77	0.40

Table 4.10 *Erosion and formation parameters from BSEM images, Cr, region adjacent to the defect. Er.Pm = Erosion perimeter/ Bone area (mm^{-1}), Min. Pm = Mineralising perimeter/ Bone area (mm^{-1}), Act.Pm = Active perimeter/ Bone area (mm^{-1}), Er:Min ratio = Erosion perimeter/ Mineralising perimeter.*

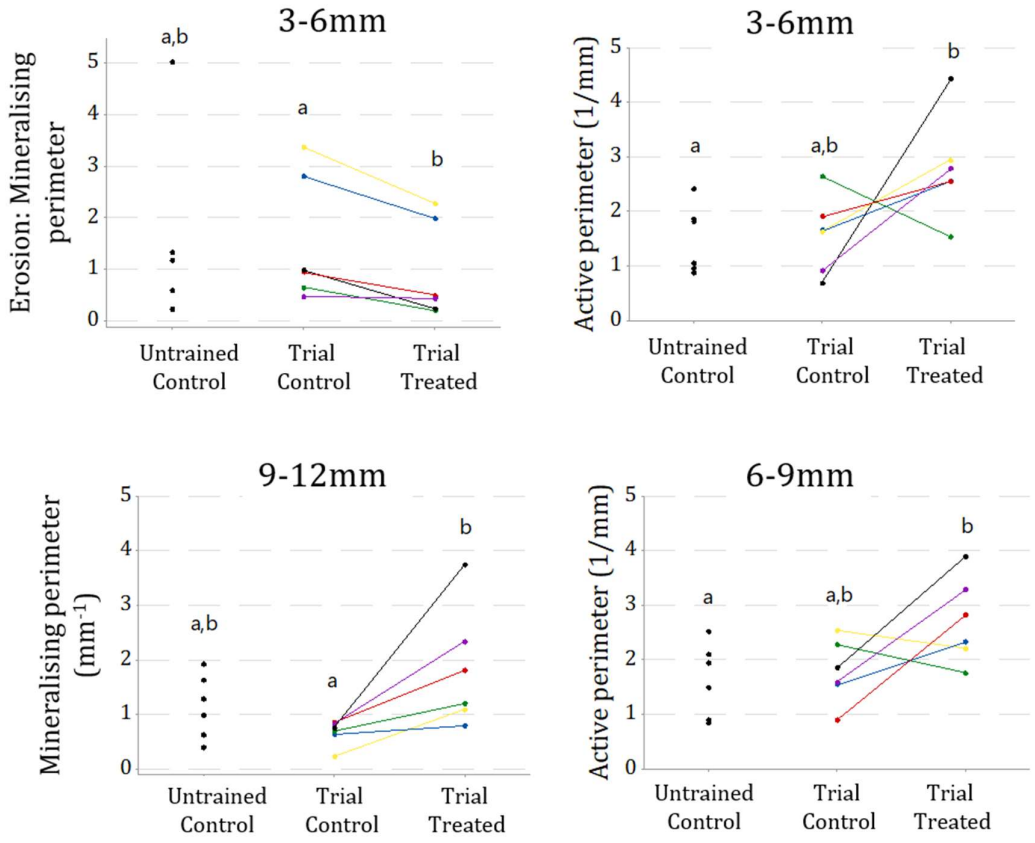

Figure 4.29 *Erosion and formation parameters measured on BSEM images, Cr, region adjacent to the lesion. Eroded to mineralising perimeter ratio, mineralising perimeter (mm-1) and active perimeter (mm-1). Different letters denote statistically different groups at a level of P<0.05.*

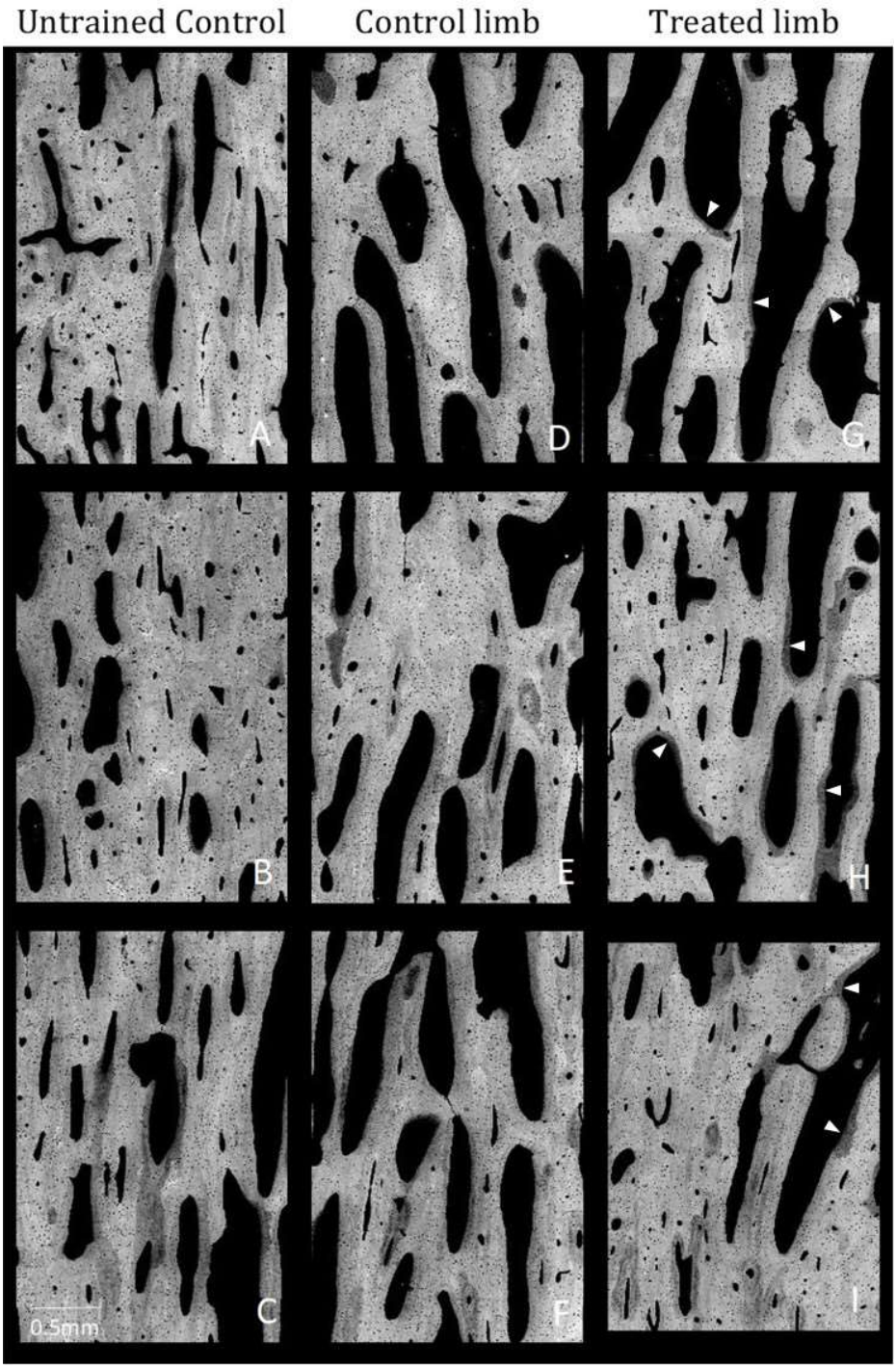

Figure 4.30 *BSEM images showing increased mineralizing perimeter (arrowheads) in treated limbs: Cr, region adjacent to the defect, 9-12mm deep to the cartilage. A= untrained control horse 3, B= untrained control horse 4, C= untrained control horse 6, D and G = Horse 3 control and treated respectively, E and H= Horse 4 control and treated respectively, F and I = Horse 5 control and treated respectively.*

On sections stained for TRAP there was no significant difference in the number of osteoclasts at either 0-3.3mm or 3.3-6.6mm deep to the cartilage when compared to either the contralateral controls or to the untrained controls (Table 4.11).

In agreement with the BSEM findings, measurements of osteoid from Masson's Goldner stained sections revealed some evidence of increased formation in the SCB in the region adjacent to the defect (Table 4.11). This was most apparent at 9-12mm deep to the cartilage where osteoid perimeter was 111% greater in treated limbs when compared with their contralateral controls (Figure 4.31). At 6-9mm below the cartilage there was a 137% increase in osteoid perimeter in treated limbs when compared with the contralateral controls that approached significance (P=0.07, Figure 4.31). There was no difference in osteoid area or osteoid width between the two limbs of the trial animals at any depth.

Depth below cartilage (For O'clast N)	Parameter	Mean (Median), Range			P-value		
		Trial treated	Trial Control	Untrained control	Trial treated v Trial control	Trial treated v Untrained control	Untrained control v Trial control
0-3mm (0-3.3)	Osteoclast N (cells/mm^2)	12.2 (9.50), 32.2	5.99 (2.78), 13.4	4.83 (2.88), 14.9	0.13	0.24	0.73
	O.Pm/B.Pm (%)	36.2 (35.1), 26.2	25.5 (26.3), 36.7	25.7 (22.2), 43.4	0.29	0.22	0.98
	O.Wi (um)	7.07 (6.52), 5.92	7.89 (7.85), 5.35	5.96 (5.61), 4.22	0.60	0.32	0.11
	O.Ar/B.Ar (%)	1.61 (1.32), 2.27	1.42 (1.35), 2.33	1.25 (0.728), 3.04	0.79	0.57	0.77
3-6mm (3.3-6.6)	Osteoclast N (cells/mm^2)	8.91 (10.3), 5.66	3.99 (3.38), 7.88	4.66 (2.53), 16.3	0.24	0.34	0.81
	O.Pm/B.Pm (%)	33.2 (30.0), 55.3	14.4 (11.5), 32.9	9.41 (8.36), 11.4	0.11	**0.04**	0.37
	O.Wi (um)	7.77 (7.82), 5.23	6.86 (7.15), 6.49	4.50 (3.98), 5.80	0.60	**0.03**	0.11
	O.Ar/B.Ar (%)	1.47 (1.56), 2.08	0.856 (0.615), 2.55	0.380 (0.238), 0.944	0.25	**0.04**	0.28
6-9mm	O.Pm/B.Pm (%)	32.0 (21.5), 52.4	13.5 (12.0), 12.3	10.7 (8.31), 20.4	0.07	0.06	0.45
	O.Wi (um)	7.75 (8.42), 5.29	6.67 (5.60), 8.20	4.19 (4.16), 2.91	0.33	**0.01**	0.10
	O.Ar/B.Ar (%)	1.79 (1.42), 3.46	0.757 (0.602), 1.69	0.329 (0.185), 0.710	0.12	**0.05**	0.16
9-12mm	O.Pm/B.Pm (%)	33.2 (30.9), 51.1	15.7 (13.7), 11.3	9.17 (6.45), 18.1	**0.05**	**0.02**	0.08
	O.Wi (um)	7.38 (8.16), 4.92	8.87 (7.87), 7.03	3.91 (3.83), 2.75	0.45	**0.005**	**0.008**
	O.Ar/B.Ar (%)	2.11 (1.79), 5.07	0.977 (0.767), 1.14	0.300 (0.245), 0.701	0.13	0.06	**0.02**

Table 4.11 *Cellular markers of remodelling, Cr, region adjacent to the defect**.** Osteoclast numbers (cells/mm^2) from cryosections stained for TRAP, O.Wi = osteoid width (um) and O.Pm = Osteoid perimeter/Bone perimeter (%) from Masson's Goldner stained sections.*

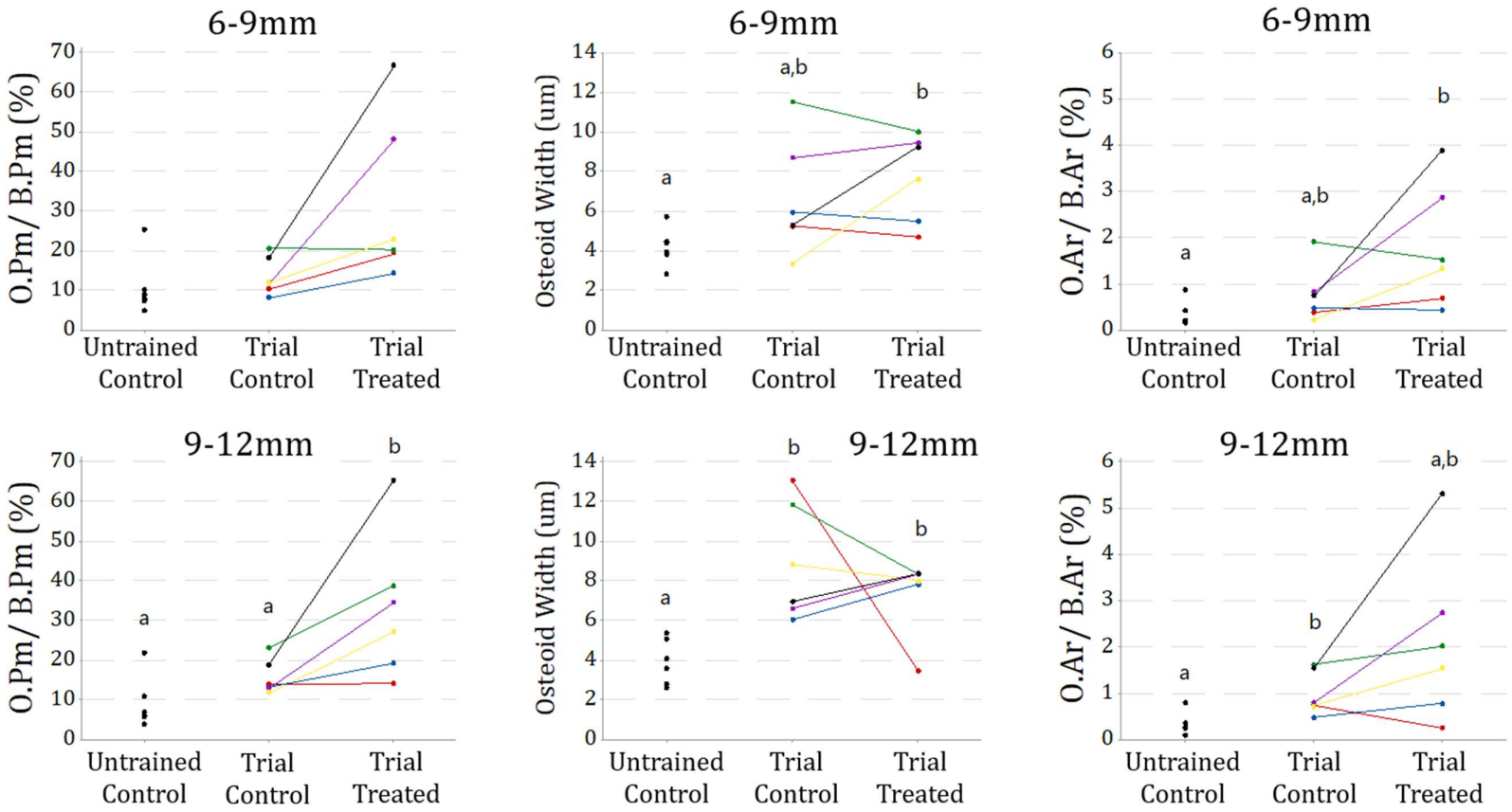

Figure 4.31 *Osteoid parameters from MG stained sections, Cr, region adjacent to the defect, 6-9mm and 9-12mm deep to the cartilage. O.Pm/B.Pm = osteoid perimeter as a percentage of bone perimeter (%), O.Ar/B.Ar = osteoid area as a percentage of bone area (%). Different letters denote statistically different groups at a level of P<0.05.*

At 3-6, 6-9 and 9-12mm deep to the cartilage the treated limbs had consistently greater osteoid perimeter and width, resulting in a greater osteoid area, than the untrained controls although these differences did not always quite reach significance (Figures 4.31-4.34, Table 4.11).

At 9-12mm deep to the cartilage the control limbs of the trial animals also had a greater osteoid width and area than the untrained controls (Figures 4.31 and 4.34).

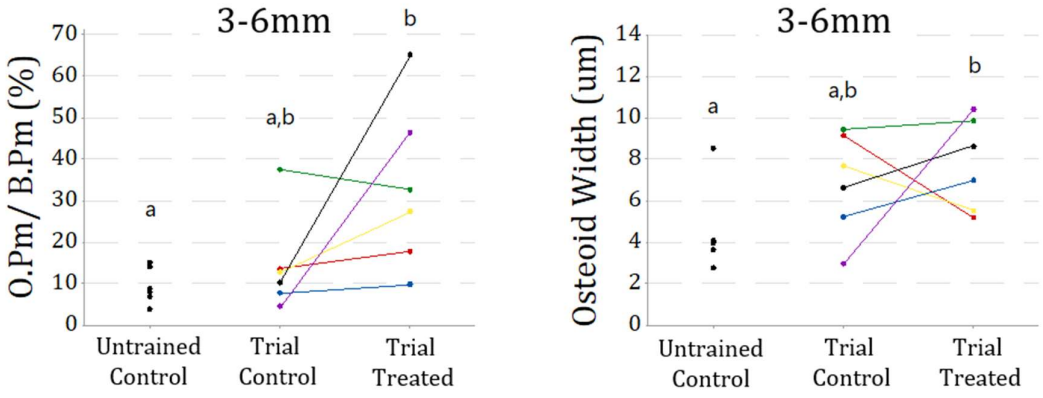

Figure 4.32 *Osteoid perimeter as a percentage of bone perimeter and osteoid width (µm), on MG stained sections, Cr, region adjacent to the defect, 3-6mm deep to the cartilage. Different letters denote statistically different groups at a level of P<0.05.*

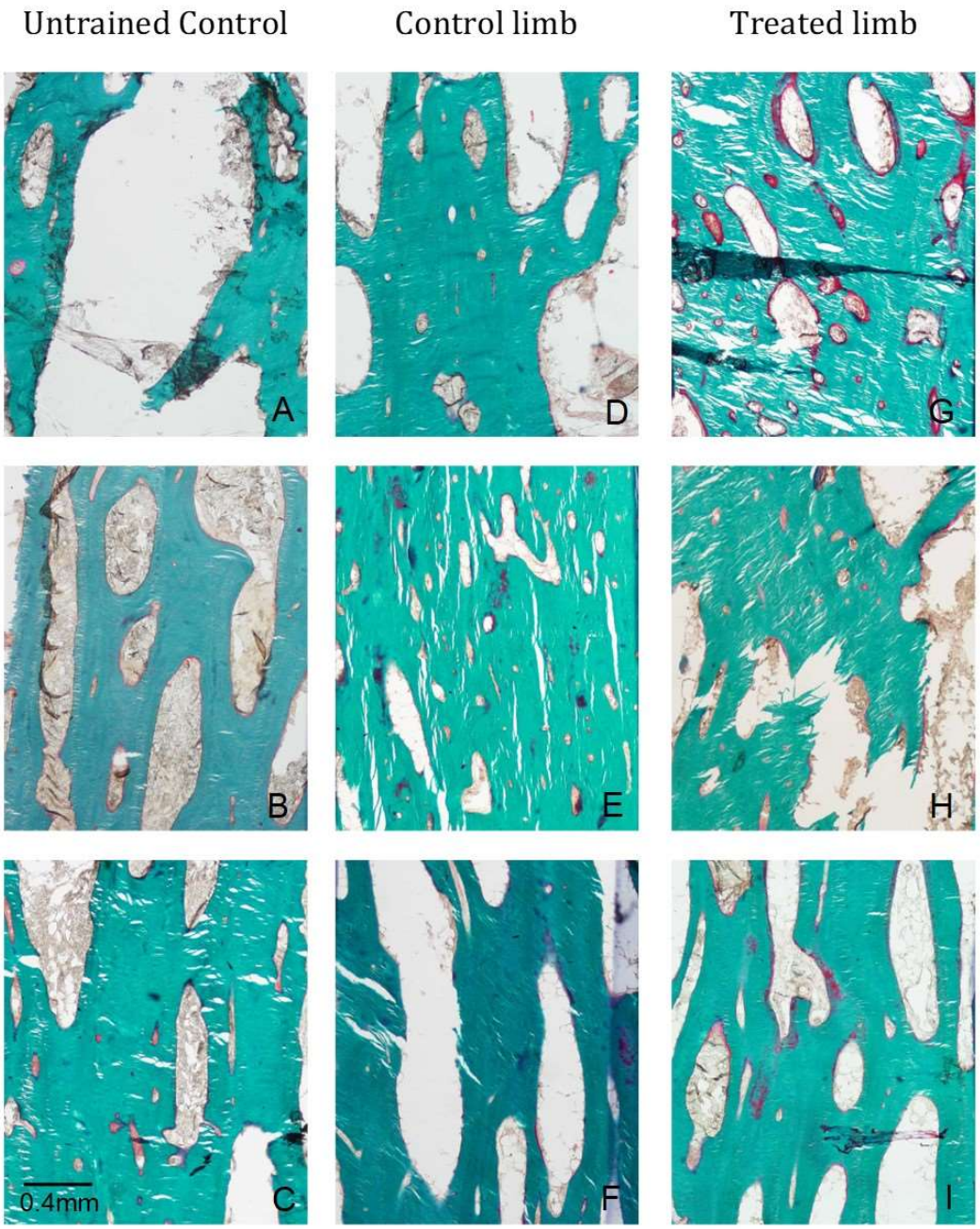

Figure 4.33 *Masson's Goldner stained sections in which osteoid is stained pink. There is an increased osteoid width and area in the treated limbs compared to the untrained controls: Cr, region adjacent to the lesion, 6-9mm deep to articular cartilage. untrained control horse 1 (A), untrained control Horse 2 (B), untrained control Horse 5 (C), Horse 1 control (D) and treated (G) limbs, Horse 2 control (E) and treated (H) limbs and Horse 5 control (F) and treated (I) limbs. Light microscopy.*

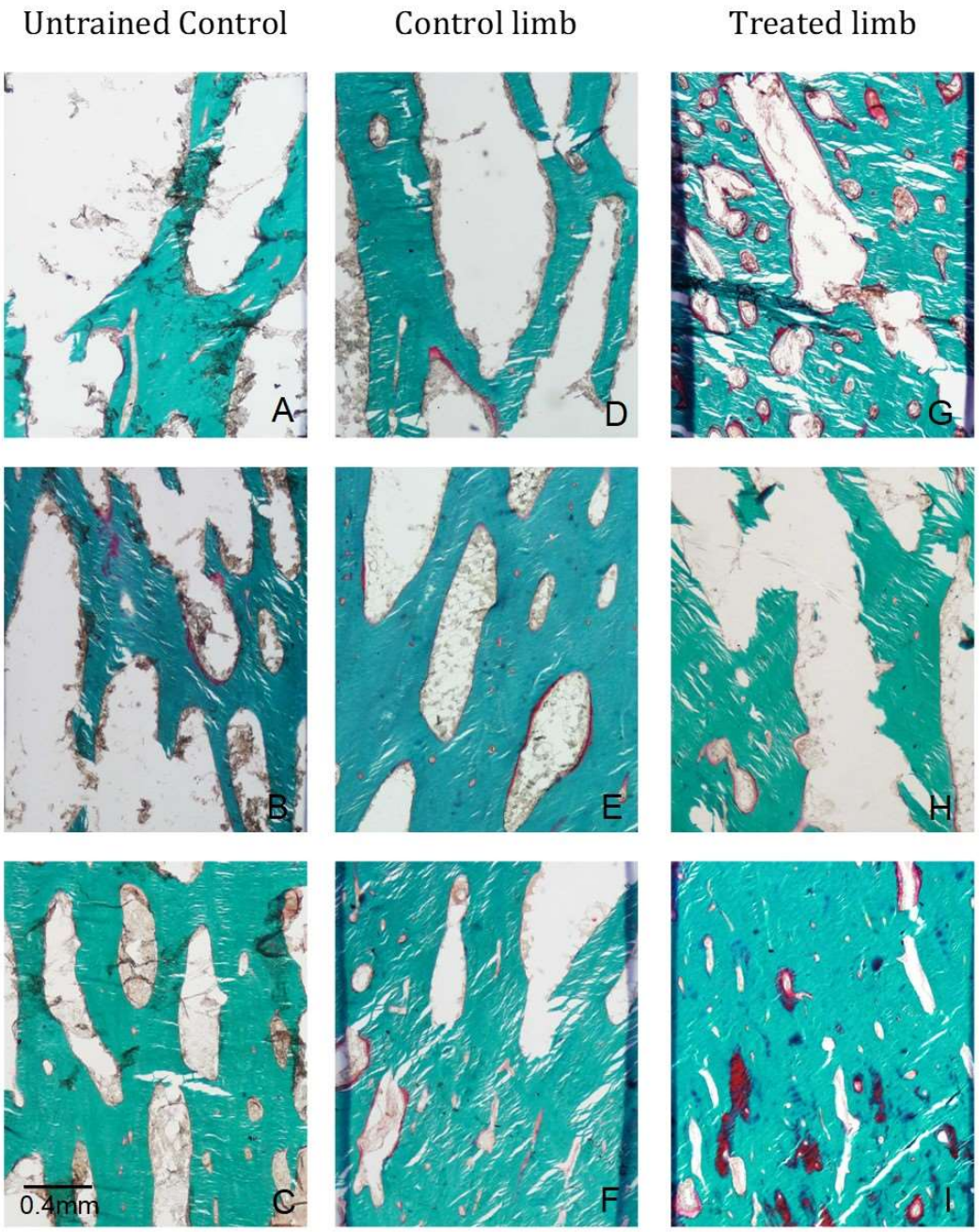

Figure 4.34 *Masson's Goldner stained sections in which osteoid is stained pink. Osteoid width is greater in treated limbs compared to the untrained controls: Cr, region adjacent to the lesion, 9-12mm deep to articular cartilage. untrained control horse 1 (A), untrained control horse 4 (B), untrained control horse 6 (C), Horse 1 control (D) and treated (G) limbs, Horse 3 control (E) and treated (H) limbs and Horse 6 control (F) and treated (I) limbs. Light microscopy.*

The increases in markers of formation seen on BSEM images and MG stained sections were not reflected in the analysis of fluorochrome labels. There were no significant differences between the treated and control limbs at any depth below the cartilage, however there was a 5-fold increase in single labelled perimeter in treated limbs at 3-6mm below the cartilage that approached significance (P=0.07, Figure 4.35, Table 4.12).

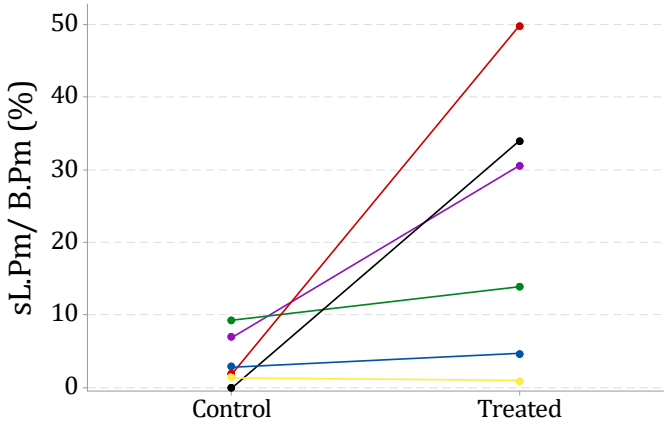

Figure 4.35 *Single-labelled perimeter as a percentage of bone perimeter (%), Cr, region adjacent to the lesion, 3-6mm deep to the cartilage.*

Depth below cartilage	Parameter	Mean (Median), Range		P-value
		Trial treated	Trial Control	Trial treated v Trial control
0-3mm	L.Pm/B.Pm (%)	15.1 (11.8), 29.9	6.82 (7.69), 12.6	0.08
	sL.Pm/B.Pm (%)	22.1 (16.5), 54.8	9.86 (10.5), 16.6	0.15
	dL.Pm/B.Pm (%)	4.07 (3.01), 10.4	1.89 (1.71), 4.30	0.13
	BFR/B.Ar (%/d)	0.063 (0.053), 0.122	0.040 (0.042), 0.074	0.12
3-6mm	L.Pm/B.Pm (%)	14.6 (16.1), 26.7	5.05 (1.20), 22.2	0.19
	sL.Pm/B.Pm (%)	22.3 (22.2), 48.9	3.72 (2.40), 9.20	0.07
	dL.Pm/B.Pm (%)	3.45 (1.56), 11.9	3.19 (0.00), 17.6	0.35
	BFR/B.Ar (%/d)	0.060 (0.067), 0.094	0.045 (0.026), 0.108	0.51
6-9mm	L.Pm/B.Pm (%)	15.3 (13.3), 35.4	2.15 (1.83), 6.12	0.08
	sL.Pm/B.Pm (%)	20.4 (14.4), 45.9	3.68 (2.91), 10.2	0.09
	dL.Pm/B.Pm (%)	5.07 (2.28), 13.6	0.308 (0.000), 1.02	0.12
	BFR/B.Ar (%/d)	0.064 (0.075), 0.107	0.010 (0.008), 0.023	0.18
9-12mm	L.Pm/B.Pm (%)	8.65 (7.25), 21.0	6.05 (6.47), 11.6	0.53
	sL.Pm/B.Pm (%)	13.1 (10.9), 30.4	6.16 (4.84), 16.5	0.23
	dL.Pm/B.Pm (%)	2.12 (1.23), 6.27	2.97 (2.59), 6.41	0.63
	BFR/B.Ar (%/d)	0.041 (0.041), 0.089	0.042 (0.058), 0.072	0.25

Table 4.12 *Measures of fluorochrome labels, Cr, region adjacent to the defect, from undecalcified, unstained sections. L.Pm/B.Pm = labelled perimeter/ bone perimeter (%), sL.Pm/B.Pm = single labelled perimeter/ bone perimeter (%), dL.Pm/B.Pm = double labelled perimeter/ bone perimeter (%) and BFR/B.Ar = bone formation rate/bone area (%/day).*

4.4 Discussion

4.4.1 Summary of major findings

Ten weeks after their creation, osteochondral defects were filled to varying degrees with fibrocartilaginous tissue with minimal evidence of bony healing in the Cr of horses in training

At the base of the defect SCB showed a marked increase in measures of both erosion and formation with a net loss of bone volume, whereas in the deeper bone formation was increased, erosion activity became less prominent and there was no change in bone volume.

In SCB from below the intact joint surface adjacent to the defect there was no change in bone volume but a tendency towards formation activity with a decrease in the ratio of erosion to mineralising perimeter at 3-6mm deep to the cartilage and an absolute increase in mineralising and osteoid perimeter at 9-12mm deep to the cartilage.

4.4.2 Comparison with current literature

The observations from the SCB of Cr in this study share similarities with those from other studies of equine chondral and osteochondral defect models. In a study of 6mm diameter OC defects on the proximal facet of C4, Kulmala et al. (2012) measured a 22% decrease in BV/TV and an 83% increase in BS/BV at the defect site compared with adjacent SCB,

very similar to the current study (372). Salonius et al. (2018) observed cyst-like lesions with a marked loss of bone below OC defects of various sizes in the equine carpus (371).

Increased porosity of SCB below chondral and osteochondral defects and sclerosis of surrounding SCB has also been reported in studies of defects in femoral condyles of horses and ponies (340, 370). These observations are consistent with the loss of bone volume immediately below the defect and the tendency towards formation adjacent to the defect in the current study. However in the current study there was no increase in the amount of bone at the periphery of defects after 10 weeks which was a subjective observation in the study by Kold and Hickman (1986) after 6 months, likely due to this difference in duration (340).

The observation of increased remodelling, including increased numbers of osteoclasts and increased labelled perimeter, at 0-3mm deep to the cartilage in the region below the lesion in the current study is also consistent with observations of increased osteoclastic resorption, increased uptake of fluorescent markers and increased amounts of woven bone at the periphery of osteochondral defects in the equine model used by Kold et al. (340).

More marked loss of bone including the formation of cavitatory lesions has been associated with deeper osteochondral defects in multiple other large animal models (1, 365, 368, 374). Reduced bone volume (371, 373, 375) or cyst formation (377, 378) within SCB below cartilage defects has also been reported in horses and other species, however these are not consistent findings in other studies (370, 379-381).

I am not aware of existing studies with which to compare the increase in formation activity at 3-12 mm deep to the cartilage in the region below the defect in the current study. Most previous studies have investigated bone only up to two mm deep to the defect base (1, 202, 340, 365, 368, 374). Fisher et al. (2015) reported normal BV/TV at 3-5mm deep to the osteochondral junction below chondral defects in pigs, consistent with the unchanged BV/TV at 3-6mm deep in the current study, however they did not report measures of formation (364).

Sclerosis in bone adjacent to osteochondral defects has been observed in studies of both deep osteochondral defects and superficial cartilage defects in several species and the tendency towards formation observed in the adjacent weight bearing SCB in the current study may be an early sign of increasing bone volume (1, 3, 365, 368, 370, 375). It is possible that had bone closer to the edge of the defect been investigated in the current study, as has been done in previous work, an increase in bone volume may have been observed (1, 3, 365, 368, 370, 375). In addition, the initial BV/TV in the superficial SCB in the current study may have been too high or the duration of the study too short to document an increase in BV/TV.

Filling of the defects with fibrocartilaginous tissue as observed in the current investigation is similar to existing reports of osteochondral defects in horses and other species (1, 202, 361, 365, 366, 368, 370, 371). The presence of chondroid tissue within spaces in the SCB at the border of defects has also been reported in previous work (202, 324, 376). The lack of new bone within the defect is not consistent with the findings of previous equine models, where some degree of bony filling of defects sometimes with advancement of the SCB into the region previously occupied by cartilage has been observed (202, 324, 366,

370, 371). These studies were of longer duration than the current study and time since defect creation may be an important factor in healing. Orth et al. (2012) found 5mm deep osteochondral defects in rabbits progressively filled with bone between 6 weeks and 6 months after creation, while advancement of the SCB was observed at 12 months. Depth of the lesion may also be important as Hanie et al. (202) reported advancement of the SCB plate after 4 and 6 months in equine C3 cartilage defects but not in deeper defects which also involved SCB, and Qiu et al. (421) reported SCB advancement by 4 months after creation of a defect 3mm deep in a rabbit model.

4.4.3 Interpretation of major findings

4.4.3.a Healing of the defect

The lack of significant bony healing indicates that the defect resulted in incongruity of the joint surface for the entire 10 weeks of the study. The presence of fibrocartilaginous tissue within the defect may have gone some way to restoring congruity of the articular surface however it has been demonstrated that filling of osteochondral defects with either alginate or osteochondral transplants does not normalise the contact pressures across the joint surface and that fibrocartilage within osteochondral defects does not contribute significantly to load bearing (2, 3, 361).

Although the length of the study may not have allowed time for bony healing of the defect, it is interesting that there was minimal evidence of osteoid or newly mineralised bone within the defect despite extensive osteoid production and mineralisation activity within marrow spaces immediately deep to the defect. There was also no evidence of ossification

within the fibrocartilage filling the defect. This suggests that at 10 weeks after creation of a SCB defect, osteoblasts, while being active in the adjacent marrow spaces, are not present within the defect itself. It is possible that this is due to the lack of bone lining cells which play a role in the bone healing process and are a source of osteoprogenitor cells (383, 422) however it has been shown that marrow-derived mesenchymal stem cells and the systemic circulation can also provide osteoprogenitor cells (423, 424). It is possible that joint fluid movement through the defect could slow healing as high pressure fluid flow has been shown to remove cells from bone surfaces and decrease new bone formation in models of fracture healing (425). In addition, bony healing is enhanced by moderate compressive loading so unloading through loss of surface contact may have slowed bony healing of these defects (147, 387, 426, 427).

4.4.3.b Increased remodelling and loss of bone volume at the base of the defect

The marked increase in erosion and formation activity observed at the base of the defects in the treated Crs may be mediated by pro-inflammatory cytokines, growth factors or other active molecules released following trauma to the subchondral bone and articular cartilage. Concentrations of inflammatory cytokines such as tumour necrosis factor alpha (TNFα), interleukin-1 (IL-1) and interleukin-6 (IL-6) and growth factors such as transforming growth factor β (TGF-β) and bone morphogenic proteins (BMPs) have been shown to be elevated in injured bone and to enhance osteoclast recruitment and activation as well as bone formation and matrix mineralisation (229, 385, 396-398, 428). Acute inflammation is recognized to continue for up to 7 days after bone injury so is expected to have waned by the end of this study at 10 weeks, however chronic inflammation is reported and pro-inflammatory cytokines also play a role in the later phases of bone healing (385, 386). The formation activity may be part of the healing response as new

bone formation on trabecular surfaces is observed in SCB surrounding fatigue fractures and in models of fracture repair (231, 385, 429). Likewise, osteoclastic resorption of cartilaginous callus, islands of which were evident within SCB voids at the base of the defect, is a feature of fracture healing and could play a role in the observed increase in osteoclast numbers (146, 387). However loss of trabecular bone volume surrounding fracture sites was not observed at any time during normal healing in a rabbit model of metaphyseal fracture (429) suggesting that the creation and healing of the defect or the presence of pro-inflammatory cytokines alone may not explain the marked erosion activity and loss of bone volume observed at the base of the defects. The regional acceleratory phenomenon (RAP), a concept that is well accepted although not completely understood (341, 383, 430-433), may contribute to the changes observed at the base of the defects in this model, with cytokines released by creation of the defect or the healing process accelerating the SCB response to changes in loading.

Local unloading of the SCB through the loss of the overlying articular surface is likely to play a role in the observed increase in osteoclast numbers and erosion perimeter, and loss of bone volume at the base of the defects in the treated Crs. Loading of bone at the base of osteochondral defects has been estimated by finite element analysis to be reduced to 27% of normal (1) and reduced loading is known to result in a loss of bone volume due to increased osteoclastic activity (121, 150, 152, 163, 434, 435). The relationship between remodelling activity and BV/TV at the base of the defect is similar to that observed in the unloaded region of C3 and is discussed in Chapter 5.

4.4.3.c Increased remodelling favouring formation below the defect: 3-6mm deep to the cartilage

The factors involved in the increase in remodelling in the SCB at 0-3mm deep to the cartilage are also likely to be acting in the region 3-6mm deep to the cartilage. This appeared to be a region of transition where there were increases in both resorption and formation activity but the increase in resorption was less marked than in the more superficial region and there was no net loss of bone volume. Changes in loading of SCB in this region may have been less dramatic than in the bone immediately below the lesion, and concentrations of inflammatory cytokines and other effects of bone damage may have been less.

The increase in osteoclast numbers at 3-6mm deep to the cartilage in the region below the defect was not reflected by a significant increase in erosion perimeter on BSEM images as might have been expected. However the erosion perimeter was greater in treated limbs when compared to the control limbs of five of the six trial animals. The apparent discrepancy may also be because osteoclast number and eroded perimeter, although related, are not directly comparable: osteoclast counts measure the presence of cells with the capacity to resorb bone at a given point in time and the eroded perimeter is a measure of the last event that occurred on a bone surface but gives no information about when that event occurred.

4.4.3.d Increased formation below the defect: 6-12mm deep to the cartilage

The marked increase in bone formation with no increase in erosion activity at 6-9mm and 9-12mm deep to the cartilage in the region below the lesion is likely to reflect either

remodelling that has moved entirely from the erosion phase through to the formation phase or de novo bone formation. This formation activity may be a reflection of greater loads than normal being transferred from the articular surface around the defect into this deeper bone (215, 363).

Bone formation is also recognized to be stimulated by inflammatory mediators such as prostaglandins, TNF-α, IL-1 and IL-6 (385, 386, 398). PGE for example, has been shown to result in a generalized activation of remodelling with an increase in the formation phase (398). It is possible that inflammatory mediators released by bone damage at the site of the defect resulted in formation activity within the deeper bone. This does not explain why there is no concurrent increase in erosion activity. It is probable that changes in loading and the presence of inflammatory cytokines are interacting in varying ways depending on the position of bone in relation to the osteochondral defect.

4.4.3.e Tendency toward formation adjacent to the defect

The changes in the SCB of the adjacent, weight bearing region were much less pronounced than in the region below the defect. Although the palmar edge of these ROIs were as little as 0.3-3mm away from the defect, the SCB in this region did not display the marked increase in formation that was observed up to 11mm deep to the boundary of the defect suggesting differences in both the biochemical and/or biomechanical environment of the two regions.

The tendency toward formation in the weight bearing region adjacent to the osteochondral defects is likely a result of an increase in loading of this SCB (1, 3, 215). Consistent with this, defects filled with a stiff scaffold were associated with less sclerosis of surrounding

bone than either those left unfilled or filled with a softer scaffold, suggesting that the stiff scaffold was taking more load, leading to a relatively lower increase in load on the SCB and reduced sclerosis (374).

That the most significant increase in osteoid and mineralising perimeter was observed at 9-12mm deep to the cartilage in the adjacent weight bearing region may be because the changes in loading associated with the defect were greatest at this depth. Simple finite element models show increases in stress deep to induced subchondral bone defects in the adjacent bone (363). It is also possible that there was a greater bone surface available in the deeper regions on which formation might occur.

4.4.3.f Bone volume fraction

Despite the marked increase in formation 3-12 mm deep to the lesion and the milder tendency towards formation in the adjacent weight bearing region there was no change in bone volume observed at those sites. The insignificant reduction in porosity at 0-3mm deep to the cartilage in the weight bearing region of treated limbs was not reflected in the bone volume fraction on microCT analysis. It is possible that the thresholding used for the microCT analysis did not include the newer, less mineralised bone. Alternatively the increase in formation activity could have resulted in increased bone volume had the trial continued for longer, or perhaps the observed formation activity was replacing bone that had been removed by previous resorption activity.

The reduction in trabecular separation at 0-3mm deep to the cartilage in the adjacent weight bearing region may be a reflection of increases in trabecular number and thickness

that were not significant in isolation however trabecular parameters need to be interpreted with care in this ROI as the bone is predominantly compact in nature.

4.4.3.g Effect of training

Training, which has been shown to result in increased osteoid formation and increased bone volume in equine SCB, is likely to be responsible for the greater osteoid width and TMD in both limbs of the trial animals compared to the untrained controls at 9-12mm deep to the cartilage in the weight bearing and region below the lesion respectively (74, 156, 165, 333).

It appears that the effects of training and of the lesion combined to increase osteoid width and active perimeter in the treated limbs of the trial animals when compared to the untrained controls in the weight bearing region of Cr as there was no difference in these parameters between the control limbs of the trial animals and the untrained controls. This combined effect was also apparent at 9-12mm deep to the cartilage in the region below the lesion where bone volume fraction was higher in the treated limbs, but not the contralateral control limbs, when compared to the untrained controls.

At 3-6mm deep to the cartilage in the region below the lesion the treated limbs of the trial animals had a lower bone volume and higher bone surface when compared to the untrained controls but not when compared to their contralateral controls. It is difficult to explain why there was a greater difference between the treated limbs and the untrained controls in these measures.

4.4.6 Conclusion

At 10 weeks after creation of an osteochondral defect the combined effects of changes in loading and tissue damage result in a net loss of bone volume associated with increases in both erosion and formation activity at the defect base, as well as increases in formation activity in the bone deep to the defect and in bone under the adjacent weight bearing articular surface.

This equine model of osteochondral defects successfully resulted in incongruity of the articular surface for the length of the study.

Chapter 5

BONE PARAMETERS OF THE THIRD CARPAL BONE

5.1 Introduction

In treated joints there was a region of the C3 articular surface, immediately opposing the Cr defect, where there was loss of surface contact for a period resulting in reduced loading of the underlying SCB (18, 106, 360). There was also a region dorsal to the defect where surface contact had been maintained and where loading of the underlying SCB was likely increased (1, 3, 106, 233, 360). Unlike the changes observed in the SCB of Cr where the defect had been created, the responses in the opposing C3 SCB are less likely to have been affected by the tissue damage and inflammation associated with the surgical procedure.

Incongruity of joint surfaces as a result of cartilage loss, intra-articular fracture or collapse of the underlying SCB has been associated with subsequent development of degenerative changes and OA in the affected joint (18, 209, 366, 389). Joint incongruity is also a feature of OA regardless of the underlying cause (19, 33, 241). While there has been much work published on joint injuries and disease that lead to OA and on OA itself, there is little in

this body of work that has specifically studied how the SCB responds to changes in articular surface congruity. There has also been little discussion regarding whether joint congruity is actively maintained during normal homeostasis and, if so, what role the SCB plays in this process.

There have been a number of studies of induced osteochondral defects to date, some of which have investigated the cartilage of the opposing joint surface (17, 18, 366, 389). However, very few have examined the SCB opposing the defects in detail. Although not the primary purpose of their study Hanie et al. (1992) reported xeroradiographic changes in bone density of the distal articular facet of radial carpal bones opposing induced osteochondral defects on third carpal bones in an equine model (202).

As discussed in detail in Chapter 1, it is recognised that bone responds to its loading environment. Reduced loading has been shown to result in a loss of bone volume in both trabecular and cortical bone due to increased bone resorption and reduced bone formation and mineralisation (150, 152, 161-163). As loading decreases, enhanced bone resorption also results in greater remodelling activity (181). Conversely, it has been demonstrated that higher loads result in greater bone volume due to increased formation and decreased osteoclastic activity (151, 158, 159).

Specific examples of SCB responding to its loading environment also exist. Unloading of mouse hind limbs resulted in reduced BV/TV and increased TRAP staining in femoral and tibial SCB (121). Conversely SCB of canine stifles was found to have increased trabecular bone volume after strenuous training (73). Higher BV/TV through increased bone formation has also been observed to be a consequence of repetitive loading in the

SCB of horses (69, 156). More recent work has shown that repetitive loading also inhibits remodelling within equine subchondral bone (165).

The examination of joints from large animals enables the study of regional variations in the response of subchondral bone to loading. Site specific changes in equine SCB exposed to high intensity training have been observed with highly loaded regions undergoing a greater increase in bone volume than those experiencing lower load (70, 74). Additionally, there is emerging evidence that while remodelling is generally inhibited in a high load environment resorption may occur at specific sites. Whitton et al. (2013) observed increased markers of remodelling at sites of fatigue fracture in SCB of horses in training but not in surrounding bone (231). There are several possible mechanisms that might enable focal remodelling at a site of bone damage in a high load environment, including the presence of inflammation and osteocyte apoptosis (197, 227, 229, 385) in addition to local unloading of the bone due to a change in its material properties and/or a loss of surface congruity (171, 172, 436).

In order to better understand the effects of incongruity on SCB, and in light of existing evidence that bone remodelling activity may be determined by local loading patterns, the aim of this chapter was to study how changes in local loading of the articular surface affect the levels of subchondral bone remodelling activity and bone volume in adult horses undergoing regular controlled exercise. It was hypothesised that remodelling activity would increase in the SCB opposing the defect where the magnitude of cyclic loading is decreased, and would decrease in the SCB of the weight bearing region dorsal to this where the magnitude of cyclic loading is likely increased, resulting in a decrease

in bone volume in the SCB opposing the defect and an increase in bone volume in the SCB of the weight bearing surface.

5.2 Materials and Methods

Undecalcified specimens of C3 were collected and processed as described in Chapter 2 for analysis with microCT, BSEM, Masson's Goldner staining and for analysis of fluorochrome labels. Cryosections of decalcified samples were prepared and stained for TRAP as described in Chapter 2 for identification of osteoclasts.

Two series of ROIs were chosen: one in the unloaded region opposing the surgical defect and the second in the dorsal, weight bearing region. The position of each series was defined as being immediately opposite the equivalent ROIs in Cr and located on images and histological sections by measuring the defined distance for each animal palmar from the dorsal articular margin along a line parallel with the joint surface (Table 5.1, Figure 5.1a).

The dorsal articular margin was defined as the point on the dorsal edge of the bone where the articular cartilage ended. On microCT images this was not obvious as the HC cannot be seen with this modality and the CC was often indistinct from the SCB. On microCT images of treated limbs the point immediately proximal to the peri-articular modelling was defined as the articular margin. The distance between this point and a line drawn along the proximal surface of the CC was measured and this distance used to define the

articular margin on images of C3 from control limbs where the articular margin was not otherwise obvious (Figure 5.1b).

Horse	Position of dorsal edge of ROIs (distance palmar to dorsal articular margin)	
	Weight bearing	**Opposing Lesion**
1	1.0 mm	6.0 mm
2	0.4 mm	5.5 mm
3	2.0 mm	7.0 mm
4	0.5 mm	4.0 mm
5	1.0 mm	4.0 mm
6	2.0 mm	6.0 mm
Untrained Control	1.2 mm	5.5 mm

Table 5.1 *Location of dorsal edge of C3 ROIs in individual horses, mm palmar to the dorsal articular margin in a line parallel to joint surface.*

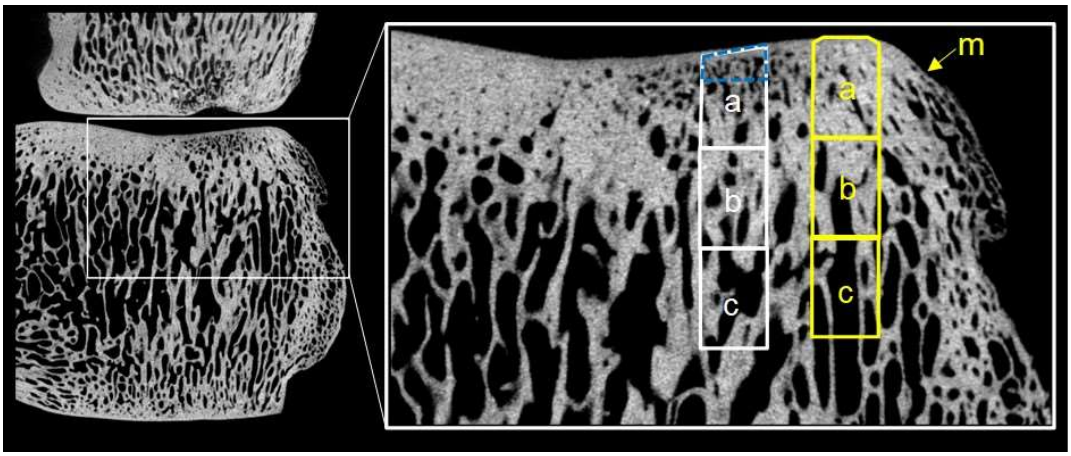

Figure 5.1a *Left: MicroCT images of Cr (top) and C3 (bottom) from the treated limb of Horse 5. The white box indicates the enlarged area on the right. Right: C3 ROIs: yellow = weight bearing region, white = region opposing the lesion, a = 0-3mm, b = 3-6mm, c = 6-9mm deep to articular surface. Blue dotted box = 0-1mm deep to articular surface. m = dorsal articular margin. Not to scale.*

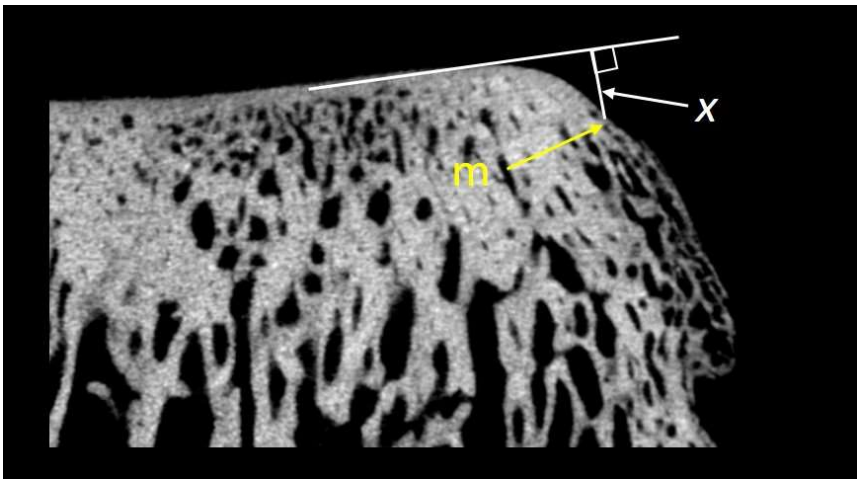

Figure 5.1b *MicroCT image of dorso-proximal C3 from the treated limb of Horse 5 showing measurement of the position of the dorsal articular margin.* ***x*** *= distance between the dorsal articular margin (m) and a line parallel to the surface of the calcified cartilage.* ***x*** *was measured from images of treated limbs and used to define the dorsal articular margin in the contralateral control limbs.*

There were three primary ROIs defined in each series for evaluation in microCT and BSEM images, Masson's Goldner stained sections and for analysis of fluorochrome labels (Figure 5.1a). These ROIs were 0-3, 3-6 and 6-9mm deep to the cartilage. Each of these ROIs was 2mm wide in the dorso-palmar direction. For analysis of the 3D microCT data, each ROI was 2.4mm deep with the exception of those in the specimen from the control limb of Horse 5, where the thickness of the specimen limited the depth of the ROIs to 1.9mm. The ROI 0-3mm deep to the cartilage included the predominantly compact bone between the cement line and 3mm deep to this with the exception of the microCT images. In the microCT images the CC was included as it was not possible to differentiate it from the underlying bone. The ROIs at 3-6mm and 6-9mm were positioned immediately deep to the more superficial ROI in the series. The ROI 3-6mm deep to the cartilage included the transitional region between compact and trabecular bone while the ROI 6-9mm deep to the cartilage included bone that was predominantly trabecular in structure (437).

In addition to the ROIs described above a smaller, more superficial ROI was defined only in the ROI series opposing the lesion: 0-1mm deep to the CC and 2mm wide in the dorso-palmar direction (Figure 5.1). For microCT images, where the cement line was not visible, the superficial boundary of the ROI was defined as 0.3mm deep to the surface of the calcified tissue, this being the maximum CC thickness in this region as measured on BSEM images.

Cryosections used for TRAP staining did not include the deeper bone so only two ROIs were defined in each series for osteoclast counts. The positions of ROIs opposing the defect and in the adjacent weight bearing region were chosen to be immediately opposite

the equivalent ROIs in Cr and measured from the dorsal articular margin, as previously defined, along a line parallel to the articular surface (Figure 5.2). The region opposing the surgical defect and the dorsal weight bearing region were defined as 5.5-7.7mm and 0.55-2.75mm from the dorsal articular margin in the sagittal plane respectively. The two ROIs in each group were 0-3.3mm and 3.3-6.6mm deep to the cartilage (see Chapter 4 for justification of these ROIs).

Measurements were made in each ROI described above using each technique as specified in Chapter 2. All observations were analysed with the statistical methods described in Chapter 2.

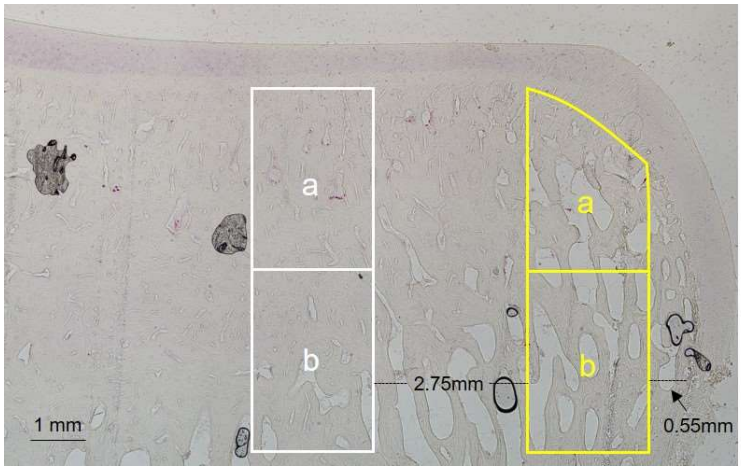

Figure 5.2 *Image of a cryosection stained for TRAP, C3, Horse 4, control limb depicting ROIs: yellow = weight bearing region, white = region opposing the lesion, a = 0-3.3mm deep to cartilage, b = 3.3-6.6mm deep to cartilage, each is 2.2mm wide in the dorso-palmar direction. Dorsal to the right, palmar to the left of the image.*

5.3 Results

On all images and histological sections the C3 SCB appeared intact with no evidence of pathology except in one horse. In C3 from the control limb of horse 6 microCT images revealed a superficial defect extending through the CC into the SCB at 3.1 mm palmar to the dorsal edge of the bone (Fig. 5.3). In BSEM images of this specimen there was a lesion at an equivalent position which appeared as multiple microcracks within the CC and an area of focal resorption in the SCB immediately below. This lesion was positioned just palmar to the weight bearing ROIs in this animal.

All trained horses had focal clusters of resorption spaces in the SCB of C3 immediately deep to the CC in the region opposing the Cr defect visible on microCT (Figure 5.4), BSEM (Figure 5.8) and histological sections (Figure 5.15) although the size and number of these spaces varied greatly between animals.

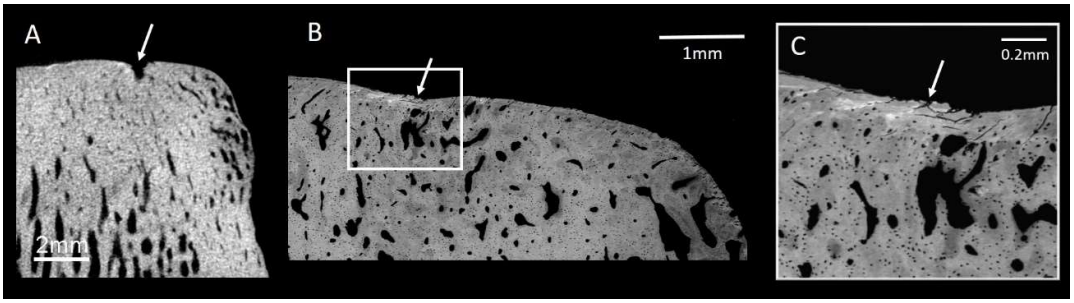

Figure 5.3 *MicroCT (A) and BSEM (B and C) images showing an area of calcified cartilage and subchondral bone damage (arrows) in the proximal articular surface of C3 from the control limb of Horse 6.White box in B shows area enlarged in C.*

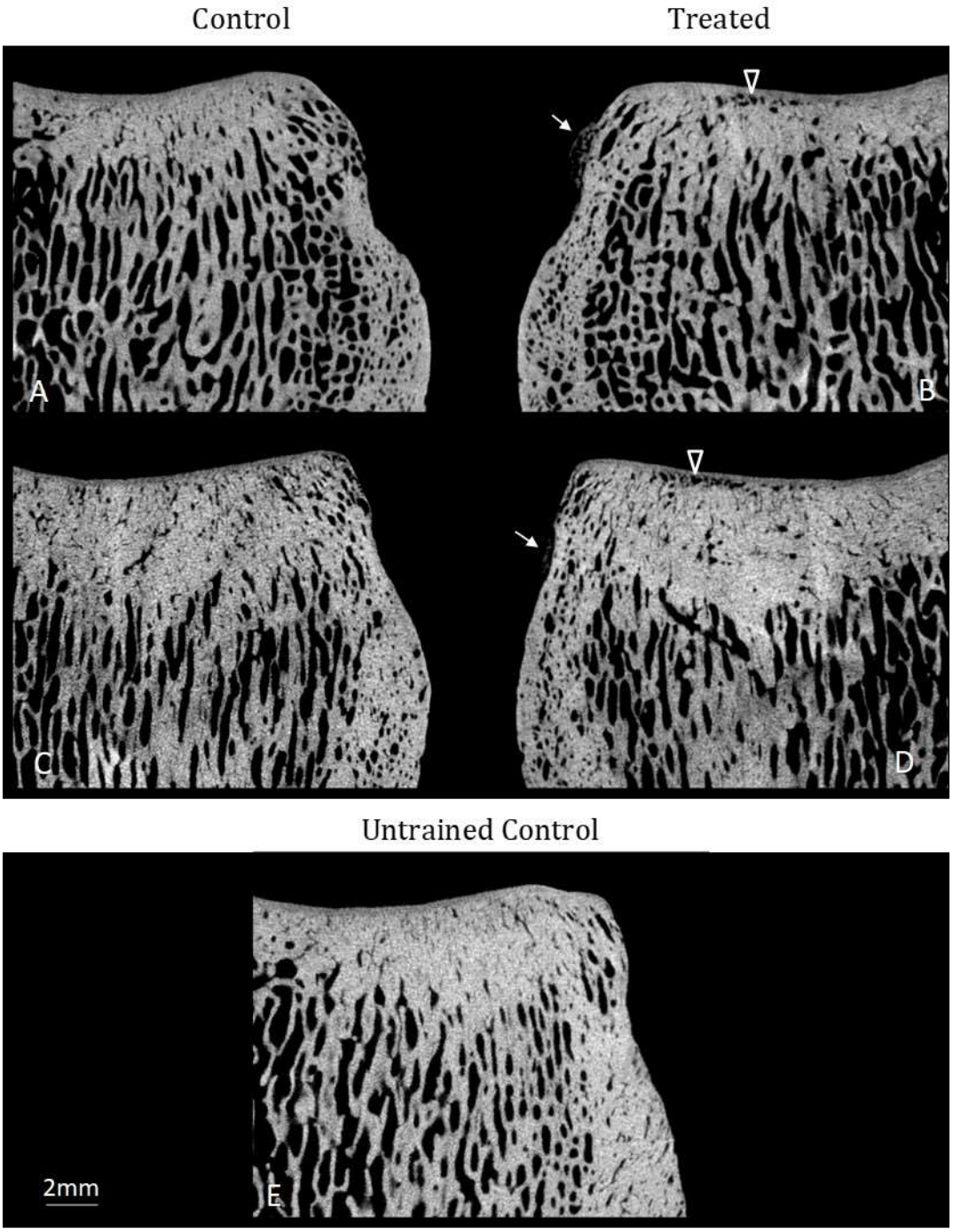

Figure 5.4 *MicroCT images of C3 bones. A and B: control and treated limbs of Horse 1 respectively, C and D: control and treated limbs of Horse 2 respectively, E: Untrained control horse 3. Arrow heads indicate resorption spaces. Arrows indicate peri-articular modelling. Dorsal edge of bone to centre of image for Horse 1 and 2 images, dorsal edge to right of untrained control horse 3 image.*

There was evidence of varying degrees of peri-articular modelling on the dorsal aspect of C3 from all treated joints in both microCT and BSEM images (Figs 5.4 and 5.5).

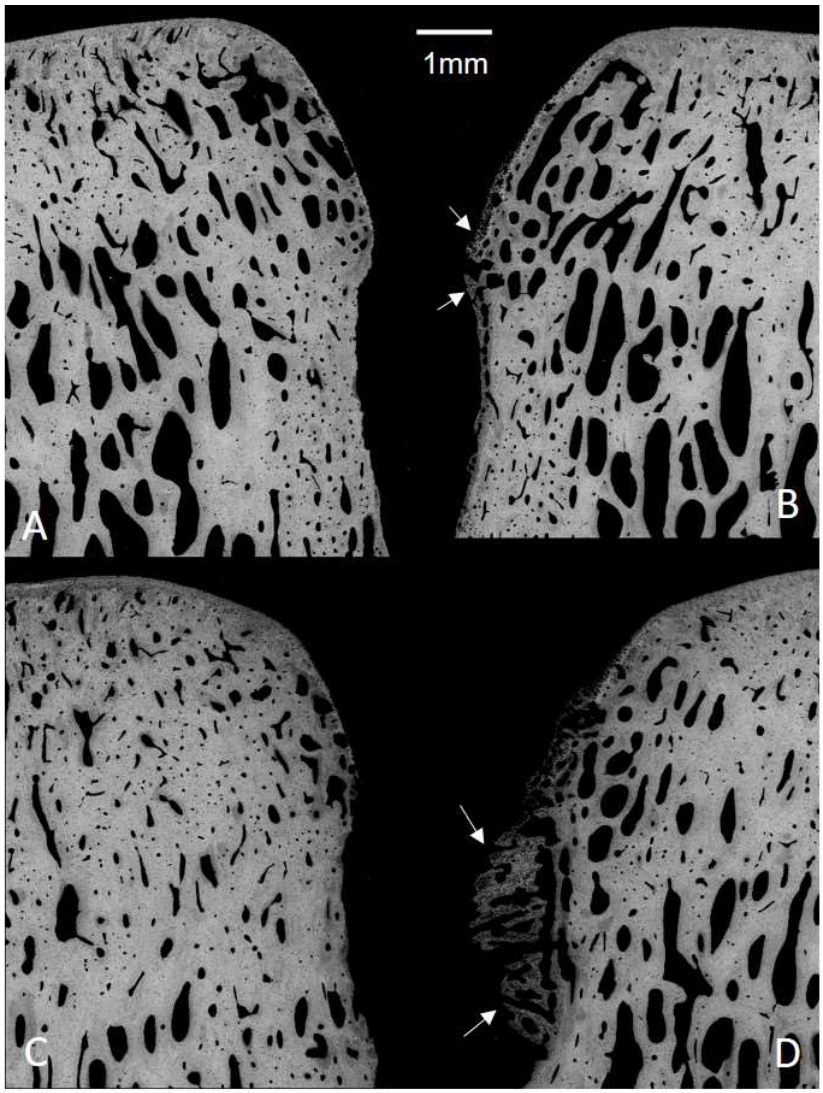

Figure 5.5 *Examples of mild (B, Horse 3) and more marked (D, Horse 4) peri-articular modelling (arrows) at the dorsal articular margin of C3 from the treated limbs. A and C: C3 from control limbs of horse 3 and 4 respectively. BSEM images.*

5.3.1 Region opposing the defect

In the region opposing the defect there was a decrease in bone volume and increase in bone surface in treated limbs when compared with the contralateral controls (Table 5.1). Differences in measures of bone volume were most marked at 0-1mm and 3-6mm deep to the cartilage with microCT analysis showing BV/TV 5.3% lower at 0-3mm and 12% lower at 3-6mm deep to the cartilage (P = 0.04 and P=0.02 respectively, Fig 5.4 and 5.6) and BSEM analysis revealing porosity 59% higher at 0-1mm deep to the cartilage (P=0.05; Fig 5.6 and 5.8). There was a 13% decrease in microCT BV/TV at 6-9mm deep to the cartilage that was not quite significant (P=0.06, Figure 5.6).

Differences were also observed between the treated limbs of the trial horses and the untrained control limbs with the BV/TV of treated limbs at 0-3mm and 3-6mm deep to the cartilage 5.0% lower and 16% lower respectively than the untrained controls (P=0.05 and P=0.01 respectively, Figure 5.6).

The decreased BV/TV was matched by an increase in bone surface in treated limbs when compared with the contralateral controls with a 33% increase in BS/BV on microCT at 3-6mm deep to the cartilage (P = 0.02, Figure 5.7, Table 5.2), an 18% increase in pore perimeter on BSEM at 0-1mm and an 8.7% increase in pore perimeter at 0-3mm deep to the cartilage (P = 0.01 and P = 0.03 respectively; Figure 5.7).

The treated limbs of the trial horses had a higher BS/BV than the untrained controls at 3-6mm deep to the cartilage on microCT images (Figure 5.7). Additionally, the control limbs of the trial horses had a lower pore perimeter than the untrained controls at a depth of 0-1mm on BSEM (Figure 5.7).

Depth below cartilage	Parameter	Mean (Median), Range			P-value		
		Trial treated	Trial Control	Untrained control	Trial treated v Trial control	Trial treated v Untrained control	Untrained control v Trial control
0-1mm	BV/TV (%)	84.7 (88.4), 47.7	96.1 (96.8), 10.3	93.9 (94.6), 10.3	0.09	0.17	0.36
	BS/BV (mm^{-1})	6.75 (5.35), 12.78	3.78 (3.77), 1.74	3.44 (3.69), 3.21	0.09	0.07	0.57
	Porosity (%)	19.0 (18.9), 23.6	12.0 (10.8), 10.9	16.0 (15.6), 9.22	**0.05**	0.47	0.10
	Pore perim. (mm^{-1})	9.37 (9.94), 3.02	7.94 (8.00), 2.40	9.90, (9.50), 3.71	**0.01**	0.51	**0.02**
0-3mm	BV/TV (%)	89.4 (92.6), 31.8	96.5 (97.8), 7.2	97.2 (97.5), 4.1	**0.04**	**0.05**	0.60
	BS/BV (mm^{-1})	4.01 (3.23), 7.25	2.51 (2.41), 1.46	2.40 (2.43), 0.94	0.06	0.19	0.68
	Porosity (%)	15.7 (14.1), 24.3	11.3 (10.6), 10.1	14.6 (13.5), 10.7	0.14	0.79	0.19
	Pore perim. (mm^{-1})	7.48 (7.64), 1.48	6.88 (6.63), 2.06	8.08 (7.52), 3.59	**0.03**	0.36	0.10
3-6mm	BV/TV (%)	74.3 (74.0), 21.2	84.7 (88.9), 29.5	88.1 (88.2), 15.2	**0.02**	**0.01**	0.54
	BS/BV (mm^{-1})	5.56 (5.17) 3.37	4.17 (3.42), 4.57	3.62 (3.62), 2.08	**0.02**	**0.02**	0.52
	Porosity (%)	25.2 (24.7), 22.2	25.2 (24.7), 23.4	16.6 (18.5), 9.62	0.06	0.054	0.55
	Pore perim. (mm^{-1})	5.20 (5.13), 1.18	4.80 (4.79), 1.70	5.54 (5.33), 4.01	0.07	0.61	0.30
6-9mm	BV/TV (%)	56.4 (54.6), 23.2	65.0 (64.1), 38.7	67.1 (65.4), 30.4	0.06	0.10	0.78
	BS/BV (mm^{-1})	8.40 (8.12), 5.56	7.31 (7.02), 6.60	6.91 (6.94), 4.21	0.09	0.16	0.72
	Porosity (%)	38.5 (35.4), 45.3	36.7 (37.0), 39.6	33.9 (33.3), 31.2	0.86	0.57	0.71
	Pore perim. (mm^{-1})	4.02 (3.80), 1.88	4.28 (4.33), 2.03	4.67 (4.37), 2.72	0.56	0.21	0.47

Table 5.2 *Measures of bone volume and bone surface in the region opposing the defect, C3. BV/TV = Bone volume/ Total volume (%), BS/BV = Bone surface/ Bone volume (mm^{-1}) measured from microCT images; Porosity = pore area/bone area (%) and pore perim. = pore perimeter/ bone area (mm^{-1}) measured from BSEM images. P-values ≤ 0.05 in bold.*

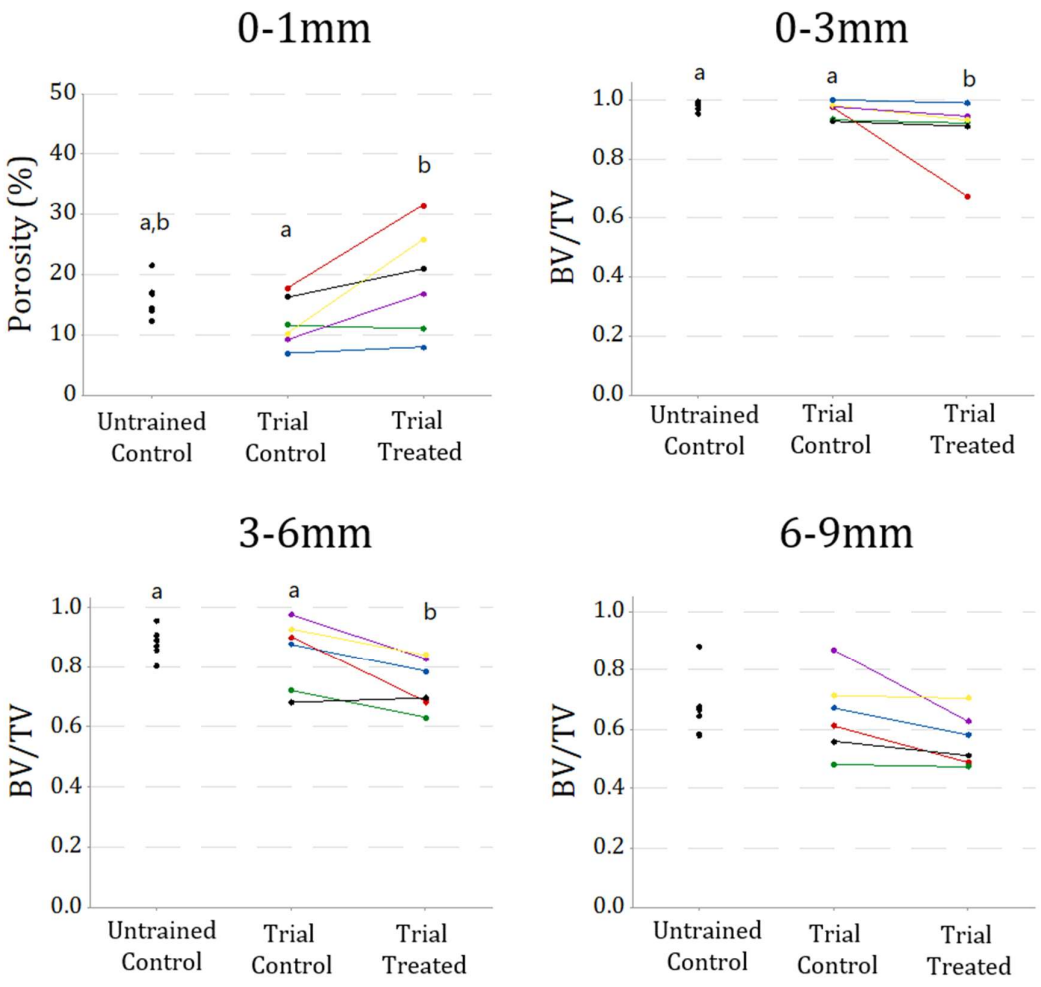

Figure 5.6 *Bone Volume Fraction (BV/TV) measured on microCT images and porosity (%) measured on BSEM images, C3, region opposing the defect. Different letters denote statistically different groups at a level of P<0.05.*

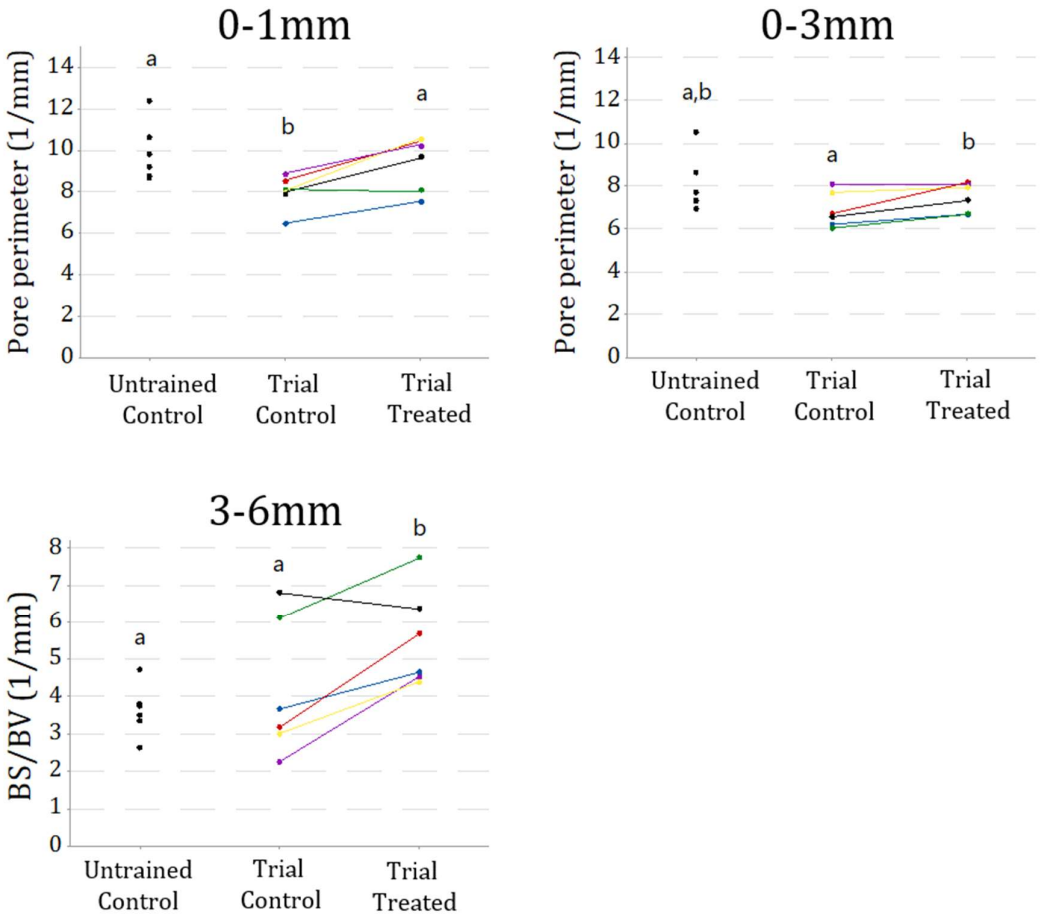

Figure 5.7 *Measures of bone surface, C3, region opposing the lesion. Bone Surface Ratio (BV/TV, mm-1), from microCT images, 3-6mm deep to the cartilage and pore perimeter (mm-1) from BSEM images, 0-1mm and 0-3mm deep to the cartilage. Different letters denote statistically different groups at a level of P<0.05.*

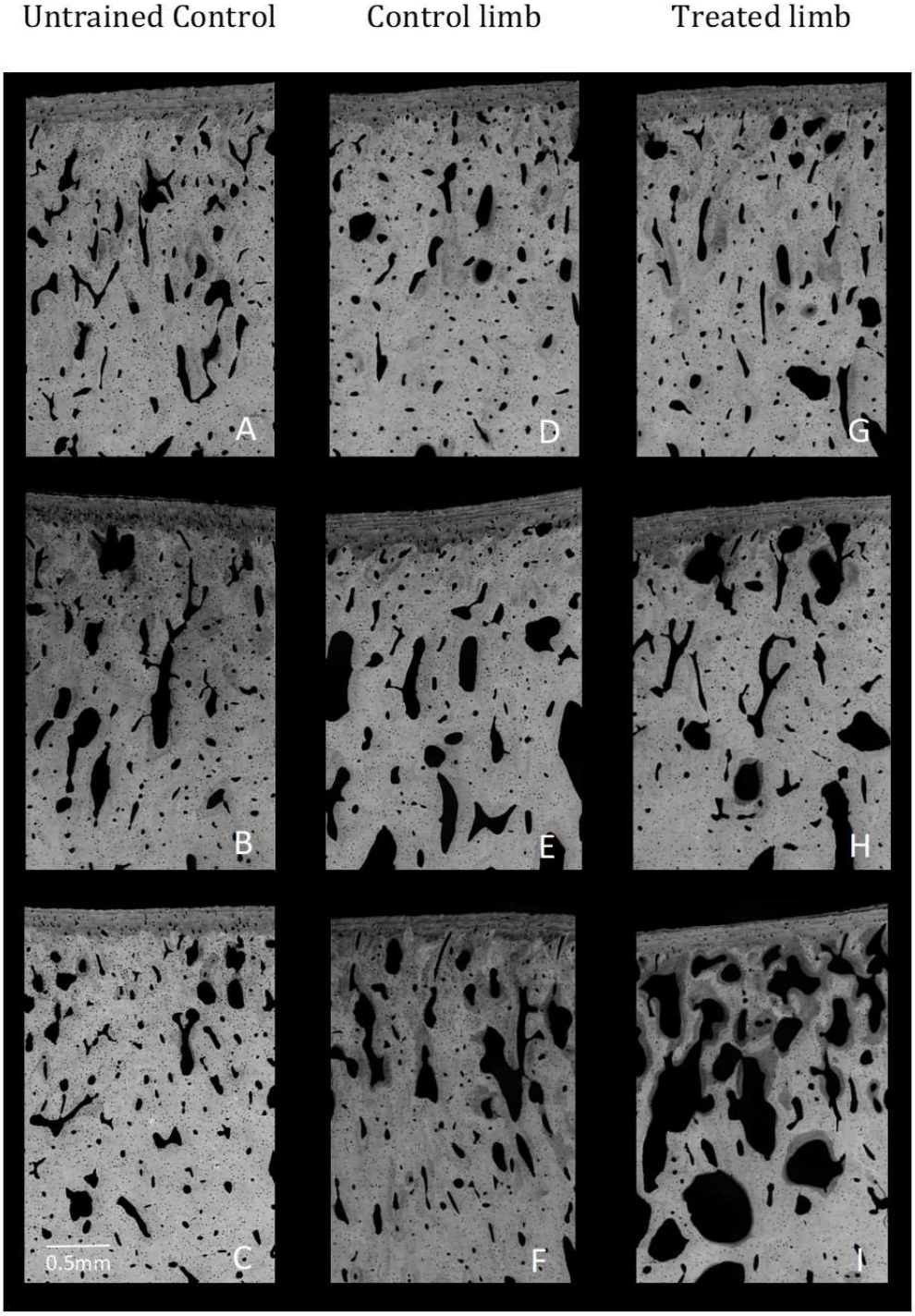

Figure 5.8 *BSEM images, C3, region opposing the defect, 0-3mm deep to the cartilage showing increased porosity and pore perimeter in treated compared to the contralateral control limbs. A= untrained control horse 2, B= untrained control horse 4, C= untrained control horse 5, D and G = Horse 1 control and treated respectively, E and H= horse 6 control and treated respectively, F and I = horse 5 control and treated respectively.*

The bone surface area was also observed to vary within individual C3s, increasing with increasing distance from the articular surface. When all C3 were considered together the ROIs at 3-6mm and 6-9mm deep to the cartilage had 50% and 150% greater bone surface area respectively when compared to the 0-3mm depth (P=0.009 and P<0.001 respectively, Figure 5.14). The bone at 6-9mm also had a 69% greater bone surface area when compared to the 3-6mm depth (P<0.001, Figure 5.9).

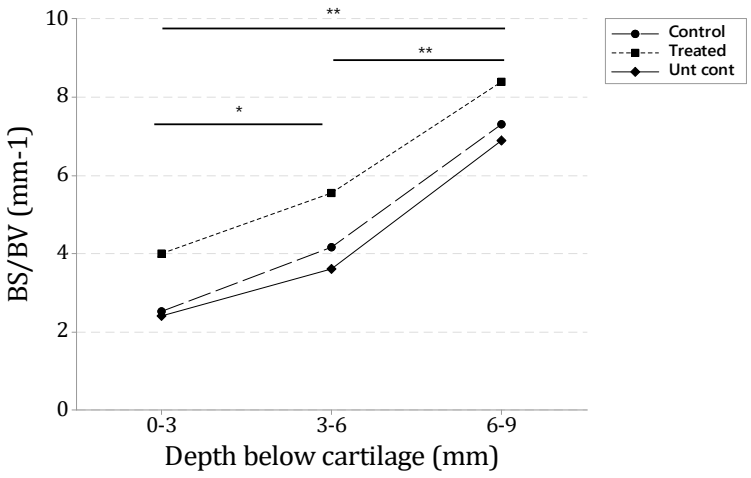

Figure 5.9 *Bone surface per bone volume (mm-1) C3, at different depths deep to the cartilage in the region opposing the lesion, measured on microCT images. * indicates groups differ significantly at P<0.01, ** indicates groups differ significantly at P<0.001.*

The SCB was observed to transition from a compact to a more trabecular structure at 3-6mm deep to the cartilage. A lower Tb.Th and greater Tb.Sp were associated with the reduction in bone volume in treated compared with contralateral control limbs in this region on microCT images (P=0.03 and P=0.02 respectively, Figures 5.10).

There was also an 8.5% decrease in tissue mineral density (TMD) measured on microCT images in treated limbs when compared with their contralateral controls at 3-6mm deep to the cartilage (P=0.04, Figure 5.10). At 6-9mm deep to the cartilage there was an 8.9% decrease in TMD in treated limbs when compared with their contralateral controls that approached significance (P=0.06, Figure 5.10). This reduction in TMD appeared to be driven predominantly by the decrease in BV/TV as there was no difference in BMD between the treated and control limbs at any depth. The TMD of the treated limbs was also 10% lower than that of the untrained controls at 3-6mm deep to the cartilage (P = 0.02, Figure 5.10). See Table 5.3 for all trabecular and mineral density results

Depth below cartilage	Parameter	Mean (Median), Range			P-value		
		Trial treated	Trial Control	Untrained control	Trial treated v Trial control	Trial treated v Untrained control	Trial control v Untrained control
0-3mm	Tb.N (mm^{-1})	3.31 (3.51), 1.16	3.22 (3.51), 1.94	3.23 (3.32), 1.06	0.63	0.78	0.97
	Tb.Th (mm)	0.469 (0.454), 0.429	0.579 (0.494), 0.691	0.555 (0.520), 0.218	0.19	0.26	0.84
	Tb.Sp (mm)	0.141 (0.144), 0.104	0.103 (0.086), 0.086	0.096 (0.089), 0.084	0.06	0.06	0.72
	BMD ($mgHA/cm^3$)	765 (766), 83.3	772 (767), 69.3	764 (757), 68.2	0.65	0.91	0.55
	TMD ($mgHA/cm^3$)	717 (732), 174	753 (750), 101	748 (742), 68.1	0.23	0.31	0.76
3-6mm	Tb.N (mm^{-1})	2.88 (2.90), 0.695	2.93 (2.94), 0.438	2.90 (2.93), 0.387	0.32	0.90	0.76
	Tb.Th (mm)	0.366 (0.387), 0.181	0.462 (0.522), 0.294	0.467 (0.467), 0.131	**0.02**	**0.01**	0.93
	Tb.Sp (mm)	0.278 (0.279), 0.164	0.198 (0.207), 0.161	0.190 (0.193), 0.114	**0.03**	**0.02**	0.78
	BMD ($mgHA/cm^3$)	774 (765), 42.6	782 (782), 30.2	775 (782), 36.0	0.48	0.91	0.43
	TMD ($mgHA/cm^3$)	643 (645), 136	703 (733), 158	716 (715), 82.0	**0.04**	**0.02**	0.68
6-9mm	Tb.N (mm^{-1})	2.50 (2.58), 1.05	2.76 (2.62), 0.819	2.74 (2.65), 0.771	0.15	0.27	0.90
	Tb.Th (mm)	0.254 (0.258) 0.132	0.277 (0.280), 0.185	0.288 (0.288), 0.131	0.29	0.22	0.72
	Tb.Sp (mm)	0.345 (0.309), 0.258	0.274 (0.291), 0.162	0.262 (0.283), 0.150	0.08	0.10	0.74
	BMD ($mgHA/cm^3$)	752 (741), 42.6	755 (759), 27.5	748 (747), 51.4	0.61	0.72	0.38
	TMD ($mgHA/cm^3$)	532 (524), 157	584 (580), 211	595 (576), 176	0.06	0.11	0.81

Table 5.3 *Trabecular parameters and mineral density measurements from MicroCT images, C3, region opposing the lesion. Tb.N = trabecular number (mm^{-1}), Tb.Th = trabecular thickness (mm), Tb.Sp = trabecular separation (mm), BMD = bone material density (mg hydroxyapatite/cm^3), TMD = tissue mineral density (mg hydroxyapatite/cm^3). P-values ≤ 0.05 in bold.*

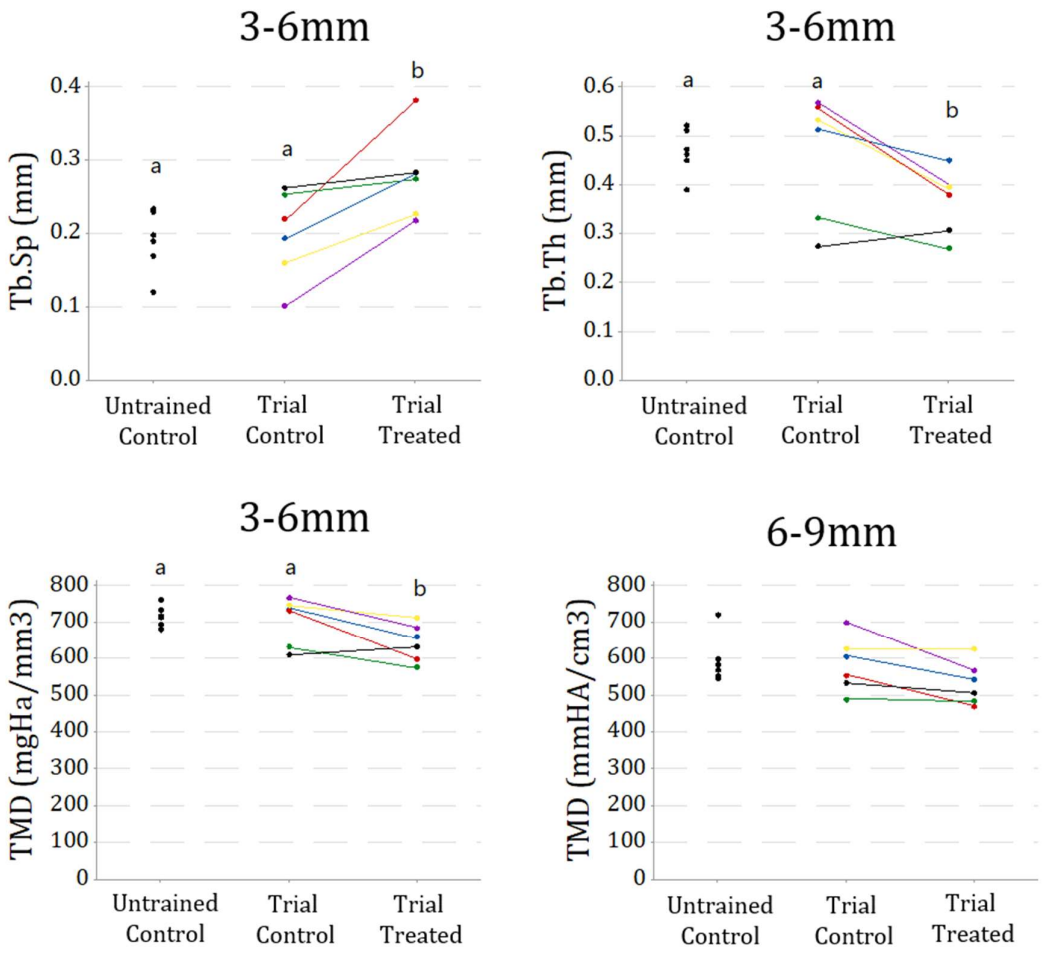

Figure 5.10 *Trabecular parameters and tissue mineral density measured on microCT images, C3, region opposing the lesion, 3-6mm and 9-9mm deep to the cartilage. Tb.Sp = trabecular separation (mm), Tb.Th =trabecular thickness (mm), TMD = tissue mineral density (mgHa/mm3). Different letters denote statistically different groups at a level of P<0.05.*

The above changes in bone volume, surface and structure were also associated with increased bone remodelling as evidenced by increases in measures of combined erosion and formation perimeter (active perimeter) in treated limbs when compared with the contralateral control limbs (Table 5.4). A 47% increase in active perimeter on BSEM, was observed at 0-1mm deep to the cartilage (P= 0.03, Figure 5.11).

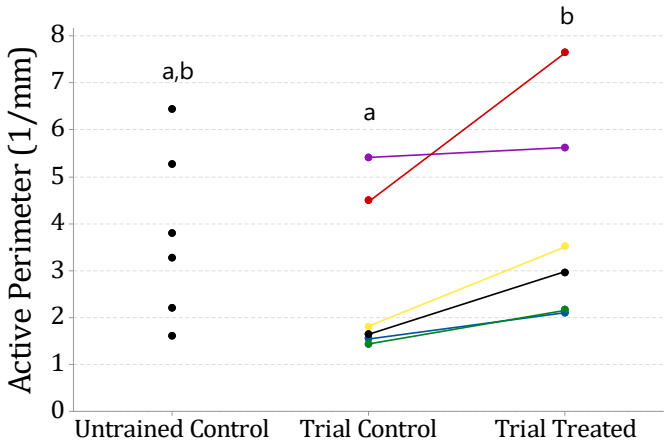

Figure 5.11 *Active perimeter per bone area (mm-1) measured on BSEM images, C3, region opposing the lesion, 0-1mm deep to the cartilage. Different letters signify groups that differ significantly at a level of P<0.05.*

Depth below cartilage	Parameter	Mean (Median), Range			P-value		
		Trial Treated	Trial Control	Untrained Control	Trial treated v Trial control	Trial treated v Untrained control	Untrained control v Trial control
0-1mm	Er.Pm (mm^{-1})	1.13 (1.11), 1.35	0.795 (0.764), 0.943	1.60 (1.40), 1.73	0.26	0.18	**0.03**
	Min.Pm (mm^{-1})	2.87 (1.77), 6.03	1.93 (1.14), 4.72	2.17 (1.84), 3.52	0.21	0.55	0.81
	Act.Pm (mm^{-1})	4.00 (3.24), 5.54	2.72 (1.72), 3.98	3.77 (3.54), 4.83	**0.03**	0.85	0.34
0-3mm	Er.Pm (mm^{-1})	0.882 (0.985), 0.717	0.703 (0.605), 1.02	1.04 (1.02), 0.574	0.30	0.31	0.12
	Min.Pm (mm^{-1})	1.77 (1.30), 3.97	1.02 (0.644), 2.59	1.02 (0.644), 2.59	0.21	0.72	0.36
	Act.Pm (mm^{-1})	2.65 (2.33), 3.34	1.73 (1.74), 2.13	2.55 (2.32), 2.50	0.15	0.14	0.88
3-6mm	Er.Pm (mm^{-1})	0.778 (0.790), 0.368	0.684 (0.608), 1.00	0.730 (0.414), 2.01	0.90	0.89	0.61
	Min.Pm (mm^{-1})	0.702 (0.701), 1.06	0.727 (0.549), 1.13	0.733 (0.597), 1.83	0.61	0.92	0.99
	Act.Pm (mm^{-1})	1.48 (1.52), 0.803	1.41 (1.37), 1.15	1.46 (1.09), 3.83	0.51	0.98	0.93
6-9mm	Er.Pm (mm^{-1})	0.639 (0.558), 0.854	0.611 (0.449), 1.38	0.790 (0.625), 1.86	0.93	0.64	0.62
	Min.Pm (mm^{-1})	0.672 (0.720), 0.984	0.867 (0.846), 0.854	1.09 (1.16), 1.09	0.28	0.09	0.34
	Act.Pm (mm^{-1})	1.31 (1.23), 1.28	1.48 (1.51), 1.64	1.88 (1.86), 2.35	0.64	0.09	0.37

Table 5.4 *Erosion and formation parameters from BSEM images, C3, region opposing the lesion. Er.Pm = Erosion perimeter/ Bone area (mm^{-1}), Min. Pm = Mineralising perimeter/ Bone area (mm^{-1}), Act.Pm = Active perimeter/ Bone area (mm^{-1}). P-values ≤ 0.05 in bold.*

There was no significant difference between the treated and control limbs of the trial animals at any depth below the cartilage when either erosion or mineralising perimeter was considered in isolation. However, at 0-1mm deep to the cartilage, erosion perimeter was increased in the treated limb of 5 of the 6 trial animals and mineralising perimeter was increased in the treated limb in 5 of the 6 trial animals when compared with their contralateral controls (Figure 5.12). In the animal where there was a decrease in erosion perimeter there was the greatest increase in mineralising perimeter. Similarly, the animal that had a decrease in mineralising perimeter had the greatest increase in erosion perimeter.

The erosion perimeter of the control limbs of the trial animals was 50% lower than that of the untrained controls at 0-1mm deep to the cartilage (P = 0.03, Figure 5.12). See Table 5.4 for all erosion and formation results.

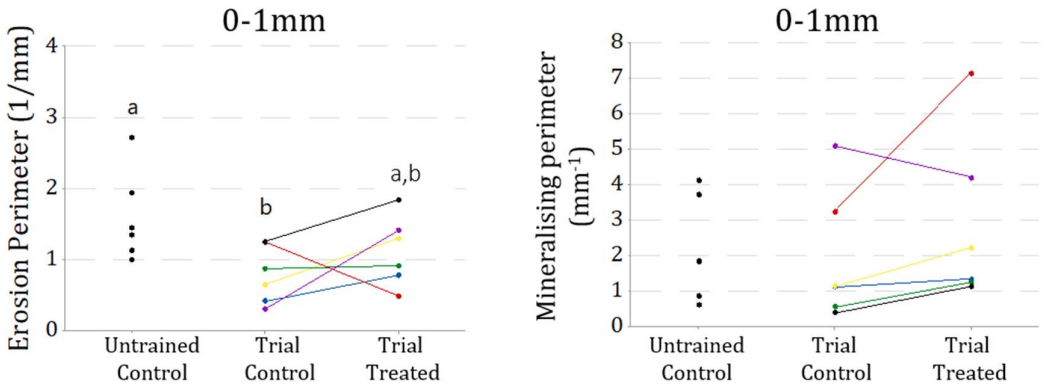

Figure 5.12 *Erosion perimeter and mineralising perimeter per bone area (mm-1) measured on BSEM images, C3, region opposing the lesion, 0-1mm deep to the cartilage. Different letters signify groups that differ significantly at a level of P<0.05.*

Despite no difference between groups in the erosion perimeter at 3-6mm deep to the cartilage on BSEM images, an increase in the number of osteoclasts on TRAP stained cryosections was observed. This was observed at a depth of 3.3-6.6mm deep to the cartilage but not in the more superficial ROI at 0-1.1mm or 0-3.3mm deep to the cartilage (Figures 5.13 and 5.14, Table 5.5).

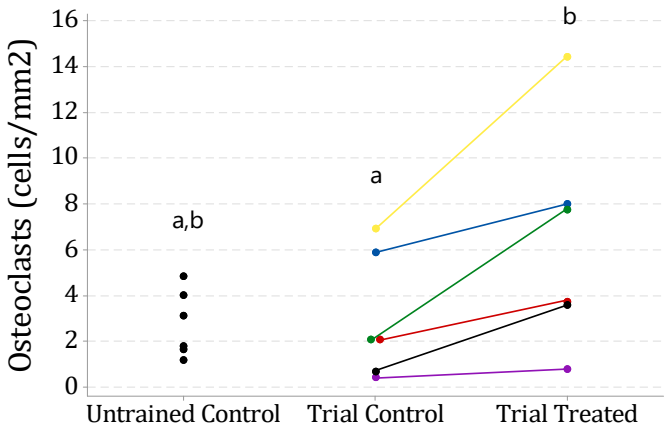

Figure 5.13 *Osteoclast number (cells/mm2) measured on TRAP stained cryosections, C3, region opposing the lesion, 3.3-6.6mm deep to the cartilage. Different letters denote significantly different groups at a level of P<0.05.*

Depth below cartilage (For O'clast N)	Parameter	Mean (Median), Range			P-value		
		Trial treated	Trial Control	Untrained control	Trial treated v Trial control	Trial treated v Untrained control	Trial control v Untrained control
0-1mm (0-1.1mm)	Osteoclast N (cells/mm^2)	7.92 (6.41), 20.1	4.33 (2.90), 9.60	3.72 (3.44), 9.09	0.30	0.24	0.79
	O.Pm (%)	0.514 (0.443), 0.736	0.395 (0.400), 0.317	0.452 (0.427), 0.617	0.29	0.67	0.59
	O.Wi (um)	8.31 (7.63), 12.0	4.94 (4.84), 2.18	5.29 (5.33), 3.39	0.09	0.15	0.56
0-3mm (0-3.3mm)	Osteoclast N (cells/mm^2)	5.95 (5.46), 14.0	3.00 (2.64), 6.43	3.04 (2.32) 8.40	0.18	0.25	0.98
	O.Pm (%)	32.5 (26.5), 60.9	24.7 (24.5), 22.4	31.1 (30.9), 42.6	0.41	0.91	0.45
	O.Wi (um)	9.44 (8.76), 10.8	5.80 (6.10), 2.20	5.61 (5.12), 2.83	**0.04**	0.06	0.75
	dL.Pm/L.Pm (%)	40.1 (44.5), 56.2	32.0 (38.7), 45.0	NA	**0.04**	NA	NA
3-6mm (3.3-6.6mm)	Osteoclast N (cells/mm^2)	6.38 (5.75), 13.64	3.01 (2.07), 6.5	2.76 (2.46), 3.63	**0.03**	0.14	0.85
	O.Pm (%)	14.0 (14.4), 21.3	12.3 (12.4), 13.3	17.0 (12.4), 30.8	0.73	0.66	0.45
	O.Wi (um)	8.88 (9.13), 11.9	7.86 (8.91), 6.46	6.18 (5.74), 7.49	0.72	0.21	0.33
	N.dL/B.Ar (mm^{-2})	0.991 (0.688), 2.52	0.081 (0.061), 0.192	NA	**0.04**	NA	NA
6-9mm	O.Pm (%)	15.3 (16.0), 29.3	17.4 (16.2), 27.8	10.7 (9.5), 21.9	0.81	0.44	0.27
	O.Wi (um)	9.55 (8.94), 14.31	8.00 (7.31), 8.54	5.78 (4.71), 5.59	0.29	0.12	0.22
	N.dL/B.Ar (mm^{-2})	0.977 (0.871), 1.56	0.521 (0.244), 1.72	NA	**0.04**	NA	NA

Table 5.5 *Cellular markers of remodelling and measures of fluorochrome labelling, C3, region opposing the defect. Osteoclast numbers (cells/mm^2) from TRAP stained sections, O.Wi = osteoid width (um) and O.Pm = Osteoid perimeter/Bone perimeter (%) from Masson's Goldner stained sections, dL.Pm/L.Pm = proportion of double labelled perimeter (%) and N.dL/B.Ar = number of double labels/ bone area (number of labels/ mm^2) from fluorochrome analysis. P-values ≤ 0.05 in bold.*

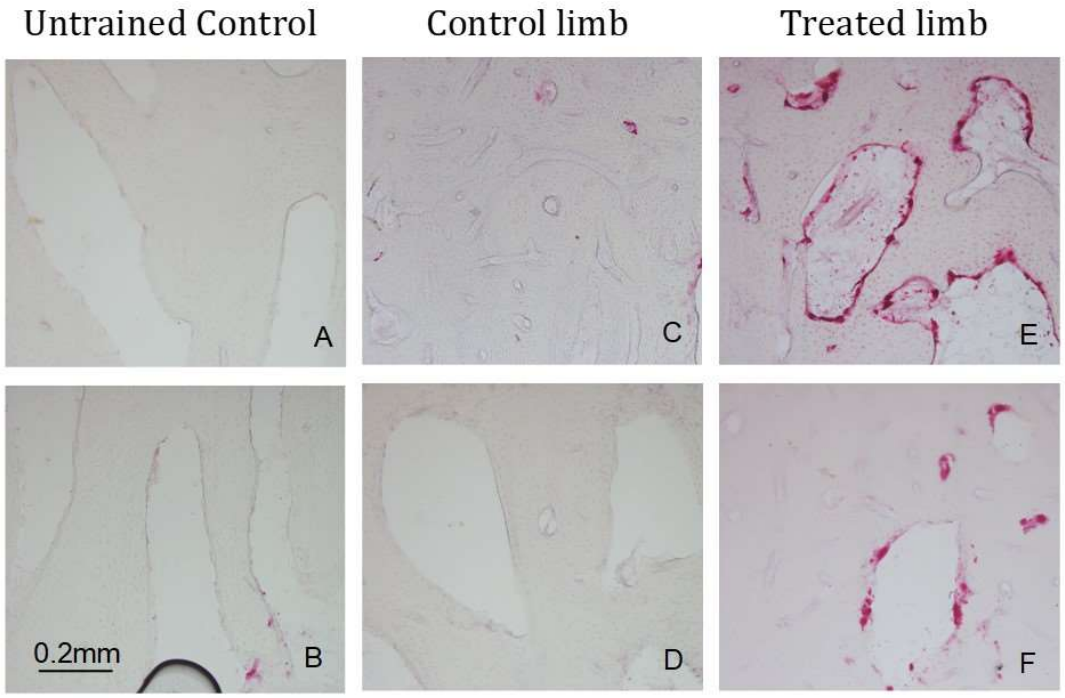

Figure 5.14 *TRAP stained sections, C3, region opposing the lesion, 3.3-6.6mm deep to the cartilage where there is a greater number of osteoclasts in treated compared to control limbs of the trial horses. untrained control horse 1 (A), untrained control horse 4 (B), Horse 2 control (C) and treated (E) limbs, horse 3 control (D) and treated (F) limbs. Light microscopy.*

An increase in osteoid width at 0-3mm deep to the cartilage in the treated limbs compared to the contralateral control limbs was observed on MG stained sections (P = 0.04, Figures 5.15 and 5.16). There was no difference in osteoid perimeter or area at any depth below the cartilage.

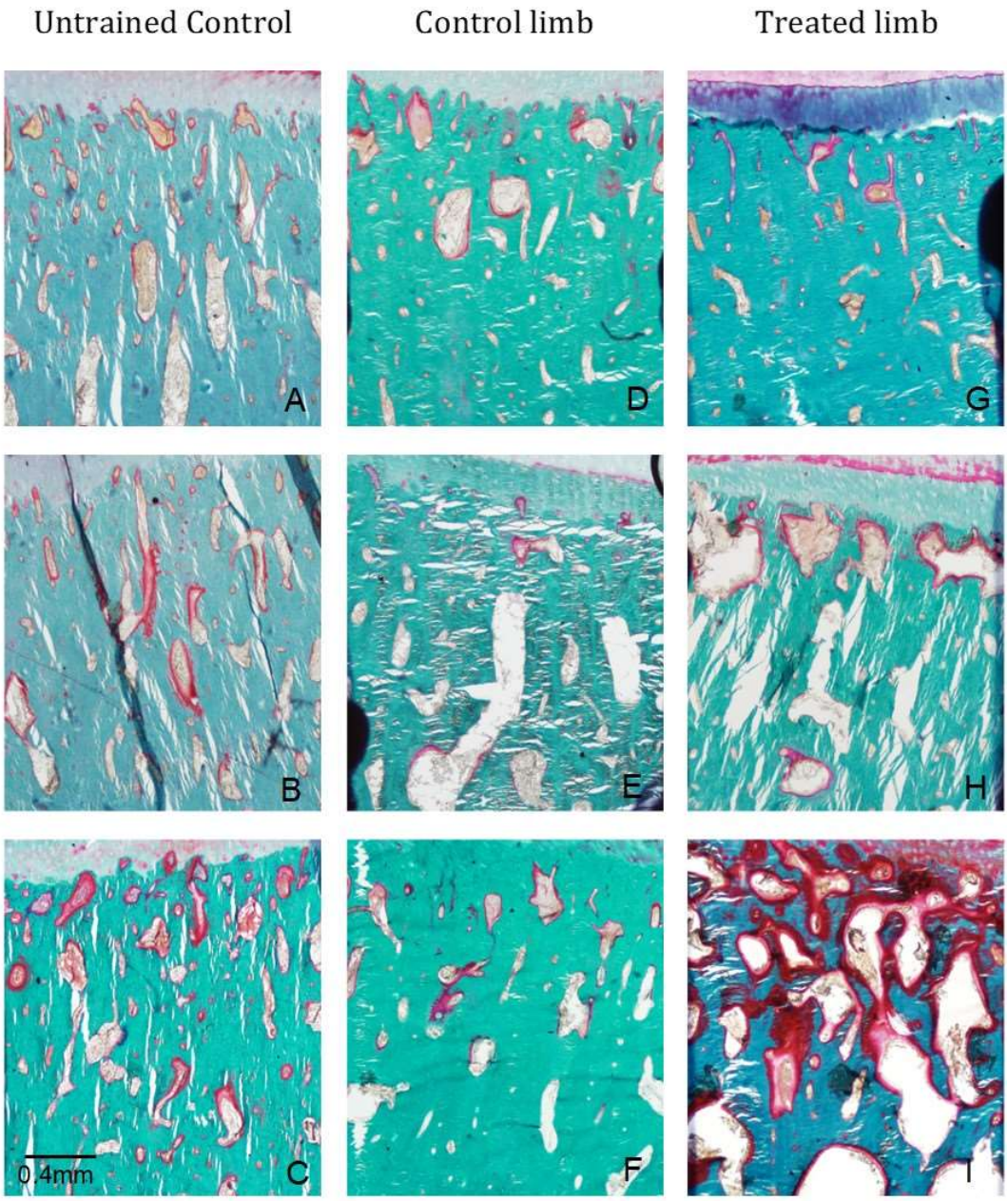

Figure 5.15 *Masson's Goldner stained sections of C3, region opposing the lesion, 0-3mm deep to cartilage where osteoid width is greater in the treated limbs compared to control limbs of the trial horses. untrained control horse 6 (A), untrained control horse 3 (B), untrained control horse 4 (C), Horse 3 control (D) and treated (G) limbs, Horse 1 control (E) and treated (H) limbs and Horse 5 control (F) and treated (I) limbs. Light microscopy.*

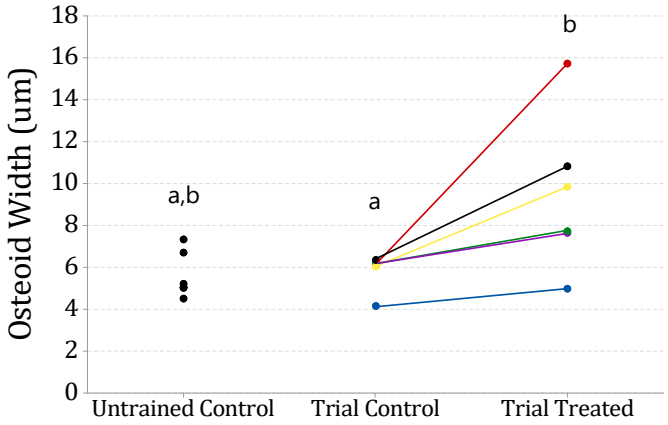

Figure 5.16 *Osteoid width (um) measured on Masson's-Goldner stained sections, C3, region opposing the lesion, 0-3.0mm deep to the cartilage. Different letters denote significantly different groups at a level of P<0.05.*

A more sustained bone formation over time in the treated limbs compared to the contralateral controls was suggested by fluorochrome labels (Figures 5.17-5.19). There was a 25% increase in the ratio of double labelled surface to total labelled surface at a depth of 0-3mm deep to the cartilage (P=0.04, Figure 5.17), an approximately 10-fold increase in the number of double labels at 3-6mm deep to the cartilage (P = 0.04, Figure 5.17) and an 88% increase in the number of double labels at 6-9mm deep to the cartilage (P = 0.04, Figure 5.17). See Table 5.5 for all osteoid and fluorochrome results.

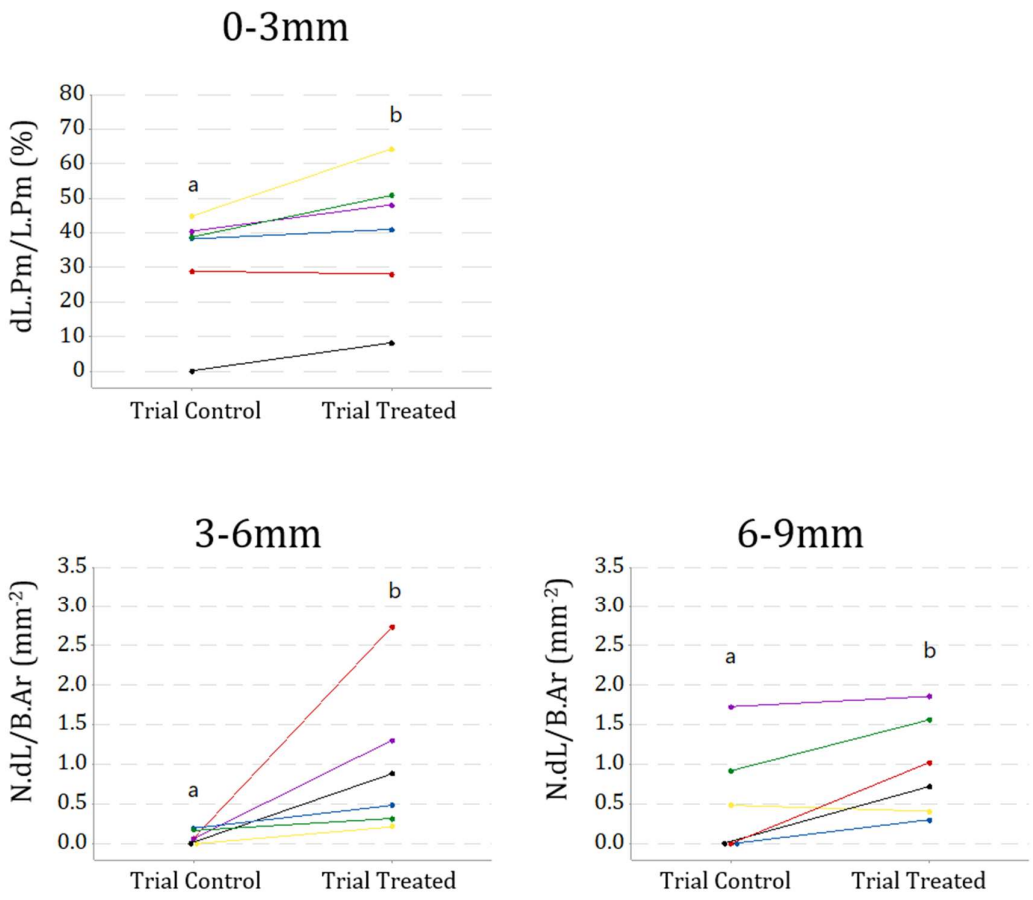

Figure 5.17 *Measures of fluorochrome labelling, C3, region opposing the lesion. Measured on unstained sections. dL.Pm/L.Pm = ratio of Double-labelled perimeter to Labelled perimeter (%), 0-3.0mm deep to the cartilage. N.dL/B.Ar = Number of double labels per bone area (mm-2) 3-6mm and 6-9mm deep to the cartilage. Different letters denote significantly different groups at a level of P<0.05.*

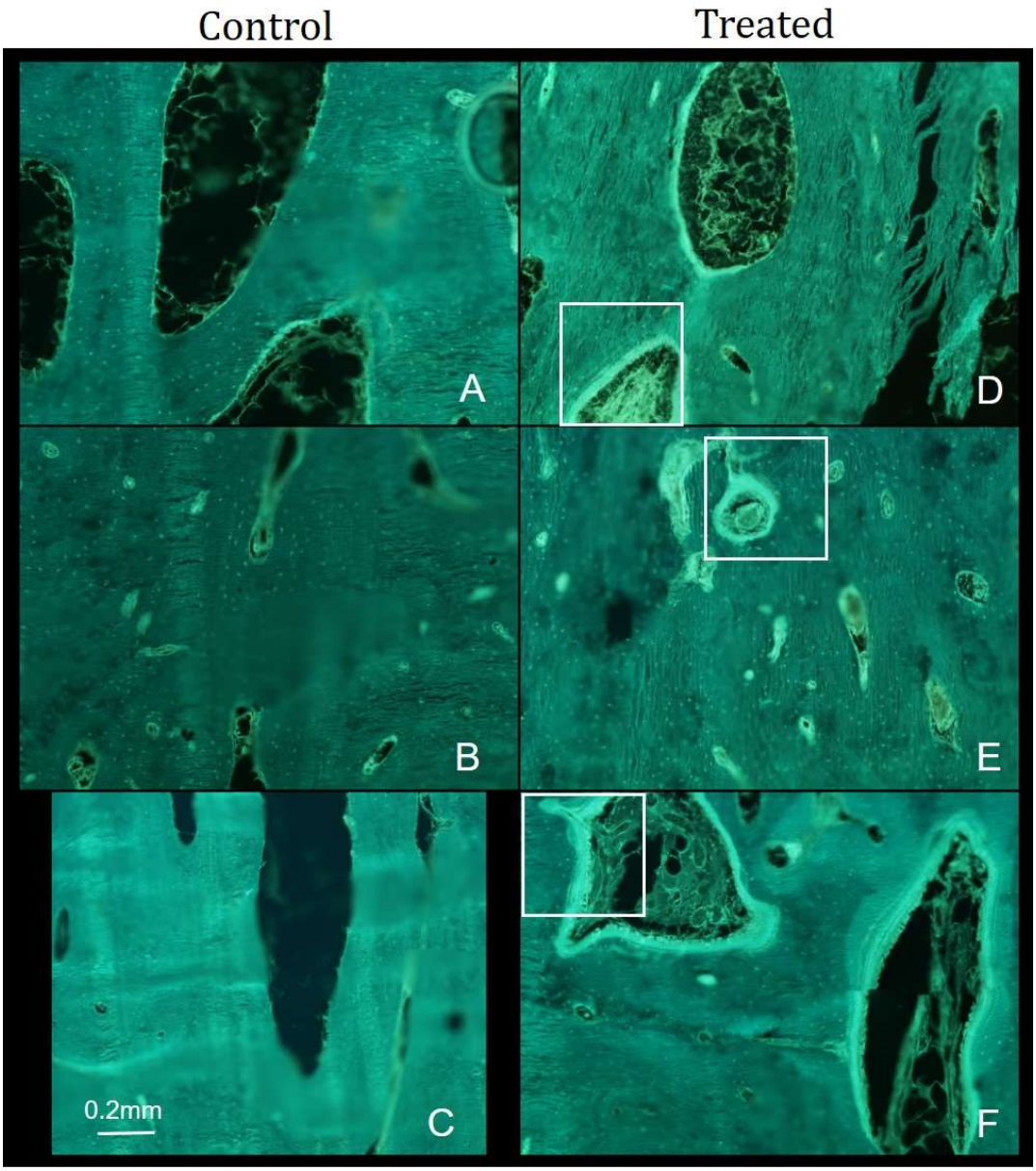

Figure 5.18 *Unstained, undecalcified sections, fluorescent light microscopy of C3, region opposing the lesion, 3-6mm deep to the surface. Control and treated limbs respectively of Horse 1 (A and D), Horse 2 (B and E) and Horse 5 (C and F). White boxes show areas enlarged in Figure 5.26.*

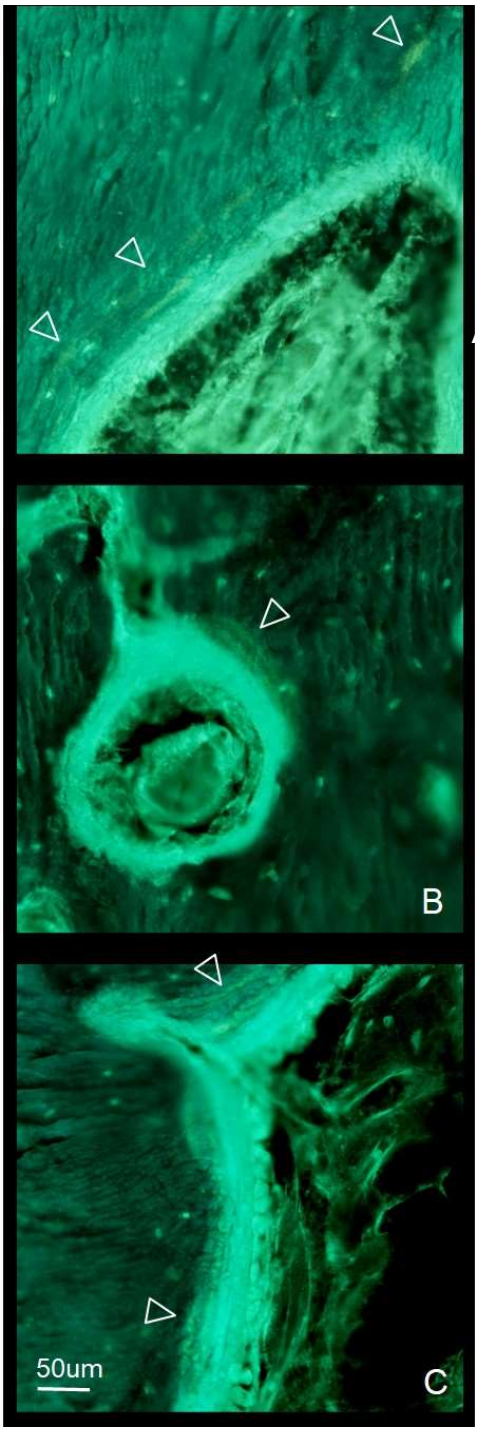

Figure 5.19 *Enlargements from Figure 5.18 showing fluorescent labels (arrowheads) in treated limbs of Horse 1 (A), Horse 2 (B) and Horse 5 (C). C3, region opposing the lesion, 3-6mm deep to surface where there is an increased proportion of double labelled perimeter and an increased incidence of double labels in the treated limbs. Unstained, undecalcified sections, fluorescent light microscopy.*

5.3.2 Weight bearing region

In the region of C3 where articular surface contact had been maintained, there was no overall difference in bone volume between any of the groups at any depth when measured on either microCT or BSEM (Table 5.6). There was also no difference between groups in trabecular structure in this region (data not shown).

However, there was an 18% reduction in pore perimeter on BSEM in the treated limbs of the trial animals when compared with their contralateral controls at 0-3mm deep to the cartilage (P=0.03, Figure 5.20 and 5.21).

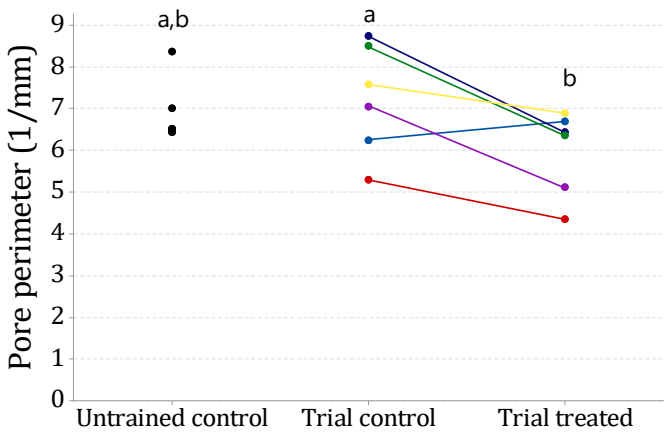

Figure 5.20 *Pore perimeter (mm-1), measured on BSEM images, C3, weight bearing region, 0-3mm deep to the cartilage. Different letters denote statistically different groups at a level of P<0.05.*

Depth below cartilage	Parameter	Mean (Median), Range			P-value		
		Trial treated	Trial Control	Untrained control	Trial treated v Trial control	Trial treated v Untrained control	Untrained control v Trial control
0-3mm	BV/TV (%)	91.6 (90.4) 106	86.7 (91.8), 39.5	91.4 (91.8), 130	0.44	0.94	0.49
	BS/BV (mm^{-1})	3.44 (3.69), 2.57	4.45 (3.57), 7.35	3.53 (3.50), 2.81	0.38	0.87	0.47
	Porosity (%)	15.6 (17.5), 9.53	21.5 (19.5), 31.8	21.4 (20.1), 16.9	0.19	0.12	0.99
	Pore perim. (mm^{-1})	5.97 (6.40), 2.54	7.23 (7.31), 3.45	6.87 (6.51), 1.92	**0.03**	0.11	0.58
3-6mm	BV/TV (%)	73.2 (73.9) 22.3	77.0(82.2), 40.1	76.5 (74.8), 28.5	0.47	0.54	0.95
	BS/BV (mm^{-1})	6.15(6.05), 4.04	5.74 (4.74), 6.28	5.74(5.90), 4.49	0.65	0.65	1.0
	Porosity (%)	31.6 (33.4), 13.8	24.3 (23.2), 25.4	25.6 (27.9), 21.4	0.12	0.18	0.83
	Pore perim. (mm^{-1})	5.55 (5.24), 2.10	5.29 (5.46), 1.05	5.95 (5.95), 2.39	0.46	0.43	0.15
6-9mm	BV/TV (%)	55.8(57.3), 26.1	62.2(63.7), 39.8	61.7 (58.4), 35.2	0.19	0.41	0.96
	BS/BV (mm^{-1})	9.06 (8.34) 6.21	7.75 (7.35), 5.91	8.40 (9.14), 5.38	0.11	0.60	0.63
	Porosity (%)	43.1 (45.1), 31.0	36.9 (32.7), 37.6	33.7 (36.3), 37.5	0.33	0.24	0.73
	Pore perim. (mm^{-1})	5.36 (5.30), 1.19	5.38 (5.42), 1.70	5.50 (5.60), 2.51	0.88	0.77	0.81

Table 5.6 *Measures of bone volume and bone surface in the weight bearing region, C3***.** *BV/TV = Bone volume/ Total volume (%), BS/BV = Bone surface/ Bone volume (mm^{-1}) measured from microCT images. Porosity = pore area/bone area (%) and pore perim. = pore perimeter/ bone area (mm^{-1}) measured from BSEM images. P-values ≤ 0.05 in bold.*

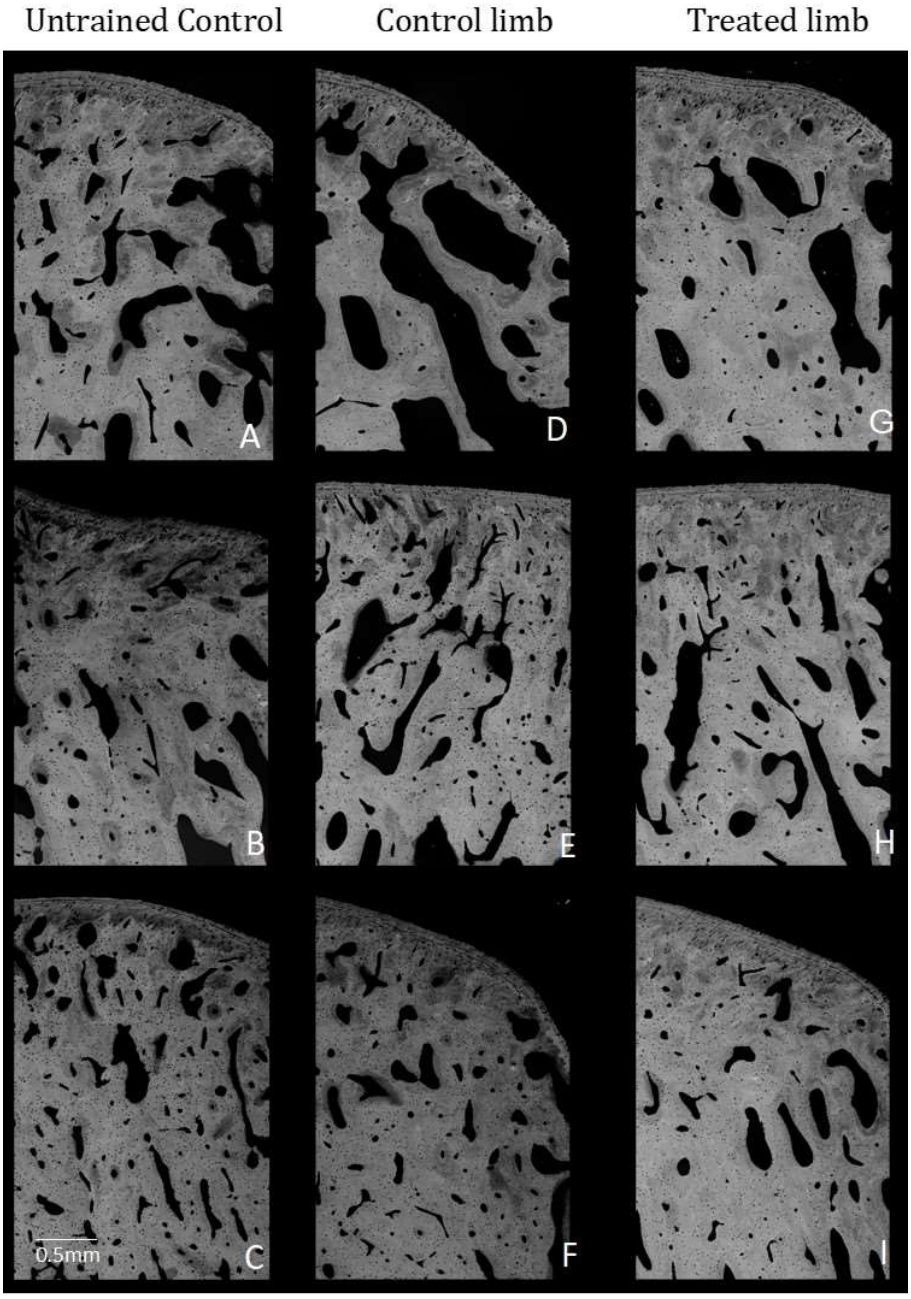

Figure 5.21 *BSEM images, C3, weight bearing region, 0-3mm deep to the cartilage. In this region there is decreased pore perimeter and decreased active surface in treated limbs compared to the contralateral control limbs of the trial horses. A= untrained control horse 1, B= untrained control horse 3, C= untrained control horse 4, D and G = Horse 1 control and treated respectively, E and H= Horse 3 control and treated respectively, F and I = Horse 4 control and treated respectively.*

This reduction in pore perimeter at 0-3mm deep to the cartilage in treated limbs was associated with evidence of reduced remodelling (Table 5.7). Active perimeter at 0-3mm deep to the cartilage in treated limbs was 29% lower than that in the contralateral controls and 40% lower than that in untrained controls (P= 0.01 and P= 0.01 respectively, Figure 5.22).

There was also a 47% reduction in erosion perimeter in the treated limbs when compared to the contralateral controls at 0-3mm deep to the cartilage that was not quite significant (P=0.06, Figure 5.22). Erosion perimeter was lower in the treated limb than in the sham operated limb in all but one of the trial horses, Horse 5, which had the most dramatic increase in erosion in the region opposing the lesion.

The mineralising perimeter at 0-3mm deep to the cartilage on BSEM images of the treated limbs was 32% lower than that in the untrained controls (P= 0.02, Figure 5.22), however, there was no difference between the two limbs of the trial animals in this parameter.

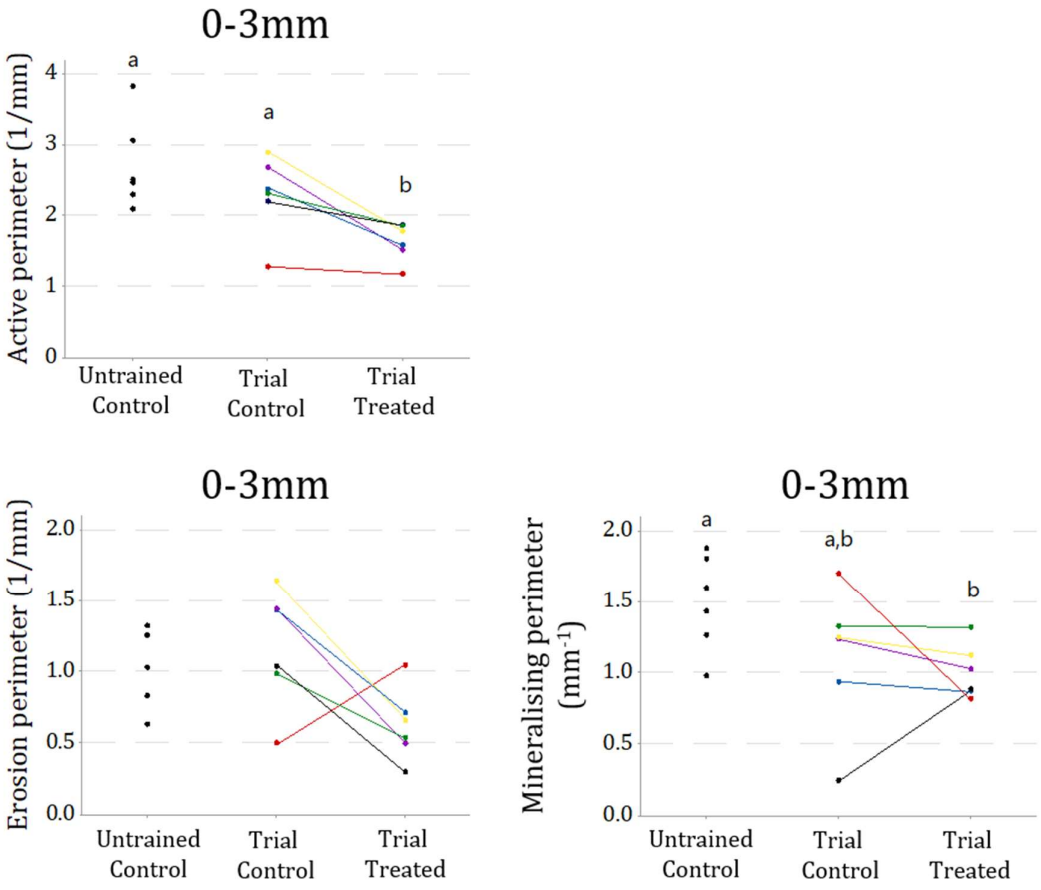

Figure 5.22 *Erosion and formation parameters from BSEM images, C3, weight bearing region, 0-3mm deep to the cartilage. Different letters denote statistically different groups at a level of P<0.05.*

Depth below cartilage (For O'clast N)	Parameter	Mean (Median), Range			P-value		
		Trial treated	Trial Control	Untrained control	Trial treated v Trial control	Trial treated v Untrained control	Untrained control v Trial control
0-3mm (0-3.3)	Er.Pm (mm^{-1})	0.623 (0.597), 0.750	1.17 (1.24), 1.14	1.21 (1.14), 1.59	0.06	0.06	0.89
	Min.Pm(mm^{-1})	1.01 (0.953),0.500	1.12 (1.24), 1.46	1.49 (1.52) 0.900	0.61	**0.02**	0.16
	Act.Pm(mm^{-1})	1.63 (1.68), 0.684	2.29 (2.34), 1.61	2.70 (2.48), 1.73	**0.01**	**0.01**	0.26
	Osteoclast N (cells/mm^2)	4.25 (3.58), 8.59	4.58 (4.12), 8.01	2.15 (2.16), 3.44	0.86	0.20	0.11
	O.Ar (%)	0.642 (0.481), 0.957	1.25 (1.30), 1.85	1.56 (1.44), 2.14	**0.05**	**0.05**	0.50
	O.Wi. (um)	6.01 (6.12), 3.04	7.67 (7.60), 4.34	6.73 (6.53), 4.48	0.06	0.43	0.34
3-6mm (3.3-6.6)	Er.Pm (mm^{-1})	0.646 (0.609), 0.435	0.652 (0.581), 0.842	0.674 (0.554), 1.66	0.96	0.92	0.94
	Min.Pm(mm^{-1})	0.907 (1.12), 1.30	0.902 (0.642), 1.83	1.04 (0.907), 2.11	0.99	0.72	0.75
	Act.Pm(mm^{-1})	1.55 (1.71), 1.53	1.56 (1.11), 1.70	1.71 (1.56), 1.45	1.0	0.66	0.70
	Osteoclast N (cells/mm^2)	2.74 (2.07), 6.77	2.33 (2.04), 5.05	3.23 (3.28), 5.33	0.43	0.71	0.41
	O.Ar (%)	0.673 (0.486), 1.67	1.01 (0.923), 2.46	0.731(0.769), 0.976	0.48	0.85	0.53
	O.Wi. (um)	7.58 (7.57), 4.08	7.80 (8.15), 10.4	6.42 (5.73), 7.18	0.89	0.38	0.48
6-9mm	Er.Pm (mm^{-1})	0.490 (0.484), 0.575	0.591 (0.541), 1.18	0.777 (0.460), 2.15	0.51	0.42	0.62
	Min.Pm(mm^{-1})	0.919 (0.978), 1.66	1.37 (1.01), 2.35	1.20 (0.98), 1.61	0.35	0.46	0.71
	Act.Pm(mm^{-1})	1.41 (1.56), 2.12	1.97 (1.87), 1.94	1.98 (1.74), 1.94	0.19	0.24	0.98
	O.Ar (%)	0.730 (0.697), 1.39	1.12 (0.861), 1.44	1.05 (0.834), 1.99	0.12	0.41	0.85
	O.Wi. (um)	7.11 (6.98), 5.22	8.59 (8.69), 5.28	6.00 (6.38), 4.90	0.25	0.30	**0.04**
	O.Pm (%)	12.2 (12.5), 16.6	17.3 (19.6), 14.6	16.3 (16.9), 23.9	**0.03**	0.36	0.82

Table 5.7 *Erosion and formation parameters from BSEM images and cellular markers of erosion and formation, C3, weight bearing region. Er.Pm = Erosion perimeter/ Bone area (mm^{-1}), Min. Pm = Mineralising perimeter/ Bone area (mm^{-1}), Act.Pm = Active perimeter/ Bone area (mm^{-1}) from BSEM images. Osteoclast numbers (cells/mm^2) from TRAP stained sections. O.Wi = Osteoid width (um) and O.Ar = Osteoid area/ Bone area (%) and O.Pm = osteoid perimeter/ bone perimeter (%) from Masson's Goldner stained sections. P-values ≤ 0.05 in bold.*

There were no differences in osteoclast numbers between groups at any depth below the cartilage in the weight bearing region (Table 5.7). However, in horse 6 the number of osteoclasts in the control limb was markedly higher than in the treated limb at 0-3.3mm deep to the cartilage (Figure 5.23).

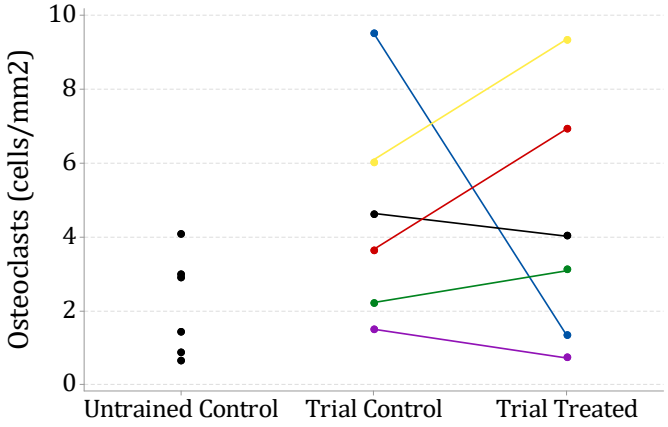

Figure 5.23 *Osteoclast number (cells/mm2) measured on TRAP stained cryosections, C3, weight bearing region, 0-3.3mm deep to the cartilage. Values for horse 6 are in light blue.*

There was further evidence for decreased formation in the weight bearing region of treated limbs when compared to the contralateral controls on MG stained sections (Figure 5.25, Table 5.7). Osteoid area in treated limbs was 49% lower than in the contralateral controls and 59% lower than in the untrained controls at a depth of 0-3mm deep to the cartilage (P= 0.05 and P=0.05 respectively, Figure 5.24). At 6-9mm deep to the cartilage there was a 29% reduction in osteoid perimeter in the treated limbs compared with their contralateral controls (P= 0.03, Figure 5.24).

The osteoid width in the control limbs of the trial animals was 43% greater than in the untrained controls at 6-9mm deep to the cartilage in this region (P= 0.04, Figure 5.24, Table 5.7).

There was no difference between any of the groups in any parameter measured from the fluorochrome labels in any ROI in this weight bearing region.

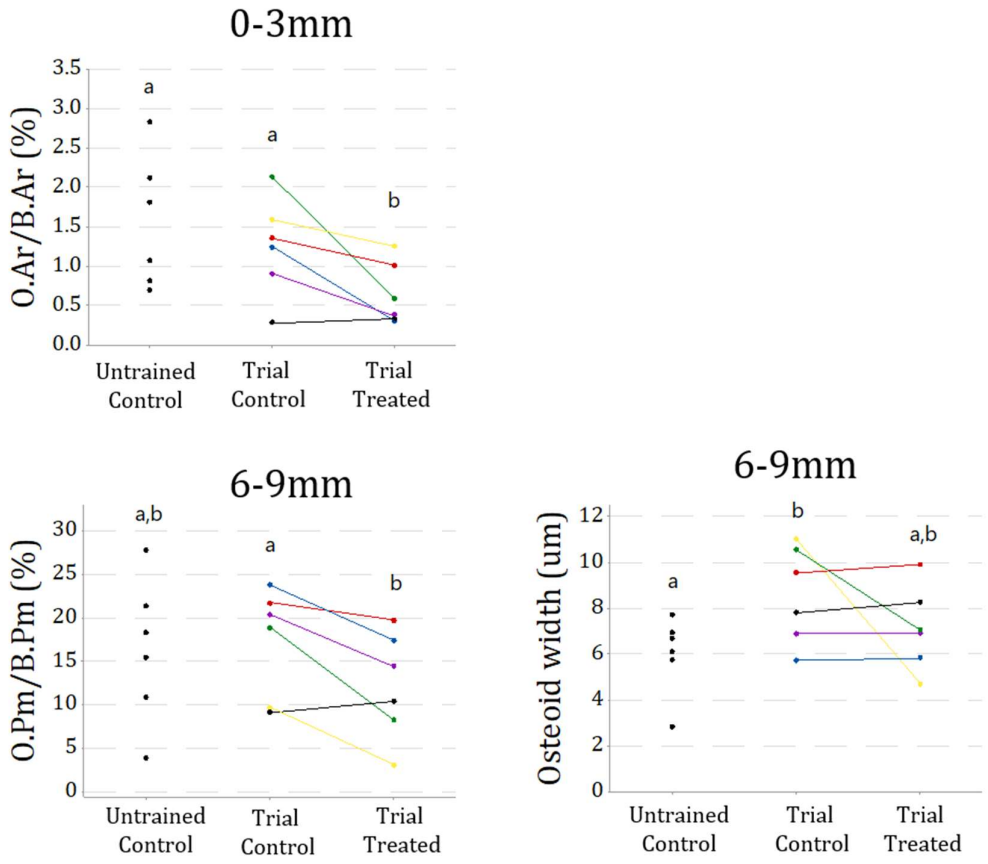

Figure 5.24 *Osteoid parameters measured on Masson's Goldner stained sections, C3, region adjacent to the defect. O.Ar/B.Ar = osteoid area as a percentage of bone area at 0-3mm deep to the cartilage, O.Pm/B.Pm = osteoid perimeter as a percentage of bone perimeter at 6-9mm deep to the cartilage, and osteoid width (um) at 6-9mm deep to the cartilage. Different letters denote statistically different groups at a level of P<0.05.*

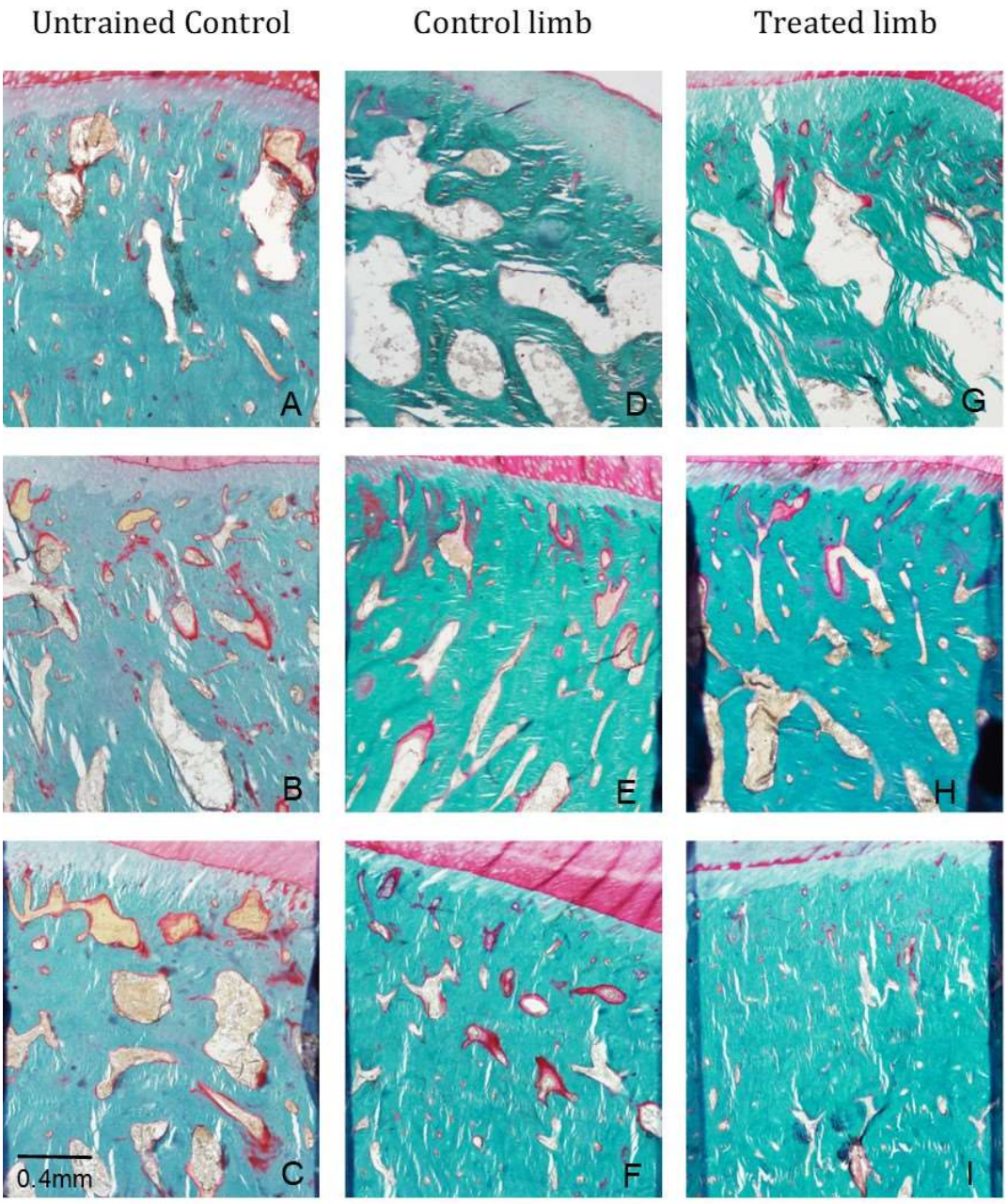

Figure 5.25 *Masson's Goldner stained sections, C3, weight bearing region, 0-3mm deep to cartilage showing lower osteoid area in the treated limbs when compared with the contralateral control limbs. untrained control horse 2 (A), untrained control horse 3 (B), untrained control horse 6 (C), Horse 1 control (D) and treated (G) limbs, Horse 3 control (E) and treated (H) limbs and Horse 6 control (F) and treated (I) limbs. Light microscopy.*

5.4 Discussion

5.4.1 Summary of major findings

Ten weeks after creation of a defect in the opposing Cr joint surface, SCB underlying an unloaded region of articular surface of the C3 displayed evidence of increased bone remodelling and a net decrease in bone volume fraction in treated limbs. The increase in remodelling activity was manifest as an increase in active perimeter on BSEM images that was most marked at 0-1mm deep to the cartilage and an increase in the number of osteoclasts most marked at 3.3-6.6mm deep to the cartilage. The reduction in bone volume fraction was most marked at 3-6mm deep to the cartilage. There was also an increase in osteoid width most marked at 0-3mm deep to the cartilage.

In SCB from the region of the C3 articular surface where weight bearing had been maintained in treated limbs there was evidence of reduced remodelling with no change in bone volume fraction over the 10 weeks. There was, however, a reduction in pore perimeter observed on BSEM images at 0-3mm deep to the cartilage. The reduction in remodelling activity was demonstrated by a decrease in active perimeter and a decrease in osteoid area at 0-3mm deep to the cartilage and a reduction in osteoid perimeter at 6-9mm deep to the cartilage.

5.4.2 Comparison with current literature

Comparison of observations from the current investigation with those of existing literature is complicated in many instances by inherent differences between the current

study and others, and by a lack of consistency of methods used in the other studies. Variations between investigations include: species differences, with morphology and biomechanics of bone in small animals likely quite different to that of horses; differences in duration of the trials, with time since loading change being an important determinant of the response observed as discussed later; and differences in the imaging and histological methods used.

Using a similar equine model to the current study Hanie et al. (1992) observed bony lysis radiographically in Crs opposing an induced C3 articular surface defect from 4 weeks until the end of the study at 6 months(202). Although they did not specify the depth to which this lysis extended it is consistent with the loss of bone volume in the SCB opposing the defect observed in the current trial. Increased remodelling at the OC junction has been reported in equine C3s opposite Cr osteochondral fragments which might also be consistent with the increase in remodelling seen in the unloaded region of C3 in this study, however the mechanical environment opposite an osteochondral fragment is likely to be different to that opposing a defect (244).

The loss of BV/TV in the unloaded SCB in the current study is also consistent with what is known about the effects of reduced loading on bone in general and subchondral bone in particular. Unloading of long bones results in reduced cortical and trabecular bone volume (150, 152), and in unloaded hind limbs of mice, Nomura et al. (2017) observed a decrease in BV/TV across entire femoral and tibial epiphyses however no attempt was made to quantify these changes at different depths below the cartilage (121).

The observed decrease in trabecular thickness and increase in trabecular separation 3-6mm deep to the cartilage in the unloaded region of C3 are consistent with other studies of unloading that have reported these parameters (150, 438). In addition Li et al. (1991) found a decrease in trabecular number in their rat hind limb-unloading model that was not observed in the current study (152). The larger size of equine trabeculae means a greater absolute loss of bone is required to penetrate their full thickness.

Increased numbers of osteoclasts is not a consistent finding in studies examining unloading of bone. Increased osteoclast numbers have been observed in murine femoral and tibial epiphyses and vertebral bodies after unloading by tail-suspension (121, 163, 199) or back suspension (435). Increased erosion perimeter, suggesting increased osteoclast activity, has also been reported in the tibial metaphysis after hind limb unloading in rats (150). However osteoclast numbers may depend on the duration of unloading with Nomura et al. (2017) observing increases at 2 weeks but normal counts after 8 weeks of unloading(121). Other studies of tail-suspended rats have reported no change in osteoclast numbers in the tibia, however these studies did not use specific stains to identify osteoclasts (434, 435). To my knowledge no previous studies have examined osteoclasts in subchondral bone at specific depths.

The increase in osteoid width and increase in fluorochrome double labelling are contrary to many other studies of unloading that have demonstrated a decrease in measures of bone formation activity (150, 152, 161-163, 199, 434, 435). However, most of these studies have not reported osteoid width, rather focusing on osteoid or osteoblast perimeter and osteoblast numbers (162, 163, 434, 435). Aguirre et al. (2006) observed a reduction in osteoid width at three days post unloading that was not apparent at seven days or

later(199). More consistent with observations in the current study, Weinreb et al. (1991) reported an increase in osteoid area in rat tibia at all time points up to 12 days after hind limb immobilisation(439). Studies of unloaded bone that have measured formation parameters from fluorochrome labelling have observed a reduction in labelled perimeter, MAR and BFR (150, 152, 162). The measures of MAR and BFR are imprecise in the current study due to the inability to differentiate between each label and therefore it was not possible to define the time between labels.

The reduction in active perimeter in the weight bearing region of C3 in treated limbs in this study was driven by a reduction in erosion perimeter in all but one horse. This is consistent with observed reductions in erosion perimeter in the subchondral bone of horses at high intensity exercise compared with less intense exercise levels (70, 74, 156, 165). However, it is contrary to findings in dogs following high intensity training where resorption surface is increased (73). The animals in this canine study were immature which may have affected the degree of erosion activity. The observed increase in remodelling in the unloaded region of C3 despite continued repetitive loading of the entire joint is similar to observations of increased local erosion around sites of fatigue fracture in horses that have remained in training (231).

The reduction in osteoid area and perimeter in the weight bearing region of treated limbs in this study is somewhat consistent with the observation of lower osteoid width in dorsal sites of carpal bones, which have been shown to experience higher intermittent loads during locomotion, when compared to the palmar sites which experience lower, more continuous loading (74, 106). However it is contrary to observations of increased osteoid

perimeter in horses and increased osteoid volume in dogs undergoing high intensity training when compared to lower intensity training (73, 74, 165).

5.4.3 Interpretation of major findings

5.4.3.a Effect of loss of congruity

Although subchondral loads opposing articular surface defects have not been measured, observations of reduced surface contact pressure opposing defects and increased pressures on the articular surface surrounding defects (3, 18, 106, 233, 360) suggest it is likely that the SCB opposing the defect was under reduced loading and the SCB in the weight bearing ROIs was under increased loading in the treated limbs.

The net reduction in bone volume observed in SCB opposing the lesion is evidence that the well-accepted concept of bone loss in conditions of unloading holds true on a local scale as well as at an organ level (121, 150, 152). Additionally, the increase in remodelling activity in the unloaded region suggests that focal remodelling activity might be enabled in SCB of joints that are under conditions of repetitive loading by local unloading of the overlying joint surface. This supports other studies that have made similar conclusions regarding SCB at regions of low strain within loaded bone where focal remodelling is observed (171, 172).

Although erosion and formation activity were similarly increased in the unloaded region at the termination of the trial, the net loss of bone volume in this region suggests that erosion activity was favoured soon after defect creation but that there was a subsequent

increase in formation activity. Subchondral bone volume fraction will stabilise at a lower level once the bone is adapted to the new, lower level of loading (168). In laboratory animals this stabilisation of bone volume takes much longer. For example in unloaded hind limbs of adult rats the bone volume in the tibial metaphysis was found to plateau at approximately 45% that of age-matched controls after 18 weeks of unloading (150). However mathematical modelling of data from the subchondral bone of the equine fetlock joint found that under reduced loading a decrease of 10% from 90% BV/TV took 12 weeks to completely stabilise and was mostly achieved by 7 weeks. It is also possible that filling of the Cr defect with fibrocartilage through the course of the trial somewhat restored loading on the opposing C3 SCB leading to the increase in formation activity observed at 10 weeks.

Observed differences between individual animals could be a result of variation in the time course of the response to the induced incongruity. The individual that showed a markedly increased mineralisation perimeter and reduced erosion perimeter in the treated limb at 0-1mm deep to the cartilage in the region opposing the defect had likely already been through a marked resorptive phase (this animal showed the most marked decrease in bone volume in the region opposing the lesion) and had progressed to marked mineralisation, while the individual that had a marked increase in erosion perimeter and lower mineralising perimeter at the same site had a slower resorptive response to the loss of congruity and had not yet begun the mineralising phase. Variation in baseline bone surface and osteoclast numbers may have influenced the difference between individual animals in the observed response of SCB to unloading (438).

Increased osteoid width but not perimeter at 0-3mm deep to the cartilage in the unloaded region opposing the defect suggests an increase in the rate of osteoid production by individual osteoblasts and/or a reduction in the rate of mineralisation of the osteoid, without an increase in the number of osteoblasts along bone surfaces. Interestingly the mineralisation of matrix may be more sensitive to unloading than its production which is consistent with thicker osteoid in an unloaded area (439). It is also possible that there was an increase in the rate of production of osteoid by the osteoblasts that were present, without an increase in their number, due to ongoing erosion activity resulting in osteoclasts and osteoblasts competing for the available bone surface. The increase in osteoid width was observed in relatively small pores in otherwise compact bone which may also have affected the way that osteoid was deposited and measured. I am not aware of any other evidence to support these suggestions.

The observed reduction in active perimeter in the weight bearing region of treated limbs on BSEM images, despite being likely to be influenced by the decrease in total pore perimeter, was predominantly driven by a reduction in erosion activity. This supports other evidence that suppression of erosion activity by high cyclic loads may be dose dependent, that is, the greater the magnitude of the loading, the greater the reduction in erosion activity. This phenomenon has previously been demonstrated in loaded rat vertebra (171) and by the observation of reduced erosion at sites of larger cyclic loads when compared to sites of lower, more continuous loading in the equine carpus (74).

It might have been expected that an increase in formation activity and BV/TV would have been observed due to increased loading in the weight bearing region as existing literature consistently shows SCB experiencing greater loading has a greater bone volume than that

under lower loading (69, 74, 156, 293), however this was not evident in the current study. In contrast there was some evidence of decreased formation activity in the weight bearing region of treated limbs, suggested by reduced osteoid formation on the Masson's Goldner stained sections. As there was no difference in bone volume between the untrained controls and either limb of the trial animals in the weight bearing region it is possible that the duration of training was too short to result in a measurable change in bone volume. However this is unlikely as others have found increased bone volume in response to training by 8 weeks (156, 440). In addition, studies of increased loading in other species have observed an increase in formation concurrently with a decrease in erosion (151). It is possible that the decrease in osteoid area was a reflection of the decreased pore perimeter and likely reduced area of individual pores, which may itself be secondary to reduced erosion. A lack of available bone surface on which formation could occur due to the already high bone volume fraction, especially at 0-3mm deep to the cartilage may also account for the fact that no increase in BV/TV was observed. Alternatively, the difference in the magnitude of loading between the treated and contralateral control limbs may not have been great enough to result in a measurable increase in formation despite the decrease in erosion. Schulte et al. (2103) suggested that resorption is more tightly controlled by strain energy density than formation in a mouse vertebral model of loading(171).

The results from this chapter provide further evidence that local loading of a joint surface plays a role in the regulation of bone volume fraction and erosion and formation activity in the underlying SCB. This agrees with previous suggestions that bone volume of equine and human SCB may be dependent on local loading of the joint surface (69, 74, 101, 334)

and that resorption and formation activity in trabecular bone is controlled by local strains (171, 172, 231).

5.4.3.b Erosion perimeter and osteoclast numbers

Possible reasons for the apparent discrepancy between erosion perimeter on BSEM images and osteoclast numbers on sections stained for TRAP have been discussed above in section 4.4.3.c. In addition, the two observations were made in different sections of bone: the sections used for osteoclast counts were taken from the region closest to the edge of the lesion while the sections used for BSEM imaging were from the centre. It is also possible that osteoclast numbers were elevated in treated limbs at 0-1mm deep to the cartilage in the region opposing the lesion during the study to create the observed increase in erosion perimeter but had begun to decline by the time that the trial concluded.

5.4.3.c Effect of depth below the cartilage and available bone surface

The response of SCB to changes in congruity varied not only with site along the articular surface but also depth below the articular surface. In the region of loss of surface contact the magnitude of changes varies depending on depth below the surface, being most marked at 0-1mm and 3-6mm deep to the cartilage. This may reflect a balance between the magnitude of the change in load, which is likely to be greater close to the articular surface (335), and the availability of bone surface and osteoclast progenitor cells which are greater in the more trabecular bone at 3-6mm deep compared to the more compact bone superficially.

5.4.3.d Effect of training

There were few significant differences between the untrained control group and either limb of the trial animals. However, at 0-1mm below the cartilage in the region opposing the lesion there was lower pore perimeter and erosion perimeter in the control limbs of the trial animals when compared with the untrained controls. This may be an effect of training in the control limbs of the trial animals as others have previously associated training with reduced erosion perimeter on BSEM (165).

5.4.6 Conclusion

The SCB of synovial joints responds in a focal manner to local changes in joint surface congruity. Areas of SCB underlying a joint surface that has lost surface contact undergo increased remodelling and a reduction in bone volume while SCB in adjacent regions where surface contact has been maintained experience reduced remodelling activity.

This occurs in adult animals and below an intact joint surface in the absence of direct injury. These focal responses may play a role in normal joint homeostasis as well as in the pathogenesis of conditions that result in a loss of joint congruity.

Chapter 6

CARTILAGE PARAMETERS

6.1 Introduction

As discussed in previous chapters, surface contact pressures are greater than normal on cartilage surrounding osteochondral defects and lower than normal on cartilage opposing defects (1, 3, 4, 106, 233, 360). However, cartilage opposing osteochondral defects has been shown to bulge into the defects upon loading suggesting that it may also be experiencing abnormal strain (2, 4, 362).

It is recognised that articular cartilage is mechanosensitive both *in vitro* and *in vivo*. *In vitro* studies have shown that chondrocyte proliferation, differentiation and matrix production in hyaline cartilage are affected by both hydrostatic pressure and tensile strains (84, 85, 88, 441-444). In addition, hyaline cartilage has been shown to be thicker in regions of local unloading and thinner in regions of increased surface pressures in step defect models in sheep and rabbits (209, 211) and has been observed to be thicker over regions of collapse of the underlying SCB in POD lesions in horses (166).

Additionally, both the rate of advancement of the tidemark and the rate of endochondral ossification have been shown to be greater, and the CC thinner in areas of lower surface pressure compared with areas of higher surface pressure in growing horses (68). Moreover, hind limb unloading in rats has been shown to increase the rate of advancement of the tidemark, while immobilisation in addition to unloading resulted in an increased rate of endochondral ossification without advancement of the tidemark (131).

The primary aim of this chapter was to investigate how articular cartilage responds to focal changes in congruity and loading in an *in vivo* adult equine model. It also aimed to assess cartilage degeneration on Cr, C3 and Cu, as osteochondral defects have previously been found to be associated with degenerative changes in the cartilage surrounding, opposing and distant to the defect (18, 365, 366).

It was hypothesised that the hyaline cartilage would become thinner in the weight bearing regions of Cr and C3 and thicker in the unloaded region of C3 opposing the defect; and that advancement of the tidemark may be seen in the unloaded region of C3. It was also hypothesised that this model would result in degenerative changes in cartilage throughout the middle carpal joint.

6.2 Materials and Methods

6.2.1 Cartilage histomorphology - C3 and Cu

Methylene blue stained semi-thin sections from C3 and Cu were prepared and viewed as described in Chapter 2 to assess cartilage histomorphology.

Cartilage was assessed in two ROIs on C3, one in the region opposing the lesion and one in the dorsal weight bearing region. The distance (mm) from the dorsal edge of each Cr to the dorsal margin of the lesion, and the length of the lesion in the dorso-palmar direction were measured and used to define the position of the ROIs for assessment on C3. The ROI opposing the defect on C3 was taken from the joint surface opposing the Cr defect. The weight bearing ROI was positioned so that it was wholly within the region that had maintained surface contact. The position of the ROIs in the untrained control C3s were the mean of all the trial horses. Cartilage and SCB at 2-7mm palmar to the dorsal edge of the bone was cut from the joint surface of all Cu sections. All sections included cartilage and the most superficial 3mm of SCB. Due to difficulties in sectioning, the region opposing the lesion of C3 from horse 2 was excluded from these analyses.

To maintain consistency with other equine models, cartilage pathology was graded using a modification of the validated histological grading system described by McIlwraith et al. (2010) (Table 6.1). As it is designed for use with H and E and safranin O fast green (SOFG) stained sections an assessment of metachromatic staining was substituted for SOFG stain uptake in this study. All other parameters in the scoring system can be assessed on MB stained sections (Table 6.1, Figure 6.1). These parameters were scored on three sections from each specimen and the mean of these scores used as the final

observation for that specimen. A total cartilage pathology score was assigned using the sum of all scores for the individual parameters.

In order to account for changes in the cartilage opposing the boundary of the defect in the assessment of C3 cartilage pathology, and to attempt to quantify the overall effect of the Cr lesion on C3 cartilage, a combined cartilage pathology score was created using the formula in Figure 6.2.

Due to the ordinal nature of the data, a Wilcoxon signed rank test was used to compare cartilage pathology scores between treated and control limbs while a Mann-Whitney U test was used to compare scores between the untrained controls and either limb of the trial animals.

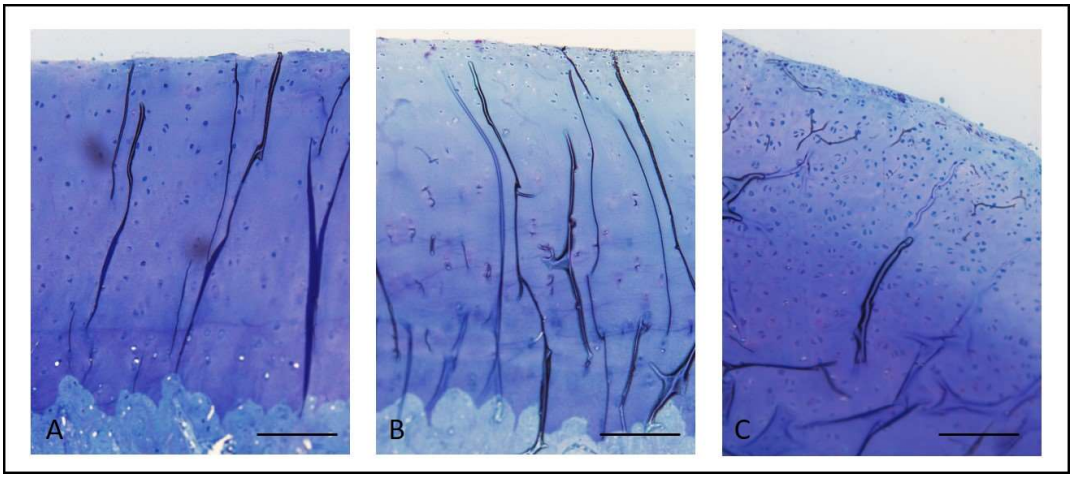

Figure 6.1 *Methylene blue stained semi-thin sections showing examples of metachromatic staining score 0 (A), score 2 (B) and score 4 (C). Scale bar = 0.5mm.*

Parameter	Score	Description
Chondrocyte necrosis	0	Normal - no necrosis
	1	≤ 1 necrotic cell near the surface per 20x field
	2	1-2 necrotic cells near the surface per 20x field
	3	2-3 necrotic cells near the surface per 20x field
	4	3-4 necrotic cells near the surface per 20x field
Cluster formation	0	No cluster formation
	1	Two chondrocytes in same lacunae in superficial cartilage
	2	2-3 chondrocytes in same lacunae in superficial cartilage
	3	3-4 chondrocytes in same lacunae in superficial cartilage
	4	> 4 chondrocytes in same lacunae in superficial cartilage
Fibrillation/ fissuring	0	No fibrillation/fissuring
	1	Fibrillation/fissuring restricted to surface and superficial zone
	2	Fissuring that extends to middle zone
	3	Fissuring that extends to the level of the deep zone
	4	Fissuring that extends into the deep zone
Focal cell loss	0	Normal cell population throughout the section
	1	10-20% area of acellularity per 20x field
	2	20-30% area of acellularity per 20x field
	3	40-50% area of acellularity per 20x field
	4	>50% area of acellularity per 20x field
Metachromatic staining	0	Staining of superficial layer similar to or slightly more intense than deeper cartilage
	2	Staining of superficial layer slightly less intense than deeper cartilage
	4	Staining of superficial layer significantly less intense than deeper cartilage

Table 6.1 *Semi-quantitative scoring system used to assess cartilage pathology on methylene blue stained semi-thin sections (Modified from McIlwraith et al. 2010).*

$$\frac{[\text{Path score}_{(\text{lesion})} + \text{Path score}_{(\text{weight bear})}]}{2} + \text{Fib/fiss score}_{(\text{entire})}$$

Figure 6.2 *Formula for calculating the combined cartilage pathology score for the entire surface of C3. Path score$_{(lesion)}$ = the total pathology score from MB stained sections, without the fibrillation and fissuring score, for the region opposing the lesion. Path score$_{(weight\ bear)}$ = the total pathology score from MB stained sections, without the fibrillation and fissuring score, for the weight bearing region. Fib/fiss score $_{(DIC\ entire)}$ = the fibrillation and fissuring score (assigned using the criteria in Table 6.2) of the entire surface of C3 from reconstructed bright field images of the unstained cryosections used for DIC imaging (see section 2.2.5.d).*

Bone histomorphometry software (OsteoMeasure^{TM}) was used to measure hyaline cartilage thickness (HC.Th, mm), calcified cartilage thickness (CC.Th, um) as well as chondrocyte size (μm^2/cell) and chondrocyte density (cells/mm^2) in the hyaline cartilage. Measurements were made on a region 0.6mm wide (width of a single field at 20x magnification), through the entire depth of the hyaline cartilage, on each of three sections from each specimen and the mean used as the final observation for that specimen.

6.2.2 *Differential Interference Contrast microscopy - C3 cartilage*

Sections of C3 cartilage used for DIC microscopy were prepared and imaged as described in Chapter 2.

Two ROIs were chosen for analysis, one in the region opposing the lesion and the other in the dorsal weight bearing region. Having no Cr sections to measure the position of the lesions for this method, a reasonable estimation was made for each horse based on the gross changes visible on the C3s from the treated limbs. Sites an equivalent distance from the dorsal edge of the cartilage were used on C3s from the control limbs for each horse. Effort was made to avoid the region of cartilage at the boundary between the weight bearing region and that opposing the lesion. Images at 4x, 10x and 20x magnification were taken from each ROI.

Hyaline cartilage thickness (HC.Th, mm) was calculated from 4x magnification images by measuring the area between the articular surface and the most superficial tidemark then dividing this area by the length of the cartilage on a line equidistant between the articular surface and the calcified cartilage. Total cartilage thickness was measured similarly using the cement line as the deep boundary (Figure 6.3).

Calcified cartilage thickness (CC.Th, mm) was measured on 20x magnification images by measuring the area bounded by the tidemark, the cement line and either end of the image. This area was then divided by the length of the CC measured on a line equidistant between the tidemark and the cement line (Figure 6.3).

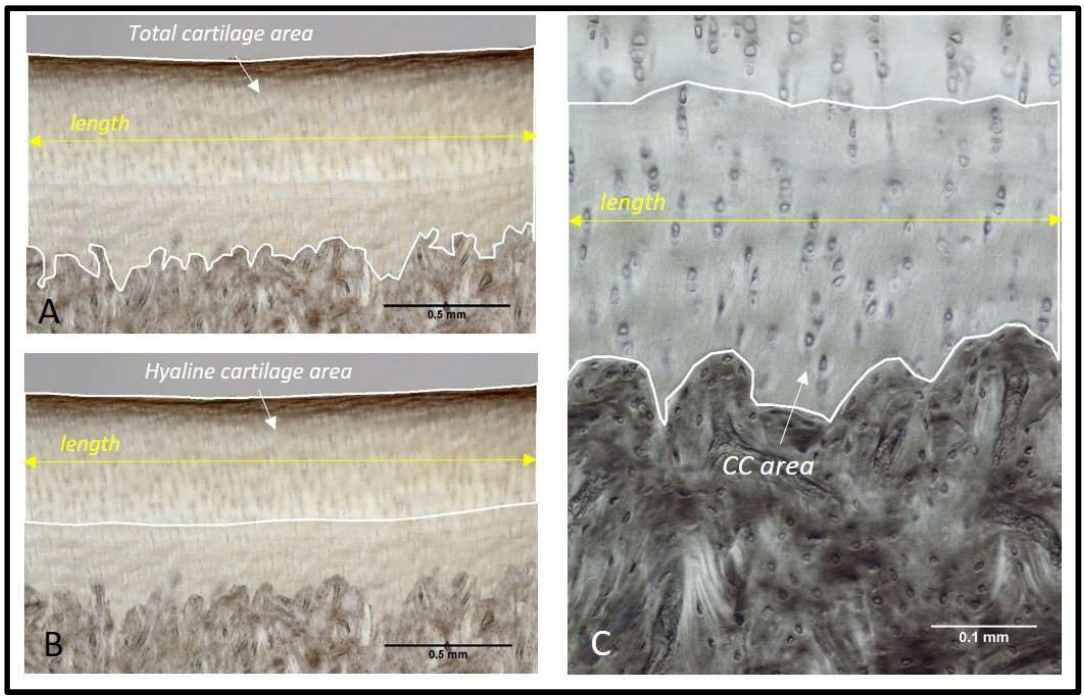

Figure 6.3 *Measurement of total (A), hyaline (B) and calcified (C) cartilage thickness from DIC images. Area was divided by length in each to calculate thickness (mm).*

The tangential layer of the hyaline cartilage was defined as the region in which the chondrocytes were aligned tangentially to the cartilage surface. Its thickness (Tang.Th, mm) was calculated from 20x magnification images by dividing its area by the length of the articular surface. The area of the tangential layer was measured with one boundary along the articular surface and the opposing boundary along a line where chondrocyte orientation changed from a tangential to oblique. The ends of the images were defined as the other two boundaries of the area (Figure 6.4). If there were no chondrocytes aligned tangentially, the thickness of this layer was defined as zero.

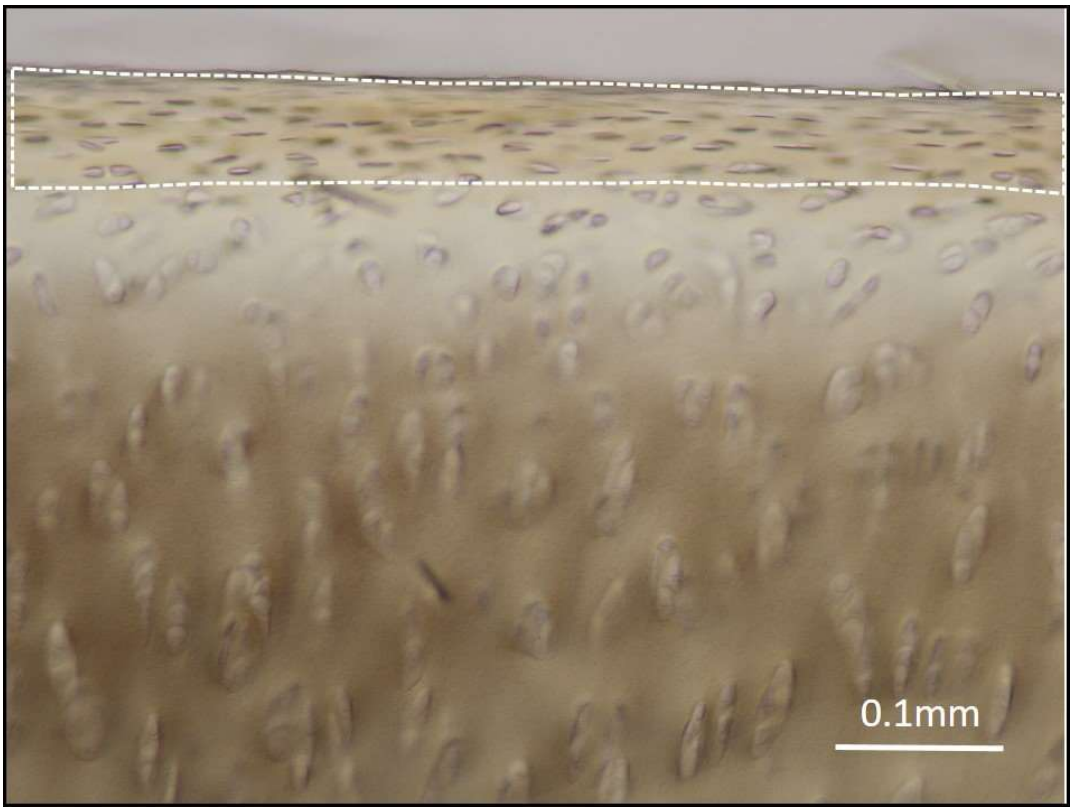

Figure 6.4 *Tangential layer thickness measurement on DIC images. The area of the tangential layer was measured as the area between the articular surface and the line where chondrocyte orientation changed from tangential to the cartilage surface to oblique to it (area within the white dotted box), then divided by the length of the cartilage surface to calculate thickness. DIC image.*

Cell aspect ratios were measured on 20x magnification images for five chondrocytes within the tangential layer and the mean calculated for each section. The ratio was calculated by dividing the length of the cell (parallel to the articular surface) by its width at the widest point in a line perpendicular to the length (Figure 6.5).

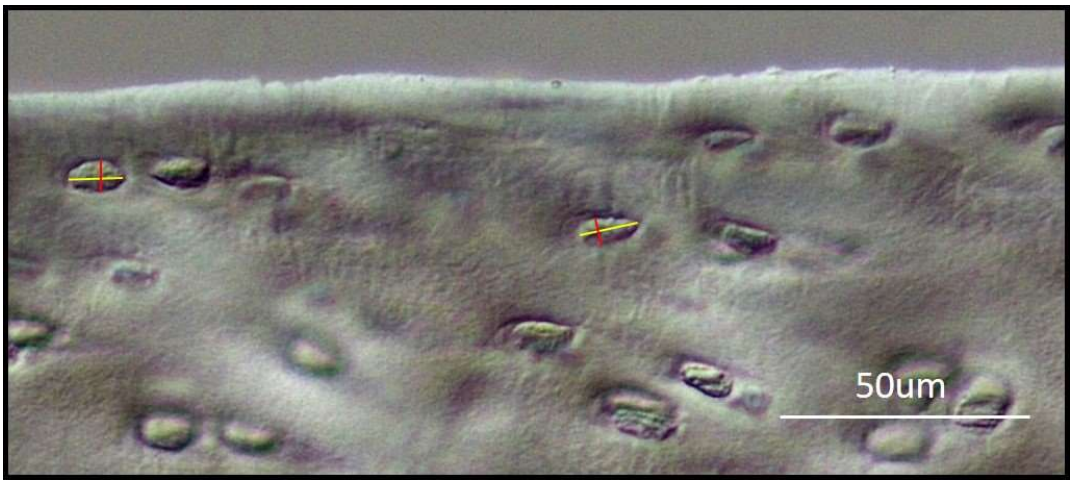

Figure 6.5 *Measurement of tangential cell aspect ratio. The length of the cell (yellow line) was divided by its width at the widest point on a line perpendicular to the length (red line). DIC image.*

The degree of rugosity (irregularity) of the cement line, and presence and morphology of bone spicules extending from SCB into the CC layer were assessed on 20x magnification images of the CC. The rugosity of the cement line was estimated by dividing the length of the cement line by the length of a straight line drawn between the intersections of the cement line with either end of the image (Figure 6.6).

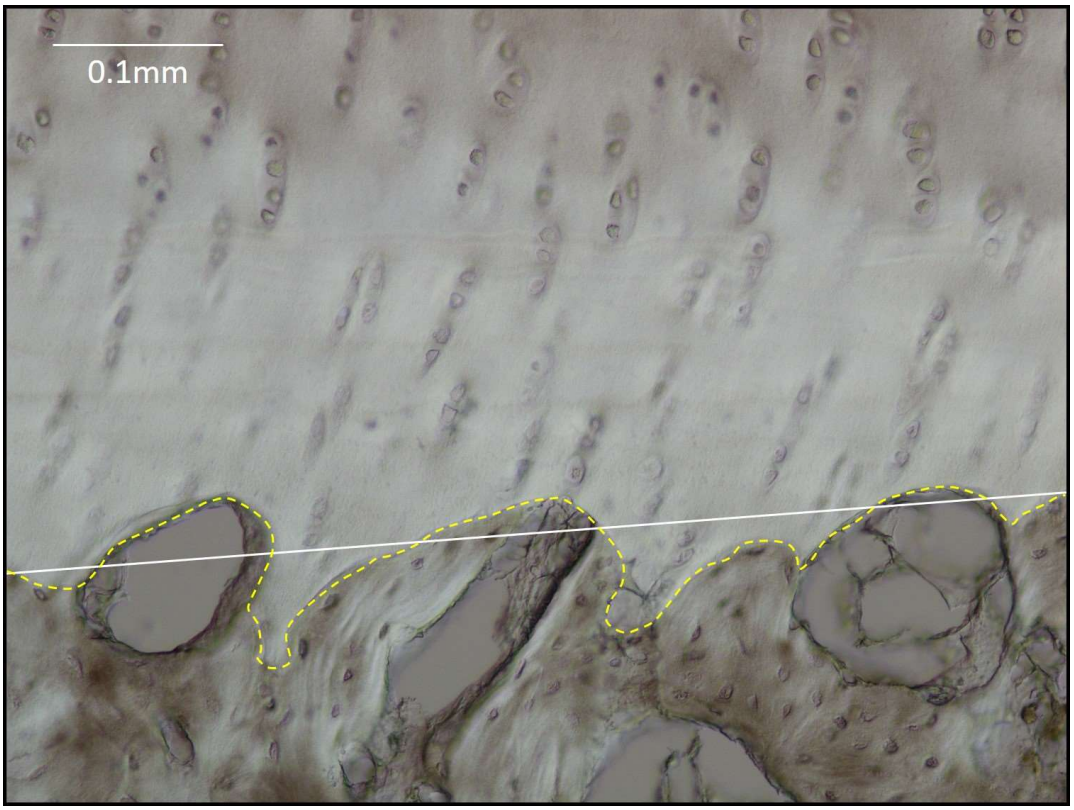

Figure 6.6 *Estimation of rugosity from DIC images. The length of the cement line (yellow dotted line) was divided by the length of a straight line drawn between the points of the cement line at either end of the image (solid white line).*

Degree of clustering of chondrocytes in the superficial region of the hyaline cartilage and fibrillation of the surface of the cartilage were graded as for the semi-thin sections (Table 6.1, Figure 6.7). In addition, the degree of crimping of collagen fibres was graded using the following key: 0 = no crimping, 1 = mild crimping (tangential layer only), 2 = moderate crimping, 3 = severe crimping.

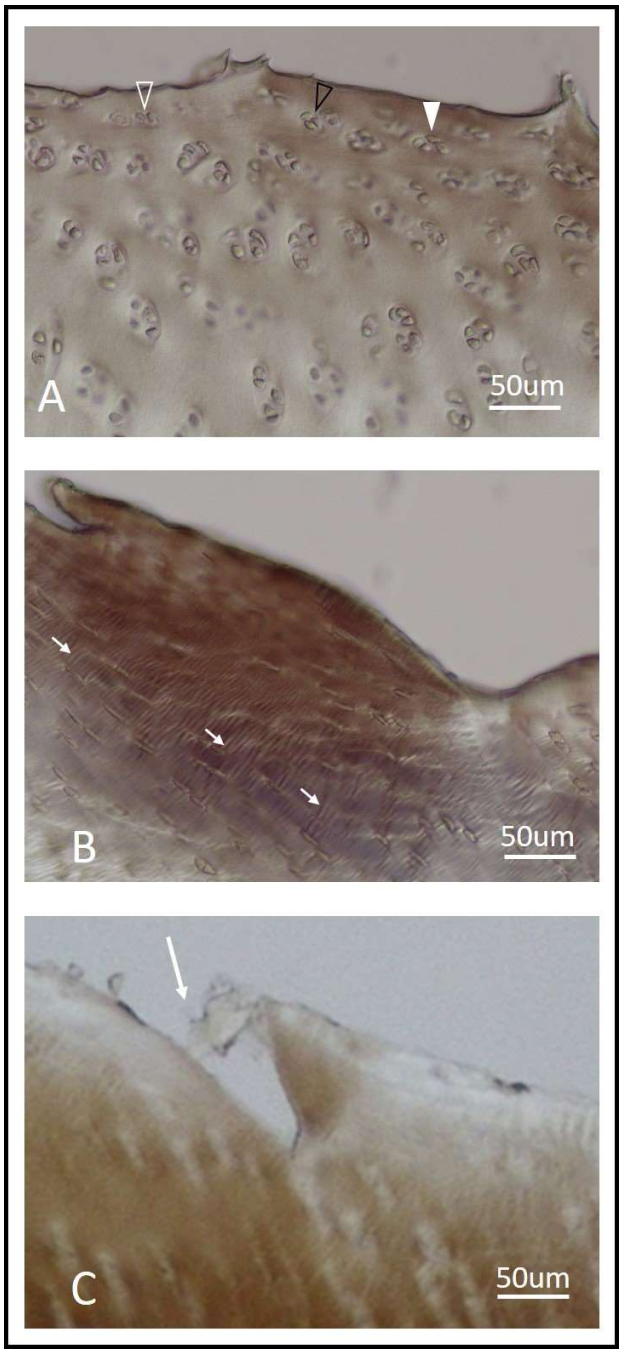

Figure 6.7 *DIC images showing: chondrocyte clustering (A) with 2 (open white arrowhead) 3 (open black arrowhead) and 4 (filled white arrowhead) cells per lacuna; collagen crimping score 2 (B); and fissuring, score 1 (C).*

6.2.3 *Cartilage thickness on Masson's Goldner stained sections - Cr and C3*

HC and CC thickness (mm) were measured from MG stained sections under light microscopy at a magnification of 10x using bone histomorphometry software (OsteoMeasure^{TM}). HC and CC thickness were calculated by dividing the area of each layer by the length of the cartilage surface for that ROI (Figure 6.8). Measurements were made in the ROI opposing the lesion in C3 as defined in Chapter 5; and in the palmar half of the weight bearing ROIs of both C3 and Cr, as defined in Chapters 4 and 5. The dorsal half of the weight bearing ROI was excluded as measurement of cartilage thickness at this site was complicated by the curved shape of the dorsal rim of the bone.

6.2.4 *Calcified cartilage thickness and tidemark number on BSEM - Cr and C3*

Calcified cartilage thickness (CC.Th, mm) and the mean number of tidemarks (Tm.N) were calculated from 200x magnification BSEM images of the weight bearing ROI of Cr and the ROIs both opposing the lesion and in the weight bearing region of C3 as defined in Chapters 4 and 5.

CC.Th was calculated from BSEM images by dividing CC area by CC length (Figure 6.9). Both CC area and length were measured using freely available image analysis software (ImageJ 1.50i, National Institutes of Health, USA(391)).

Tm.N was calculated from five individual TM counts taken at regular intervals along each ROI (Figure 6.10). A tidemark was defined as a distinct black or dark grey line within the CC. The superficial boundary of the CC (the most superficial TM) was included.

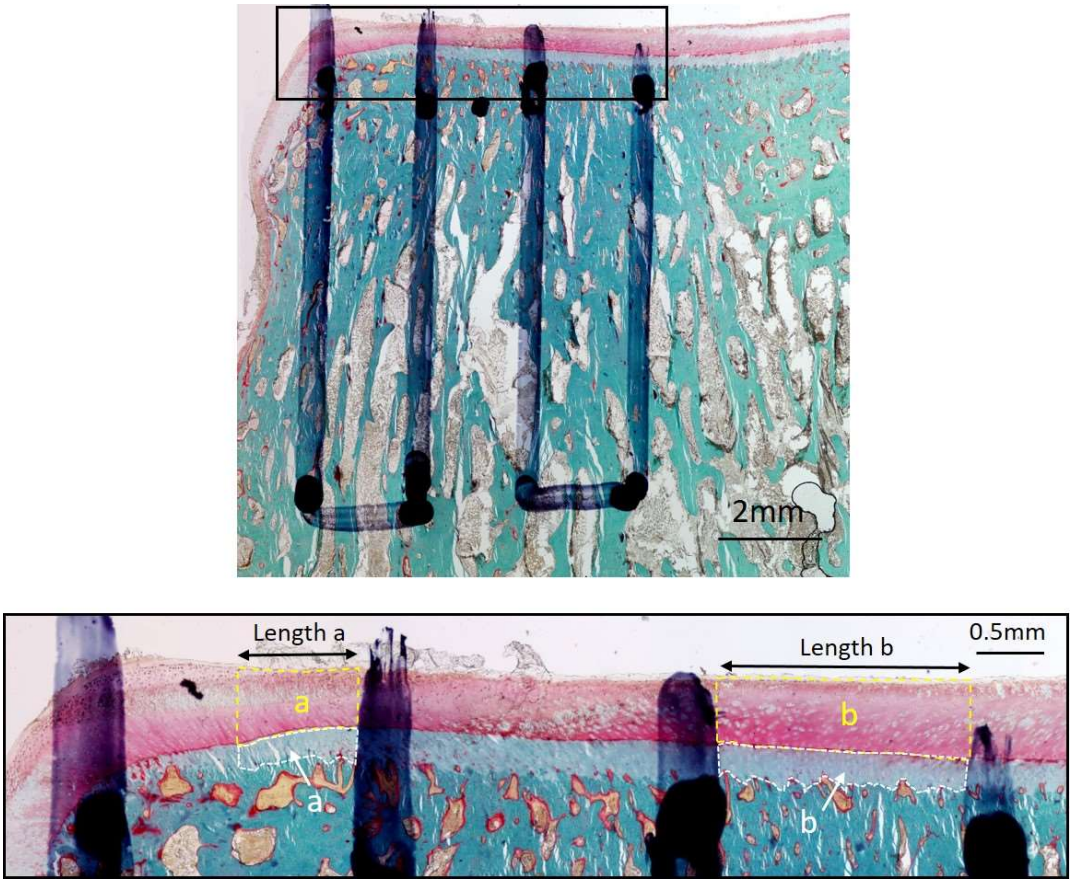

Figure 6.8 *Areas used for C3 cartilage thickness measurements from Masson's Goldner stained sections. Region in black box of top image enlarged in bottom image. Hyaline cartilage areas bounded by yellow dashed boxes and calcified cartilage areas bounded by white dashed boxes for the weight bearing region (a) and region opposing the lesion (b). Areas were divided by the length of the hyaline cartilage surface for each ROI.*

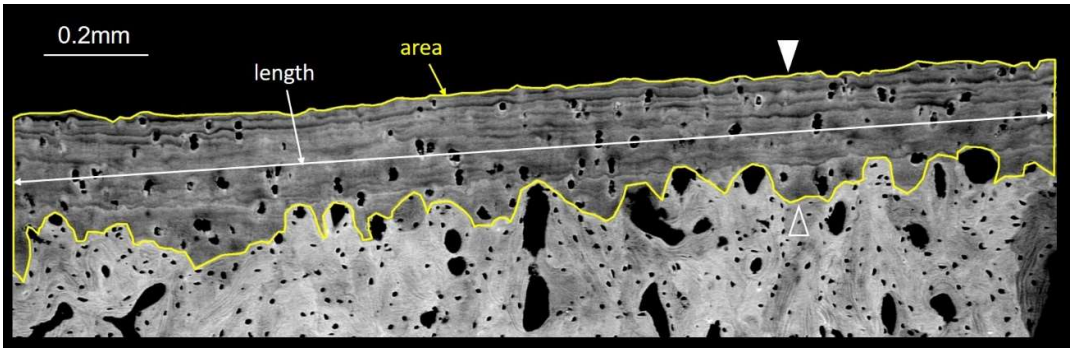

Figure 6.9 *Calcified cartilage (CC) thickness on BSEM images was calculated by dividing CC area (area bounded by yellow outline) by CC length (white line). CC length was measured midway between the osteochondral junction (open arrow head) and the most superficial tidemark (filled arrow head).*

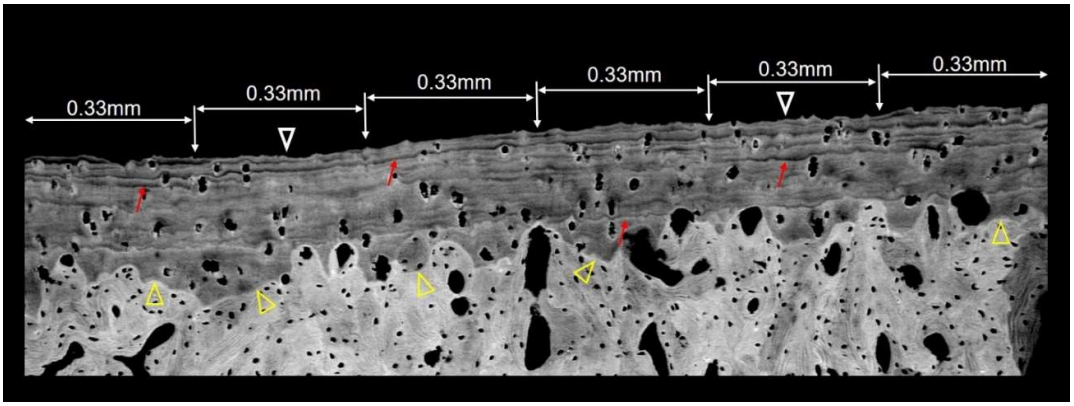

Figure 6.10 *Positions of measurements of number of tidemarks (white arrows) and examples of tidemarks (red arrows) on BSEM images. White arrow heads = most superficial tidemark. Yellow arrow heads = osteochondral junction.*

6.2.5 *Tidemark fluorescence*

Undemineralised, unstained sections of C3 were prepared and oxytetracycline labels viewed as described in Chapter 2. A bone histomorphometry system (OsteoMeasure^{TM}) was used to measure the length of the most superficial tidemark (Tm, mm) within each ROI and the length of oxytetracycline labelled tidemark (L.Tm, mm). The proportion of tidemark that was labelled was then calculated (L.Tm/Tm).

6.3 *Results*

In addition to the parameters measured in the defined ROIs several abnormalities of the cartilage were observed in joints from the trial animals. While there was no fibrillation or fissuring of the hyaline cartilage in either of the defined ROIs, it was present in the region of C3 opposing the dorsal edge of the Cr defect in treated limbs on the bright field images taken of the entire surface (Figures 6.11 and 6.12). In this region opposing the edge of the defect a subjective increase in cloning of chondrocytes and collagen crimping was also noted in (Figure 6.12). There were also a number of minor cartilage abnormalities present on both C3 and Cr that were unlikely to be related to the experimental intervention and which are documented in Appendix 4.

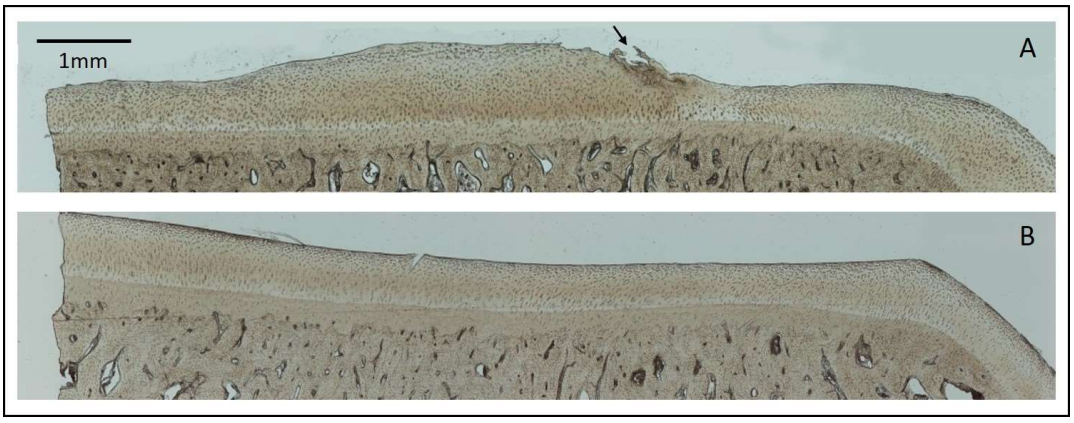

Figure 6.11 *Fibrillation and fissuring (arrow) of hyaline cartilage opposing the dorsal edge of the osteochondral defect. Brightfield images of C3 from Horse 5 treated (A) and control (B) limbs.*

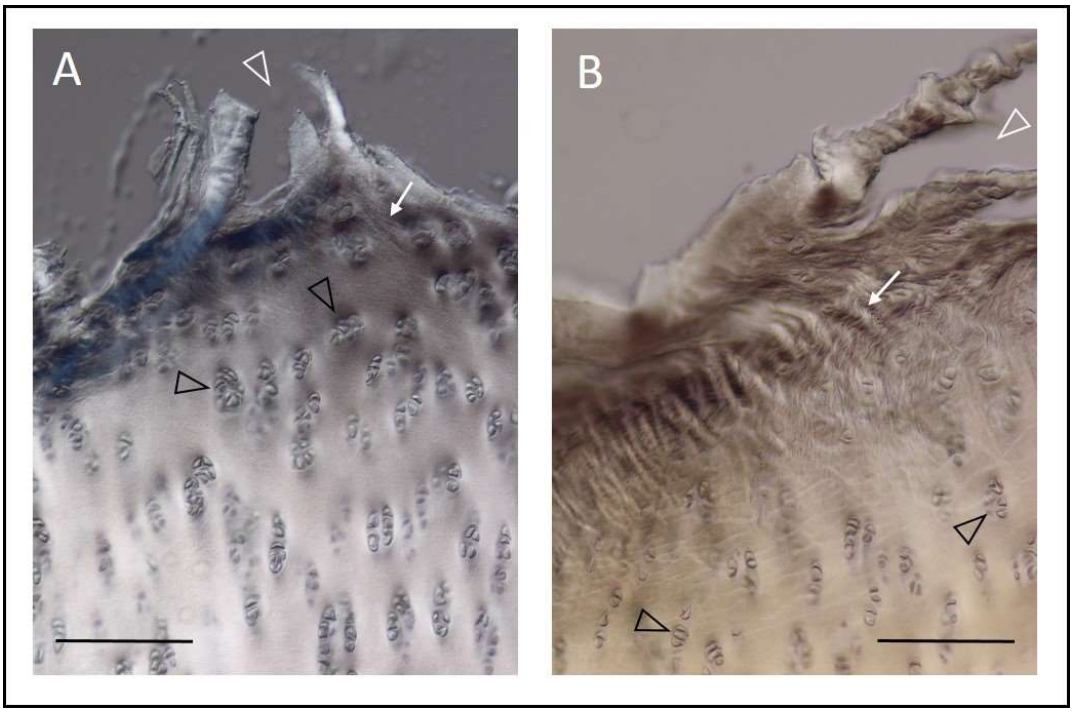

Figure 6.12 *DIC images of the superficial cartilage of C3 in the region opposing the edge of the defect from horse 4 (A) and horse 5 (B), showing collagen crimping (white arrows), fissuring (white arrowheads) and multiple chondrocytes within individual lacunae (black arrowheads). Scale bar 0.1mm.*

When the entire surface of C3 was considered the combined cartilage pathology score was higher in treated limbs (mean = 7.3, median = 6.3, range = 5.7) when compared to the contralateral control limbs (mean = 4.1, median = 4.2, range = 1.3) in a manner that approached significance (P= 0.06, Figure 6.13).

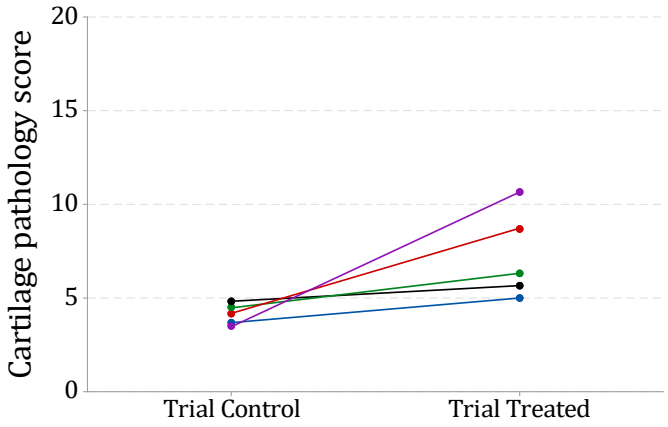

Figure 6.13 *Combined Cartilage pathology score for the entire C3 articular surface (region opposing the lesion, boundary region and weight bearing region combined) as defined in Figure 6.2. From MB stained semi-thin sections and DIC images. Untrained controls were excluded as there were no DIC images for this group.*

6.3.1 Radial Carpal bone adjacent to the defect

6.3.1.a Hyaline cartilage

The hyaline cartilage of the Cr weight bearing region was 30% thinner in treated limbs compared to the contralateral controls on MG stained sections (Figure 6.14 and 6.15, Table 6.2).

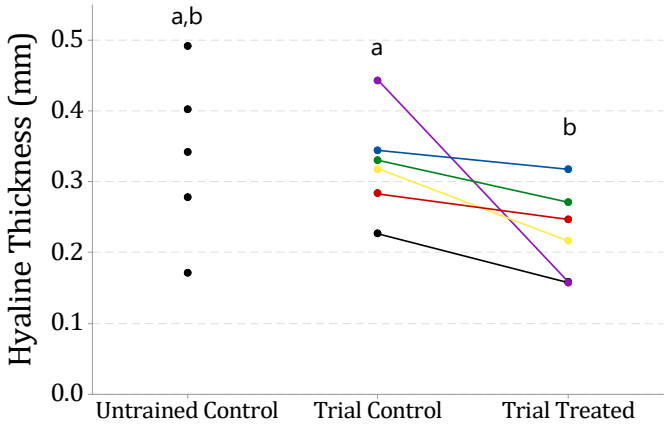

Figure 6.14 *Hyaline cartilage thickness (mm), Cr, weight bearing region. From Masson's Goldner stained sections. Different letters denote significantly different groups at a level of P<0.05.*

		Mean (Median), Range			P-value		
		Trial Treated	Trial Control	Untrained Control	Trial Treated v Trial Control	Trial Treated v Untrained Control	Trial Control v Untrained Control
HC.Th (mm)	MG stained	0.228 (0.232), 0.160	0.324 (0.324), 0.217	0.337 (0.342), 0.322	**0.04**	0.13	0.84
CC.Th (mm)	BSEM	0.163 (0.164), 0.079	0.155 (0.146), 0.045	0.178 (0.159), 0.112	0.54	0.51	0.29
	MG stained	0.123 (0.122), 0.070	0.145 (0.154), 0.058	0.143(0.118), 0.088	0.41	0.59	0.96
TM number	BSEM	5.77 (5.90), 2.80	6.67 (6.50), 4.00	4.06 (4.20), 2.20	0.17	**0.009**	**0.006**

Table 6.2 *Cartilage thickness and TM number in the weight bearing region of Cr. From Masson's Goldner stained sections (MG stained) and BSEM images (BSEM). HC.Th = hyaline cartilage thickness (mm), CC.Th = calcified cartilage thickness (mm), TM number = mean number of tidemarks.*

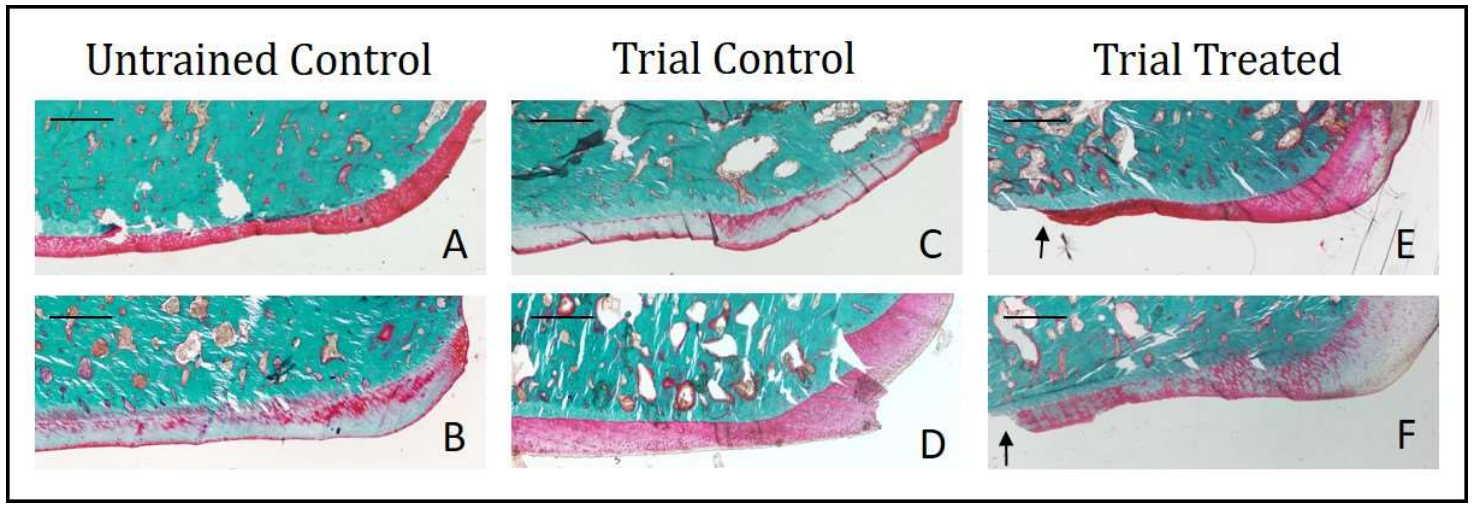

Figure 6.15 *Hyaline cartilage (pink or pink and pale green) of the weight bearing region of Cr, dorsal to the defect (arrow) which is thinner in the treated compared to the control limbs of the trial animals. A: untrained control horse 1, B: untrained control horse 5, C and E: control and treated limbs respectively of horse 1, D and F: control and treated limbs respectively of horse 2. Dorsal to right of image, proximal to top. Scale bar = 1mm. Composite images of Masson's Goldner stained sections, original magnification 4x.*

6.3.1.b *Calcified cartilage*

There was no difference in CC thickness between any groups in the Cr weight bearing region on either BSEM images or MG stained sections (Table 6.2). However, the number of tidemarks on BSEM images were greater in both the treated and control limbs of the trial animals when compared with the untrained controls (Figure 6.16, Table 6.2).

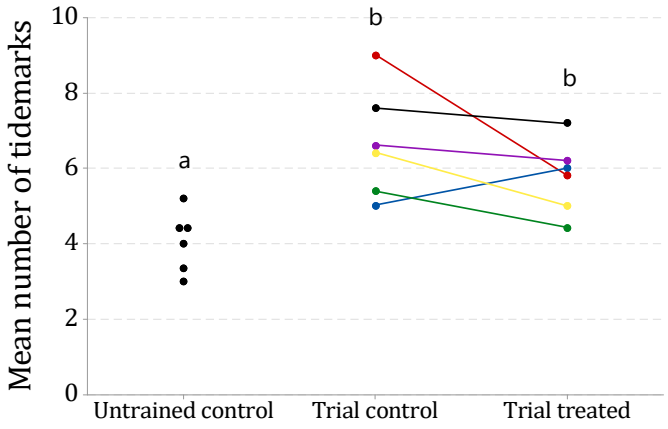

Figure 6.16 *Mean number of tidemarks, Cr, weight bearing region from BSEM images (original magnification 200x). Different letters denote significantly different groups at a level of P<0.05.*

6.3.2 *Third Carpal bone opposing the defect*

6.3.2.a *Hyaline cartilage*

Hyaline cartilage thickness was greater in the treated limbs and in the untrained controls when compared to the contralateral control group on MG stained sections in the region of C3 opposing the defect (P=0.04 and P=0.05 respectively, Table 6.3, Figure 6.17 and 6.18). There was no difference between groups in HC thickness on DIC images or MB stained sections.

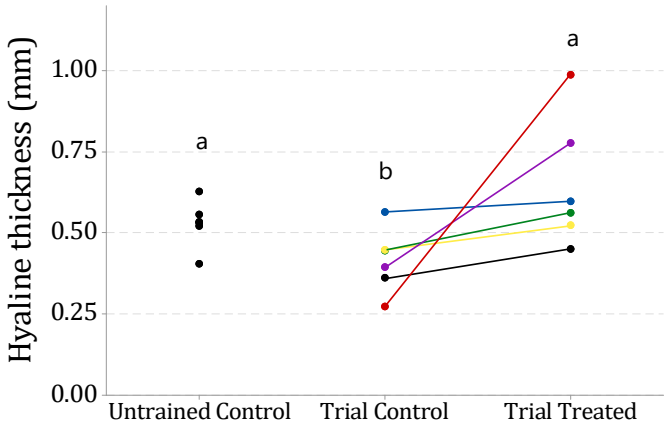

Figure 6.17 *Hyaline cartilage thickness (mm), C3, region opposing the lesion. From MG stained sections. Different letters denote significantly different groups at a level of P<0.05.*

		Mean (Median), Range			P-value		
		Trial Treated	Trial Control	Untrained Control	Trial Treated v Trial Control	Trial Treated v Untrained Control	Untrained Control v Trial Control
HC.Th (mm)	MG stained	0.649 (0.579) 0.539	0.413 (0.420) 0.293	0.528 (0.532) 0.223	**0.04**	0.21	**0.05**
CC.Th (mm)	BSEM	0.224 (0.229) 0.066	0.228 (0.219) 0.100	0.251 (0.245) 0.080	0.74	0.14	0.29
	MG stained	0.211 (0.208) 0.101	0.199 (0.208) 0.081	0.243 (0.233) 0.106	0.40	0.18	0.06
Labelled TM	Fluoro.	0.855 (0.861) 0.357	0.312 (0.136) 0.869	NA	**0.01**	NA	NA
TM number	BSEM	8.6 (8.9), 3.4	8.1 (7.9), 4.0	6.3 (6.7), 6.0	0.63	**0.05**	0.10

Table 6.3 *Cartilage thickness (mm) and tidemark observations, C3, region opposing defect. From Masson's Goldner stained sections (MG stained), BSEM images (BSEM) and fluorescence microscopy (Fluoro.). HC.Th = hyaline cartilage thickness (mm), CC.Th = calcified cartilage thickness (mm), Labelled TM = length of oxytetracycline labelled tidemark/ length of tidemark, TM number = mean number of tidemarks.*

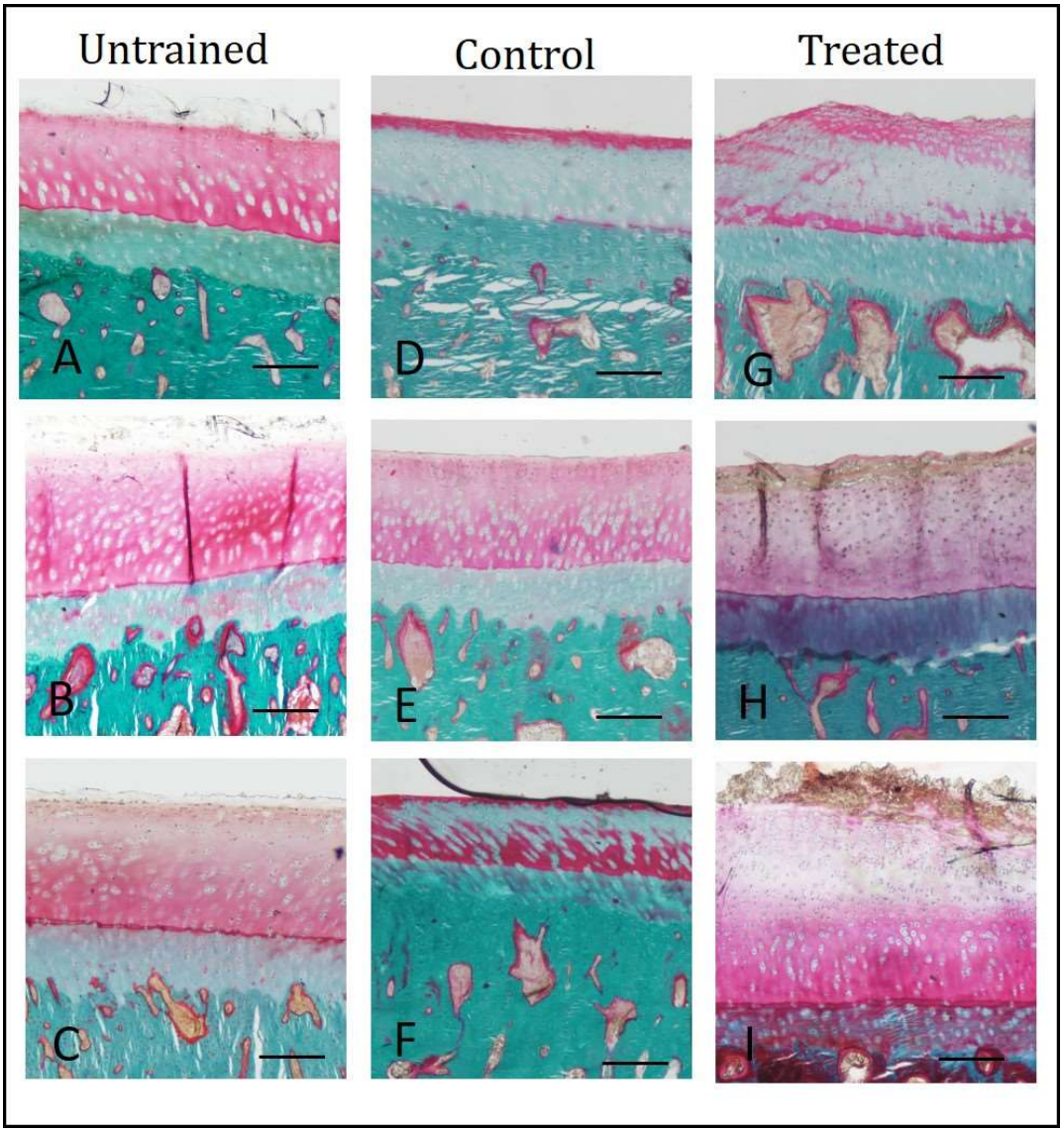

Figure 6.18 *Masson's Goldner stained sections, C3, region opposing the defect, showing thicker hyaline cartilage (pink or pink/light green) in the untrained controls (A-C) and treated limbs (G-I) compared to the control limbs (D-F) of horses 1,3 and 5 respectively. Scale bar 0.4mm*

In addition to being thicker, hyaline cartilage in the region opposing the defect in C3s from treated limbs had a thinner tangential layer (P=0.03), lower tangential cell aspect ratio (the cells were rounder, P=0.03) and greater chondrocyte clustering in the superficial cartilage to a degree that approached significance (P=0.06) on DIC images (Table 6.4, Figures 6.19 and 6.20).

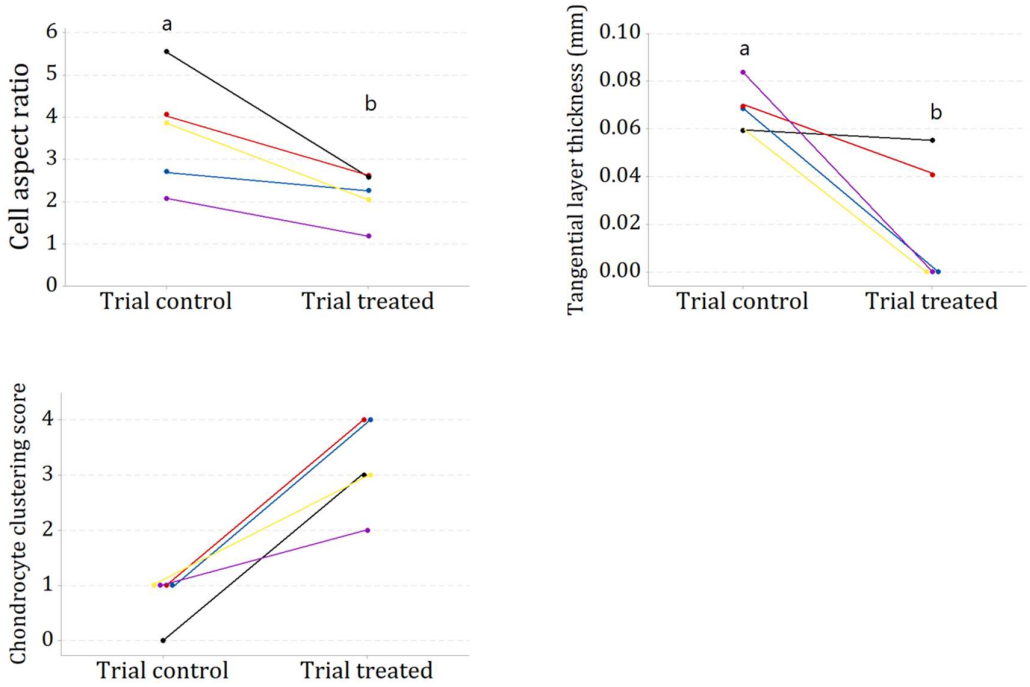

Figure 6.19 *Cell aspect ratio (width: depth), tangential cell layer thickness (mm) and chondrocyte clustering score, C3, region opposing the defect. From DIC images. Tangential layer thickness 0 = no cells aligned tangentially (i.e. all cells round). Different letters denote significantly different groups at a level of P<0.05.*

		Mean (Median),Range			P-value		
		Trial Treated	Trial Control	Untrained Control	Trial Treated v Trial Control	Trial Treated v Untrained Control	Trial Control v Untrained Control
Tangential Th. (mm)	DIC	0.019 (0.00), 0.055	0.068 (0.068), 0.024	NA	**0.03**	NA	NA
Tang. cell aspect ratio	DIC	2.14 (2.27), 1.44	3.65 (3.86), 3.47	NA	**0.03**	NA	NA
C'cyte area ($x10^{-5}$ mm^2)	MB	3.4 (3.4), 1.2	2.7 (2.8), 1.6	2.17(2.09), 1.06	0.10	**0.003**	0.14
Clustering	DIC	3.2 (3.0), 2.0	0.80 (1.0), 1.0	NA	0.06	NA	NA
Metachromatic staining	MB	1.9 (0.67), 3.3	0.0 (0.0), 0.0	0.56 (0.67), 1.3	0.06	0.20	0.12
Total pathology score	MB	7.8 (7.0), 8.7	4.5 (4.3), 2.0	4.1 (4.7), 2.7	0.10	0.06	0.93

Table 6.4 *Hyaline cartilage morphology, C3, region opposing the defect. From DIC images (DIC) and methylene blue stained semi-thin sections (MB). Tang. thickness = tangential layer thickness (mm), Tang. Cell aspect ratio = Tangential cell aspect ratio, C'cyte area = chondrocyte area ($x10^{-5}$ mm^2/cell), Clustering = chondrocyte clustering score (of a maximum possible total of 4), C'cyte necrosis = chondrocyte necrosis score (maximum possible total of 4), Metachromatic staining = metachromatic staining score (of a maximum possible total of 4) and Total pathology score = total pathology score (of a maximum possible total of 20).*

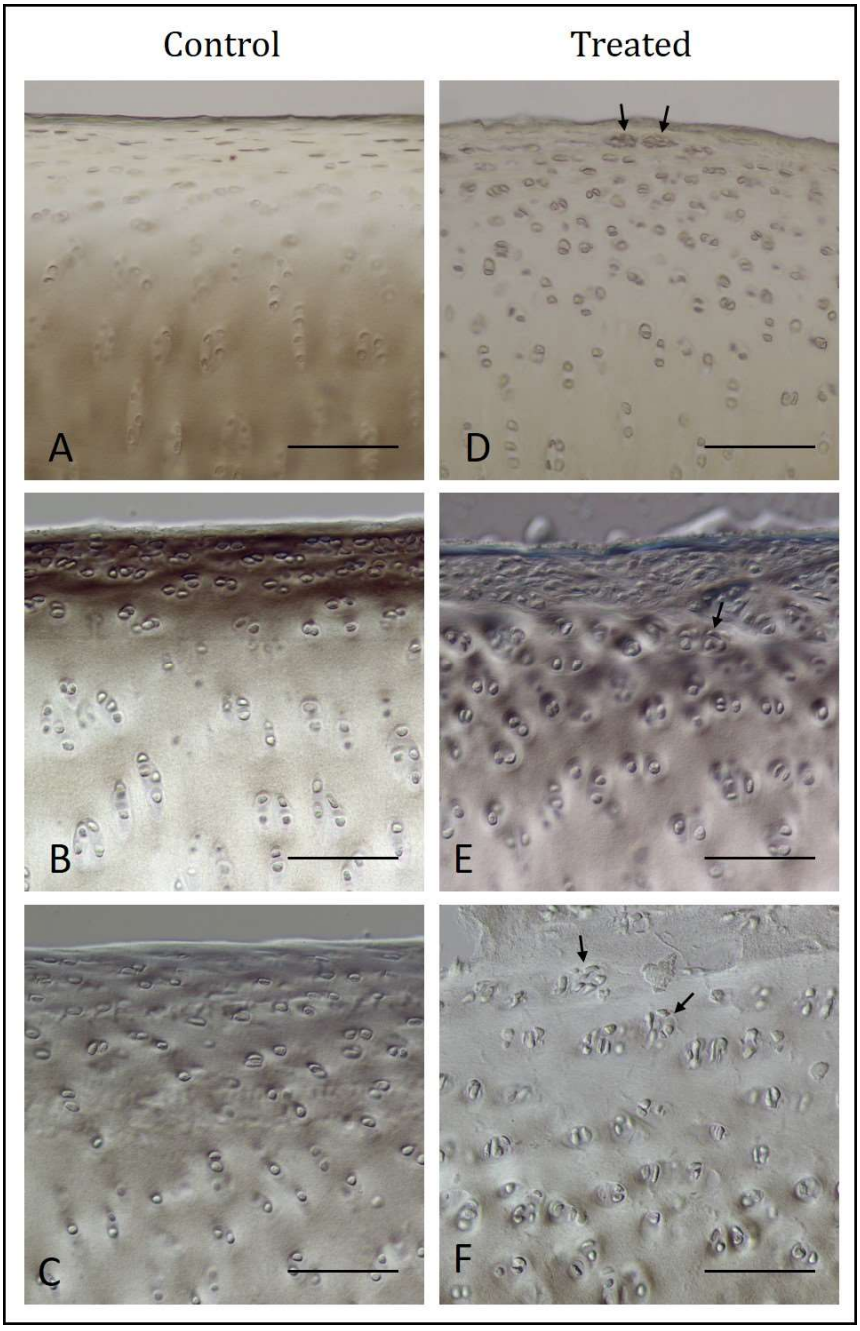

Figure 6.20 *DIC Images of hyaline cartilage of C3 in the region opposing the lesion, showing varying degrees of clustering (arrows), rounding and loss of tangential alignment in the superficial layer. Control and treated limbs respectively of Horse 1 (A and D), horse 4 (B and E) and horse 6 (C and F). Scale bar = 0.1mm.*

Chondrocyte size, when measured on cells through the entire depth of hyaline cartilage on MB stained semi-thin sections, was significantly greater in treated limbs when compared with the untrained controls (P=0.003), and was greater in treated limbs when compared with the contralateral controls in four of the five animals used for cartilage histology, however this did not translate to a statistically significant difference (P=0.10, Table 6.4, Figures 6.21 and 6.22).

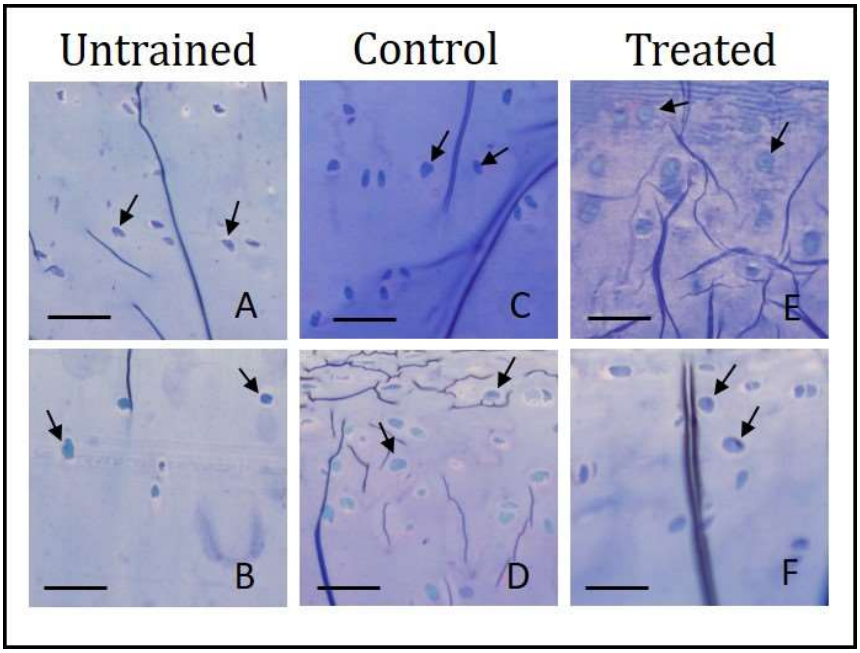

Figure 6.21 *Chondrocytes (arrows) in hyaline cartilage of C3 in the region opposing the defect: untrained control horse 2 (A) and untrained control horse 3 (B), control and treated limbs respectively of limbs of horse 4 (C and D) and 3 (E and F). Chondrocytes are larger in treated limbs in this region compared to both the untrained control horses and contralateral control limbs. Methylene blue stained semi-thin sections. Scale bar 50µm.*

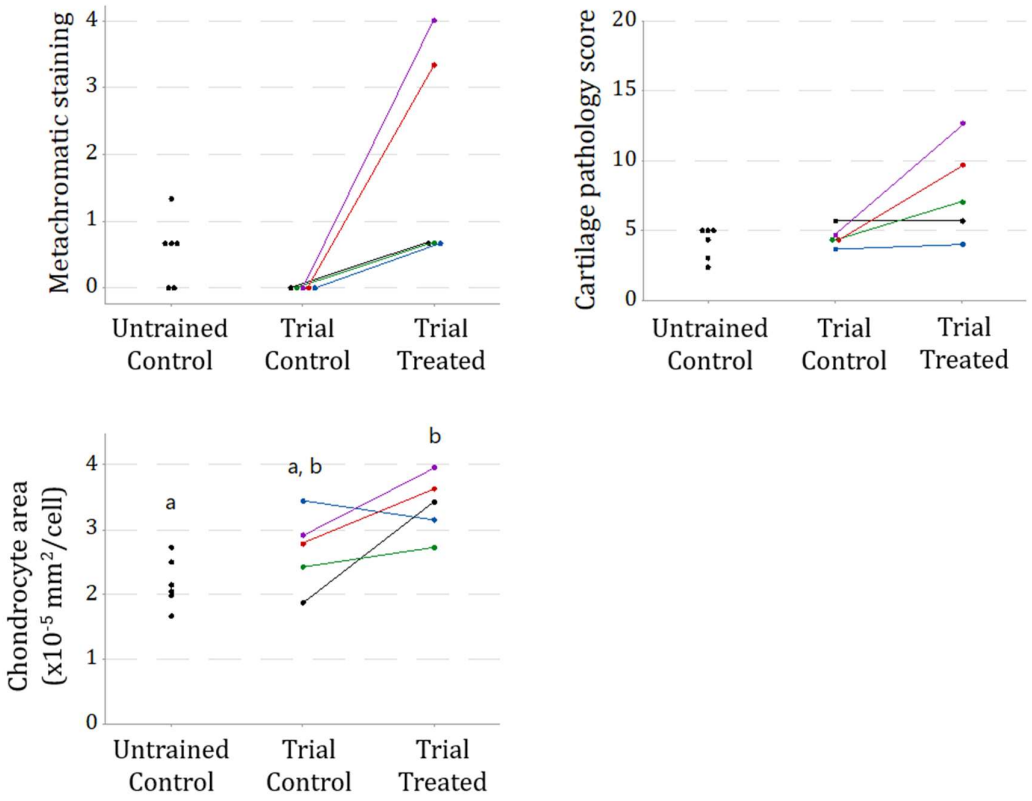

Figure 6.22 *Metachromatic staining score, cartilage pathology score and chondrocyte area (x10-5 mm2/cell), C3, region opposing the defect, from MB stained sections. Different letters denote significantly different groups at a level of P<0.05.*

The metachromatic staining score was higher in the treated limbs compared to the control limbs in all of the trial animals used for cartilage histology while the total cartilage pathology score was higher in the treated compared to the control limbs in four of the five of the trial animals used for this measurement, however the differences between groups were not quite significant (P=0.06 and P=0.10 respectively, Figure 6.22, Table 6.4).

6.3.2.b Calcified cartilage

Calcified cartilage thickness did not differ between groups on any analysis in the region opposing the lesion. There was a greater number of tidemarks on BSEM images in both limbs of the trial animals when compared with untrained controls, however this was statistically significant only when comparing the treated limbs with the untrained controls (P=0.05, Table 6.3, Figure 6.23). A greater proportion of the TM was oxytetracycline-labelled in treated limbs compared to the contralateral controls (Figures 6.24 and 6.25, Table 6.3).

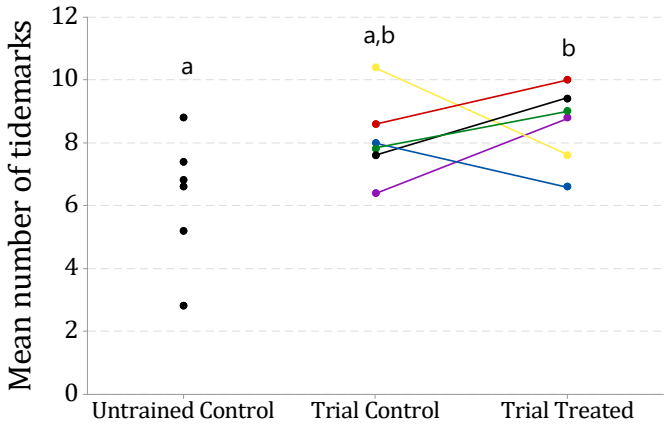

Figure 6.23 *Mean number of tidemarks, C3, region opposing the lesion. Measured on BSEM images. Different letters denote significantly different groups at a level of P<0.05.*

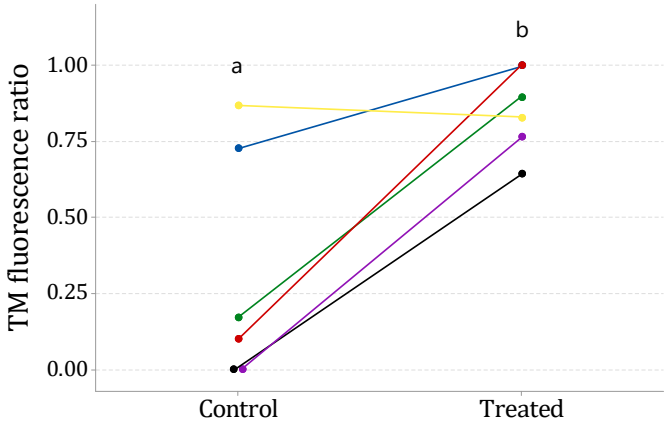

Figure 6.24 *Proportion of tidemark fluorescence C3, region opposing the lesion. Measured on unstained, undecalcified sections under UV fluorescent light. Different letters denote significantly different groups at a level of P<0.05.*

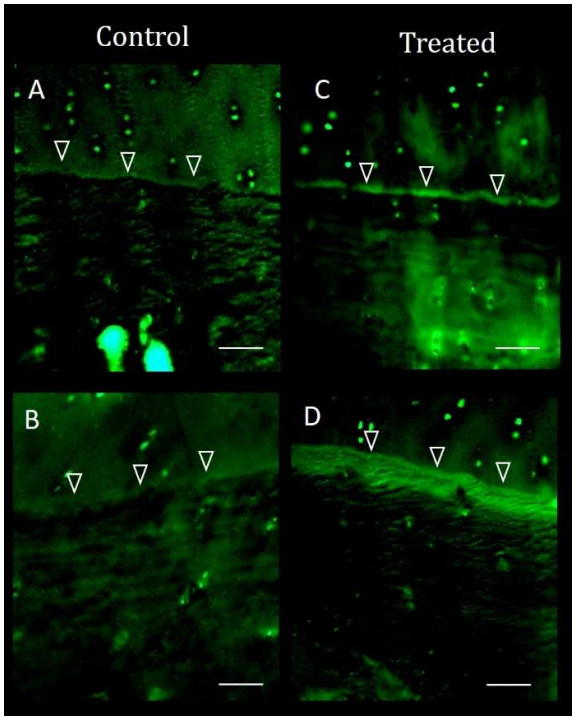

Figure 6.25 *Fluorescent microscopy images of C3, region opposing the defect from the control (A and B) and treated (C and D) limbs of horse 3 and 5 respectively. Moderate (C) and more marked (D) fluorescence of the TM (arrow heads) is observed in the treated limbs. Scale bar 50µm.*

6.3.3 Third Carpal bone weight bearing region

6.3.3.a Hyaline cartilage

Hyaline cartilage thickness of treated limbs was significantly lower than that of the untrained controls and lower than contralateral controls but not significantly so in the weight bearing region of C3 on MG stained sections (P=0.02 and P=0.08 respectively, Figures 6.26 and 6.28, Table 6.5). There was no difference in HC thickness in this region on DIC or MB measurements (data not shown).

Chondrocyte area measured on MB stained semi-thin sections was greater in the control limb of the trial animals when compared to the untrained controls (P=0.003, Figure 6.27). There was no difference in chondrocyte area in the treated limbs when compared with either of the control groups. The total pathology score was increased in the treated compared to control limbs of four of six trial animals on MB stained semi-thin sections although this difference was not significant (P=0.14, Figure 6.27, Table 6.5).

		Mean (Median), Range			P-value		
		Trial Treated	Trial Control	Untrained Control	Trial treated v Trial control	Trial treated v Untrained control	Untrained control v Trial control
HC.Th (mm)	MG stained	0.330 (0.333), 0.201	0.403 (0.355), 0.253	0.455 (0.419) 0.226	0.08	**0.02**	0.35
CC.Th (mm)	BSEM	0.171 (0.167), 0.095	0.133 (0.137) 0.065	0.155 (0.157) 0.050	**0.01**	0.32	0.10
	MG stained	0.163 (0.161), 0.086	0.116 (0.105), 0.083	0.174 (0.166), 0.069	**0.02**	0.53	**0.01**
TM number	BSEM	6.7 (6.8), 3.2	6.4 (6.5), 4.2	5.1 (4.8), 4.0	0.72	0.07	0.17
C'cyte area ($x10^{-5}$ mm^2)	MB	2.61 (2.84), 2.68	2.93 (2.92), 0.751	2.11 (2.07), 1.02	0.29	0.26	**0.003**
Total Pathology Score	MB	4.94 (5.17), 2.33	3.17 (3.17), 3.00	4.50 (4.83), 4.67	0.14	0.59	0.16

Table 6.5 *Cartilage thickness, tidemark number and hyaline cartilage morphology, C3, weight bearing region. From Masson's Goldner stained sections (MG stained), BSEM images (BSEM), methylene blue stained semi-thin sections (MB) and DIC images (DIC). HC.Th = hyaline cartilage thickness (mm), CC.Th = calcified cartilage thickness (mm), TM number = mean number of tidemarks, C'cyte area = chondrocyte area ($x10^{-5}$ mm^2/cell), Total pathology score = total pathology score (maximum possible total of 20).*

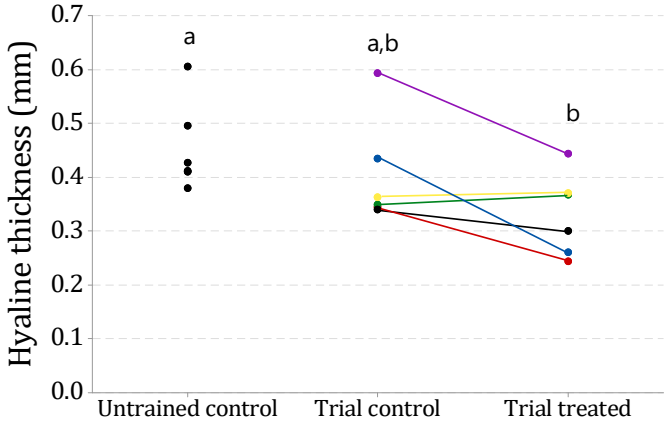

Figure 6.26 *Hyaline cartilage thickness (mm), C3, weight bearing region. From Masson's Goldner stained sections. Different letters denote statistically different groups at a level of P<0.05.*

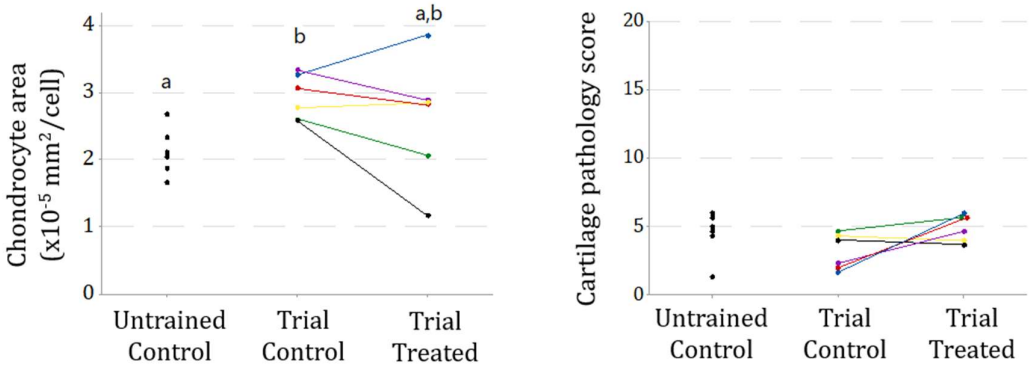

Figure 6.27 *Chondrocyte area (x10-5 mm2/cell) and cartilage pathology score (maximum possible score = 20), C3, weight bearing region. From MB stained semi-thin sections. Different letters denote significantly different groups at a level of P<0.05.*

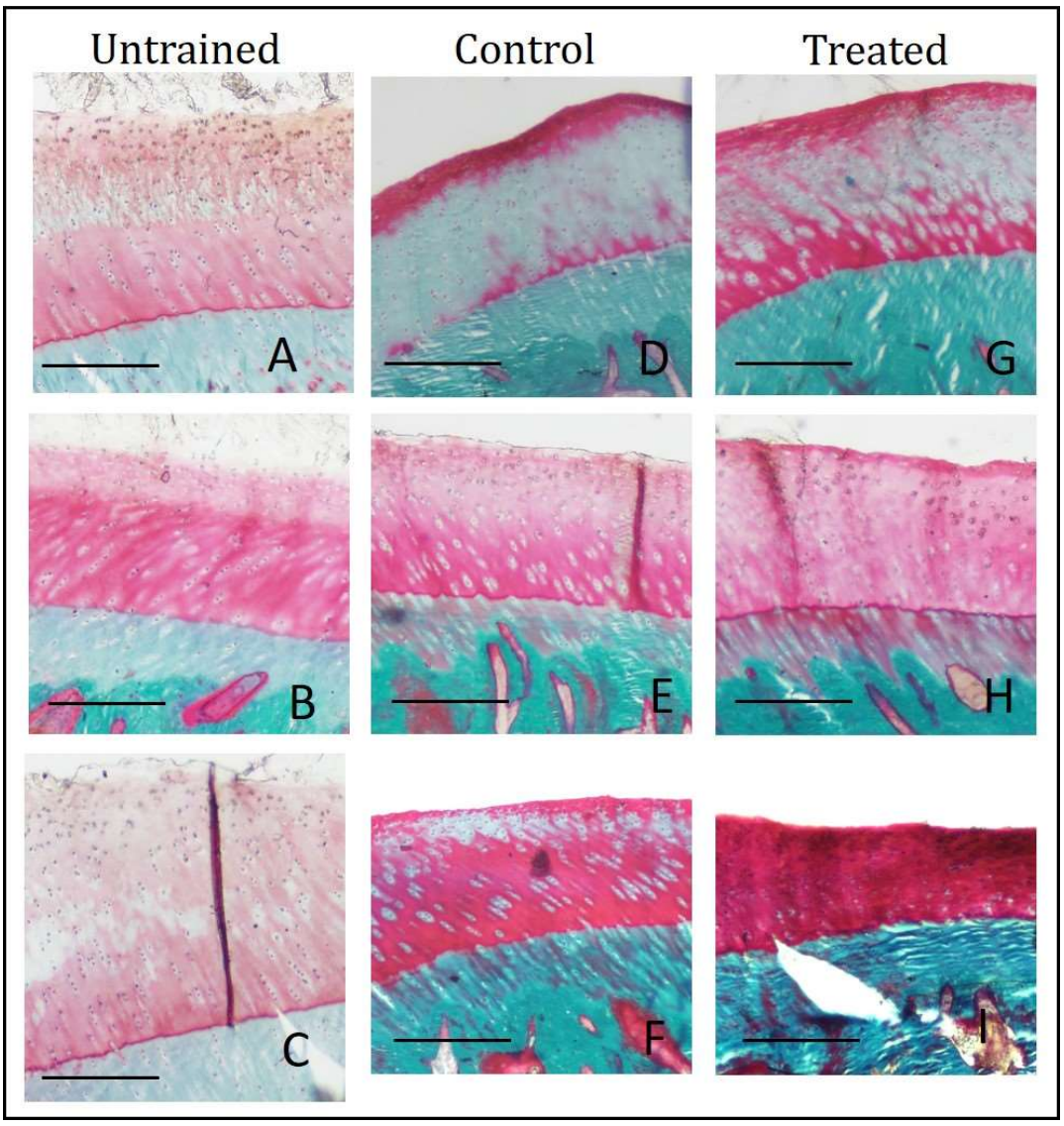

Figure 6.28 *Masson's Goldner stained sections of C3, weight bearing region showing thinner hyaline cartilage (pink or pink/light green) in treated limbs when compared to the untrained controls. Untrained control horse 6, 4, 3 (A-C respectively), control limbs (D-F) and treated limbs (G-I) of horses 1, 3 and 5 respectively. Scale bar 0.4mm.*

6.3.3.b Calcified cartilage

Calcified cartilage thickness in the weight bearing region of C3 was greater in the treated limbs when compared to the contralateral controls when measured on both BSEM and MG stained sections (Figures 6.29 and 6.30, Table 6.5). The number of tidemarks in the weight bearing region of C3 was greater in the treated limb of the trial horses compared with the untrained controls although this difference was not quite significant (P=0.07, Figure 6.29, Table 6.5).

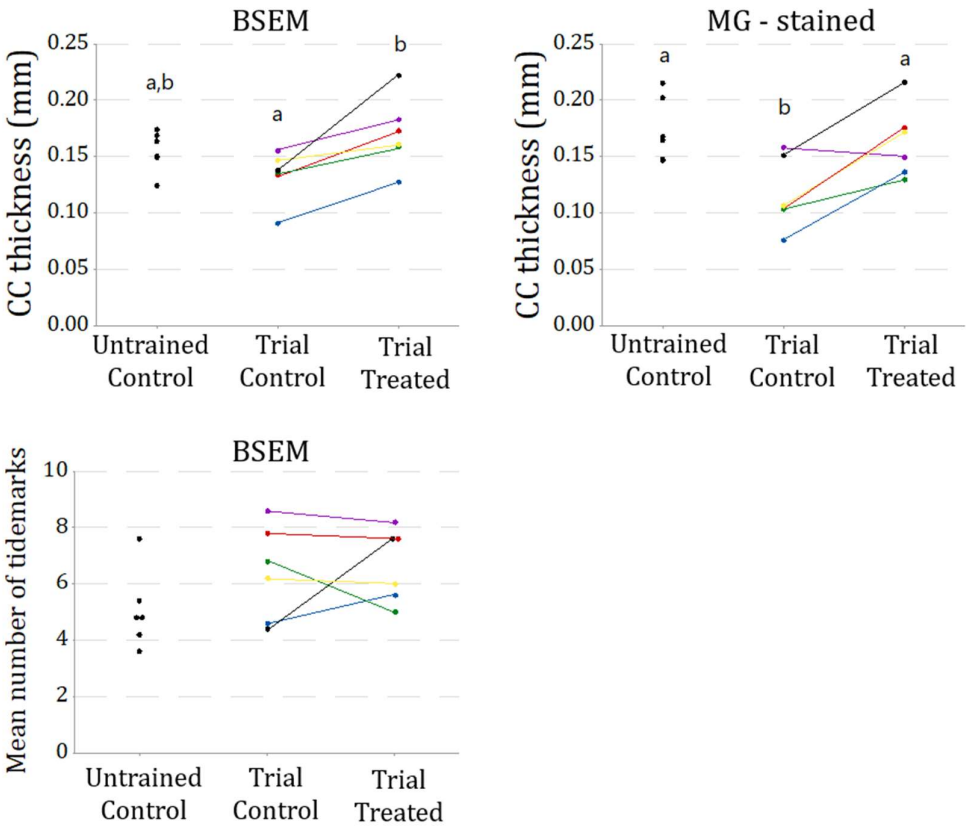

Figure 6.29 *Calcified cartilage thickness, C3, weight bearing region. From BSEM images and MG-stained sections and mean number of tidemarks from BSEM images. Different letters denote significantly different groups at a level of P<0.05.*

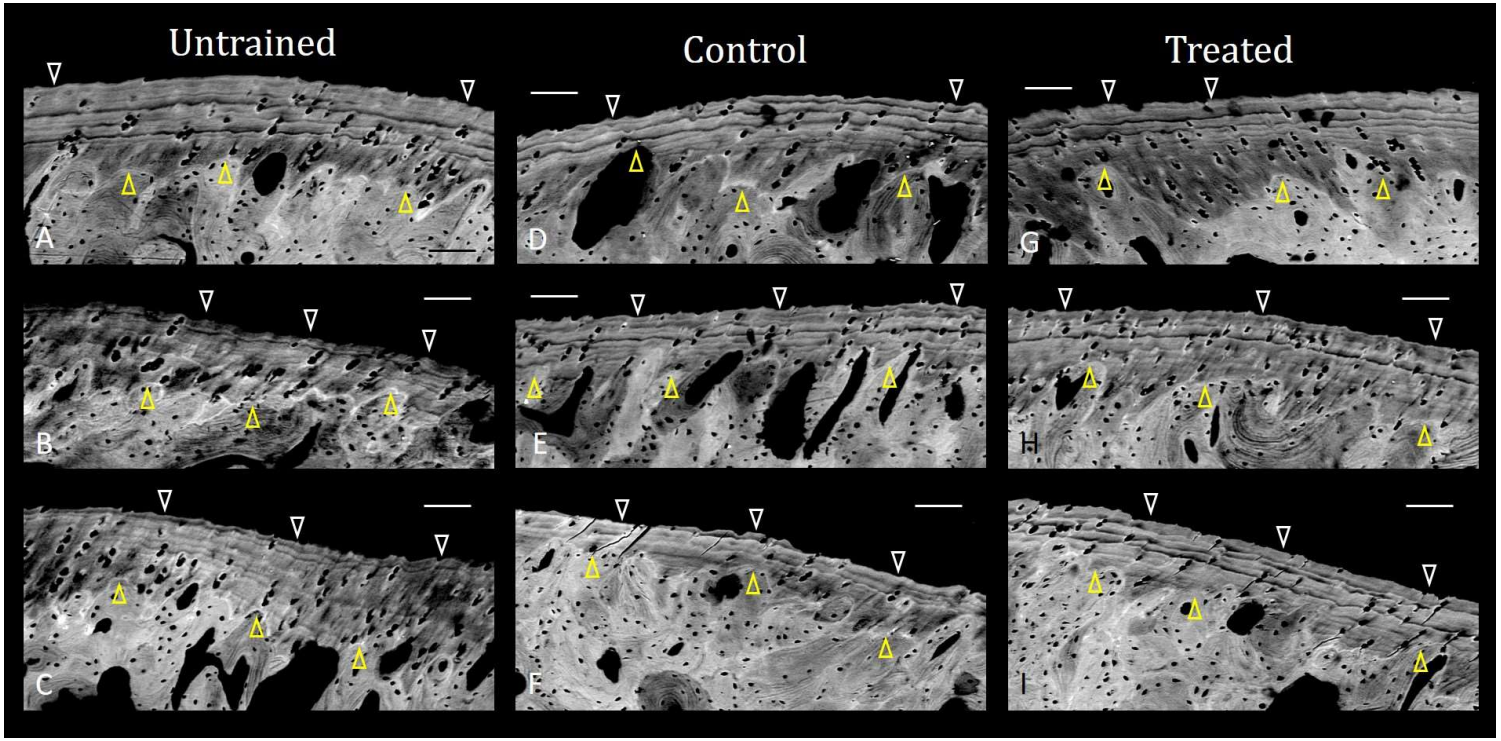

Figure 6.30 *BSEM images of the weight bearing region of C3 showing thicker CC in the treated limbs of horses 2, 3 and 6 (G, H, I respectively) compared with their control limbs (D, E, F respectively). CC in the weight bearing region of untrained control horse 1, 3 and 6 shown in A, B, C respectively. White arrow heads = most superficial TM, Yellow arrow heads = osteochondral junction. Scale bar 0.1mm.*

6.3.4 *Ulnar Carpal bone*

There were no differences in Cu histomorphology between treated and control groups on MB stained semi-thin sections. However, within treated joints the total cartilage pathology score was lower in Cu than in either the region opposing the lesion or the weight bearing region in C3 to a degree that approached significance (median difference = 3.5, P= 0.06 and median difference = 1.7, P= 0.08 respectively, Figure 6.31).

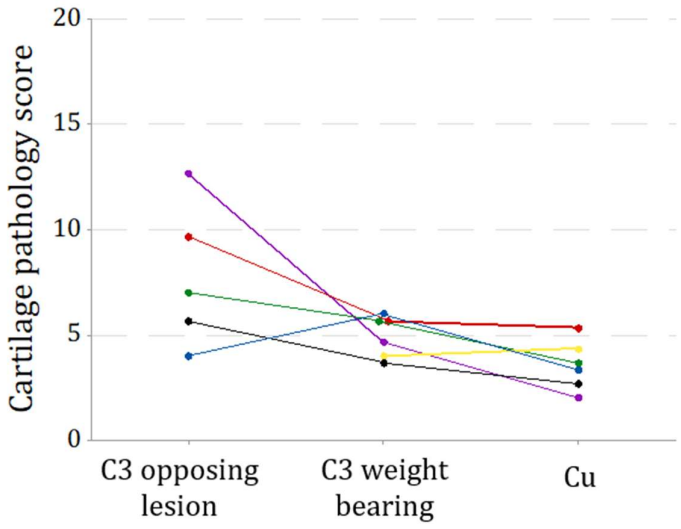

Figure 6.31 *Total cartilage pathology scores (out of a possible score of 20) for sites within the midcarpal joint of treated limbs. From MB stained semi-thin sections.*

6.4 Discussion

6.4.1 Summary of major findings

Ten weeks after creation of a Cr articular surface defect, in the region of C3 opposing the Cr defect hyaline cartilage was thicker, with larger chondrocytes that were rounder and showed evidence of proliferation in the superficial layer. Calcified cartilage thickness was similar to controls but there was increased fluorescent labelling of the tidemark.

Hyaline cartilage was thinner and CC thickness unchanged in the dorsal weight bearing region of Cr adjacent to the defect. In the directly opposing weight bearing region of C3 there was no change in hyaline cartilage thickness, whereas CC thickness was increased.

6.4.2 Comparison with current literature

6.4.2.a Cartilage thickness

Overall, hyaline and calcified cartilage thicknesses measured in the current study are consistent with previous reports of hyaline (0.3-1.0 mm) and calcified (0.1-0.4mm) cartilage thickness in equine radial and third carpal bones (59, 69, 97).

Most previous investigations of osteochondral defects in horses have not specifically measured cartilage thicknesses either adjacent to or opposing the defects. However, Kold et al. (340) reported that cartilage became subjectively thinner closer to the edge of osteochondral defects on equine femoral condyles, and grossly raised areas of cartilage have been observed on Crs opposing C3 osteochondral defects which is consistent with

observations in the current study (202, 388). Salonius et al. (2018) found that cartilage adjacent to OC defects in the equine carpus was thinner than the repair tissue within the defect itself but did not compare it to normal cartilage (371). Thickened cartilage has been observed overlying cystic SCB lesions created in femoral condyle of ponies (340) and over regions of SCB collapse in equine fetlock joints (212), both of which are likely to have been associated with loss of surface congruity.

Additionally, cartilage has been shown to be thicker on the low side of step defects in rabbits and sheep, where surface pressures are reduced, and thinner on the high side, where surface pressures are increased when compared to normal joint surfaces (209, 211).

However, observations from models of incongruity differ from studies of normal cartilage which find that HC is thicker in regions of greater habitual loading (110, 126, 445-447). This difference may be because incongruity is likely to result in supra-physiological loads. While moderate exercise has been shown to increase hyaline cartilage thickness, strenuous exercise results in thinning in canine stifles (92, 118). Additionally, in contrast to the other studies and more in keeping with findings from the current study, HC thickness on radial and third carpal bones of horses has been found to be greater in palmar sites than more dorsal sites where loading is greatest (69, 106, 112).

The findings from the unloaded region in the current study also differ from studies of whole joint unloading in which HC thickness is observed to decrease (119, 121, 131, 448-450). However, cartilage opposing defects has been shown to bulge into defects and is likely to be subject to different strains than cartilage in whole limb unloading which may impact HC thickness (2, 4, 362).

Calcified cartilage thickness has been observed to be greater within joints at sites of higher loading in both horses and man and in limbs experiencing greater loads in dogs and horses which is consistent with the increase in CC thickness in the weight bearing region of C3 in the current study (59, 68, 72, 79, 110). Interestingly there was no corresponding decrease in calcified cartilage thickness in the unloaded region of C3 which may also have been expected based on findings from previous studies (59, 68, 79, 110). The current trial may have been too short in duration for a measurable change in CC thickness in the unloaded region to be detected. In addition, hind limb unloading due to tail suspension or immobilisation in mice and rats has been associated with both no change and increased CC thickness suggesting that CC thickness may depend on other factors in addition to axial load (79, 121, 131).

6.4.2.b Tidemark changes

The greater number of tidemarks observed in all regions in the trial animals when compared with the untrained controls in the current study is contrary to another study which found a lower number of tidemarks in the fetlock joint of trained animals compared with untrained animals (126). Doube et al. (2007) found a lower number of tidemarks in fetlocks of young, trained horses compared with untrained horses only at one site, on the palmar sagittal ridge, but the number of tidemarks was negatively correlated with the rate of advancement of the calcification front (68). These differences in observations may be related to intensity of training, which was short and of lower intensity in the current study relative to the others. In addition, tidemark behaviour may be different in immature animals such as those studied in Doube et al. (2007) compared to adults as in the current

study (68). Finally the prior training history of animals in the current study is unknown and may have affected the number of tidemarks present.

In keeping with the observation of increased fluorescent labelling of the TM in the region opposing the defect in C3 an increased rate of TM advancement has been observed both in joints of unloaded limbs and in regions of joint surface under lower loading when compared to those with higher loading (68, 131). Interestingly, Llinas et al. (1993) observed an increased TM advancement on both the low side (decreased loading) and high side (increased loading) of intra-articular step defects in rabbit stifles (211). While the increased advancement on the low side is consistent with findings in the unloaded region of C3, an equivalent change was not seen in the loaded region in the current study. The reason for this difference is not clear. Greater translational movement between the two surfaces of stifle joints compared to that in the mid-carpal joint may play a role in this difference as it has been hypothesised that shear strains stimulate TM advancement during growth (67), however the differences in motion between joints is poorly understood and there is also a degree of sliding motion between the two articular surfaces of the mid-carpal joint.

6.4.2.c Chondrocyte changes in the region opposing the defect

Similar to the current study, chondrocyte clustering was observed in tibial plateau cartilage opposing osteochondral defects in the femoral condyle of horses (366). In addition, some studies of unloaded rat hind limbs have reported chondrocyte clustering in articular cartilage (450, 451) which is consistent with the clustering observed in the unloaded region in the current study. However this is not a consistent finding as other studies of whole-limb unloading in both rodents and dogs have found no evidence of

chondrocyte clustering, and chondrocytes both *in vitro* and *in vivo* have proliferated less when mechanically unloaded (119, 121, 449, 452). Cartilage opposing the defect in the current study was likely to be subject to different strains to cartilage in unloaded limbs or chondrocytes *in vitro* (2, 4). In conditions more consistent with the current study, Trumble et al. (2001) observed increased cellularity of the hyaline cartilage and hypertrophy of the chondrocytes on the low (unloaded) side of step defects in ovine tibia (209).

Rounding of chondrocytes as observed in the region opposing the defect in the current study is consistent with observations from the canine tibial plateau where regions of lower loading have rounder chondrocytes and with *in vitro* studies in which unloading of chondrocytes has resulted in rounding while loading has resulted in conversion to a more ellipsoid shape (84, 452, 453).

6.4.2.d Cartilage pathology

Studies of osteochondral defects in horses and other species report degenerative changes such as fibrillation, chondrocyte cloning and loss of cartilage both adjacent to and opposing the defects which is consistent with the increase in C3 cartilage pathology scores in treated limbs in the current study (17, 18, 202, 366). However this is not a consistent finding with Salonius et al. (2018) reporting no degenerative changes adjacent to osteochondral lesions 2-8mm in diameter (371).

The cartilage pathology scores observed on C3 from treated joints in the current study are higher than most of those reported using similar scoring systems in chip fracture models of osteoarthritis which have reported mean scores of 2.5 to 4.4 (268-270, 272) although one chip fracture model reported a median score of 7 (401). These above studies did not

include assessment of staining intensity within the total score, while a fetlock groove model of OA which did include staining intensity in the total reported scores of 7.3 and 12.4 in treated joints (454), so inclusion of metachromatic staining may account for the higher total scores in the current study. In addition, cartilage pathology scores from the control limbs in the current trial were also higher than those reported in the chip fracture models (1.04) suggesting inter-observer variation (268).

In keeping with the total cartilage pathology scores in Cu in the current study, Koenig et al. (2014) observed modified Mankin scores in cartilage distant to the site of a Cr chip fracture to be lower than that in cartilage adjacent to or opposing the injury (401). However other studies using the equine chip fracture model have reported similar modified Mankin scores at sites distant to the fracture when compared with sites adjacent to or opposite the fracture (272). Unlike the findings in the current study, cartilage fibrillation and increased cartilage pathology scores have been observed at sites distant to osteochondral defects in equine mid-carpal joints and rabbit stifles respectively (18, 202). Duration of the study, greater numbers of animals and, in the case of the rabbit study, smaller size of the joints may account for the difference between their observations and those in the current study. However, similar to findings in the current study, Vaseenon et al. (2011) found that cartilage pathology scores at the site distant to the defect were lower than at sites adjacent to or opposing it (18).

6.4.3 Interpretation of major findings

6.4.3.a Response of cartilage to incongruity

While earlier studies of joint surface pressure provided some insights into the changes in loading associated with osteochondral defects, more recent FE models have confirmed that compressive and shear strains are increased in cartilage adjacent to defects and, to a lesser degree, in cartilage of the opposing, in-contact, joint surface; that cartilage opposing the defect experiences reduced compressive strains and increased tensile strains; and that cartilage opposing the rim of defects experiences increased tensile and shear strains (4, 358, 359). There is evidence that the modelled changes in strains may have an effect at the cellular level as it is recognised that cartilage morphology varies depending on local loading patterns (68, 73, 112). One possible reason for these variations is the change in chondrocyte behaviour when exposed to different magnitudes of hydrostatic pressure and shear stress (85, 90, 442-444, 455, 456). There is therefore good evidence to suggest that the changes observed in cartilage surrounding and opposing osteochondral defects may be a result of altered strain within that cartilage.

In the current study, training in the absence of a joint defect was associated with thinner HC in C3, although differences were not always significant. When the effect of the osteochondral defect was added to the effect of training the HC was thinner still in the region of increased load, consistent with the idea that higher magnitude, cyclic loading is associated with thinner HC in adult animals and suggesting that HC thickness may decrease as the magnitude of loading increases (112).

Thinning of the HC adjacent to the defect on Cr is likely to have been the result of increased compressive strains, mediated through either physical deformation, including compression of the cartilage and deviation of the cartilage laterally into the defect and/or reduced matrix protein synthesis due to supra-physiological loading (209, 442, 456). Cartilage erosion was only observed in one horse so this process is unlikely to play a major role in HC thinning. The decrease in HC thickness in the opposing weight bearing region of C3 was less marked than that in the cartilage adjacent to the defect on Cr possibly because there was no scope for lateral deviation of the cartilage into a defect (4, 209, 211, 358).

The increased CC thickness in the weight bearing region of C3 is consistent with a reduction in remodelling at the osteochondral junction induced by increased load as suggested by others and supported by the measured decrease in remodelling activity in the underlying SCB (Chapter 5) rather than by advancement of the TM as there was minimal oxytetracycline labelling at the TM (59, 68, 73, 110, 131). The number of tidemarks was consistently higher in the trial animals than in the untrained controls, regardless of whether there was a defect in the joint, although this difference was not always significant. This may be a result of training during the trial or due to differences in the prior history of the animals.

The unchanged CC thickness in the weight bearing region of Cr of treated limbs may be explained by a smaller increase in hydrostatic pressure when compared to the weight bearing region of C3 due to the lack of constraint, and therefore fluid loss under compression, at the defect edge, as hydrostatic pressure has been suggested to reduce ossification of the CC (67, 68, 128, 131). A difference in the mechanical properties of

cartilage from either joint surface may also have resulted in different responses to the change in loading (457, 458).

Loss of surface contact leading to decreased compressive but increased tensile strains in the region of C3 opposing the defect is the likely cause of the observed increase in HC thickness and the increased proportion of tetracycline labelled TM. These observations are consistent with the hypothesis that reduced hydrostatic pressure stimulates advancement of articular cartilage towards the opposing surface (68, 136). Despite increased tetracycline labelling of the TM, CC thickness was unchanged which could be due to a concurrent increase in resorption of CC at the osteochondral junction (68, 121, 131, 136, 244). This suggestion is supported by the observed increase in remodelling activity in SCB in the unloaded region of C3 (Chapter 5).

The increase in chondrocyte size and reduction in staining of the superficial zone in the region of C3 opposing the defect, although not quite significant, may be a direct result of loss of compression allowing the cells to expand and the water content of the ECM to increase (459). The loss of staining could also be due to a loss of glycosaminoglycans as cartilage under conditions of lower loading has lower PG content than more highly loaded cartilage (79, 92, 123, 124, 460), or reflect a change in the quality of the matrix proteins as decreased aggregation of PGs has been reported in cartilage from unloaded limbs (119). While the net protein content of the cartilage is lower, the rate of production of matrix proteins by chondrocytes is greater in regions of cartilage under lower loads (123, 124, 461) and chondrocytes in this region may have become larger due to increased matrix production (55). Hypertrophy of chondrocytes also occurs prior to calcification in growth cartilage (142) and upregulation of this process in the region opposing the defect is

consistent with the hypothesis that advancement of the TM through calcification of the HC is stimulated by lower loading (68, 128, 131, 136, 453). However I am not aware of any other evidence that hypertrophic differentiation occurs in regions of unloading.

Chondrocyte clustering as seen in HC of the unloaded region of C3 was also observed, although not quantified, in the region opposing the edge of the defect where there were increased shear strains (4, 358). While this feature has been associated with degeneration of hyaline cartilage (331, 462), and may be a reflection of this process in the current study, its presence is also consistent with cartilage growth and the hypothesis that hydrostatic loading inhibits and tensile strains promote cartilage growth (128, 136). There is evidence that chondrocytes in the superficial layer of articular cartilage of young animals act as progenitor cells, providing a source of cells for the deeper layers (463-465) however, I am not aware of work suggesting that chondrocytes in adult articular cartilage have the capacity to initiate the growth process.

The cartilage of C3 opposing the edge of the lesion was the only region in which notable fibrillation and fissuring were observed, which may indicate that after loss of congruity increased shear strains have a greater role in the pathogenesis of fibrillation than increased compressive strains. This would be consistent with the views of others that collagen fibers are damaged by shear stresses but are more able to withstand hydrostatic forces due to the relatively incompressible fluid within the ECM (18, 67, 466).

6.4.3.b Discrepancy between methods of investigation

The increase in CC thickness in the weight bearing region of C3 in treated limbs measured on BSEM images and MG stained sections, and the increase in HC thickness in the region of C3 opposing the defect in treated limbs measured on MG stained sections were not apparent on either DIC images or semi-thin sections. The DIC images were taken from thicker sections (20µm compared to 8-10µm for the MG stained sections and the surface imaged by BSEM) and from specimens collected from closer to the region opposing the axial edge of the defect, both of which may make it more difficult to detect changes in HC and CC thickness using this method. The tidemark was sometimes difficult to define on semi-thin sections and, being taken from small specimens of articular surface, thickness measurements from these sections are more likely to be affected by alterations in the angle at which sections were cut. Therefore, it is likely that the measurements of CC thickness from BSEM images and MG stained sections, and the HC thickness measured on MG-stained sections, are more accurate than those measured from DIC images or semi-thin sections.

Additionally, chondrocyte clustering was measurably different between the treated and control limbs of the trial animals on DIC images but not on semi-thin sections. This may be because it is easier to visualise multiple cells within individual lacunae on thicker sections such as those used for DIC imaging (20µm) compared to thinner sections as used for MB staining (0.5-1.0µm).

6.4.6 Conclusion

Increased strains, possibly in conjunction with a loss of constraint at the defect edge, result in thinning of the HC of the joint surface adjacent to an OC defect.

Hyaline cartilage of an intact articular surface in adult horses responds to a focal loss of surface contact, and subsequent biomechanical changes, with an increase in thickness and an increase in mineralisation at the TM, while a focal increase in strain results in thickening of the CC possibly due to a reduction in remodelling activity at the OC junction.

Hyaline cartilage on a joint surface opposing an osteochondral defect displays histological features consistent with degenerative change in a focal manner, which may be directly related to the local changes in surface loading. These focal responses may play a role in normal joint homeostasis as well as in the pathogenesis of conditions that result in a loss of joint congruity. The focal nature of these diseases is an important consideration in understanding their pathophysiology.

Chapter 7

GENERAL DISCUSSION

7.1 Summary

This equine model of joint incongruity has demonstrated that articular cartilage and subchondral bone of adult animals respond focally to local changes in joint surface contact and loading. It was found that within a joint experiencing high magnitude repetitive loading adjacent regions of cartilage and bone behave differently depending on local surface contact. The results of this study also provide evidence that a defect in one joint surface can directly affect the behaviour of cartilage and bone of the opposing surface. The major findings of this project are summarised schematically in figure 7.1.

While the SCB changes in Cr are likely to be influenced by tissue damage associated with creation of the defect, the findings in C3 demonstrate that cartilage and SCB of an intact joint surface respond directly to a loss of congruity and changes in loading, in the absence of the inflammation and cell death associated with injury (385, 386).

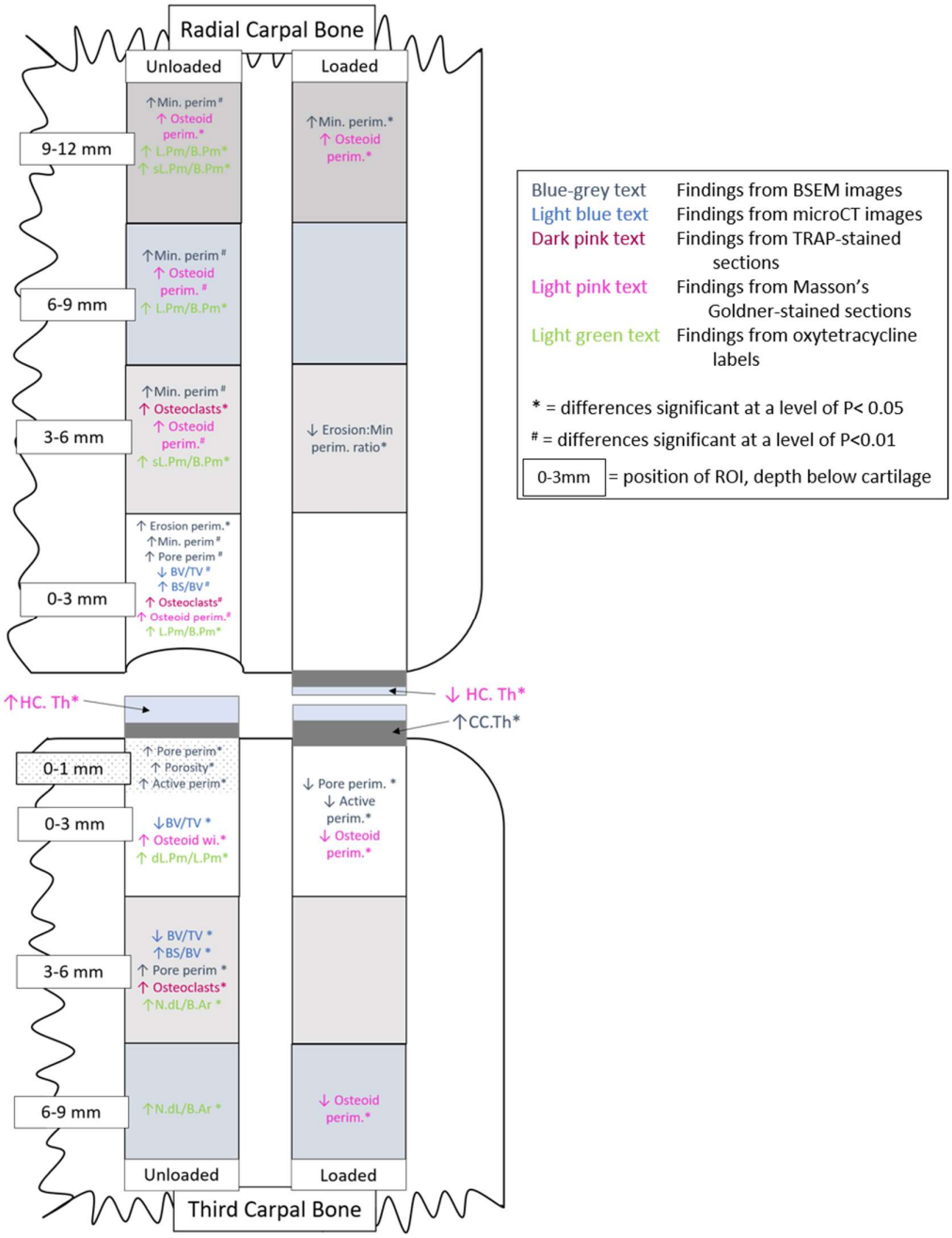

Figure 7.1 *Schematic representation of the major differences between the treated and control limbs of the trial animals from all chapters. HC.Th = hyaline cartilage thickness, CC.Th = calcified cartilage thickness, BV/TV = Bone volume/ total volume, BS/BV = bone surface/bone volume, Min.Perim = mineralising perimeter, L.Pm/B.Pm = oxytetracycline labelled perimeter/ bone perimeter, sL.Pm/B.Pm = single oxytetracycline labelled perimeter/ bone perimeter, dL.Pm/L.Pm = double oxytetracycline labelled perimeter/ total labelled perimeter, N.dL/B.Ar = number of double oxytetracycline labels/ bone area.*

There were differences between the measured responses in Cr and C3. The increase in remodelling activity in the unloaded region of C3 was less marked and more localised than that observed in the unloaded region immediately below the defect in Cr. Similarly, the loss of BV/TV in the unloaded region of C3 was less marked than that in the unloaded region immediately below the defect in Cr but extended deeper below the articular surface. The deeper SCB in the region below the lesion of Cr demonstrated increased BV/TV which was not observed in C3. Likewise, the increase in formation activity in the overloaded region adjacent to the defect in Cr was not repeated on the opposing weight bearing surface of C3, where there was instead a reduction in remodelling activity, driven primarily by a reduction in erosion. The more marked response observed in Cr likely reflects the biochemical changes associated with tissue damage at the site of the defect (227, 229, 341, 385, 386, 430). In addition, changes in strain surrounding an osteochondral defect may differ from those of the opposing joint surface (1, 215, 363).

7.2 Interpretation

7.2.1 Effect of articular surface incongruity on joint homeostasis

The findings from this study provide evidence that the inhibition of remodelling and increase in bone volume observed in SCB in situations of high magnitude repetitive loading, such as in horses in training, are directly related to increased loading of the joint surface (69, 156, 165). They also support the theory that differences in surface loading between sites within joints results in the differences in remodelling activity and BV/TV observed at these sites (74, 165).

This investigation revealed that chondrocytes in the articular cartilage of adult animals respond focally on a cellular level to local changes in strains within the cartilage and that local unloading may stimulate proliferation and hypertrophy of chondrocytes in addition to ECM changes (209, 211).

Observations from the different regions of the articular surface in this trial support the hypothesis that joint tissues have mechanisms to develop and maintain congruity which are regulated by changes in loading (77, 78, 136). In the region of C3 opposing the defect thickened HC, TM calcification and resorption at the osteochondral junction result in advancement of the articular surface, CC and SCB towards the opposing joint surface, which would tend towards restoration of surface contact (68, 209, 211, 212). In contrast, in the adjacent weight bearing region of C3 decreased remodelling at the osteochondral junction tends to slow any advancement of SCB towards the opposing joint surface (68, 136). A region of increased advancement of the articular surface where there is reduced compressive load adjacent to a region of slower advancement where there is increased compressive load would act together to increase congruity and even-out loading across the joint surface.

7.2.2 Role of articular surface incongruity in joint pathology

Local loss of surface contact in this model resulted in a focal region of cartilage changes similar to those associated with OA (19, 33, 57, 241, 243). This is in agreement with the concept that OA pathology may be in part the result of chondrocyte responses to changes in loading and that unloading in addition to overloading may play a role in the disease (125, 129, 130, 303, 467-469). It adds to previous work in which whole-limb unloading

resulted in OA-like changes by demonstrating that this can occur in focal regions of a joint surface (119, 120, 122, 448). However it is possible that although chondrocytes respond in a similar way to unloading and to degenerative disease, unloading does not directly cause degeneration. I am not aware that focal regions of unloading have previously been associated with OA.

Results from the current study suggest that local unloading of the joint surface either through loss of cartilage as occurs in naturally occurring OA in C3 of athletic horses (144, 248) or due to flattening of the articular surface of the distal femoral condyle as occurs commonly early in the development of SCB cysts in this region (215), could be a stimulus for osteoclast recruitment and focal SCB remodelling. This remodelling may play a role in the focal regions of SCB collapse and increased porosity observed deep to cartilage lesions in OA of C3 as well as in the initiation and expansion of SCB cysts in the femoral condyle (215, 248). While finite element modelling has demonstrated that flattening of the distal femoral condyle results in reduced compressive strains within the underlying SCB I am not aware of work that has investigated strains in bone under cartilage only defects (215). Interestingly, Bertuglia et al. (2015) found that in naturally occurring equine OA lesions osteoclast numbers in the SCB were more strongly correlated with RANKL expression in the middle and deep layers of the articular cartilage than in the SCB itself which could suggest that loss of the superficial cartilage layer stimulates expression of RANKL by the deeper layers either through unloading or some other mechanism (144). Once again, I am not aware of other work supporting this.

This work also supports the theory that local unloading of SCB due to loss of surface congruity is one mechanism by which remodelling is enabled in an otherwise high load

environment. In addition to the presence of inflammatory cytokines and growth factors as a result of a focal bone injury, loss of congruity and/or local unloading due to altered mechanical properties of damaged bone may contribute to increased remodelling at the site of fatigue fractures in SCB of horses in training (227, 229, 231, 470, 471).

The increase in formation activity below and adjacent to the defect in Cr is also consistent with the increase in formation activity observed surrounding naturally-occurring fatigue damage in equine SCB (231). Increased strains within the bone surrounding the fatigue fractures, similar to increased strains surrounding osteochondral defects and bone cysts, may be one mechanism by which this modelling is stimulated (1, 215).

This investigation has further highlighted the importance of understanding the focal nature of joint conditions in which incongruity is a feature, such as OA (472). It is well recognised that OA in horses and man is characterized by focal regions of cartilage loss and regions of both sclerosis and lysis in SCB and that a strong correlation exists between sites of cartilage loss and underlying SCB changes in both horses and man (144, 248, 249, 254, 473, 474). Observations from the current study have further demonstrated that at a given point in time adjacent regions of cartilage and of bone may be behaving differently and that these differences may be related to local differences in loading of the joint surface.

7.2.3 The role of inflammation and biochemical changes within the joint

Peri-articular modelling was consistently observed in treated joints and may have been a result of biochemical changes within the joint due to release of growth factors or other cytokines from the damaged bone at the defect (280, 406, 418). TGF-β, IGF-1 and BMP-

2, in addition to being associated with bone damage and implicated in the pathophysiology of peri-articular modelling, are also known to affect chondrocyte behaviour and matrix metabolism. Therefore, if these molecules in the synovial fluid are responsible for the peri-articular modelling they could also be playing a role in the observed cartilage changes, as could other pro-inflammatory cytokines released into the synovial fluid from the defect (35, 229, 394, 406, 416, 417, 420).

Pro-inflammatory cytokines and growth factors released from the defect could also modulate remodelling activity in the SCB of C3, as could cytokines released by chondrocytes in the overlying cartilage, if they had access to this bone (385, 386, 420). While it has been shown that small molecules (approximately 400-1550 Da) are able to diffuse through articular cartilage into SCB (475, 476), I am not aware that this has been demonstrated for larger molecules such as the pro-inflammatory cytokines (477). It has been suggested that microcracks or neovascularisation of CC in diseased joints may facilitate transfer of cytokines between the HC and SCB (478) however CC microcracks were observed only in one horse and blood vessels were never seen to completely penetrate the CC so these are unlikely to be significant pathways in this study.

It might be expected that any biochemical changes in synovial fluid would have a similar effect on the cartilage both opposing and adjacent to the lesion rather than the focally different responses observed in this study. In addition, significant levels of inflammatory mediators within the synovial fluid might be expected to be associated with synovitis, however there was no difference in synovial inflammation between the treated and control joints of the trial animals (394, 415). These observations suggest that the differences in bone remodelling activity and cartilage morphology of C3 between the

two limbs are unlikely to be a result of inflammatory mediators released at the site of the Cr defect. It is possible that concentrations of cytokines and growth factors were highest in the synovial fluid in the joint space immediately opposing the defect resulting in local hyaline cartilage changes in this region, without affecting adjacent cartilage or synovium. However, this would seem unlikely and I am not aware that this possibility has been investigated in studies of osteochondral defects.

7.3 Limitations

There are several limitations associated with this study. The low number of animals impacted the ability to show significant differences in some instances. It also meant that results were influenced by the variation between individual horses in the degree and timing of the SCB response. The total number of six animals, chosen based on power calculations after a pilot study with three horses, was kept as low as possible for ethical and financial reasons.

Secondly, the sham-operated contralateral limbs may not be true controls due to overloading as a result of lameness on the treated limb. In addition, persistent mild lameness in the control limb of horse 3, which may have been related to unidentified carpal joint pathology, and spontaneous lesions arising in the control limbs of horses 2 and 6 may have influenced any observed differences between the control and treated limbs of these individuals. There was, however, no obvious evidence of this in the data aside from high osteoclast numbers in the region opposing the lesion in C3 of the control limb of Horse 2 and in the weight bearing region of control C3 of Horse 6. Lameness in

all cases was only subtle to mild so its effect is likely to be minimal. Inclusion of the untrained control group was an attempt to assess the impact of increased loading or pathology in the control limbs of the trial animals.

Although an attempt was made to create all lesions of similar depth there was some variation in lesion depth between animals and within individual lesions. This may have impacted the response to these lesions, especially in those sections taken from the periphery of the lesion where there was the greatest variation in depth. Use of a guide on the burr or some other mechanism to improve consistency of lesion depth may be beneficial if this model is to be used in the future.

Another limitation of the study is the lack of information about the training history of the animals prior to inclusion in the trial. The initial degree of adaption to loading may have affected how the SCB of individual horses responded to the induced lesion and the training regimen. A prolonged period of rest for all animals with or without a short training period prior to surgery may enable the SCB of all individuals to be in a similar state at the beginning of the trial and therefore give more consistent results between horses. However, this would increase both the cost and time commitment of the study. Interpretation of the results from the untrained control group is also limited by a lack training history as it may be that they were recently trained at the time of euthanasia.

Lack of evidence for how the creation of the defect in the Cr articular surface changed the loading patterns within Cr and across the C3 articular surface also limits the interpretations drawn from this study. While assumptions of reduced loading below the defect in Cr and in the region opposing the defect on C3 and increased loading in the

adjacent regions are reasonable based on previous work, there is currently no specific data on the changes in loading experienced by the cartilage and SCB in this model. It is likely that the changes in both magnitude and direction of the loading are complex.

The position of each series of ROIs was defined so that they were entirely below the lesion in Cr, opposing the lesion in C3 or entirely within the adjacent weight bearing region in both bones. The two series within each bone were kept as far apart as possible in an attempt to avoid the region at the edge or opposing the edge of the defect. However the Cr defects were as close as 3-4mm from the dorsal articular margin in some animals meaning that the weight bearing ROIs were inevitably close to both the defect and the dorsal edge of the bone. As there is some translational movement between the two surfaces of the mid-carpal joint it is possible that the edge of the defect was sometimes opposing the C3 weight bearing ROIs (479). The 20x magnification DIC images of the weight bearing region in Horse 4 in particular were taken from very close to the boundary between the weight bearing and the unloaded region so care was required in interpreting the measurements from this region in this animal.

Positioning of the specimens for microCT images and the angle at which sections were cut for histological analyses and BSEM imaging could also have affected the relative positions of the ROIs. Reasonable attempts were made to ensure that all specimens were level for microCT and that all sections were cut perpendicular to the dorsal surface of the bone in the sagittal plane however it was not possible to make them perfectly so. As a consequence, tilting of the sample could have potentially meant that the ROIs were in slightly different anatomical positions in treated and control limbs and that the C3 ROIs may not have been immediately opposite those in Cr. In addition, there were differences

in the shape of the dorsal edge of C3 between treated and control specimens in some horses (especially horse 1 and 5) which may have arisen due to true anatomical differences between limbs or the angle at which the sections were cut from the bone. These differences in shape meant that some of the difference in the cartilage and SCB between the treated and control limbs may have been related to the difference in position rather than the presence of the defect.

The Cr specimens from which cryosections were cut and stained for TRAP were taken from the medial edge of the surgical defect where it was narrower and shallower than at the centre. The ROIs below the defect may therefore not have been entirely below the defect for this analysis. In the treated limb of Horse 1 the Cr section stained for TRAP was collected from just adjacent to the defect so the defect ROIs in this bone were not truly below the defect. This may account for the fact that the increase in numbers of osteoclasts in the treated limb was not as great in this animal as in the others. In addition, the Cr section stained for TRAP from the treated limb of Horse 3 was not completely decalcified prior to sectioning so osteoclasts in the region 3.3-6.6mm deep to the cartilage could not be counted in this specimen.

Interpretation of the oxytetracycline labels was limited by the inability to differentiate between the labels. Had all four labels been consistently visible the time points that they each represented would have been obvious however this was never the case. Oxytetracycline was chosen for all four labels rather than different fluorescent markers due to the high cost of other labels when dosing large animals.

Finally, all histological assessments would have ideally been performed by multiple, experienced, independent histologists, however resources were not available to enable this.

7.4 Further study

Having observed the structural and histological changes caused by loss of joint surface congruity in this trial, it would now be interesting to investigate the biochemical pathways through which they were mediated and how they affect the biomechanical properties and function of the joint surface.

The HC and SCB responses in this trial are likely to have been effected through alterations in several biochemical pathways (35, 121, 184-186, 188, 189, 191, 396, 480). Investigation of these molecular changes would improve understanding of the roles they play in joint homeostasis and possibly identify potential targets for pharmacological intervention to prevent or slow the progression of disease in incongruous joints.

There are many molecular candidates for investigation in the SCB but two of the most relevant would be sclerostin, the expression of which by osteocytes has been shown to reduce bone formation by osteoblasts and to be increased in both unloaded bone and at sites of fracture in horses (186, 188, 230); and RANKL which is required for osteoclast differentiation and development, and has been shown to be elevated in conditions of unloading and osteoarthritis (191) (144).

RANKL expression by chondrocytes has been associated with SCB osteoclast numbers and it would be of interest to investigate whether its expression is increased in chondrocytes of CC in the unloaded region of C3 (121, 144). Other candidates for gene expression or protein synthesis studies of cartilage surrounding and opposing osteochondral defects include collagen II, collagen X, aggrecan, VEGF, MMP13, Runx2, Sox 9 all of which are involved in either normal cartilage growth, homeostasis or pathology and may play important roles in cartilage response to incongruity (35, 121, 142, 220, 481, 482).

To aid in interpretation of the observed increase in chondrocyte size in the unloaded region of C3, it would be valuable to measure chondrocyte size in the different layers of HC to determine whether the increase is occurring at the superficial layer and therefore more likely to be a result of reduced hydrostatic pressure and loss of constraint of the cells (459) or in the deeper layer which may be a function of hypertrophic differentiation prior to calcification of the cartilage (142, 482). Looking for molecular markers of hypertrophy, such as collagen type X would also be of interest (482). Another method to examine the cartilage in greater detail is transmission electron microscopy (TEM) which facilitates observation of ultrastructural changes in chondrocytes and may provide more information about whether cells in the unloaded region of C3 appear like hypertrophic chondrocytes in growth cartilage or are undergoing some other phenotypic change (356, 483-485).

BV/TV, BMD and TMD have been found to be determinants of mechanical properties of equine SCB and the proteoglycan and collagen content of HC, amongst other things, have been linked to its biomechanical properties and susceptibility to damage (53, 97, 458, 467, 470, 486, 487). It would be beneficial to investigate whether the changes in cartilage

and bone structure as a result of the defect in this study were associated with changes in mechanical properties of these tissues, whether this has any impact on the function of the joint and how it might relate to progression of degenerative disease.

Investigation of concentrations of inflammatory cytokines such as IL-1, IL-6 and TNF-α, and growth factors such as TGF-β and IGF-1, VEGF as well as bone regulatory proteins such as OC and BMP-2 in the synovial fluid of joints with focal osteochondral defects would help to determine what role they might play in the cartilage and SCB changes observed, particularly in relation to development of peri-articular modelling and cartilage degeneration (35, 385, 386, 406, 418). There are also suggestions that some of these have potential for use as markers of joint disease in a clinical setting (326, 327, 488).

The osteocyte lacunar-canalicular network is increasingly recognised to be involved in bone homeostasis and mechanosensation (489, 490). Additionally, perilacunar remodelling by osteocytes has been shown to be regulated by sclerostin and hence possibly by changes in loading (491). Further investigation of this lacunar-canalicular network in models of joint incongruity via measurement of osteocyte lacunae size, SEM imaging of acid-etched bone (492) or silver nitrate staining (493) may enhance understanding of subchondral bone homeostasis and its response to changes in loading.

Development of a finite element model of the joint surfaces in this study, in order to better understand how the presence of the Cr defect affected the strains within the surrounding and opposing cartilage and bone, would allow more specific conclusions to be drawn about how joint surfaces respond to altered loading conditions.

Finally, this study made observations at a single point in a process that is likely to have been changing over time (150-152, 168, 365, 366, 494). Observation of changes in the SCB surrounding the defect both earlier and later after creation of the defect would provide more information on the progression of the cartilage and SCB changes. This knowledge may improve understanding of the development of degeneration within incongruous joints and aid decision making when managing joint conditions in which focal defects are a feature.

7.5 Conclusion

This investigation demonstrated that focal changes in joint surface loading have local effects on cartilage morphology and bone remodelling activity.

In response to a loss of congruity due to an osteochondral defect, adult equine articular cartilage and SCB change in ways that would tend towards restoration of congruity, with the rate of advancement of the articular surface and osteochondral junction towards the opposing joint surface increased in regions where surface contact is lost and reduced in regions of increased loading.

These findings have added to what is known regarding the behaviour of cartilage and SCB. This will improve understanding of the pathophysiology of synovial joint injuries and diseases which may ultimately improve management of these conditions.

REFERENCES

1. Duda GN, Maldonado ZM, Klein P, Heller MO, Burns J, Bail H. On the influence of mechanical conditions in osteochondral defect healing. Journal of biomechanics. 2005;38(4):843-51.

2. Braman JP, Bruckner JD, Clark JM, Norman AG, Chansky HA. Articular cartilage adjacent to experimental defects is subject to atypical strains. Clinical orthopaedics and related research. 2005(430):202-7.

3. Kock NB, Smolders JM, van Susante JL, Buma P, van Kampen A, Verdonschot N. A cadaveric analysis of contact stress restoration after osteochondral transplantation of a cylindrical cartilage defect. Knee surgery, sports traumatology, arthroscopy : official journal of the ESSKA. 2008;16(5):461-8.

4. Gratz K, Wong B, Bae W, Sah R. The effects of focal articular defects on intra-tissue strains in the surrounding and opposing cartilage. Biorheology. 2008;45(3-4):193-207.

5. Harrison C, Britt H, Miller G, Henderson J. Prevalence of Chronic Conditions in Australia. Plos One. 2013;8(7).

6. Knox SA, Harrison CM, Britt HC, Henderson JV. Estimating prevalence of common chronic morbidities in Australia. Medical Journal of Australia. 2008;189(2):66-70.

7. Pool RR. Pathologic Manifestations of Joint Disease in the Athletic Horse. In: McIlwraith CW, Trotter GW, editors. Joint Disease in the Horse. Philadelphia: W.B. Saunders; 1996.

8. Kawcak CE, McIlwraith CW, Norrdin RW, Park RD, James SP. The role of subchondral bone in joint disease: a review. Equine veterinary journal. 2001;33(2):120-6.

9. Frisbie DD. Chapter 78 - Synovial Joint Biology and Pathobiology. In: Auer JA, Stick JA, editors. Equine Surgery (Fourth Edition). Saint Louis: W.B. Saunders; 2012. p. 1096-114.

10. Ness MG, Abercromby RH, May C, Turner BM, Carmichael S. A survey of orthopaedic conditions in small animal veterinary practice in Britain. Veterinary and Comparative Orthopaedics and Traumatology. 1996;9(2):43-52.

11. Benito J, Gruen ME, Thomson A, Simpson W, Lascelles BDX. Owner-assessed indices of quality of life in cats and the relationship to the presence of degenerative joint disease. Journal of Feline Medicine and Surgery. 2012;14(12):863-70.

12. Lascelles BDX, Henry JB, Brown J, Robertson I, Sumrell AT, Simpson W, et al. Cross-Sectional Study of the Prevalence of Radiographic Degenerative Joint Disease in Domesticated Cats. Veterinary Surgery. 2010;39(5):535-44.

13. Bani Hassan E, Mirams M, Mackie EJ, Whitton RC. Prevalence of subchondral bone pathological changes in the distal metacarpi/metatarsi of racing Thoroughbred horses. Aust Vet J. 2017;95(10):362-9.

14. McCoy AM, Toth F, Dolvik NI, Ekman S, Ellermann J, Olstad K, et al. Articular osteochondrosis: a comparison of naturally-occurring human and animal disease. Osteoarthritis and cartilage / OARS, Osteoarthritis Research Society. 2013;21(11):1638-47.

15. Moreira CA, Bilezikian JP. Stress Fractures: Concepts and Therapeutics. The Journal of clinical endocrinology and metabolism. 2017;102(2):525-34.

16. Buckwalter JA. Articular cartilage injuries. Clinical Orthopaedics and Related Research®. 2002(402):21-37.

17. Schinhan M, Gruber M, Vavken P, Dorotka R, Samouh L, Chiari C, et al. Critical-size defect induces unicompartmental osteoarthritis in a stable ovine knee. Journal of Orthopaedic Research. 2012;30(2):214-20.

18. Vaseenon T, Tochigi Y, Heiner AD, Goetz JE, Baer TE, Fredericks DC, et al. Organ-Level Histological and Biomechanical Responses from Localized Osteoarticular Injury in the Rabbit Knee. Journal of Orthopaedic Research. 2011;29(3):340-6.

19. McIlwraith CW. General Pathobiology of the Joint and Response to Injury. In: McIlwraith CW, Trotter GW, editors. Joint Disease in the Horse. Philadelphia: W.B. Saunders; 1996.

20. Strauss EJ, Goodrich LR, Chen CT, Hidaka C, Nixon AJ. Biochemical and biomechanical properties of lesion and adjacent articular cartilage after chondral defect repair in an equine model. American Journal of Sports Medicine. 2005;33(11):1647-53.

21. Edge A, Porter K. Osteochondritis dissecans: A review. Trauma. 2011;13(1):23-33.

22. Messner K, Maletius W. The long-term prognosis for severe damage to weight-bearing cartilage in the knee: A 14-year clinical and radiographic follow-up in 28 young athletes. Acta Orthopaedica Scandinavica. 1996;67(2):165-8.

23. Brandt KD, Dieppe P, Radin E. Etiopathogenesis of Osteoarthritis. Medical Clinics of North America. 2009;93(1):1-24.

24. Pool RR, Meagher DM. Pathological findings and pathogenesis of racetrack injuries. Veterinary Clinics of North America-Equine Practice. 1990;6(1):1-30.

25. Neundorf RH, Lowerison MB, Cruz AM, Thomason JJ, McEwen BJ, Hurtig MB. Determination of the prevalence and severity of metacarpophalangeal joint osteoarthritis in Thoroughbred racehorses via quantitative macroscopic evaluation. American journal of veterinary research. 2010;71(11):1284-93.

26. Little CB, Hunter DJ. Post-traumatic osteoarthritis: from mouse models to clinical trials. Nature reviews Rheumatology. 2013;9(8):485-97.

27. DeFrate LE, Kim-Wang SY, Englander ZA, McNulty AL. Osteoarthritis year in review 2018: mechanics. Osteoarthritis and cartilage / OARS, Osteoarthritis Research Society. 2018.

28. Mandl LA. Osteoarthritis year in review 2018: clinical. Osteoarthritis and Cartilage. 2018.

29. Dyce KM, Wensing CJG. Chapter 2 The Locomotor Apparatus. Textbook of veterinary anatomy. 4th ed. St. Louis, Mo.: Saunders/Elsevier; 2010. p. xii, 834 p.

30. Todhunter RJ. Anatomy and Physiology of Synovial Joints. In: McIlwraith CW, Trotter GW, editors. Joint Disease in the Horse. Philadelphia: W.B. Saunders 1996.

31. Burr DB. Anatomy and physiology of the mineralized tissues: role in the pathogenesis of osteoarthrosis. Osteoarthritis and cartilage / OARS, Osteoarthritis Research Society. 2004;12 Suppl A:S20-30.

32. Akers RM, Denbow DM. Chapter 6: Bones and Skeletal System. 2013. In: Anatomy and Physiology of Domestic Animals [Internet]. Hoboken: Wiley,; [133-68]. Available from: Connect to ebook (University of Melbourne only) http://UNIMELB.eblib.com.au.ezp.lib.unimelb.edu.au/patron/FullRecord.aspx?p=1160885.

33. Johnston SA. Osteoarthritis. Joint anatomy, physiology, and pathobiology. The Veterinary clinics of North America Small animal practice. 1997;27(4):699-723.

34. van Dijk CN, Reilingh ML, Zengerink M, van Bergen CJ. Osteochondral defects in the ankle: why painful? Knee surgery, sports traumatology, arthroscopy : official journal of the ESSKA. 2010;18(5):570-80.

35. Martel-Pelletier J, Boileau C, Pelletier JP, Roughley PJ. Cartilage in normal and osteoarthritis conditions. Best practice & research Clinical rheumatology. 2008;22(2):351-84.

36. Poole AR, Kojima T, Yasuda T, Mwale F, Kobayashi M, Laverty S. Composition and structure of articular cartilage: a template for tissue repair. Clinical Orthopaedics and Related Research®. 2001(391 Suppl):S26-S33.

37. Chen S, Fu P, Wu H, Pei M. Meniscus, articular cartilage and nucleus pulposus: a comparative review of cartilage-like tissues in anatomy, development and function. Cell and tissue research. 2017;370(1):53-70.

38. Poole AR. Cartilage in Health and Disease. In: McIlwraith CW, Trotter GW, editors. Joint Disease in the Horse. Philadelphia: W.B. Saunders; 1996.

39. Lyons TJ, Stoddart RW, McClure SF, McClure J. The tidemark of the chondro-osseous junction of the normal human knee joint. Journal of Molecular Histology. 2005;36(3):207-15.

40. Currey JD. Bones : structure and mechanics. 2nd ed. Princeton, N.J. ; Woodstock: Princeton University Press; 2006. xii, 436 p. p.

41. Currey JD. The structure of bone tissue. Bones. Structure and Mechanics: Princeton University Press; 2002. p. 3-26.

42. Tsourdi E, Jahn K, Rauner M, Busse B, Bonewald LF. Physiological and pathological osteocytic osteolysis. Journal of Musculoskeletal & Neuronal Interactions. 2018;18(3):292-303.

43. Miller SC, Jee WS. The bone lining cell: a distinct phenotype? Calcified Tissue International. 1987;41(1):1-5.

44. Bertone AL. Chapter 2.4 - Joint physiology: responses to exercise and training. In: Hinchcliff KW, Geor RJ, Kaneps AJ, editors. Equine Exercise Physiology. Edinburgh: W.B. Saunders; 2008. p. 132-42.

45. Todhunter PG, Kincaid SA, Todhunter RJ, Kammermann JR, Johnstone B, Baird AN, et al. Immunohistochemical analysis of an equine model of synovitis-induced arthritis. American journal of veterinary research. 1996;57(7):1080-93.

46. McIlwraith CW, Frisbie DD, Kawcak CE. The horse as a model of naturally occurring osteoarthritis. Bone & joint research. 2012;1(11):297-309.

47. Budras KD, Sack WO, Rock S, Horowitz A, Berg R. Chapter 2: The Thoracic Limb. Anatomy of the Horse. Hannover, GERMANY: Schluetersche, Germany; 2012. p. 4-15.

48. March LM, Bagga H. Epidemiology of osteoarthritis in Australia. Medical Journal of Australia. 2004;180(5):S6-S10.

49. Webster J. Animal Welfare: Freedoms, Dominions and "A Life Worth Living". Animals : an open access journal from MDPI. 2016;6(6).

50. Suri S, Walsh DA. Osteochondral alterations in osteoarthritis. Bone. 2012;51(2):204-11.

51. van Weeren PR. 1 - General Anatomy and Physiology of Joints. In: McIlwraith CW, Frisbie DD, Kawcak CE, van Weeren PR, editors. Joint Disease in the Horse (Second Edition). Edinburgh: W.B. Saunders; 2016. p. 1-24.

52. Kawcak CE. 2 - Biomechanics in Joints. In: McIlwraith CW, Frisbie DD, Kawcak CE, van Weeren PR, editors. Joint Disease in the Horse (Second Edition). Edinburgh: W.B. Saunders; 2016. p. 25-32.

53. Maroudas AI. Balance between swelling pressure and collagen tension in normal and degenerate cartilage. Nature. 1976;260(5554):808-9.

54. Helminen HJ, Kiviranta I, Saamanen AM, Jurvelin JS, Arokoski J, Oettmeier R, et al. Effect of motion and load on articular-cartilage in animal-models. Kuettner KE, Schleyerbach R, Peyron JG, Hascall VC, editors. New York: Raven Press; 1992. 501-10 p.

55. Wong M, Carter DR. Articular cartilage functional histomorphology and mechanobiology: a research perspective. Bone. 2003;33(1):1-13.

56. Radin EL, Paul IL. Does cartilage compliance reduce skeletal impact loads? The relative force-attenuating properties of articular cartilage, synovial fluid, periarticular soft tissues and bone. Arthritis and rheumatism. 1970;13(2):139-44.

57. Brandt KD, Dieppe P, Radin EL. Etiopathogenesis of Osteoarthritis. Rheumatic Disease Clinics of North America. 2008;34(3):531-59.

58. Malekipour F, Whitton C, Oetomo D, Lee PVS. Shock absorbing ability of articular cartilage and subchondral bone under impact compression. Journal of the Mechanical Behavior of Biomedical Materials. 2013;26:127-35.

59. Murray RC, Whitton RC, Vedi S, Goodship AE, Lekeux P. The effect of training on the calcified zone of equine middle carpal articular cartilage / Equine Veterinary Journal. Supplement. 1999.

60. Burr DB, Schaffler MB. The involvement of subchondral mineralized tissues in osteoarthrosis: quantitative microscopic evidence. Microscopy research and technique. 1997;37(4):343-57.

61. Mente PL, Lewis JL. Elastic-modulus of calcified cartilage is an order of magnitude less-than that of subchondral bone. Journal of Orthopaedic Research. 1994;12(5):637-47.

62. Hargrave-Thomas E, van Sloun F, Dickinson M, Broom N, Thambyah A. Multi-scalar mechanical testing of the calcified cartilage and subchondral bone comparing healthy vs early degenerative states. Osteoarthritis and cartilage / OARS, Osteoarthritis Research Society. 2015;23(10):1755-62.

63. Gupta HS, Schratter S, Tesch W, Roschger P, Berzlanovich A, Schoeberl T, et al. Two different correlations between nanoindentation modulus and mineral content in the bone-cartilage interface. Journal of structural biology. 2005;149(2):138-48.

64. Doube M, Firth EC, Boyde A, Bushby AJ. Combined nanoindentation testing and scanning electron microscopy of bone and articular calcified cartilage in an equine fracture predilection site. European cells & materials. 2010;19:242-51.

65. Granke M, Does MD, Nyman JS. The Role of Water Compartments in the Material Properties of Cortical Bone. Calcif Tissue Int. 2015;97(3):292-307.

66. Imhof H, Breitenseher M, Kainberger F, Rand T, Trattnig S. Importance of subchondral bone to articular cartilage in health and disease. Topics in magnetic resonance imaging. 1999;10(3):180-92.

67. Beaupre GS, Carter D, Wong M, Smith RL, Andriacchi T, Schurman D. The Mechanobiology of Articular Cartilage Development and Degeneration. Clinical orthopaedics and related research. 2004;427(427 Suppl):S69-S77.

68. Doube M, Firth EC, Boyde A. Variations in articular calcified cartilage by site and exercise in the 18-month-old equine distal metacarpal condyle. Osteoarthritis and cartilage / OARS, Osteoarthritis Research Society. 2007;15(11):1283-92.

69. Firth EC, Rogers CW. Musculoskeletal responses of 2-year-old Thoroughbred horses to early training. 7. Bone and articular cartilage response in the carpus. New Zealand veterinary journal. 2005;53(2):113-22.

70. Firth EC, Rogers CW, Doube M, Jopson NB. Musculoskeletal responses of 2-year-old Thoroughbred horses to early training. 6. Bone parameters in the third metacarpal and third metatarsal bones. New Zealand Veterinary Journal. 2005;53(2):101-12.

71. Murray RC, Birch HL, Lakhani K, Goodship AE. Biochemical composition of equine carpal articular cartilage is influenced by short-term exercise in a site-specific manner. Osteoarthritis and Cartilage. 2001;9(7):625-32.

72. Tranquille CA, Blunden AS, Dyson SJ, Parkin TD, Goodship AE, Murray RC. Effect of exercise on thicknesses of mature hyaline cartilage, calcified cartilage, and subchondral bone of equine tarsi. American journal of veterinary research. 2009;70(12):1477-83.

73. Oettmeier R, Arokoski J, Roth AJ, Helminen HJ, Tammi M, Abendroth K. Quantitative study of articular-cartilage and subchondral bone remodeling in the knee-joint of dogs after strenuous running training. Journal of Bone and Mineral Research. 1992;7:S419-S24.

74. Murray RC, Vedi S, Birch HL, Lakhani KH, Goodship AE. Subchondral bone thickness, hardness and remodelling are influenced by short-term exercise in a site-specific manner. Journal of orthopaedic research : official publication of the Orthopaedic Research Society. 2001;19(6):1035-42.

75. Wolff J. Das Gesetz der Transformation der Knocken. A Hirschwald. 1892.

76. Buckwalter JA, Mankin HJ. Articular cartilage. Part I: Tissue design and chondrocyte-matrix interactions. Journal of Bone and Joint Surgery - Series A. 1997;79(4):600-11.

77. Eckstein F, Lohe F, Schulte E, Muller-Gerbl M, Milz S, Putz R. Physiological incongruity of the humero-ulnar joint: a functional principle of optimized stress distribution acting upon articulating surfaces? Anatomy and embryology. 1993;188(5):449-55.

78. Goodfellow J, Mitsou A. Joint surface incongruity and its maintenance: an experimental study. J Bone Joint Surg Br. 1977;59-b(4):446-51.

79. Kiviranta I, Jurvelin J, Tammi M, Saamanen AM, Helminen HJ. Weight bearing controls glycosaminoglycan concentration and articular-cartilage thickness in the knee joints of young beagle dogs. Arthritis and rheumatism. 1987;30(7):801-9.

80. Little B, Ghosh P, Rose R. The effect of strenuous versus moderate exercise on the metabolism of proteoglycans in articular cartilage from different weight-bearing regions of the equine third carpal bone. Osteoarthritis and Cartilage. 1997;5(3):161-72.

81. Kim YJ, Sah RL, Grodzinsky AJ, Plaas AH, Sandy JD. Mechanical regulation of cartilage biosynthetic behavior: physical stimuli. Archives of biochemistry and biophysics. 1994;311(1):1-12.

82. Buschmann MD, Gluzband YA, Grodzinsky AJ, Hunziker EB. Mechanical compression modulates matrix biosynthesis in chondrocyte/agarose culture. Journal of cell science. 1995;108 (Pt 4):1497-508.

83. Gray ML, Pizzanelli AM, Grodzinsky AJ, Lee RC. Mechanical and physiochemical determinants of the chondrocyte biosynthetic response. Journal of orthopaedic research : official publication of the Orthopaedic Research Society. 1988;6(6):777-92.

84. Sharma G, Saxena RK, Mishra P. Differential effects of cyclic and static pressure on biochemical and morphological properties of chondrocytes from articular cartilage. Clinical biomechanics. 2007;22(2):248-55.

85. Mizuno S, Tateishi T, Ushida T, Glowacki J. Hydrostatic fluid pressure enhances matrix synthesis and accumulation by bovine chondrocytes in three-dimensional culture. Journal of Cellular Physiology. 2002;193(3):319-27.

86. Mellor LF, Steward AJ, Nordberg RC, Taylor MA, Loboa EG. Comparison of Simulated Microgravity and Hydrostatic Pressure for Chondrogenesis of hASC. Aerospace medicine and human performance. 2017;88(4):377-84.

87. Burton-Wurster N, Vernier-Singer M, Farquhar T, Lust G. Effect of compressive loading and unloading on the synthesis of total protein, proteoglycan, and fibronectin by canine cartilage explants. Journal of orthopaedic research : official publication of the Orthopaedic Research Society. 1993;11(5):717-29.

88. Wu QQ. Mechanoregulation of Chondrocyte Proliferation, Maturation, and Hypertrophy: Ion-Channel Dependent Transduction of Matrix Deformation Signals. Experimental cell research. 2000;256(2):383-91.

89. Jin M, Frank EH, Quinn TM, Hunziker EB, Grodzinsky AJ. Tissue shear deformation stimulates proteoglycan and protein biosynthesis in bovine cartilage explants. Archives of biochemistry and biophysics. 2001;395(1):41-8.

90. Lane Smith R, Trindade MCD, Ikenoue T, Mohtai M, Das P, Carter DR, et al. Effects of shear stress on articular chondrocyte metabolism. Biorheology. 2000;37(1-2):95-107.

91. Madej W, van Caam A, Davidson EB, Buma P, van der Kraan PM. Unloading results in rapid loss of TGF beta signaling in articular cartilage: role of loading-induced TGF beta signaling in maintenance of articular chondrocyte phenotype? Osteoarthritis and Cartilage. 2016;24(10):1807-15.

92. Kiviranta I, Tammi M, Jurvelin J, Saamanen AM, Helminen HJ. Moderate running exercise augments glycosaminoglycans and thickness of articular-cartilage in the knee-joint of young beagle dogs. Journal of Orthopaedic Research. 1988;6(2):188-95.

93. Kiviranta I, Jurvelin J, Saamanen AM, Arokoski J, Tammi M, Helminen HJ. Strenuous running exercise attenuates the increase of articular-cartilage proteoglycans observed after moderate running program of young beagle dogs. Scandinavian Journal of Rheumatology. 1986:43-.

94. Arokoski J, Jurvelin J, Kiviranta I, Tammi M, Helminen HJ. Softening of the lateral condyle articular-cartilage in the canine knee-joint after long-distance (up to

40km/day) running training lasting one-year. International Journal of Sports Medicine. 1994;15(5):254-60.

95. Arokoski J, Kiviranta I, Jurvelin J, Tammi M, Helminen HJ. Long-distance running causes site-dependent decrease of cartilage glycosaminoglycan content in the knee joints of beagle dogs. Arthritis and rheumatism. 1993;36(10):1451-9.

96. King KB, Opel CF, Rempel DM. Cyclical articular joint loading leads to cartilage thinning and osteopontin production in a novel in vivo rabbit model of repetitive finger flexion. Osteoarthritis and Cartilage. 2005;13(11):971-8.

97. Murray RC, Zhu CF, Goodship AE, Lakhani KH, Agrawal CM, Athanasiou KA. Exercise affects the mechanical properties and histological appearance of equine articular cartilage. Journal of Orthopaedic Research. 1999;17(5):725-31.

98. Palmer JL, Bertone AL, Malemud CJ, Carter BG, Papay RS, Mansour J. Site-specific proteoglycan characteristics of 3rd carpal articular-cartilage in exercised and nonexercised horses. American journal of veterinary research. 1995;56(12):1570-6.

99. Koo S, Andriacchi T. A comparison of the influence of global functional loads vs. local contact anatomy on articular cartilage thickness at the knee. Journal of biomechanics. 2007;40(13):2961-6.

100. Koo S, Rylander JH, Andriacchi TP. Knee joint kinematics during walking influences the spatial cartilage thickness distribution in the knee. Journal of biomechanics. 2011;44(7):1405-9.

101. Roberts BC, Solomon LB, Mercer G, Reynolds KJ, Thewlis D, Perilli E. Relationships between in vivo dynamic knee joint loading, static alignment and tibial subchondral bone microarchitecture in end-stage knee osteoarthritis. Osteoarthritis and cartilage / OARS, Osteoarthritis Research Society. 2018;26(4):547-56.

102. Sánchez Egea A, Valera M, Parraga Quiroga J, Proubasta I, Noailly J, Lacroix D. Impact of hip anatomical variations on the cartilage stress: A finite element analysis towards the biomechanical exploration of the factors that may explain primary hip arthritis in morphologically normal subjects. Clinical biomechanics. 2014;29(4):444-50.

103. Chen GX, Yang L, Li K, He R, Yang B, Zhan Y, et al. A Three-Dimensional Finite Element Model for Biomechanical Analysis of the Hip. Cell Biochemistry and Biophysics. 2013;67(2):803-8.

104. Harris MD, Anderson AE, Henak CR, Ellis BJ, Peters CL, Weiss JA. Finite element prediction of cartilage contact stresses in normal human hips. Journal of Orthopaedic Research. 2012;30(7):1133-9.

105. Anderson AE, Ellis BJ, Maas SA, Peters CL, Weiss JA. Validation of finite element predictions of cartilage contact pressure in the human hip joint. Journal of Biomechanical Engineering-Transactions of the Asme. 2008;130(5).

106. Palmer JL, Bertone AL, Litsky AS. Contact area and pressure distribution changes of the equine 3rd carpal bone during loading. Equine veterinary journal. 1994;26(3):197-202.

107. Brama PAJ, Karssenberg D, Barneveld A, van Weeren PR. Contact areas and pressure distribution on the proximal articular surface of the proximal phalanx under sagittal plane loading. Equine veterinary journal. 2001;33(1):26-32.

108. Harrison SM, Whitton RC, Kawcak CE, Stover SM, Pandy MG. Relationship between muscle forces, joint loading and utilization of elastic strain energy in equine locomotion. Journal of experimental biology. 2010;213(23):3998-4009.

109. von Eisenhart R, Adam C, Steinlechner M, Müller Gerbl M, Eckstein F, Muller Gerbl M. Quantitative determination of joint incongruity and pressure distribution during simulated gait and cartilage thickness in the human hip joint. Journal of orthopaedic research. 1999;17(4):532-9.

110. Mullergerbl M, Schulte E, Putz R. The thickness of the calcified layer of articular-cartilage - a function of the load supported. Journal of Anatomy. 1987;154:103-11.

111. Li G, Park SE, DeFrate LE, Schutzer ME, Ji L, Gill TJ, et al. The cartilage thickness distribution in the tibiofemoral joint and its correlation with cartilage-to-cartilage contact. Clinical biomechanics. 2005;20(7):736-44.

112. Murray RC, Debowes RM, Gaughan EM, Mosier DE, Athanasiou KA. Variations in the biomechanical properties of articular-cartilage of the midcarpal joint of normal horses. Veterinary and Comparative Orthopaedics and Traumatology. 1995;8(3):133-40.

113. Palmer JL, Bertone AL, Mansour J, Carter BG, Malemud TJ. Biomechanical properties of third carpal articular Cartilage in exercised and nonexercised horses. Journal of Orthopaedic Research. 1995;13(6):854-60.

114. Brama PAJ, TeKoppele JM, Bank RA, van Weeren PR, Barneveld A. Influence of site and age on biochemical characteristics of the collagen network of equine articular cartilage. American journal of veterinary research. 1999;60(3):341-5.

115. Brama PA, Tekoppele JM, Bank RA, Karssenberg D, Barneveld A, van Weeren PR. Topographical mapping of biochemical properties of articular cartilage in the equine fetlock joint. Equine veterinary journal. 2000;32(1):19-26.

116. van Weeren PR, Firth EC, Brommer H, Hyttinen MM, Helminen AE, Rogers CW, et al. Early exercise advances the maturation of glycosaminoglycans and collagen in the extracellular matrix of articular cartilage in the horse. Equine veterinary journal. 2008;40(2):128-35.

117. Kawcak CE, McIlwraith CW, Firth EC. Effects of early exercise on metacarpophalangeal joints in horses. American journal of veterinary research. 2010;71(4):405-11.

118. Kiviranta I, Tammi M, Jurvelin J, Arokoski J, Saamanen AM, Helminen HJ. Articular-cartilage thickness and glycosaminoglycan distribution in the canine knee-joint after strenuous running exercise. Clinical orthopaedics and related research. 1992(283):302-8.

119. Palmoski MJ, Colyer RA, Brandt KD. Joint motion in the absence of normal loading does not maintain normal articular-cartilage. Arthritis and rheumatism. 1980;23(3):325-34.

120. Basso N, Heersche JN. Effects of hind limb unloading and reloading on nitric oxide synthase expression and apoptosis of osteocytes and chondrocytes. Bone. 2006;39(4):807-14.

121. Nomura M, Sakitani N, Iwasawa H, Kohara Y, Takano S, Wakimoto Y, et al. Thinning of articular cartilage after joint unloading or immobilization. An experimental investigation of the pathogenesis in mice. Osteoarthritis and Cartilage. 2017;25(5):727-36.

122. Palmoski M, Perricone E, Brandt KD. Development and reversal of a proteoglycan aggregation defect in normal canine knee cartilage after immobilization. Arthritis and rheumatism. 1979;22(5):508-17.

123. Richardson DW. Biochemical-changes in articular-cartilage opposing full-thickness and partial-thickness cartilage lesions in horses. American journal of veterinary research. 1990;51(1):118-22.

124. Little CB, Ghosh P. Variation in proteoglycan metabolism by articular chondrocytes in different joint regions is determined by post-natal mechanical loading. Osteoarthritis and Cartilage. 1997;5(1):49-62.

125. Smith RL, Thomas KD, Schurman DJ, Carter DR, Wong M, Vandermeulen MC. Rabbit knee immobilization - bone remodeling precedes cartilage degradation. Journal of Orthopaedic Research. 1992;10(1):88-95.

126. Muir P, Peterson AL, Sample SJ, Scollay MC, Markel MD, Kalscheur VL. Exercise-induced metacarpophalangeal joint adaptation in the Thoroughbred racehorse. Journal of Anatomy. 2008;213(6):706-17.

127. Blazek K, Favre J, Asay J, Erhart-Hledik J, Andriacchi T. Age and obesity alter the relationship between femoral articular cartilage thickness and ambulatory loads in individuals without osteoarthritis. Journal of Orthopaedic Research. 2014;32(3):394-402.

128. Carter DR, Wong M. Modelling cartilage mechanobiology. Philosophical Transactions of the Royal Society of London Series B-Biological Sciences. 2003;358(1437):1461-71.

129. Maldonado DC, da Silva MCP, Neto SER, de Souza MR, de Souza RR. The effects of joint immobilization on articular cartilage of the knee in previously exercised rats. Journal of Anatomy. 2013;222(5):518-25.

130. Jortikka MO, Inkinen RI, Tammi MI, Parkkinen JJ, Haapala J, Kiviranta I, et al. Immobilisation causes longlasting matrix changes both in the immobilised and contralateral joint cartilage. Annals of the Rheumatic Diseases. 1997;56(4):255-61.

131. Oconnor KM. Unweighting accelerates tidemark advancement in articular cartilage at the knee joint of rats. Journal of Bone and Mineral Research. 1997;12(4):580-9.

132. Yellowley CE, Jacobs CR, Li Z, Zhou Z, Donahue HJ. Effects of fluid flow on intracellular calcium in bovine articular chondrocytes. The American journal of physiology. 1997;273(1 Pt 1):C30-6.

133. Lv MX, Zhou YL, Chen XY, Han L, Wang LY, Lu XL. Calcium signaling of in situ chondrocytes in articular cartilage under compressive loading: Roles of calcium sources and cell membrane ion channels. Journal of Orthopaedic Research. 2018;36(2):730-8.

134. Lane LB, Bullough PG. Age-related-changes in the thickness of the calcified zone and the number of tidemarks in adult human articular-cartilage. Journal of Bone and Joint Surgery-British Volume. 1980;62(3):372-5.

135. Oegema TR, Carpenter RJ, Hofmeister F, Thompson RC. The interaction of the zone of calcified cartilage and subchondral bone in osteoarthritis. Microscopy research and technique. 1997;37(4):324-32.

136. Beaupre GS, Stevens SS, Carter DR. Mechanobiology in the development, maintenance, and degeneration of articular cartilage. Journal of Rehabilitation Research and Development. 2000;37(2):145-51.

137. Muir P, McCarthy J, Radtke CL, Markel MD, Santschi EM, Scollay MC, et al. Role of endochondral ossification of articular cartilage and functional adaptation of the subchondral plate in the development of fatigue microcracking of joints. Bone. 2006;38(3):342-9.

138. Gannon JM, Walker G, Fischer M, Carpenter R, Thompson RC, Jr., Oegema TR, Jr. Localization of type X collagen in canine growth plate and adult canine articular cartilage. Journal of orthopaedic research : official publication of the Orthopaedic Research Society. 1991;9(4):485-94.

139. Eerola I, Salminen H, Lammi P, Lammi M, von der Mark K, Vuorio E, et al. Type X collagen, a natural component of mouse articular cartilage: association with growth, aging, and osteoarthritis. Arthritis and rheumatism. 1998;41(7):1287-95.

140. Jiang J, Leong NL, Mung JC, Hidaka C, Lu HH. Interaction between zonal populations of articular chondrocytes suppresses chondrocyte mineralization and this process is mediated by PTHrP. Osteoarthritis and cartilage / OARS, Osteoarthritis Research Society. 2008;16(1):70-82.

141. Hoemann CD, Lafantaisie-Favreau CH, Lascau-Coman V, Chen G, Guzman-Morales J. The cartilage-bone interface. The journal of knee surgery. 2012;25(2):85-97.

142. Mackie EJ, Ahmed YA, Tatarczuch L, Chen KS, Mirams M. Endochondral ossification: How cartilage is converted into bone in the developing skeleton. International Journal of Biochemistry and Cell Biology. 2008;40(1):46-62.

143. Orth P, Cucchiarini M, Wagenpfeil S, Menger MD, Madry H. PTH [1-34]-induced alterations of the subchondral bone provoke early osteoarthritis. Osteoarthritis and cartilage / OARS, Osteoarthritis Research Society. 2014;22(6):813-21.

144. Bertuglia A, Lacourt M, Girard C, Beauchamp G, Richard H, Laverty S. Osteoclasts are recruited to the subchondral bone in naturally occurring post-traumatic equine carpal osteoarthritis and may contribute to cartilage degradation. Osteoarthritis and cartilage / OARS, Osteoarthritis Research Society. 2015.

145. Bouaziz W, Funck-Brentano T, Lin H, Marty C, Ea HK, Hay E, et al. Loss of sclerostin promotes osteoarthritis in mice via beta-catenin-dependent and -independent Wnt pathways. Arthritis research & therapy. 2015;17:24.

146. Dittmer KE, Firth EC. Mechanisms of bone response to injury. Journal of Veterinary Diagnostic Investigation. 2017;29(4):385-95.

147. Lee CS, Szczesny SE, Soslowsky LJ. Remodeling and repair of orthopedic tissue: role of mechanical loading and biologics: part II: cartilage and bone. American journal of orthopedics (Belle Mead, NJ). 2011;40(3):122-8.

148. Frost HM. A determinant of bone architecture - the minimum effective strain. Clinical orthopaedics and related research. 1983(175):286-92.

149. Frost HM. Bone ?mass? and the ?mechanostat?: A proposal. The anatomical record. 1987;219(1):1-9.

150. Jee WSS, Li X, Chow S-Y, Woodbury D. Adaptation of cancellous bone to aging and immobilization in the rat: A single photon absorptiometry and histomorphometry study. The anatomical record. 1990;227(1):12-24.

151. Jee WSS, Li XJ. Adaptation of cancellous bone to overloading in the adult-rat - a single photon-absorptiometry and histomorphometry study. Anatomical Record. 1990;227(4):418-26.

152. Li XJ, Jee WSS. Adaptation of diaphyseal structure to aging and decreased mechanical loading in the adult-rat - a densitometric and histomorphometric study. Anatomical Record. 1991;229(3):291-7.

153. Firth EC. The response of bone, articular cartilage and tendon to exercise in the horse. J Anat. 2006;208(4):513-26.

154. Boyde A. The real response of bone to exercise. Journal of Anatomy. 2003;203(2):173-89.

155. Lerebours C, Buenzli PR, Scheiner S, Pivonka P. A multiscale mechanobiological model of bone remodelling predicts site-specific bone loss in the femur during osteoporosis and mechanical disuse. Biomechanics and modeling in mechanobiology. 2016;15(1):43-67.

156. Boyde A, Firth EC. Musculoskeletal responses of 2-year-old Thoroughbred horses to early training. 8. Quantitative back-scattered electron scanning electron microscopy and confocal fluorescence microscopy of the epiphysis of the third metacarpal bone. New Zealand Veterinary Journal. 2005;53(2):123-32.

157. Young DR, Nunamaker DM, Markel MD. Quantitative evaluation of the remodeling response of the proximal sesamoid bones to training-related stimuli in Thoroughbreds. American journal of veterinary research. 1991;52(8):1350-6.

158. Forwood MR, Turner CH. The response of rat tibiae to incremental bouts of mechanical loading: a quantum concept for bone formation. Bone. 1994;15(6):603-9.

159. Hillam RA, Skerry TM. Inhibition of bone resorption and stimulation of formation by mechanical loading of the modeling rat ulna in vivo. Journal of bone and mineral research : the official journal of the American Society for Bone and Mineral Research. 1995;10(5):683-9.

160. Webster D, Wasserman E, Ehrbar M, Weber F, Bab I, Muller R. Mechanical loading of mouse caudal vertebrae increases trabecular and cortical bone mass-dependence on dose and genotype. Biomechanics and modeling in mechanobiology. 2010;9(6):737-47.

161. Drissi H, Lomri A, Lasmoles F, Holy X, Zerath E, Marie PJ. Skeletal unloading induces biphasic changes in insulin-like growth factor-I mRNA levels and osteoblast activity. Experimental Cell Research. 1999;251(2):275-84.

162. Machwate M, Zerath E, Holy X, Hott M, Modrowski D, Malouvier A, et al. Skeletal unloading in rat decreases proliferation of rat bone and marrow-derived osteoblastic cells. American Journal of Physiology. 1993;264(5):E790-E9.

163. Kondo H, Nifuji A, Takeda S, Ezura Y, Rittling SR, Denhardt DT, et al. Unloading induces osteoblastic cell suppression and osteoclastic cell activation to lead to bone loss via sympathetic nervous system. Journal of Biological Chemistry. 2005;280(34):30192-200.

164. Lee TC, Taylor D. Quantification of ovine bone adaptation to altered load: morphometry, density, and surface strain. European journal of morphology. 2003;41(3-4):117-25.

165. Holmes JM, Mirams M, Mackie EJ, Whitton RC. Thoroughbred horses in race training have lower levels of subchondral bone remodelling in highly loaded regions of the distal metacarpus compared to horses resting from training. Veterinary Journal. 2014;202(3):443-7.

166. Bani Hassan E, Mirams M, Ghasem-Zadeh A, Mackie EJ, Whitton RC. Role of subchondral bone remodelling in collapse of the articular surface of Thoroughbred racehorses with palmar osteochondral disease. Equine veterinary journal. 2016;48(2):228-33.

167. Firth EC, Rogers CW, van Weeren PR, Barneveld A, Kawcak CE, McIlwraith CW, et al. Changes in diaphyseal and epiphyseal bone parameters in thoroughbred horses after withdrawal from training. J Musculoskelet Neuronal Interact. 2007;7(1):74-6.

168. Hitchens PL, Pivonka P, Malekipour F, Whitton RC. Mathematical modelling of bone adaptation of the metacarpal subchondral bone in racehorses. Biomechanics and modeling in mechanobiology. 2018;17(3):877-90.

169. Eckstein F, Jacobs CR, Merz BR. Mechanobiological adaptation of subchondral bone as a function of joint incongruity and loading. Med Eng Phys. 1997;19(8):720-8.

170. Muller-Gerbl M, Putz R, Kenn R, Kierse R. People in different age groups show different hip-joint morphology. Clinical biomechanics. 1993;8(2):66-72.

171. Schulte FA, Ruffoni D, Lambers FM, Christen D, Webster DJ, Kuhn G, et al. Local Mechanical Stimuli Regulate Bone Formation and Resorption in Mice at the Tissue Level. PLOS ONE. 2013;8(4):e62172.

172. Webster D, Schulte FA, Lambers FM, Kuhn G, Muller R. Strain energy density gradients in bone marrow predict osteoblast and osteoclast activity: a finite element study. Journal of biomechanics. 2015;48(5):866-74.

173. Carriero A, Pereira AF, Wilson AJ, Castagno S, Javaheri B, Pitsillides AA, et al. Spatial relationship between bone formation and mechanical stimulus within cortical bone: Combining 3D fluorochrome mapping and poroelastic finite element modelling. Bone Reports. 2018;8:72-80.

174. Cowin SC, Moss-Salentijn L, Moss ML. Candidates for the mechanosensory system in bone. J Biomech Eng. 1991;113(2):191-7.

175. Lanyon LE. Osteocytes, strain detection, bone modeling and remodeling. Calcif Tissue Int. 1993;53 Suppl 1:S102-6; discussion S6-7.

176. Skerry TM, Bitensky L, Chayen J, Lanyon LE. Early strain-related changes in enzyme activity in osteocytes following bone loading in vivo. Journal of bone and mineral research : the official journal of the American Society for Bone and Mineral Research. 1989;4(5):783-8.

177. Weinbaum S, Cowin SC, Zeng Y. A model for the excitation of osteocytes by mechanical loading-induced bone fluid shear stresses. Journal of biomechanics. 1994;27(3):339-60.

178. Burger EH, Klein-Nulen J. Responses of bone cells to biomechanical forces in vitro. Advances in dental research. 1999;13:93-8.

179. Burger EH, Klein-Nulend J. Mechanotransduction in bone--role of the lacuno-canalicular network. FASEB journal : official publication of the Federation of American Societies for Experimental Biology. 1999;13 Suppl:S101-12.

180. Huiskes R, Ruimerman R, van Lenthe GH, Janssen JD. Effects of mechanical forces on maintenance and adaptation of form in trabecular bone. Nature. 2000;405(6787):704-6.

181. van Oers RFM, Ruimerman R, Tanck E, Hilbers PAJ, Huiskes R. A unified theory for osteonal and hemi-osteonal remodeling. Bone. 2008;42(2):250-9.

182. Tan SD, de Vries TJ, Kuijpers-Jagtman AM, Semeins CM, Everts V, Klein-Nulend J. Osteocytes subjected to fluid flow inhibit osteoclast formation and bone resorption. Bone. 2007;41(5):745-51.

183. You L, Temiyasathit S, Lee P, Kim CH, Tummala P, Yao W, et al. Osteocytes as mechanosensors in the inhibition of bone resorption due to mechanical loading. Bone. 2008;42(1):172-9.

184. Wasserman E, Webster D, Kuhn G, Attar-Namdar M, Muller R, Bab I. Differential load-regulated global gene expression in mouse trabecular osteocytes. Bone. 2013;53(1):14-23.

185. Goldring SR. The osteocyte: key player in regulating bone turnover. RMD open. 2015;1(Suppl 1):e000049.

186. Metzger C, Brezicha J, Elizondo J, Narayanan SA, Hogan H, Bloomfield S. Differential responses of mechanosensitive osteocyte proteins in fore- and hindlimbs of hindlimb-unloaded rats. Bone (New York, NY). 2017;105:26-34.

187. Robling AG, Castillo AB, Turner CH. Biomechanical and molecular regulation of bone remodeling. Annual Review of Biomedical Engineering2006. p. 455-98.

188. Winkler DG, Sutherland MK, Geoghegan JC, Yu C, Hayes T, Skonier JE, et al. Osteocyte control of bone formation via sclerostin, a novel BMP antagonist. The EMBO journal. 2003;22(23):6267-76.

189. Robling AG, Niziolek PJ, Baldridge LA, Condon KW, Allen MR, Alam I, et al. Mechanical stimulation of bone in vivo reduces osteocyte expression of Sost/sclerostin. Journal of Biological Chemistry. 2008;283(9):5866-75.

190. Ishijima M. Enhancement of Osteoclastic Bone Resorption and Suppression of Osteoblastic Bone Formation in Response to Reduced Mechanical Stress Do Not Occur in the Absence of Osteopontin. The Journal of experimental medicine. 2001;193(3):399-404.

191. Xiong J, Onal M, Jilka R, Weinstein R, Manolagas S, O'Brien C. Matrix-embedded cells control osteoclast formation. Nature Medicine. 2011;17(10):1235-41.

192. Boyle WJ, Simonet WS, Lacey DL. Osteoclast differentiation and activation. Nature. 2003;423(6937):337-42.

193. Moester MJC, Papapoulos SE, Lowik C, van Bezooijen RL. Sclerostin: Current Knowledge and Future Perspectives. Calcified Tissue International. 2010;87(2):99-107.

194. Manolagas SC. Wnt signaling and osteoporosis. Maturitas. 2014;78(3):233-7.

195. Duan PP, Bonewald LP. The role of the wnt/beta-catenin signaling pathway in formation and maintenance of bone and teeth. International Journal of Biochemistry & Cell Biology. 2016;77:23-9.

196. Tatsumi S, Ishii K, Amizuka N, Li M, Kobayashi T, Kohno K, et al. Targeted ablation of osteocytes induces osteoporosis with defective mechanotransduction. Cell metabolism. 2007;5(6):464-75.

197. Jilka RL, Noble B, Weinstein RS. Osteocyte apoptosis. Bone. 2013;54(2):264-71.

198. Noble P, Singer ER, Jeffery NS. Does subchondral bone of the equine proximal phalanx adapt to race training? Journal of Anatomy. 2016;229(1):104-13.

199. Aguirre JI, Plotkin LI, Stewart SA, Weinstein RS, Parfitt AM, Manolagas SC, et al. Osteocyte apoptosis is induced by weightlessness in mice and precedes osteoclast recruitment and bone loss. Journal of Bone and Mineral Research. 2006;21(4):605-15.

200. Linden B. Osteochondritis dissecans of the femoral condyles. A long-term follow-up study. Journal of Bone and Joint Surgery - Series A. 1977;59(6):769-76.

201. Anderson DD, Chubinskaya S, Guilak F, Martin JA, Oegema TR, Olson SA, et al. Post-traumatic osteoarthritis: improved understanding and opportunities for early intervention. Journal of orthopaedic research : official publication of the Orthopaedic Research Society. 2011;29(6):802-9.

202. Hanie EA, Sullins KE, Powers BE, Nelson PR. Healing of full-thickness cartilage compared with full-thickness cartilage and subchondral bone defects in the equine third carpal bone. Equine veterinary journal. 1992;24(5):382-6.

203. Goetz JE, Fredericks D, Petersen E, Rudert MJ, Baer T, Swanson E, et al. A clinically realistic large animal model of intra-articular fracture that progresses to post-traumatic osteoarthritis. Osteoarthritis and cartilage / OARS, Osteoarthritis Research Society. 2015;23(10):1797-805.

204. Beals TR, Harris R, Auston DA. Articular Incongruity in the Lower Extremity: How Much Is Too Much? The Orthopedic clinics of North America. 2018;49(2):167-80.

205. Samoy Y, Van Ryssen B, Gielen I, Walschot N, van Bree H. Review of the literature: elbow incongruity in the dog. Veterinary and comparative orthopaedics and traumatology : VCOT. 2006;19(1):1-8.

206. McKinley TO, Tochigi Y, Rudert MJ, Brown TD. The effect of incongruity and instability on contact stress directional gradients in human cadaveric ankles. Osteoarthritis and cartilage. 2008;16(11):1363-9.

207. Bullough P, Goodfellow J, Greenwald AS, O'Connor J. Incongruent surfaces in the human hip joint. Nature. 1968;217(5135):1290.

208. Goodfellow JW, Bullough PG. The pattern of ageing of the articular cartilage of the elbow joint. J Bone Joint Surg Br. 1967;49(1):175-81.

209. Trumble T, Allan CH, Miyano J, Clark JM, Ott S, Jones DEC, et al. A preliminary study of joint surface changes after an intraarticular fracture: A sheep model of a tibia fracture with weight bearing after internal fixation. Journal of Orthopaedic Trauma. 2001;15(5):326-32.

210. Trumble TMD, Verheyden JMD. Remodeling of Articular Defects in an Animal Model. Clinical Orthopaedics & Related Research June. 2004;423:59-63.

211. Llinas A, McKellop HA, Marshall GJ, Sharpe F, Lu B, Kirchen M, et al. Healing and remodeling of articular incongruities in a rabbit fracture model. Journal of Bone and Joint Surgery - Series A. 1993;75(10):1508-23.

212. Hassan EB. Investigation of the osteochondral response to injury in racing Thoroughbreds [Thesis]. Melbourne, Australia: The University of Melbourne; 2013.

213. McIlwraith CW. 6 - Subchondral Cystic Lesions. In: McIlwraith CW, Frisbie DD, Kawcak CE, van Weeren PR, editors. Joint Disease in the Horse (Second Edition). Edinburgh: W.B. Saunders; 2016. p. 85-90.

214. van Weeren PR. 5 - Osteochondritis Dissecans. In: McIlwraith CW, Frisbie DD, Kawcak CE, van Weeren PR, editors. Joint Disease in the Horse (Second Edition). Edinburgh: W.B. Saunders; 2016. p. 57-84.

215. Frazer LL, Santschi EM, Fischer KJ. The impact of subchondral bone cysts on local bone stresses in the medial femoral condyle of the equine stifle joint. Medical Engineering & Physics. 2017;48:158-67.

216. Fubini SL, Erb HN, Freeman KP, Todhunter RJ. Prognostic factors affecting survival of 507 horses with joint disease: (1983 to 1990). Canadian journal of veterinary research. 1999;63(4):253-60.

217. McIlwraith CW. 3 - Traumatic Arthritis and Posttraumatic Osteoarthritis in the Horse. In: McIlwraith CW, Frisbie DD, Kawcak CE, van Weeren PR, editors. Joint Disease in the Horse (Second Edition). Edinburgh: W.B. Saunders; 2016. p. 33-48.

218. Axling JM, Castle K, Velie BD, Tammen I, Thomson PC, Hamilton NA, et al. Use of diagnostic reports to estimate prevalence and distribution of skeletal lesions in young Thoroughbreds. Vet J. 2016;214:72-6.

219. van Weeren PR, Jeffcott LB. Problems and pointers in osteochondrosis: Twenty years on. Vet J. 2013;197(1):96-102.

220. Mirams M, Tatarczuch L, Ahmed YA, Pagel CN, Jeffcott LB, Davies HM, et al. Altered gene expression in early osteochondrosis lesions. Journal of orthopaedic research : official publication of the Orthopaedic Research Society. 2009;27(4):452-7.

221. Olstad K, Ekman S, Carlson CS. An Update on the Pathogenesis of Osteochondrosis. Vet Pathol. 2015;52(5):785-802.

222. Kawcak CE. 4 - Pathologic Manifestations of Joint Disease. In: McIlwraith CW, Frisbie DD, Kawcak CE, van Weeren PR, editors. Joint Disease in the Horse (Second Edition). Edinburgh: W.B. Saunders; 2016. p. 49-56.

223. Philipson MR, Parker PJ. Stress fractures. Orthopaedics and Trauma. 2009;23(2):137-43.

224. Norrdin RW, Kawcak CE, Capwell BA, McIlwraith CW. Subchondral bone failure in an equine model of overload arthrosis. Bone. 1998;22(2):133-9.

225. Hassan EB, Mirams M, Ghasem-Zadeh A, Mackie EJ, Whitton RC. Role of subchondral bone remodelling in collapse of the articular surface of Thoroughbred racehorses with palmar osteochondral disease. Equine veterinary journal. 2016;48(2):228-33.

226. Whitton RC, Ayodele BA, Hitchens PL, Mackie EJ. Subchondral bone microdamage accumulation in distal metacarpus of Thoroughbred racehorses. Equine veterinary journal. 2018;50(6):766-73.

227. Wu AC, Kidd LJ, Cowling NR, Kelly WL, Forwood MR. Osteocyte expression of caspase-3, COX-2, IL-6 and sclerostin are spatially and temporally associated following stress fracture initiation. BoneKEy reports. 2014;3:571.

228. Verborgt O, Gibson GJ, Schaffler MB. Loss of osteocyte integrity in association with microdamage and bone remodeling after fatigue in vivo. Journal of Bone and Mineral Research. 2000;15(1):60-7.

229. Kidd LJ, Stephens AS, Kuliwaba JS, Fazzalari NL, Wu ACK, Forwood MR. Temporal pattern of gene expression and histology of stress fracture healing. Bone. 2010;46(2):369-78.

230. Hopper N, Singer E, Henson F. Increased sclerostin associated with stress fracture of the third metacarpal bone in the Thoroughbred racehorse. Bone Joint Res. 2018;7(1):94-102.

231. Whitton RC, Mirams M, Mackie EJ, Anderson GA, Seeman E. Exercise-induced inhibition of remodelling is focally offset with fatigue fracture in racehorses. Osteoporosis international. 2013;24(7):2043-8.

232. Martig S, Lee PVS, Anderson GA, Whitton RC. Compressive fatigue life of subchondral bone of the metacarpal condyle in thoroughbred racehorses. Bone. 2013;57(2):392-8.

233. Guettler JH, Demetropoulos CK, Yang KH, Jurist KA. Osteochondral deflects in the human knee - Influence of defect size on cartilage rim stress and load redistribution to surrounding cartilage. American Journal of Sports Medicine. 2004;32(6):1451-8.

234. Shelbourne KD, Jari S, Gray T. Outcome of untreated traumatic articular cartilage defects of the knee: a natural history study. The Journal of bone and joint surgery American volume. 2003;85-A Suppl 2:8-16.

235. Giannoudis PV, Tzioupis C, Papathanassopoulos A, Obakponovwe O, Roberts C. Articular step-off and risk of post-traumatic osteoarthritis. Evidence today. Injury. 2010;41(10):986-95.

236. Frisbie DD, McIlwraith CW. Evaluation of gene therapy as a treatment for equine traumatic arthritis and osteoarthritis. Clinical orthopaedics and related research. 2000(379):S273-S87.

237. Arden N, Nevitt MC. Osteoarthritis: epidemiology. Best practice & research Clinical rheumatology. 2006;20(1):3-25.

238. Molloy MG, Molloy CB. Contact sport and osteoarthritis. British journal of sports medicine. 2011;45(4):275-7.

239. Sharma AR, Kapoor M. Epidemiology of Osteoarthritis. In: Moskowitz RW, Altman RD, Hochberg MC, Buckwalter JA, Goldberg VM, editors. Osteoarthritis: diagnosis and medical/ surgical management. Philadelphia: Lippincott, Williams, Wilkins; 2007.

240. Slingerland LI, Hazewinkel HAW, Meij BP, Picavet P, Voorhout G. Cross-sectional study of the prevalence and clinical features of osteoarthritis in 100 cats. Veterinary Journal. 2011;187(3):304-9.

241. Carmona JU, Prades M. Pathophysiology of osteoarthritis. Comp Equine. 2009;4:28-40.

242. Poole AR, Guilak F, Abramson SB. Etiopathogenesis of Osteoarthritis. In: Moskowitz RW, Altman RD, Hochberg MC, Buckwalter JA, Goldberg VM, editors. Osteoarthritis : diagnosis and medical/ surgical management. 4th ed. Philadelphia: Lippincott, Williams, Wilkins; 2007.

243. Daubs BM, Markel MD, Manley PA. Histomorphometric analysis of articular cartilage, zone of calcified cartilage, and subchondral bone plate in femoral heads from clinically normal dogs and dogs with moderate or severe osteoarthritis. American journal of veterinary research. 2006;67(10):1719-24.

244. Norrdin RW, Kawcak CE, Capwell BA, McIlwraith CW. Calcified cartilage morphometry and its relation to subchondral bone remodeling in equine arthrosis. Bone. 1999;24(2):109-14.

245. Dequeker J, Mokassa L, Aerssens J, Boonen S. Bone density and local growth factors in generalized osteoarthritis. Microscopy research and technique. 1997;37(4):358-71.

246. Burr DB. The importance of subchondral bone in the progression of osteoarthritis. Journal of Rheumatology. 2004;31:77-80.

247. Martel-Pelletier J. Pathophysiology of osteoarthritis. Osteoarthritis and cartilage / OARS, Osteoarthritis Research Society. 2004;12 Suppl A:S31-3.

248. Lacourt M, Gao C, Li A, Girard C, Beauchamp G, Henderson JE, et al. Relationship between cartilage and subchondral bone lesions in repetitive impact trauma-induced equine osteoarthritis. Osteoarthritis and Cartilage. 2012;20(6):572-83.

249. Bowes MA, McLure SWD, Wolstenholme CBH, Vincent GR, Williams S, Grainger A, et al. Osteoarthritic bone marrow lesions almost exclusively colocate with denuded cartilage: a 3D study using data from the Osteoarthritis Initiative. Annals of the Rheumatic Diseases. 2016;75(10):1852-7.

250. Chen Y, Wang T, Guan M, Zhao W, Leung FK, Pan H, et al. Bone turnover and articular cartilage differences localized to subchondral cysts in knees with advanced osteoarthritis. Osteoarthritis and cartilage / OARS, Osteoarthritis Research Society. 2015;23(12):2174-83.

251. Pawson DJ, Glanzmann M, Luechinger R, Muller R, Stok KS. Quantitative morphometric patterns in cartilage and bone from the humeral heads of end-stage osteoarthritis patients. Osteoarthritis and cartilage / OARS, Osteoarthritis Research Society. 2015;23(8):1377-87.

252. Bonilla AG, Bertone AL, Brokken MT, Santschi EM. Concurrent or sequential tibial subchondral cystic lesions in 4 horses with medial femoral condyle subchondral cystic lesions. Javma-Journal of the American Veterinary Medical Association. 2016;249(11):1313-8.

253. Todhunter RJ, Minor RR, Wootton JAM, Krook L, Burtonwurster N, Lust G. Effects of exercise and polysulfated glycosaminoglycan on repair of articular-cartilage defects in the equine carpus. Journal of Orthopaedic Research. 1993;11(6):782-95.

254. Bobinac D, Marinovic M, Bazdulj E, Cvijanovic O, Celic T, Maric I, et al. Microstructural alterations of femoral head articular cartilage and subchondral bone in osteoarthritis and osteoporosis. Osteoarthritis and Cartilage. 2013;21(11):1724-30.

255. Chappard C, Peyrin F, Bonnassie A, Lemineur G, Brunet-Imbault B, Lespessailles E, et al. Subchondral bone micro-architectural alterations in osteoarthritis: A synchrotron micro-computed tomography study. Osteoarthritis and Cartilage. 2006;14(3):215-23.

256. Bertone AL, Bramlage LR, McIlwraith CW, Malemud CL. Comparison of proteoglycan and collagen in articular cartilage of horses with naturally developing

osteochondrosis and healing osteochondral fragments of experimentally induced fractures. American journal of veterinary research. 2005;66(11):1881-90.

257. Kim W, Kawcak CE, McIlwraith CW, Firth EC, Broom ND. Histologic and histomorphometric evaluation of midcarpal joint defects in Thoroughbreds raised with and without early conditioning exercise. American journal of veterinary research. 2012;73(4):498-507.

258. Turley SM, Thambyah A, Riggs CM, Firth EC, Broom ND. Microstructural changes in cartilage and bone related to repetitive overloading in an equine athlete model. J Anat. 2014;224(6):647-58.

259. Adams ME, Billingham MEJ. Animal-Models of Degenerative Joint Disease. Curr Topics Pathol. 1982;71:265-97.

260. McCoy AM. Animal Models of Osteoarthritis: Comparisons and Key Considerations. Veterinary Pathology. 2015;52(5):803-18.

261. Brandt KD. Animal models of osteoarthritis. Biorheology. 2002;39(1-2):221-35.

262. Thambyah A, Broom N. On new bone formation in the pre-osteoarthritic joint. Osteoarthritis and cartilage / OARS, Osteoarthritis Research Society. 2009;17(4):456-63.

263. Hargrave-Thomas EJ, Thambyah A, McGlashan SR, Broom ND. The bovine patella as a model of early osteoarthritis. Journal of Anatomy. 2013;223(6):651-64.

264. Ahern BJ, Parvizi J, Boston R, Schaer TP. Preclinical animal models in single site cartilage defect testing: a systematic review. Osteoarthritis and cartilage / OARS, Osteoarthritis Research Society. 2009;17(6):705-13.

265. Boyce MK, Trumble TN, Carlson CS, Groschen DM, Merritt KA, Brown MP. Non-terminal animal model of post-traumatic osteoarthritis induced by acute joint injury. Osteoarthritis and cartilage. 2013;21(5):746-55.

266. Kawcak CE, Norrdin RW, Frisbie DD, Trotter GW, McIlwraith CW. Effects of osteochondral fragmentation and intra-articular triamcinolone acetonide treatment on subchondral bone in the equine carpus. Equine veterinary journal. 1998;30(1):66-71.

267. Frisbie DD, Ghivizzani SC, Robbins PD, Evans CH, McIlwraith CW. Treatment of experimental equine osteoarthritis by in vivo delivery of the equine interleukin-1 receptor antagonist gene. Gene therapy. 2002;9(1):12-20.

268. Frisbie DD, Kawcak CE, McIlwraith CW, Werpy NM. Evaluation of polysulfated glycosaminoglycan or sodium hyaluronan administered intra-articularly for treatment of horses with experimentally induced osteoarthritis. American journal of veterinary research. 2009;70(2):203-9.

269. Frisbie DD, Kawcak CE, Werpy NM, Park RD, McIlwraith CW. Clinical, biochemical, and histologic effects of intra-articular administration of autologous conditioned serum in horses with experimentally induced osteoarthritis. American journal of veterinary research. 2007;68(3):290-6.

270. Frisbie DD, Kisiday JD, Kawcak CE, Werpy NM, McIlwraith CW. Evaluation of adipose-derived stromal vascular fraction or bone marrow-derived mesenchymal stem cells for treatment of osteoarthritis. Journal of orthopaedic research : official publication of the Orthopaedic Research Society. 2009;27(12):1675-80.

271. Frisbie DD, McCarthy HE, Archer CW, Barrett MF, McIlwraith CW. Evaluation of articular cartilage progenitor cells for the repair of articular defects in an equine model. The Journal of bone and joint surgery American volume. 2015;97(6):484-93.

272. McIlwraith CW, Frisbie DD, Kawcak CE. Evaluation of intramuscularly administered sodium pentosan polysulfate for treatment of experimentally induced osteoarthritis in horses. American journal of veterinary research. 2012;73(5):628-33.

273. Dedrick DK, Goldstein SA, Brandt KD, O'Connor BL, Goulet RW, Albrecht M. A longitudinal study of subchondral plate and trabecular bone in cruciate-deficient dogs with osteoarthritis followed up for 54 months. Arthritis and rheumatism. 1993;36(10):1460-7.

274. Dedrick DK, Goulet R, Huston L, Goldstein SA, Bole GG. Early bone changes in experimental osteoarthritis using microscopic computed-tomography. Journal of Rheumatology. 1991;18:44-5.

275. Pond MJ, Nuki G. Experimentally-induced osteoarthritis in the dog. Annals of the rheumatic diseases. 1973;32(4):387-8.

276. Boyd SK, Matyas JR, Wohl GR, Kantzas A, Zernicke RF. Early regional adaptation of periarticular bone mineral density after anterior cruciate ligament injury. Journal of Applied Physiology. 2000;89(6):2359-64.

277. Boyd SK, Muller R, Leonard T, Herzog W. Long-term periarticular bone adaptation in a feline knee injury model for post-traumatic experimental osteoarthritis. Osteoarthritis and cartilage / OARS, Osteoarthritis Research Society. 2005;13(3):235-42.

278. Frost-Christensen LN, Mastbergen SC, Vianen ME, Hartog A, DeGroot J, Voorhout G, et al. Degeneration, inflammation, regeneration, and pain/disability in dogs following destabilization or articular cartilage grooving of the stifle joint. Osteoarthritis and Cartilage. 2008;16(11):1327-35.

279. Gharbi M, Sanchez C, Mazzucchelli G, Pauw Ed, Henrotin Y. Identification of differential pattern of protein expression in canine osteoarthritis serum after anterior cruciate ligament transection: a proteomic analysis. Veterinary Journal. 2013;197(3):848-53.

280. Hayami T, Pickarski M, Wesolowski GA, McLane J, Bone A, Destefano J, et al. The role of subchondral bone remodeling in osteoarthritis: reduction of cartilage degeneration and prevention of osteophyte formation by alendronate in the rat anterior cruciate ligament transection model. Arthritis and rheumatism. 2004;50(4):1193-206.

281. Herzog W, Adams ME, Matyas JR, Brooks JG. Hindlimb loading, morphology and biochemistry of articular cartilage in the ACL-deficient cat knee. Osteoarthritis and cartilage / OARS, Osteoarthritis Research Society. 1993;1(4):243-51.

282. Kamekura S, Hoshi K, Shimoaka T, Chung U, Chikuda H, Yamada T, et al. Osteoarthritis development in novel experimental mouse models induced by knee joint instability. Osteoarthritis and cartilage / OARS, Osteoarthritis Research Society. 2005;13(7):632-41.

283. Tochigi Y, Vaseenon T, Heiner AD, Fredericks DC, Martin JA, Rudert MJ, et al. Instability Dependency of Osteoarthritis Development in a Rabbit Model of Graded Anterior Cruciate Ligament Transection. Journal of Bone and Joint Surgery-American Volume. 2011;93A(7):640-7.

284. Wang SX, Laverty S, Dumitriu M, Plaas A, Grynpas MD. The effects of glucosamine hydrochloride on subchondral bone changes in an animal model of osteoarthritis. Arthritis and rheumatism. 2007;56(5):1537-48.

285. Hayami T, Pickarski M, Zhuo Y, Wesolowski GA, Rodan GA, Duong le T. Characterization of articular cartilage and subchondral bone changes in the rat anterior cruciate ligament transection and meniscectomized models of osteoarthritis. Bone. 2006;38(2):234-43.

286. Little C, Smith S, Ghosh P, Bellenger C. Histomorphological and immunohistochemical evaluation of joint changes in a model of osteoarthritis induced by lateral meniscectomy in sheep. The Journal of rheumatology. 1997;24(11):2199-209.

287. Pastoureau P, Leduc S, Chomel A, De Ceuninck F. Quantitative assessment of articular cartilage and subchondral bone histology in the meniscectomized guinea pig model of osteoarthritis. Osteoarthritis and cartilage / OARS, Osteoarthritis Research Society. 2003;11(6):412-23.

288. Arunakul M, Tochigi Y, Goetz JE, Diestelmeier BW, Heiner AD, Rudert J, et al. Replication of chronic abnormal cartilage loading by medial meniscus destabilization for modeling osteoarthritis in the rabbit knee in vivo. Journal of Orthopaedic Research. 2013;31(10):1555-60.

289. Simmons EJ, Bertone AL, Weisbrode SE. Instability-induced osteoarthritis in the metacarpophalangeal joint of horses. American journal of veterinary research. 1999;60(1):7-13.

290. Flechtenmacher J, Borodkin JL, Hollister SJ, Dedrick DK. Tibial contact pressure distributions following anterior cruciate ligament transection (aclt) in canine experimental osteoarthritis (oa). Arthritis and rheumatism. 1992;35(9):S187-S.

291. Hasler EM, Herzog W, Leonard TR, Stano A, Nguyen H. In vivo knee joint loading and kinematics before and after ACL transection in an animal model. Journal of biomechanics. 1998;31(3):253-62.

292. Intema F, Sniekers YH, Weinans H, Vianen ME, Yocum SA, Zuurmond AMM, et al. Similarities and discrepancies in subchondral bone structure in two differently

induced canine models of osteoarthritis. Journal of Bone and Mineral Research. 2010;25(7):1650-7.

293. Radin EL, Martin RB, Burr DB, Caterson B, Boyd RD, Goodwin C. Effects of mechanical loading on the tissues of the rabbit knee. Journal of orthopaedic research : official publication of the Orthopaedic Research Society. 1984;2(3):221-34.

294. Radin EL, Parker HG, Pugh JW, Steinber.Rs, Paul IL, Rose RM. Response of joints to impact loading .3. Relationship between trabecular microfractures and cartilage degeneration. Journal of biomechanics. 1973;6(1):51-&.

295. Radin EL, Paul IL. RESPONSE OF JOINTS TO IMPACT LOADING .1. IN-VITRO WEAR. Arthritis and rheumatism. 1971;14(3):356-&.

296. Vener MJ, Thompson RC, Jr., Lewis JL, Oegema TR, Jr. Subchondral damage after acute transarticular loading: an in vitro model of joint injury. Journal of orthopaedic research : official publication of the Orthopaedic Research Society. 1992;10(6):759-65.

297. Rickey EJ, Cruz AM, Trout DR, McEwen BJ, Hurtig MB. Evaluation of experimental impact injury for inducing post-traumatic osteoarthritis in the metacarpophalangeal joints of horses. American journal of veterinary research. 2012;73(10):1540-52.

298. Thompson RC, Oegema TR, Lewis JL, Wallace L. Osteoarthrotic changes after acute transarticular load - an animal-model. Journal of Bone and Joint Surgery-American Volume. 1991;73A(7):990-1001.

299. Lahm A, Kreuz PC, Oberst M, Haberstroh J, Uhl M, Maier D. Subchondral and trabecular bone remodeling in canine experimental osteoarthritis. Archives of orthopaedic and trauma surgery. 2006;126(9):582-7.

300. Bolam CJ, Hurtig MB, Cruz A, McEwen BJ. Characterization of experimentally induced post-traumatic osteoarthritis in the medial femorotibial joint of horses. American journal of veterinary research. 2006;67(3):433-47.

301. Isaac DI, Meyer EG, Kopke KS, Haut RC. Chronic changes in the rabbit tibial plateau following blunt trauma to the tibiofemoral joint. Journal of biomechanics. 2010;43(9):1682-8.

302. Martin JA, Anderson DD, Goetz JE, Fredericks D, Pedersen DR, Ayati BP, et al. Complementary models reveal cellular responses to contact stresses that contribute to post-traumatic osteoarthritis. Journal of Orthopaedic Research. 2017;35(3):515-23.

303. Fu LLK, Maffulli N, Yip KMH, Chan KM. Articular cartilage lesions of the knee following immobilisation or destabilisation for 6 or 12 weeks in rabbits. Clinical Rheumatology. 1998;17(3):227-33.

304. Tolvanen E, Bergroth V, Konttinen YT, Michelsson JE. Primary inflammatory reaction in synovial fluid and tissue in rabbit immobilization osteoarthritis. Clinical orthopaedics and related research. 1990(260):280-6.

305. Scheld K, Zittermann A, Heer M, Herzog B, Mika C, Drummer C, et al. Nitrogen metabolism and bone metabolism markers in healthy adults during 16 weeks of bed rest. Clinical chemistry. 2001;47(9):1688-95.

306. Vanwanseele B, Eckstein F, Knecht H, Spaepen A, Stussi E. Longitudinal analysis of cartilage atrophy in the knees of patients with spinal cord injury. Arthritis and rheumatism. 2003;48(12):3377-81.

307. Intema F, DeGroot J, Elshof B, Vianen ME, Yocum S, Zuurmond A, et al. The canine bilateral groove model of osteoarthritis. Journal of Orthopaedic Research. 2008;26(11):1471-7.

308. Mastbergen SC, Marijnissen AC, Vianen ME, van Roermund PM, Bijlsma JW, Lafeber FP. The canine 'groove' model of osteoarthritis is more than simply the expression of surgically applied damage. Osteoarthritis and Cartilage. 2006;14(1):39-46.

309. Mastbergen SC, Pollmeier M, Fischer L, Vianen ME, Lafeber FPJG. The groove model of osteoarthritis applied to the ovine fetlock joint. Osteoarthritis and Cartilage. 2008;16(8):919-28.

310. Maninchedda U, Lepage OM, Gangl M, Hilairet S, Remandet B, Meot F, et al. Development of an equine groove model to induce metacarpophalangeal osteoarthritis: a pilot study on 6 horses. PloS one. 2015;10(2):e0115089-e.

311. Trotter GW, Yovich JV, McIlwraith CW, Norrdin RW. Effects of intramuscular polysulfated glycosaminoglycan on chemical and physical defects in equine articular

cartilage. Canadian journal of veterinary research = Revue canadienne de recherche veterinaire. 1989;53(2):224-30.

312. Goranov NV. Clinical changes in sodium monoiodoacetate-induced stifle osteoarthritis model in dogs. Veterinary World. 2012;5(3):138-44.

313. Mohan G, Perilli E, Parkinson IH, Humphries JM, Fazzalari NL, Kuliwaba JS. Pre-emptive, early, and delayed alendronate treatment in a rat model of knee osteoarthritis: effect on subchondral trabecular bone microarchitecture and cartilage degradation of the tibia, bone/cartilage turnover, and joint discomfort. Osteoarthritis and cartilage / OARS, Osteoarthritis Research Society. 2013;21(10):1595-604.

314. McIlwraith CW, Van Sickle DC. Experimentally induced arthritis of the equine carpus: histologic and histochemical changes in the articular cartilage. American journal of veterinary research. 1981;42(2):209-17.

315. Hurtig MB. Use of autogenous cartilage particles to create a model of naturally occurring degenerative joint disease in the horse. Equine veterinary journal Supplement. 1988(6):19-22.

316. White GW, Stites T, Hamm J, Pool R. Evaluation of the efficacy of various preparations of sodium hyaluronate in an induced equine carpitis model. Journal of Equine Veterinary Science. 1999;19(5):331-7.

317. Definition and classification of Lameness. Guide for Veterinary Service and Judging of Equestrian Events. 19. Lexington, Kentucky: American Association of Equine Practitioners; 1991.

318. Braganca PMS, Rhodin M, van Weeren PR. On the brink of daily clinical application of objective gait analysis: What evidence do we have so far from studies using an induced lameness model? Veterinary Journal. 2018;234:11-23.

319. Hinz A, Fischer AT, Jr. Comparison of the accuracy of radiography and ultrasonography for detection of articular lesions in horses. Veterinary surgery : VS. 2011;40(7):881-5.

320. Charles EM, Rantanen NW. An approach to imaging algorithms for equine lameness diagnosis. Vet Clin North Am Equine Pract. 2012;28(3):467-81.

321. Wulster KB. Diagnosis of Skeletal Injury in the Sport Horse. Veterinary Clinics of North America: Equine Practice. 2018;34(2):193-213.

322. Puchalski SM. Advances in equine computed tomography and use of contrast media. Vet Clin North Am Equine Pract. 2012;28(3):563-81.

323. Kawcak CE, Barrett MF, Werpy NM, Selberg K. 9 - Principles of Diagnosis. In: McIlwraith CW, Frisbie DD, Kawcak CE, van Weeren PR, editors. Joint Disease in the Horse (Second Edition). Edinburgh: W.B. Saunders; 2016. p. 119-78.

324. Rautiainen J, Lehto LJ, Tiitu V, Kiekara O, Pulkkinen H, Brunott A, et al. Osteochondral Repair: Evaluation with Sweep Imaging with Fourier Transform in an Equine Model. Radiology. 2013;269(1):113-21.

325. Steel C. Equine Synovial Fluid Analysis. The Veterinary clinics of North America Equine practice. 2008;24(2):437-54.

326. McIlwraith CW. Use of synovial fluid and serum biomarkers in equine bone and joint disease: a review. Equine veterinary journal. 2005;37(5):473-82.

327. Frisbie DD, Al-Sobayil F, Billinghurst RC, Kawcak CE, McIlwraith CW. Changes in synovial fluid and serum biomarkers with exercise and early osteoarthritis in horses. Osteoarthritis and Cartilage. 2008;16(10):1196-204.

328. Ekman S, Lindahl A, Ruetschi U, Jansson A, Bjorkman K, Abrahamsson-Aurell K, et al. Effect of circadian rhythm, age, training and acute lameness on serum concentrations of cartilage oligomeric matrix protein (COMP) neo-epitope in horses. Equine veterinary journal. 2019;51(5):674-80.

329. Alwan WH, Carter SD, Bennett D, Edwards GB. Glycosaminoglycans in horses with osteoarthritis. Equine veterinary journal. 1991;23(1):44-7.

330. Vieira FAC, Baccarin RYA, Aguiar JAK, Michelacci YM. Urinary excretion of glycosaminoglycans in horses: Changes with age, training, and osteoarthritis. Journal of Equine Veterinary Science. 2005;25(9):387-400.

331. McIlwraith CW, Frisbie DD, Kawcak CE, Fuller CJ, Hurtig M, Cruz A. The OARSI histopathology initiative - recommendations for histological assessments of

osteoarthritis in the horse. Osteoarthritis and cartilage / OARS, Osteoarthritis Research Society. 2010;18 Suppl 3:S93-105.

332. An YH, Martin KL. Handbook of histology methods for bone and cartilage. Totowa, NJ: Humana Press; 2003. xviii, 587 p. p.

333. Firth EC, Delahunt J, Wichtel JW, Birch HL, Goodship AE. Galloping exercise induces regional changes in bone density within the third and radial carpal bones of Thoroughbred horses. Equine veterinary journal. 1999;31(2):111-5.

334. Bogers SH, Rogers CW, Bolwell CF, Roe WD, Gee EK, McIlwraith CW. Impact of race training on volumetric bone mineral density and its spatial distribution in the distal epiphysis of the third metatarsal bone of 2-year-old horses. Veterinary Journal. 2014;201(3):353-8.

335. Malekipour F, Whitton CR, Lee PV. Stiffness and energy dissipation across the superficial and deeper third metacarpal subchondral bone in Thoroughbred racehorses under high-rate compression. J Mech Behav Biomed Mater. 2018;85:51-6.

336. Analysis of bone by micro-CT: General Information. Bruker microCT; 2018.

337. Bilezikian JP, Raisz LG, Martin TJ. Principles of bone biology, 3rd ed. 3rd ed. ed. Amsterdam ; London Elsevier

2008.

338. Boyde A, Jones SJ. Scanning electron microscopy of bone: instrument, specimen, and issues. Microscopy research and technique. 1996;33(2):92-120.

339. Boyde A. Scanning electron microscopy of bone. Methods in molecular biology (Clifton, NJ). 2012;816:365-400.

340. Kold SE, Hickman J, Melsen F. An experimental study of the healing process of equine chondral and osteochondral defects. Equine veterinary journal. 1986;18(1):18-24.

341. Rohde C, Anderson DE, Bertone AL, Weisbrode SE. Effects of phenylbutazone on bone activity and formation in horses. American journal of veterinary research. 2000;61(5):537-43.

342. Gruber HE. Adaptations of Goldner's Masson trichrome stain for the study of undecalcified plastic embedded bone. Biotechnic and Histochemistry. 1992;67(1):30-4.

343. Cole AA, Walters LM. Tartrate-resistant acid phosphatase in bone and cartilage following decalcification and cold-embedding in plastic. Journal of Histochemistry and Cytochemistry. 1987;35(2):203-6.

344. Goto T, Yamaza T, Tanaka T. Cathepsins in the osteoclast. Journal of electron microscopy. 2003;52(6):551-8.

345. Compston JE, Croucher PI. Histomorphometric assessment of trabecular bone remodelling in osteoporosis. Bone Miner. 1991;14(2):91-102.

346. Sakata T, Sakai A, Tsurukami H, Okimoto N, Okazaki Y, Ikeda S, et al. Trabecular bone turnover and bone marrow cell development in tail-suspended mice. Journal of bone and mineral research : the official journal of the American Society for Bone and Mineral Research. 1999;14(9):1596-604.

347. Chen Y, Huang YC, Yan CH, Chiu KY, Wei Q, Zhao J, et al. Abnormal subchondral bone remodeling and its association with articular cartilage degradation in knees of type 2 diabetes patients. Bone research. 2017;5:17034.

348. Li X, Yang J, Liu D, Li J, Niu K, Feng S, et al. Knee loading inhibits osteoclast lineage in a mouse model of osteoarthritis. Scientific reports. 2016;6:24668.

349. Hagenaars CE, Kawilarang-de Haas EW, van der Kraan AA, Spooncer E, Dexter TM, Nijweide PJ. Interleukin-3-dependent hematopoietic stem cell lines capable of osteoclast formation in vitro. Journal of bone and mineral research : the official journal of the American Society for Bone and Mineral Research. 1991;6(9):947-54.

350. Gray AW, Davies ME, Jeffcott LB. Generation and activity of equine osteoclasts in vitro: effects of the bisphosphonate pamidronate (APD). Research in Veterinary Science. 2002;72(2):105-13.

351. Freeman KP, Todhunter R, Lust G, Erb H, Rakestraw P, Slusher SH, et al. Cytology of polychrome-stained equine synovial-fluid smears - comparison with clinical findings, histologic specimens, wright-giemsa-stained smears and outcome. Acta Cytologica. 1991;35(5):512-20.

352. Staszyk C, Bienert A, Kreutzer R, Wohlsein P, Simhofer H. Equine odontoclastic tooth resorption and hypercementosis. Vet J. 2008;178(3):372-9.

353. Grill V, Zweyer M, Bareggi R, Martelli AM, Basa M, Narducci P. A simple and rapid staining technique for plastic embedded cartilage and bone. Biotechnic & histochemistry : official publication of the Biological Stain Commission. 1995;70(2):75-80.

354. Roberts IM, Hutcheson AM. Handling and staining epoxy resin sections for light microscopy. Journal of microscopy. 1975;103(1):121-6.

355. Ahmed YA, Tatarczuch L, Pagel CN, Davies HM, Mirams M, Mackie EJ. Physiological death of hypertrophic chondrocytes. Osteoarthritis and cartilage / OARS, Osteoarthritis Research Society. 2007;15(5):575-86.

356. Mirams M, Ayodele BA, Tatarczuch L, Henson FM, Pagel CN, Mackie EJ. Identification of novel osteochondrosis - Associated genes. Journal of Orthopaedic Research. 2016;34(3):404-11.

357. Broom ND, Myers DB. A study of the structural response of wet hyaline cartilage to various loading situations. Connect Tissue Res. 1980;7(4):227-37.

358. Heuijerjans A, Wilson W, Ito K, van Donkelaar CC. The critical size of focal articular cartilage defects is associated with strains in the collagen fibers. Clinical biomechanics. 2017;50:40-6.

359. Klennert BJ, Ellis BJ, Maak TG, Kapron AL, Weiss JA. The mechanics of focal chondral defects in the hip. Journal of biomechanics. 2017;52:31-7.

360. Brown TD, Pope DF, Hale JE, Buckwalter JA, Brand RA. Effects of osteochondral defect size on cartilage contact stress. Journal of Orthopaedic Research. 1991;9(4):559-67.

361. Nelson BH, Anderson DD, Brand RA, Brown TD. Effect of osteochondral defects on articular-cartilage - contact pressures studied in dog knees. Acta Orthopaedica Scandinavica. 1988;59(5):574-9.

362. Bevill SL, Thambyah A, Broom ND. New insights into the role of the superficial tangential zone in influencing the microstructural response of articular cartilage to compression. Osteoarthritis and Cartilage. 2010;18(10):1310-8.

363. Durr HR, Martin H, Pellengahr C, Schlemmer M, Maier M, Jansson V. The cause of subchondral bone cysts in osteoarthrosis - A finite element analysis. Acta Orthopaedica Scandinavica. 2004;75(5):554-8.

364. Fisher MB, Belkin NS, Milby AH, Henning EA, Bostrom M, Kim M, et al. Cartilage repair and subchondral bone remodeling in response to focal lesions in a mini-pig model: implications for tissue engineering. Tissue engineering Part A. 2015;21(3-4):850-60.

365. Jackson DW, Lalor PA, Aberman HM, Simon TM. Spontaneous repair of full-thickness defects of articular cartilage in a goat model. A preliminary study. The Journal of bone and joint surgery American volume. 2001;83-A(1):53-64.

366. Convery FR, Akeson WH, Keown GH. The repair of large osteochondral defects. An experimental study in horses. Clinical orthopaedics and related research. 1972;82:253-62.

367. Jelic M, Pecina M, Haspl M, Kos J, Taylor K, Maticic D, et al. Regeneration of articular cartilage chondral defects by osteogenic protein-1 (bone morphogenetic protein-7) in sheep. Growth Factors. 2001;19(2):101-13.

368. Nosewicz TL, Reilingh ML, van Dijk CN, Duda GN, Schell H. Weightbearing ovine osteochondral defects heal with inadequate subchondral bone plate restoration: implications regarding osteochondral autograft harvesting. Knee Surgery Sports Traumatology Arthroscopy. 2012;20(10):1919-26.

369. Orth P, Cucchiarini M, Zurakowski D, Menger MD, Kohn DM, Madry H. Parathyroid hormone [1-34] improves articular cartilage surface architecture and integration and subchondral bone reconstitution in osteochondral defects in vivo. Osteoarthritis and cartilage / OARS, Osteoarthritis Research Society. 2013;21(4):614-24.

370. Frisbie DD, Trotter GW, Powers BE, Rodkey WG, Steadman JR, Howard RD, et al. Arthroscopic subchondral bone plate microfracture technique augments healing of

large chondral defects in the radial carpal bone and medial femoral condyle of horses. Veterinary Surgery. 1999;28(4):242-55.

371. Salonius E, Rieppo L, Nissi MJ, Pulkkinen HJ, Brommer H, Brunott A, et al. Critical-sized cartilage defects in the equine carpus. Connect Tissue Res. 2018:1-12.

372. Kulmala KAM, Pulkkinen HJ, Rieppo L, Tiitu V, Kiviranta I, Brünott A, et al. Contrast-Enhanced Micro-Computed Tomography in Evaluation of Spontaneous Repair of Equine Cartilage. Cartilage. 2012;3(3):235-44.

373. Hurtig MB, Fretz PB, Doige CE, Schnurr DL. Effects of Lesion Size and Location on Equine Articular-Cartilage Repair. Canadian Journal of Veterinary Research-Revue Canadienne De Recherche Veterinaire. 1988;52(1):137-46.

374. Schlichting K, Schell H, Kleemann R, Schill A, Weiler A, Duda G, et al. Influence of scaffold stiffness on subchondral bone and subsequent cartilage regeneration in an ovine model of osteochondral defect healing. American journal of sports medicine. 2008;36(12):2379-91.

375. Marchand C, Chen G, Tran Khanh N, Sun J, Chen H, Buschmann M, et al. Microdrilled cartilage defects treated with thrombin-solidified chitosan/blood implant regenerate a more hyaline, stable, and structurally integrated osteochondral unit compared to drilled controls. Tissue Engineering, Part A. 2012;18(5-6):508-19.

376. Vasara AI, Hyttinen MM, Lammi MJ, Lammi PE, Langsjo TK, Lindahl A, et al. Subchondral bone reaction associated with chondral defect and attempted cartilage repair in goats. Calcified Tissue International. 2004;74(1):107-14.

377. Orth P, Goebel L, Wolfram U, Ong M, Gräber S, Kohn D, et al. Effect of subchondral drilling on the microarchitecture of subchondral bone: analysis in a large animal model at 6 months. American journal of sports medicine. 2012;40(4):828-36.

378. Hoemann C, Hurtig M, Rossomacha E, Sun J, Chevrier A, Shive M, et al. Chitosan-glycerol phosphate/blood implants improve hyaline cartilage repair in ovine microfracture defects. Journal of Bone & Joint Surgery - American Volume. 2005;87(12):2671-86.

379. Chen H, Chevrier A, Hoemann C, Sun J, Ouyang W, Buschmann M. Characterization of subchondral bone repair for marrow-stimulated chondral defects and its relationship to articular cartilage resurfacing. American journal of sports medicine. 2011;39(8):1731-40.

380. Dorotka R, Bindreiter U, Macfelda K, Windberger U, Nehrer S. Marrow stimulation and chondrocyte transplantation using a collagen matrix for cartilage repair. Osteoarthritis and cartilage. 2005;13(8):655-64.

381. Henderson IJP, La Valette D. Subchondral bone overgrowth in the presence of full-thickness cartilage defects in the knee. Knee (Oxford). 2005;12(6):435-40.

382. Orth P, Cucchiarini M, Kaul G, Ong MF, Gräber S, Kohn DM, et al. Temporal and spatial migration pattern of the subchondral bone plate in a rabbit osteochondral defect model. Osteoarthritis and cartilage. 2012;20(10):1161-9.

383. Frost HM. The biology of fracture healing. An overview for clinicians. Part I. Clinical orthopaedics and related research. 1989(248):283-93.

384. Giannoudis PV, Jones E, Einhorn TA. Fracture healing and bone repair. Injury. 2011;42(6):549-50.

385. Loi F, Cordova LA, Pajarinen J, Lin TH, Yao Z, Goodman SB. Inflammation, fracture and bone repair. Bone. 2016;86:119-30.

386. Marsell R, Einhorn TA. The biology of fracture healing. Injury. 2011;42(6):551-5.

387. Schindeler A, McDonald MM, Bokko P, Little DG. Bone remodeling during fracture repair: The cellular picture. Seminars in Cell & Developmental Biology. 2008;19(5):459-66.

388. Barr ARS, Wotton SF, Dow SM, Waterman AE, Goodship AE, Duance VC. Effect of central or marginal location and postoperative exercise on the healing of osteochondral defects in the equine carpus. Equine veterinary journal. 1994;26(1):33-9.

389. Lefkoe T, Trafton P, Ehrlich M, Walsh W, Dennehy D, Barrach H-J, et al. An Experimental Model of Femoral Condylar Defect Leading to Osteoarthrosis. Journal of orthopaedic trauma. 1993;7(5):458-67.

390. Dalstra M, Verna C, Cacciafesta V, Andreassen TT, Melsen B. Micro-computed tomography to evaluate bone remodeling and mineralization. Advances in experimental medicine and biology2001. p. 9-19.

391. Schneider CA, Rasband WS, Eliceiri KW. NIH Image to ImageJ: 25 years of image analysis. Nature Methods. 2012;9:671.

392. Parfitt AM, Drezner MK, Glorieux FH, Kanis JA, Malluche H, Meunier PJ, et al. Bone histomorphometry - standardization of nomenclature, symbols, and units. Journal of Bone and Mineral Research. 1987;2(6):595-610.

393. Ross MW. Chapter 38 - The Carpus. In: Dyson MWRJ, editor. Diagnosis and Management of Lameness in the Horse (Second Edition). Saint Louis: W.B. Saunders; 2011. p. 426-49.

394. Fernandes JC, Martel-Pelletier J, Pelletier JP. The role of cytokines in osteoarthritis pathophysiology. Biorheology. 2002;39(1-2):237-46.

395. de Lange-Brokaar BJE, Ioan-Facsinay A, van Osch G, Zuurmond AM, Schoones J, Toes REM, et al. Synovial inflammation, immune cells and their cytokines in osteoarthritis: a review. Osteoarthritis and Cartilage. 2012;20(12):1484-99.

396. Nakamura I, Takahashi N, Jimi E, Udagawa N, Suda T. Regulation of osteoclast function. Modern Rheumatology / The Japan Rheumatism Association. 2012;22(2):167-77.

397. Teitelbaum SL. Osteoclasts; culprits in inflammatory osteolysis. Arthritis research & therapy. 2006;8(1).

398. Norrdin RW, Jee WS, High WB. The role of prostaglandins in bone in vivo. Prostaglandins, leukotrienes and essential fatty acids. 1990;41(3):139-49.

399. Toutain P-L, Cester C. Pharmacokinetic-pharmacodynamic relationships and dose response to meloxicam in horses with induced arthritis in the right carpal joint. American journal of veterinary research. 2004;65(11):1533-41.

400. King MR, Haussler KK, Kawcak CE, McIlwraith CW, Reiser RF, Frisbie DD, et al. Biomechanical and histologic evaluation of the effects of underwater treadmill

exercise on horses with experimentally induced osteoarthritis of the middle carpal joint. American journal of veterinary research. 2017;78(5):558-69.

401. Koenig TJ, Dart AJ, McIlwraith CW, Horadagoda N, Bell RJ, Perkins N, et al. Treatment of Experimentally Induced Osteoarthritis in Horses Using an Intravenous Combination of Sodium Pentosan Polysulfate, N-Acetyl Glucosamine, and Sodium Hyaluronan. Veterinary Surgery. 2014;43(5):612-22.

402. Lane J, Massie J, Ball S, Amiel M, Chen A, Bae W, et al. Follow-up of osteochondral plug transfers in a goat model: a 6-month study. American journal of sports medicine. 2004;32(6):1440-50.

403. Vanderperren K, Raes E, Bree HV, Saunders JH. Diagnostic imaging of the equine tarsal region using radiography and ultrasonography. Part 2: bony disorders. Vet J. 2009;179(2):188-96.

404. De Lasalle J, Alexander K, Olive J, Laverty S. Comparisons among radiography, ultrasonography and computed tomography for ex vivo characterization of stifle osteoarthritis in the horse. Veterinary radiology & ultrasound : the official journal of the American College of Veterinary Radiology and the International Veterinary Radiology Association. 2016;57(5):489-501.

405. Daniel AJ, Judy CE, Rick MC, Saveraid TC, Herthel DJ. Comparison of radiography, nuclear scintigraphy, and magnetic resonance imaging for detection of specific conditions of the distal tarsal bones of horses: 20 cases (2006-2010). J Am Vet Med Assoc. 2012;240(9):1109-14.

406. Hsia AW, Emami AJ, Tarke FD, Cunningham HC, Tjandra PM, Wong A, et al. Osteophytes and fracture calluses share developmental milestones and are diminished by unloading. Journal of orthopaedic research : official publication of the Orthopaedic Research Society. 2018;36(2):699-710.

407. Stover SM, Pool RR. Effect of intra-articular gentamicin sulfate on normal equine synovial-membrane. American journal of veterinary research. 1985;46(12):2485-91.

408. Sanchez-Teran AF, Bracamonte JL, Hendrick S, Riddell L, Musil K, Hoff B, et al. Effect of repeated through-and-through joint lavage on serum amyloid A in synovial fluid from healthy horses. The Veterinary Journal. 2016;210:30-3.

409. Francoz D, Desrochers A, Latouche JS. Effect of repeated arthrocentesis and single joint lavage on cytologic evaluation of synovial fluid in 5 young calves. Canadian Journal of Veterinary Research-Revue Canadienne De Recherche Veterinaire. 2007;71(2):129-34.

410. Kwan C, Bell R, Koenig T, Bischofberger A, Horadagoda N, Perkins NR, et al. Effects of intra-articular sodium pentosan polysulfate and glucosamine on the cytology, total protein concentration and viscosity of synovial fluid in horses. Aust Vet J. 2012;90(8):315-20.

411. Rinnovati R, Bonelli F, Tognetti R, Gallo C, Bassini RF, Marchetti V, et al. Effect of Repeated Arthrocentesis on Cytology of Synovial Fluid. Journal of Equine Veterinary Science. 2017;57:112-5.

412. Berg RI, Sykes JE, Kass PH, Vernau W. Effect of repeated arthrocentesis on cytologic analysis of synovial fluid in dogs. Journal of veterinary internal medicine. 2009;23(4):814-7.

413. Simkin PA, Huang A, Benedict RS. Effects of exercise on blood flow to canine articular tissues. Journal of orthopaedic research : official publication of the Orthopaedic Research Society. 1990;8(2):297-303.

414. Palmer JL, Bertone AL. Joint Biomechanics in the Pathogenesis of Traumatic Arthritis. In: McIlwraith CW, Trotter GW, editors. Joint Disease in the Horse. 1st ed. Philadelphia: W.B. Saunders; 1996. p. 104-13.

415. Sellam J, Berenbaum F. The role of synovitis in pathophysiology and clinical symptoms of osteoarthritis. Nature Reviews Rheumatology. 2010;6(11):625-35.

416. Loeser RF. Molecular mechanisms of cartilage destruction: mechanics, inflammatory mediators, and aging collide. Arthritis and rheumatism. 2006;54(5):1357-60.

417. Scanzello CR, Goldring SR. The role of synovitis in osteoarthritis pathogenesis. Bone. 2012;51(2):249-57.

418. van der Kraan PM, van den Berg WB. Osteophytes: relevance and biology. Osteoarthritis and cartilage / OARS, Osteoarthritis Research Society. 2007;15(3):237-44.

419. Hashimoto S, Creighton-Achermann L, Takahashi K, Amiel D, Coutts RD, Lotz M. Development and regulation of osteophyte formation during experimental osteoarthritis. Osteoarthritis and cartilage / OARS, Osteoarthritis Research Society. 2002;10(3):180-7.

420. Gerstenfeld LC, Cullinane DM, Barnes GL, Graves DT, Einhorn TA. Fracture healing as a post-natal developmental process: molecular, spatial, and temporal aspects of its regulation. J Cell Biochem. 2003;88(5):873-84.

421. Qiu YS, Shahgaldi BF, Revell WJ, Heatley FW. Observations of subchondral plate advancement during osteochondral repair: a histomorphometric and mechanical study in the rabbit femoral condyle. Osteoarthritis and cartilage. 2003;11(11):810-20.

422. Einhorn TA. The science of fracture healing. J Orthop Trauma. 2005;19(10 Suppl):S4-6.

423. Matsumoto T, Kuroda R, Mifune Y, Kawamoto A, Shoji T, Miwa M, et al. Circulating endothelial/skeletal progenitor cells for bone regeneration and healing. Bone. 2008;43(3):434-9.

424. Eghbali-Fatourechi GZ, Lamsam J, Fraser D, Nagel D, Riggs BL, Khosla S. Circulating osteoblast-lineage cells in humans. The New England journal of medicine. 2005;352(19):1959-66.

425. Polzin B, Ellis T, Dirschl DR. Effects of varying pulsatile lavage pressure on cancellous bone structure and fracture healing. Journal of Orthopaedic Trauma. 2006;20(4):261-6.

426. O'Sullivan ME, Bronk JT, Chao EY, Kelly PJ. Experimental study of the effect of weight bearing on fracture healing in the canine tibia. Clinical orthopaedics and related research. 1994(302):273-83.

427. Bailon-Plaza A, van der Meulen MC. Beneficial effects of moderate, early loading and adverse effects of delayed or excessive loading on bone healing. Journal of biomechanics. 2003;36(8):1069-77.

428. Dekel S, Lenthall G, Francis MJO. Release of prostaglandins from bone and muscle after tibial fracture - an experimental-study in rabbits. Journal of Bone and Joint Surgery-British Volume. 1981;63(2):185-9.

429. Chen WT, Han DC, Zhang PX, Han N, Kou YH, Yin XF, et al. A special healing pattern in stable metaphyseal fractures. Acta Orthop. 2015;86(2):238-42.

430. Frost HM. The regional acceleratory phenomenon: A review. Henry Ford Hospital Medical Journal. 1983;31(1):3-9.

431. Barry S. Non-steroidal anti-inflammatory drugs inhibit bone healing: a review. Veterinary and comparative orthopaedics and traumatology : VCOT. 2010;23(6):385-92.

432. Mueller M, Schilling T, Minne HW, Ziegler R. A systemic acceleratory phenomenon (SAP) accompanies the regional acceleratory phenomenon (RAP) during healing of a bone defect in the rat. Journal of bone and mineral research : the official journal of the American Society for Bone and Mineral Research. 1991;6(4):401-10.

433. Schilling T, Muller M, Minne HW, Ziegler R. Influence of inflammation-mediated osteopenia on the regional acceleratory phenomenon and the systemic acceleratory phenomenon during healing of a bone defect in the rat. Calcif Tissue Int. 1998;63(2):160-6.

434. Dehority W, Halloran BP, Bikle DD, Curren T, Kostenuik PJ, Wronski TJ, et al. Bone and hormonal changes induced by skeletal unloading in the mature male rat. The American journal of physiology. 1999;276(1 Pt 1):E62-9.

435. Wronski TJ, Morey-Holton ER. Skeletal response to simulated weightlessness: a comparison of suspension techniques. Aviation, space, and environmental medicine. 1987;58(1):63-8.

436. Shirazi R, Shirazi-Adl A. Computational biomechanics of articular cartilage of human knee joint: Effect of osteochondral defects. Journal of biomechanics. 2009;42(15):2458-65.

437. Tidswell HK, Innes JF, Avery NC, Clegg PD, Barr ARS, Vaughan-Thomas A, et al. High-intensity exercise induces structural, compositional and metabolic changes in cuboidal bones - findings from an equine athlete model. Bone. 2008;43(4):724-33.

438. Squire M, Brazin A, Keng YM, Judex S. Baseline bone morphometry and cellular activity modulate the degree of bone loss in the appendicular skeleton during disuse. Bone. 2008;42(2):341-9.

439. Weinreb M, Rodan GA, Thompson DD. Depression of osteoblastic activity in immobilized limbs of suckling rats. Journal of Bone and Mineral Research. 1991;6(7):725-31.

440. Firth EC, Rogers CW, Perkins NR, Anderson BH, Grace ND. Musculoskeletal responses of 2-year-old Thoroughbred horses to early training. 1. Study design, and clinical, nutritional, radiological and histological observations. N Z Vet J. 2004;52(5):261-71.

441. Nakamura F, Tsukamoto I, Inoue S, Hashimoto K, Akagi M. Cyclic compressive loading activates angiotensin II type 1 receptor in articular chondrocytes and stimulates hypertrophic differentiation through a G-protein-dependent pathway. Febs Open Bio. 2018;8(6):962-73.

442. Hall AC, Urban JPG, Gehl KA. The effects of hydrostatic-pressure on matrix synthesis in articular-cartilage. Journal of Orthopaedic Research. 1991;9(1):1-10.

443. Wong M, Siegrist M, Cao XS. Cyclic compression of articular cartilage explants is associated with progressive consolidation and altered expression pattern of extracellular matrix proteins. Matrix Biology. 1999;18(4):391-9.

444. Li KW, Falcovitz YH, Nagrampa JP, Chen AC, Lottman LM, Shyy JYJ, et al. Mechanical compression modulates proliferation of transplanted chondrocytes. Journal of Orthopaedic Research. 2000;18(3):374-82.

445. Kurrat HJ. The thickness of the cartilage in the hip joint. Journal of anatomy. 1978;126(1):145-55.

446. Teshima R, Nawata K, Hagino H, Morio Y, Inoue M, Irizawa Y. Effects of weight bearing on the tidemark and osteochondral junction of articular cartilage: histomorphometric analyses of 7 normal femoral heads. Acta orthopaedica Scandinavica. 1999;70(4):381-6.

447. Andriacchi TP, Koo S, Scanlan SF. Gait mechanics influence healthy cartilage morphology and osteoarthritis of the knee. Journal of Bone and Joint Surgery - Series A. 2009;91(SUPPL. 1):95-101.

448. Palmoski MJ, Brandt KD. Aspirin aggravates the degeneration of canine joint cartilage caused by immobilization. Arthritis and rheumatism. 1982;25(11):1333-42.

449. Park H, Kong SY, Kim HW, Yang IH. Altered cellular kinetics in growth plate according to alterations in weight bearing. Yonsei medical journal. 2012;53(3):618-24.

450. Luan HQ, Sun LW, Huang YF, Wu XT, Niu H, Liu H, et al. Use of micro-computed tomography to evaluate the effects of exercise on preventing the degeneration of articular cartilage in tail-suspended rats. Life sciences in space research. 2015;6:15-20.

451. Wang Q, Zheng Y-P, Wang X-Y, Huang Y-P, Liu M-Q, Wang S-Z, et al. Ultrasound Evaluation of Site-Specific Effect of Simulated Microgravity on Articular Cartilage. Ultrasound in Medicine & Biology. 2010;36(7):1089-97.

452. Wuest SL, Calio M, Wernas T, Tanner S, Giger-Lange C, Wyss F, et al. Influence of Mechanical Unloading on Articular Chondrocyte Dedifferentiation. International Journal of Molecular Sciences. 2018;19(5).

453. Bullough PG. The role of joint architecture in the etiology of arthritis. Osteoarthritis and cartilage / OARS, Osteoarthritis Research Society. 2004;12 Suppl A:S2-9.

454. te Moller N. Development of an equine carpal groove model to study early changes in osteoarthritis - a pilot study. Osteoarthritis and Cartilage. 2018;26:S132-S3.

455. Smith RL, Carter DR, Schurman DJ. Pressure and shear differentially alter human articular chondrocyte metabolism: a review. Clinical orthopaedics and related research. 2004(427 Suppl):S89-95.

456. Lammi MJ, Inkinen R, Parkkinen JJ, Hakkinen T, Jortikka M, Nelimarkka LO, et al. Expression of reduced amounts of structurally altered aggrecan in articular-cartilage chondrocytes exposed to high hydrostatic-pressure. Biochemical Journal. 1994;304:723-30.

457. Athanasiou KA, Niederauer GG, Schenck RC. Biomechanical topography of human ankle cartilage. Annals of biomedical engineering. 1995;23(5):697-704.

458. Treppo S, Koepp H, Quan EC, Cole AA, Kuettner KE, Grodzinsky AJ. Comparison of biomechanical and biochemical properties of cartilage from human knee and ankle pairs. Journal of Orthopaedic Research. 2000;18(5):739-48.

459. van Donkelaar CC, Wilson W. Mechanics of chondrocyte hypertrophy. Biomechanics and modeling in mechanobiology. 2012;11(5):655-64.

460. Kiviranta I, Tammi M, Jurvelin J, Arokoski J, Saamanen AM, Helminen HJ. Articular-cartilage thickness and glycosaminoglycan distribution in the young canine knee-joint after remobilization of the immobilized limb. Journal of Orthopaedic Research. 1994;12(2):161-7.

461. Kerin A, Patwari P, Kuettner K, Cole A, Grodzinsky A. Molecular basis of osteoarthritis: biomechanical aspects. Cellular and Molecular Life Sciences. 2002;59(1):27-35.

462. Mankin HJ, Dorfman H, Lippiello L, Zarins A. Biochemical and Metabolic Abnormalities in Articular Cartilage from Osteo-Arthritic Human Hips1971 1971-04-01 00:00:00. 523-37 p.

463. Li L, Newton PT, Bouderlique T, Sejnohova M, Zikmund T, Kozhemyakina E, et al. Superficial cells are self-renewing chondrocyte progenitors, which form the articular cartilage in juvenile mice. FASEB journal : official publication of the Federation of American Societies for Experimental Biology. 2017;31(3):1067-84.

464. Dowthwaite GP, Bishop JC, Redman SN, Khan IM, Rooney P, Evans DJ, et al. The surface of articular cartilage contains a progenitor cell population. Journal of cell science. 2004;117(Pt 6):889-97.

465. Kozhemyakina E, Zhang M, Ionescu A, Ayturk UM, Ono N, Kobayashi A, et al. Identification of a Prg4-expressing articular cartilage progenitor cell population in mice. Arthritis & rheumatology (Hoboken, NJ). 2015;67(5):1261-73.

466. Wilson W, van Burken C, van Donkelaar C, Buma P, van Rietbergen B, Huiskes R. Causes of mechanically induced collagen damage in articular cartilage. Journal of

orthopaedic research : official publication of the Orthopaedic Research Society. 2006;24(2):220-8.

467. Jurvelin J, Kiviranta I, Tammi M, Helminen JH. Softening of canine articular-cartilage after immobilization of the knee-joint. Clinical orthopaedics and related research. 1986(207):246-52.

468. Tammi M, Saamanen AM, Jauhiainen A, Malminen O, Kiviranta I, Helminen H. Proteoglycan alterations in rabbit knee articular-cartilage following physical exercise and immobilization. Connective Tissue Research. 1983;11(1):45-55.

469. Videman T, Eronen I, Friman C. Glycosaminoglycan metabolism in experimental osteoarthritis caused by immobilization. The effects of different periods of immobilization and follow-up. Acta Orthop Scand. 1981;52(1):11-21.

470. Rubio-Martinez LM, Cruz AM, Gordon K, Hurtig MB. Mechanical properties of subchondral bone in the distal aspect of third metacarpal bones from Thoroughbred racehorses. American journal of veterinary research. 2008;69(11):1423-33.

471. Danova NA, Colopy SA, Radtke CL, Kalscheur VL, Markel MD, Vanderby R, et al. Degradation of bone structural properties by accumulation and coalescence of microcracks. Bone. 2003;33(2):197-205.

472. Bobinac D, Spanjol J, Zoricic S, Maric I. Changes in articular cartilage and subchondral bone histomorphometry in osteoarthritic knee joints in humans. Bone. 2003;32(3):284-90.

473. Young BD, Samii VF, Mattoon JS, Weisbrode SE, Bertone AL. Subchondral bone density and cartilage degeneration patterns in osteoarthritic metacarpal condyles of horses. American journal of veterinary research. 2007;68(8):841-9.

474. Squires GR, Okouneff S, Ionescu M, Poole AR. The pathobiology of focal lesion development in aging human articular cartilage and molecular matrix changes characteristic of osteoarthritis. Arthritis and rheumatism. 2003;48(5):1261-70.

475. Arkill KP, Winlove CP. Solute transport in the deep and calcified zones of articular cartilage. Osteoarthritis and cartilage. 2008;16(6):708-14.

476. Pouran B, Arbabi V, Bleys R, van Weeren PR, Zadpoor AA, Weinans H. Solute transport at the interface of cartilage and subchondral bone plate: Effect of micro-architecture. Journal of biomechanics. 2017;52:148-54.

477. Sauder DN. Interleukin 1. Archives of dermatology. 1989;125(5):679-82.

478. Lajeunesse D, Reboul P. Subchondral bone in osteoarthritis: a biologic link with articular cartilage leading to abnormal remodeling. Current opinion in rheumatology. 2003;15(5):628-33.

479. Whitton RC, Rose RJ. The intercarpal ligaments of the equine midcarpal joint .2. The role of the palmar intercarpal ligaments in the restraint of dorsal displacement of the proximal row of carpal bones. Veterinary Surgery. 1997;26(5):367-73.

480. Martin TJ, Seeman E. Bone remodelling: its local regulation and the emergence of bone fragility. Best Practice & Research Clinical Endocrinology & Metabolism. 2008;22(5):701-22.

481. Lories RJ, Luyten FP. The bone-cartilage unit in osteoarthritis. Nature Reviews Rheumatology. 2011;7(1):43-9.

482. van der Kraan PM, van den Berg WB. Chondrocyte hypertrophy and osteoarthritis: role in initiation and progression of cartilage degeneration? Osteoarthritis and Cartilage. 2012;20(3):223-32.

483. Bullough PG, Jagannath A. The morphology of the calcification front in articular cartilage. Its significance in joint function. J Bone Joint Surg Br. 1983;65(1):72-8.

484. Paukkonen K, Helminen HJ. Chondrocyte ultrastructure in exercise and experimental osteoarthrosis. A stereologic morphometric study of articular cartilage of young rabbits using transmission electron microscopy. Clinical orthopaedics and related research. 1987(224):284-8.

485. Borrelli J, Jr., Tinsley K, Ricci WM, Burns M, Karl IE, Hotchkiss R. Induction of chondrocyte apoptosis following impact load. J Orthop Trauma. 2003;17(9):635-41.

486. Williamson A, Chen A, Masuda K, Thonar EJMA, Sah R. Tensile mechanical properties of bovine articular cartilage: Variations with growth and relationships to collagen network components. Journal of Orthopaedic Research. 2003;21(5):872-80.

487. Oinas J, Ronkainen AP, Rieppo L, Finnilä MAJ, Iivarinen JT, van Weeren PR, et al. Composition, structure and tensile biomechanical properties of equine articular cartilage during growth and maturation. Scientific reports. 2018;8(1):11357.

488. Ma TW, Li Y, Wang GY, Li XR, Jiang RL, Song XP, et al. Changes in synovial fluid biomarkers after experimental equine osteoarthritis. Journal of Veterinary Research. 2017;61(4):503-8.

489. Hesse B, Varga P, Langer M, Pacureanu A, Schrof S, Männicke N, et al. Canalicular network morphology is the major determinant of the spatial distribution of mass density in human bone tissue: evidence by means of synchrotron radiation phase-contrast nano-CT. Journal of Bone and Mineral Research. 2015;30(2):346-56.

490. Qing H, Bonewald L. Osteocyte remodeling of the perilacunar and pericanalicular matrix. International Journal of Oral Science. 2009;1(2):59-65.

491. Kogawa M, Wijenayaka A, Ormsby R, Thomas G, Anderson P, Bonewald L, et al. Sclerostin regulates release of bone mineral by osteocytes by induction of carbonic anhydrase 2. Journal of Bone and Mineral Research. 2013;28(12):2436-48.

492. Lampi T, Dekker H, Ten Bruggenkate CM, Schulten E, Mikkonen JJW, Koistinen A, et al. Acid-etching technique of non-decalcified bone samples for visualizing osteocyte-lacuno-canalicular network using scanning electron microscope. Ultrastruct Pathol. 2018;42(1):74-9.

493. Dole NS, Mazur CM, Acevedo C, Lopez JP, Monteiro DA, Fowler TW, et al. Osteocyte-Intrinsic TGF-beta Signaling Regulates Bone Quality through Perilacunar/Canalicular Remodeling. Cell reports. 2017;21(9):2585-96.

494. Gotterbarm T, Breusch SJ, Schneider U, Jung M. The minipig model for experimental chondral and osteochondral defect repair in tissue engineering: retrospective analysis of 180 defects. Laboratory Animals. 2008;42(1):71-82.

APPENDICES

Appendix 1: Key to colours on individual value graphs

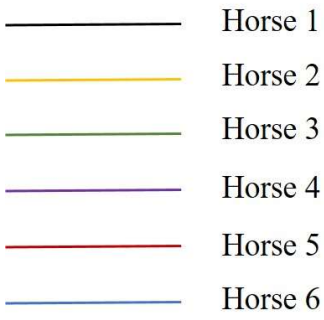

Figure A1.1 *Key to colours used for trial horses on all individual-value graphs.*

Appendix 2: Position of Cr defect on undecalcified sections

Horse	Position of defect (mm palmar to dorsal articular margin)	
	Dorsal boundary	**Palmar boundary**
1	3.9	9.8
2	3.4	11.4
3	4.8	14.4
4	2.8	8.0
5	3.5	8.0
6	5.0	9.5

Table A2.1 *Location of surgical lesion on Cr in undecalcified sections from individual horses, mm palmar to the dorsal articular margin in a line parallel to joint surface (see figure 4.1).*

Appendix 3: Osteocyte lacunae size, region below the lesion, Cr

BSEM images revealed the presence of subjectively larger osteocyte lacunae within some of the newly mineralised bone in the region deep to the lesion. These were most obvious in horses 1 and 2 (Figures A3.1 and A3.2).

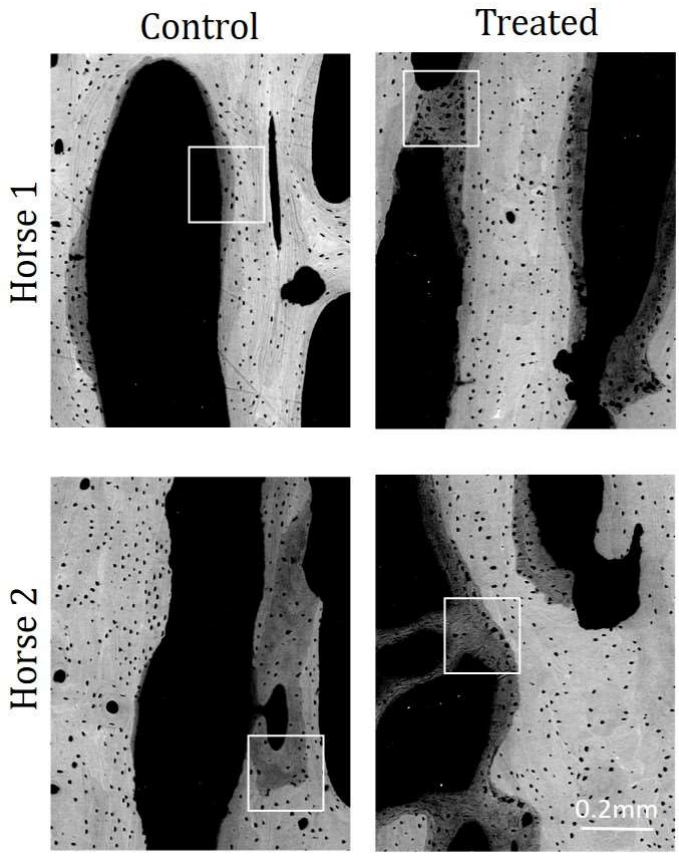

Figure A3.1 *Examples of larger osteocyte lacunae on BSEM images. Horses 1 (top) and 2 (bottom), control limbs on the left and treated on the right. All from the region 6-9mm deep to the cartilage. Areas in white boxes show area enlarged in Figure A3.2.*

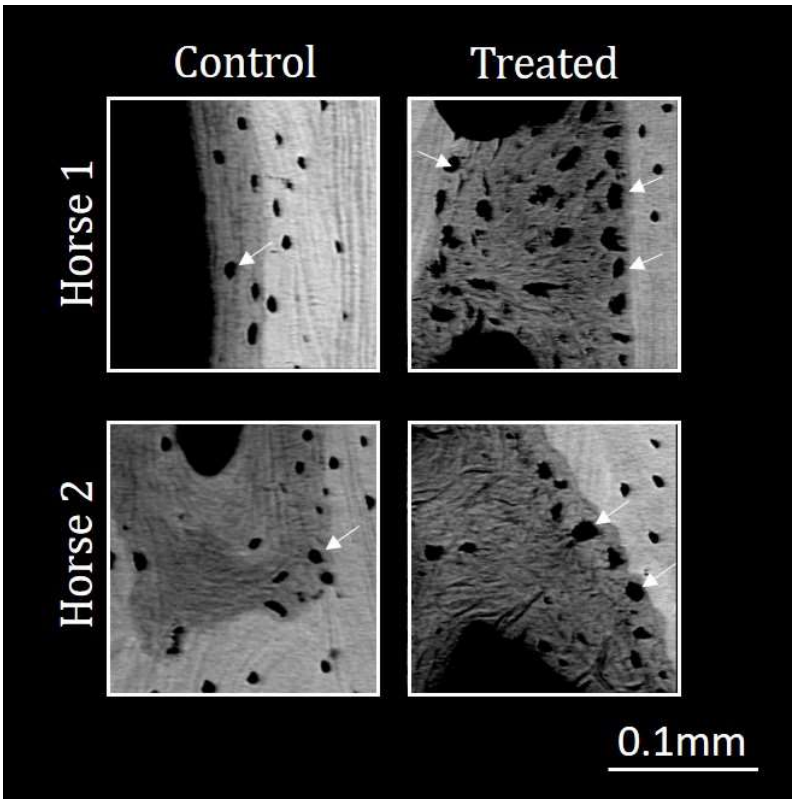

Figure A3.2 *Examples of variation in osteocyte lacunae size on BSEM images. Horses 1 (top) and 2 (bottom), control limbs on the left and treated on the right. All from the region 6-9mm deep to the cartilage. Images taken from areas shown in white boxes in Figure A3.1.*

Appendix 4: Incidental cartilage lesions

There were a number of cartilage lesions noted that were unlikely to be related to the experimental intervention. BSEM images revealed a bowl-shaped defect surrounded by a rim of increased mineralisation in the CC at 2.5mm palmar to the dorsal edge of the bone in Cr from the control limb of Horse 2 (Figure A4.1).

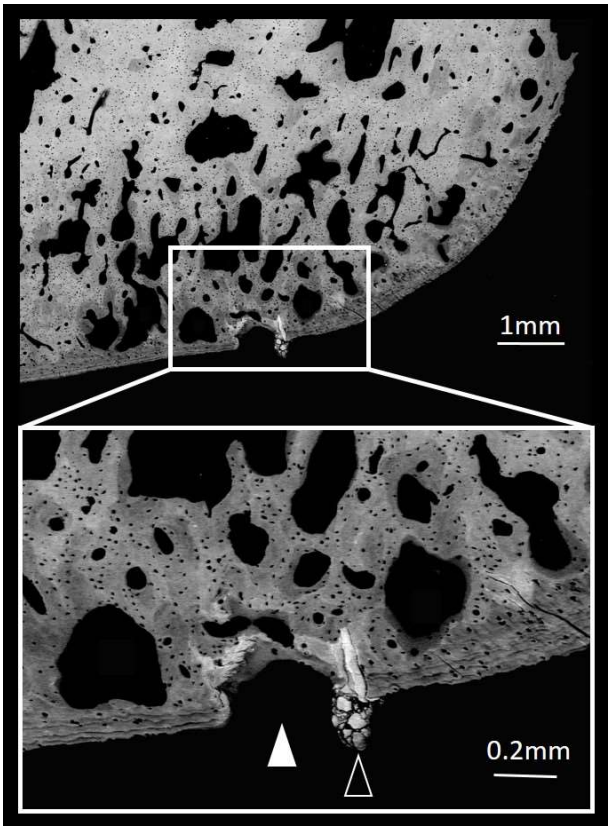

Figure A4.1 *Naturally occurring lesion (solid arrowhead) in the dorsal CC and SCB of Cr of the control limb of horse 2 associated with abnormal calcified tissue (open arrowhead). BSEM image.*

Microcracks associated with areas of increased mineralisation in the CC within the region opposing the lesion in C3 of the treated limb of Horse 6 were evident on BSEM (Figure A4.2), while bright-field images of unstained cryosections revealed an area of collapse of the CC and SCB, filled with cartilage, in the region opposing the edge of the defect (Figure A4.3). A region of increased mineralisation, cracking and thinning of the CC was also apparent in the weight bearing region of C3 from the control limb of Horse 6 (Figure A4.4).

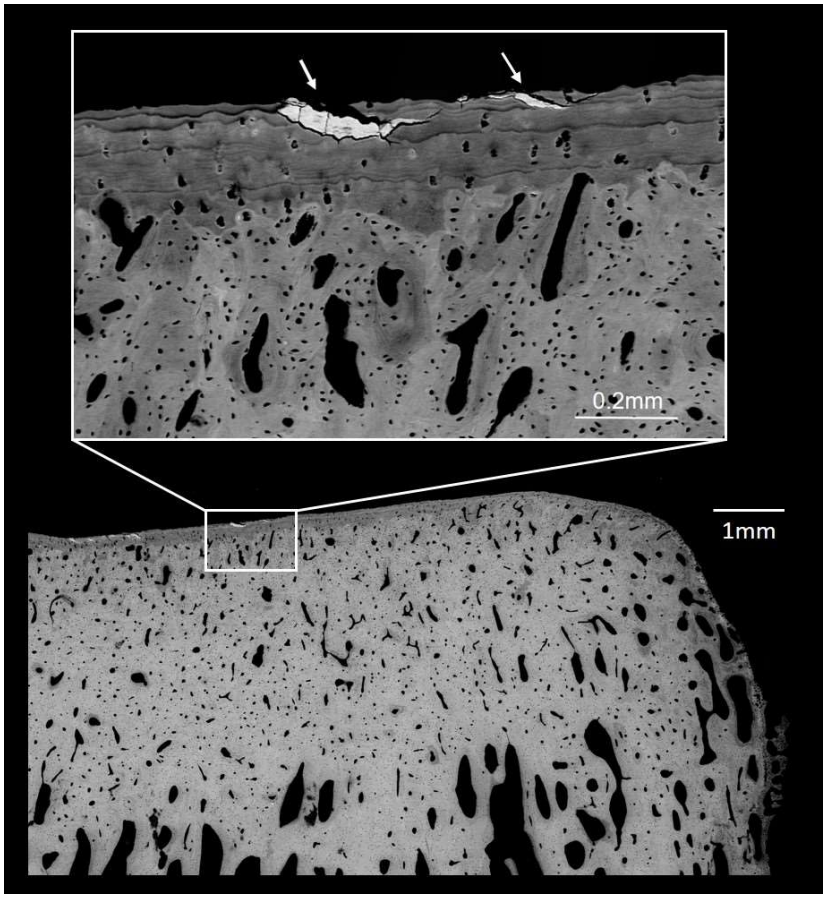

Figure A4.2 *BSEM image showing lesions (arrows) in the proximal CC of C3, in the region opposing the lesion in the treated limb of Horse 6.*

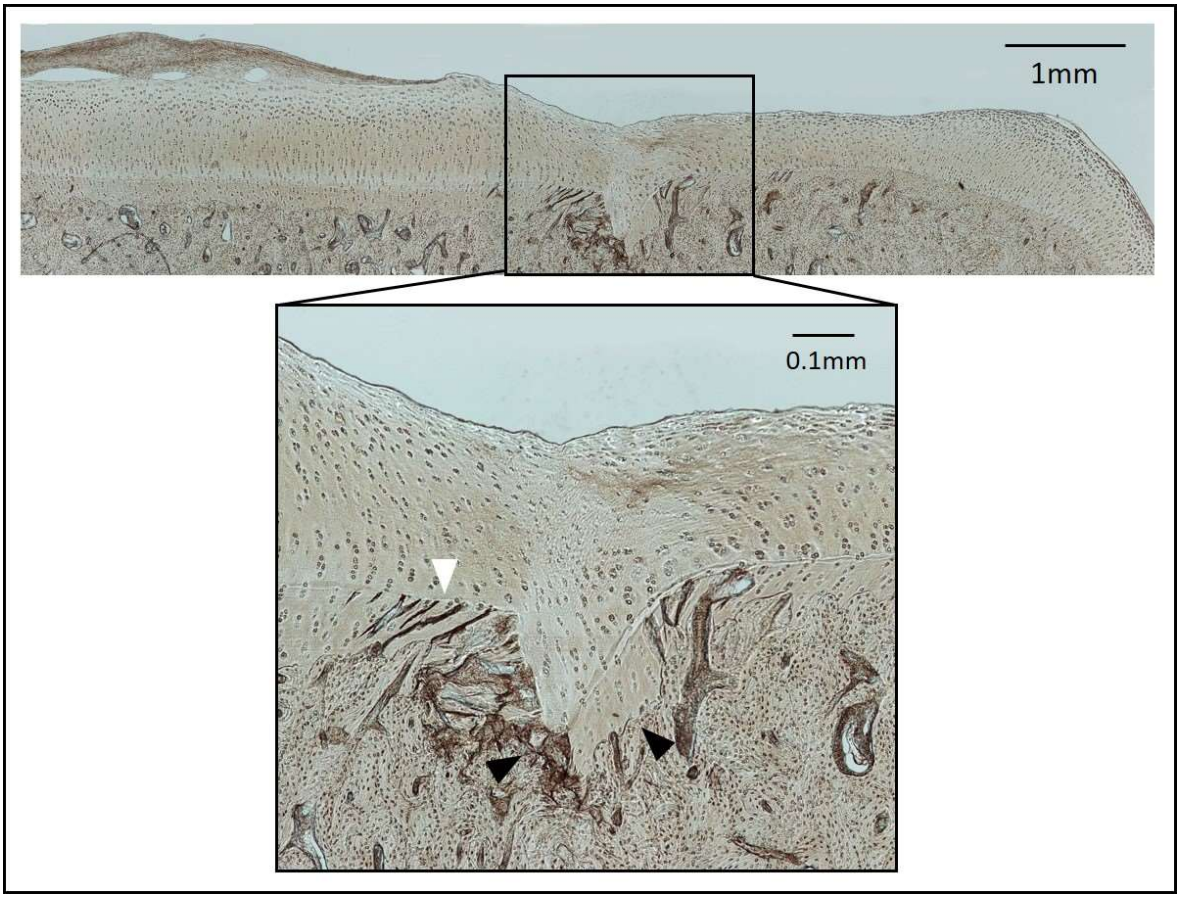

Figure A4.3 *Dorso-proximal articular surface of C3 from the treated limb of horse 6. The enlarged area shows collapse of the SCB and CC (black arrow heads) and microcracks in the adjacent CC (white arrow head) in the region opposite the edge of the osteochondral defect in Cr. Bright-field image of unstained 20um cryosections.*

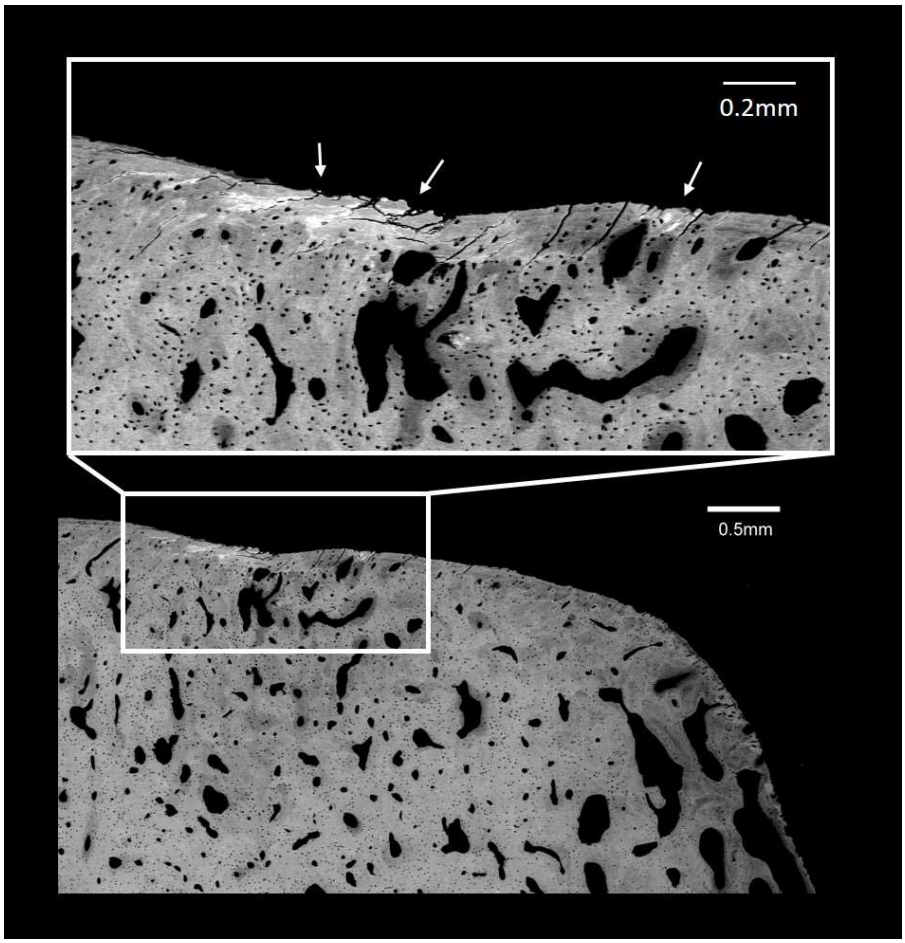

Figure A4.4 *BSEM image showing lesions (arrows) in the proximal CC of C3, in the weight bearing region of the control limb of Horse 6. Proximal to top, dorsal to right of image.*

The hyaline cartilage was intact in all untrained control joints. There was a v-shaped split in the CC of C3 from UC 2 in the region opposing the lesion which may have been artefact but was filled with resin, consistent in all sections and contained vacuolated matrix and non-viable chondrocytes suggesting that it was a pre-existing lesion (Figure A4.5). There was also a region of markedly thickened CC overlying highly mineralised SCB in the weight bearing region of Cr from UC 3 (Figure A4.6).

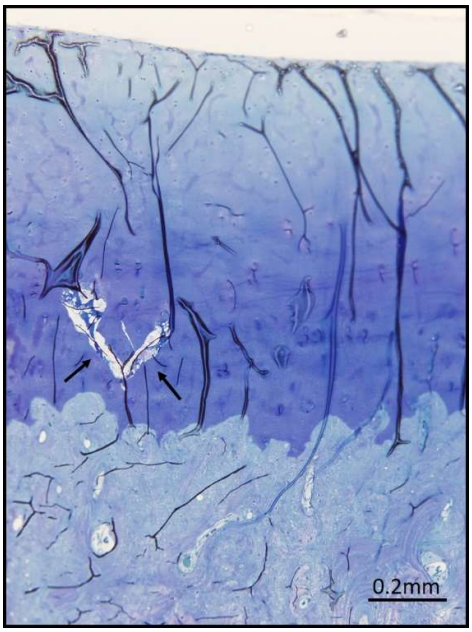

Figure A4.5 *Splitting of the CC in the region opposing the lesion of C3 of untrained control horse 2. Methylene blue stained semi-thin section, bright field image.*

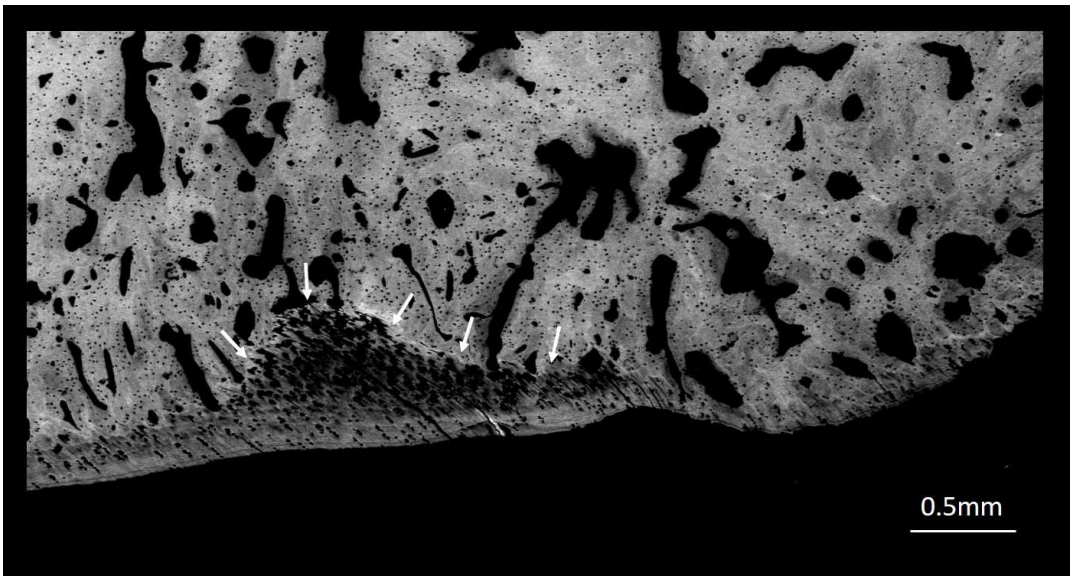

Figure A4.6 *Thickened, irregular CC (white arrows) in the dorsal region of Cr from untrained control horse 3. BSEM image. Proximal to top, dorsal to right of image.*